NOVEL FUNCTIONAL POLYOXOMETALATE (POM) MATERIALS: SYNTHETIC STRATEGIES AND APPLICATIONS

DISSERTATION
zur
Erlangung der naturwissenschaftlichen Doktorwürde
(Dr. sc. nat.)

vorgelegt der
Mathematisch-naturwissenschaftlichen Fakultät
der
Universität Zürich

von
LUBIN NI
aus
der V. R. China

Promotionskommittee
Prof. Dr. Greta R. Patzke (Vorsitz und Leitung)
Prof. Dr. Roland Sigel
Prof. Dr. Eva Freisinger

Zürich, 2013

Die vorliegende Arbeit wurde von der Mathematisch-naturwissenschaftlichen Fakultät der Universität Zürich im Herbstsemester 2013 als Dissertation angenommen.

Promotionskomitee: Prof. Dr. Greta R. Patzke (Vorsitz, Leitung der Dissertation)
Prof. Dr. Roland Sigel
Prof. Dr. Eva Freisinger

“As Heaven keeps vigor through movement, a gentleman should unremittingly practice self-improvement.”

《 *I Ching: Book of Changes*》

CONTENTS

1. General Introduction

2. Experimental Section

3. Lanthanoid-Containing Open Wells-Dawson Silicotungstates: Synthesis, Crystal Structures, and Properties

4. Trilacunary Keggin-type POMs as Versatile Building Blocks for Lanthanoid Silicotungstates

5. New Catalytic and Computational Perspectives for Polyoxometalate Design: Alcohol Oxidation with Zn/Sb-Polyoxotungstates

6. 1D- and 2D-architectures via self-assembly of the novel sandwich-type polyoxometalate $[Zn_2Sb_2(B\text{-}\alpha\text{-}ZnW_9O_{34})_2]^{14-}$

7. Zn/Sb-Polyoxotungstate Oxidation Catalysts with Tailored Cores: Structural, Computational and Reactivity Studies on a POM Family

Acknowledgments

Looking back over the last four years, I not only appreciate this precious and unforgettable experience in my life, but also I am very pleased to meet so many nice people who ever supported and encouraged me. Without all their assistance and kind help, it would have been impossible for me to accomplish my PhD work. Here I would like to acknowledge and extend my sincere gratitude to all of them.

First of all, I am deeply grateful to my supervisor Prof. Dr. Greta R. Patzke for offering me the opportunity to work with this challenging and interesting topic, for her patient teaching, careful guidance, constructive discussions, generous support and for all her kind suggestion throughout the whole time of my PhD studies. Moreover, I especially would like to express my gratitude to her for offering a creative research environment to develop my independent work. I am also grateful for her support concerning attendance of international conferences and workshops which provided me with good opportunities to enhance my knowledge and to expand my horizon.

I am indebted to Prof. Dr. Roland Sigel and Prof. Dr. Eva Freisinger as co-referees of this dissertation.

I would like to thank Prof. Dr. Kim K. Baldridge (Institute of Organic Chemistry, University of Zurich) for the important and fruitful collaboration concerning theoretical calculations. I am also grateful to Dr. Bernhard Spingler for his full support and valuable discussions about crystallographic data. I wish to thank Dr. Jörg Patscheider (Laboratory for Naoscale Materials Science, EMPA Dübendorf) for his generous support and constructive instructions with XPS measurements. I want to thank Dr. Stephen Weyeneth (Physics Institute, University of Zurich) for his full support with magnetic susceptibility measurements. Furthermore, I am grateful to Dr. Urs Stalder and Dr. Laurent Bigler (Institute of Organic Chemistry, University of Zurich) for ESI-MS measurements.

Special thanks go to Dr. Ferdinand Wild for his kind introduction to Raman and TG measurements, to Dr. Thomas Fox for his support regarding NMR measurements, and to Heinz Spring for conducting many elemental analyses.

I wish to thank Dr. Jae Kyoung Pak, Nathalie Fichter, Ramona Erni, Isabella Bieri, Beatrice Spichtig and Susanna Sprokkereef for their great help with administrative tasks as well as Manfred Jöhri and Dr. Ferdinand Wild for their support concerning electronics, hardware and software

My gratitude goes to all the present and former members of our group: Prof. Dr. Ying Zhou, Prof. Dr. Firasat Hussain, Dr. Franziska Conrad, Roman Kontic, Dr. Georg Geisberger, Dr. Min Sheng, Dr. Pierre-Emmanuel Car, Hongfei Liu, Debora Ressnig, Kim von Allmen, Fabio Evangelisti, Roger Jacot, Dr. René Moré, Michael Olah, Peter Bösiger, Dr. Yáng Zhèn, Robin Güttinger for the great and friendly working atmosphere, for their support and for all the amazing times we spent together.

I would like to thank Linlin Wu, Yuzhen Zhang, Wangqing Kong, Yujun Shen, Yanfen Jiang, Chunfang Jiang, Yan Li, Xianghua Yang, Xinjun Luan, Xia Meng, Hailin Dong and Kai Zhou for all kind help and for the recreative leisure activities.

From my heart, I wish to express to my special gratitude to my girlfriend Yuan Li for all her love, full support, encouragement and understanding so that I can face and overcome any difficulty in my life. And finally I must express my deepest appreciation to my parents Yujie Wang and Shijun Ni for their endless love, all kinds of support and care that I can always rely on.

This work was supported by the Swiss National Science foundation (SNSF Professorship PP002_114711/1, PP00P2_133483/1 and Sinergia Grant No. CRSII2_136205/1) and by the University of Zurich, which are gratefully acknowledged. Moreover, I would like to thank the China Scholarship Council for a PhD research fellowship and the Forschungskredit of the University of Zurich for doctoral level support.

Abbreviations

POM	Polyoxometalate
IPA	Isopolyanion
HPA	Heteropolyanion
LSPs	Lanthanoid substituted polyoxometalates
TMSPs	Transition-metal substituted polyoxometalates
SMMs	Single-molecule magnets
LMCT	Ligand-to-metal charge-transfer
FT-IR	Infrared spectroscopy
ATR FT-IR	Attenuated total reflectance fourier transform infrared spectroscopy
TGA	Thermogravimetric analysis
UV/Vis	Ultraviolet-visible spectroscopy
XPS	X-ray photoelectron spectroscopy
PXRD	Powder X-ray diffraction
SQUID	Superconducting quantum interference device
CV	Cyclic voltammetry
GCE	Glassy carbon electrode
ESI-MS	Electrospray ionisation mass spectrometry
GC-MS	Gas chromatography–mass spectrometry
NMR	Nuclear magnetic resonance
MRI	Magnetic resonance imaging
BVS	Bond valence sum calculations
PL	Photoluminescence

Publications

All parts of this PhD thesis have been published or are prepared for submission, and the individual chapters are based on the following publication or manuscript texts:

Chapter 3

Lubin Ni, Firsat Hussain, Bernhard Spingler, Stephen Weyeneth, and Greta R. Patzke*, Lanthanoid-Containing Open Wells-Dawson Sillcotungstates: Synthesis, Crystal Strctures, and Properties. *Inorg. Chem.* **2011**, 50, 4944–4955.

Chapter 4

Lubin Ni, Bernhard Spingler, Stephen Weyeneth, and Greta R. Patzke*, Trilacunary Keggin-type POMs as Versatile Building Blocks for Lanthanoid Silicotungstates. *Eur. J. Inorg. Chem.* **2013**, 1681–1692 (Special Issue: Polyoxometalates).

Chapter 5

Lubin Ni, Jörg Patscheider, Kim K. Baldridge*, and Greta R. Patzke*, New Perspectives on Polyoxometalate Catalysts: Alcohol Oxidation with Zn/Sb-Polyoxotungstates. *Chem. Eur. J.* **2012**, 18, 13293–13298.

Chapter 6

Lubin Ni, and Greta R. Patzke*, 1D- and 2D- architectures via self-assembly of the novel sandwich-type polyoxometalate $[Zn_2Sb_2(B\text{-}\alpha\text{-}ZnW_9O_{34})_2]^{14-}$. *CrystEngComm*. **2012**, 14, 6778–6782.

Chapter 7

Lubin Ni, Bernhard Spingler, Kim K. Baldridge*, and Greta R. Patzke*, Getting to the Core: Synthetic Control, Catalytic Activity and Reaction Pathways of Zn-Polyoxotungstate Oxidation Catalysts; to be submitted.

Synthesis, characterizations and catalytic tests of all Zn/Sb-POMs were performed by Lubin Ni, theoretical calculations were carried out by Prof. Dr. Kim K. Baldridge (Institute of Organic Chemistry, University of Zurich).

1. General introduction

Polyoxmetalates (abbreviated in the following as POMs) represent a large family of metal-oxygen clusters emerging from the condensation of polyhedra of transition metals of group V and VI (generally Mo, W, V) in their highest oxidation states to form large, closed 3D frameworks.[1] Currently, POM chemistry grows into an area of almost unmatched scope, not only in terms of molecular design and structural versatility,[2] but also regarding reactivity and relevance to analytical chemistry,[3] catalysis,[4] medicine,[5] photochemistry,[6] magneto-chemistry,[7] materials science and topology.[8]

1.1 History and development

The first report of a POM compound was made by *Berzelius* in 1826 who described the yellow precipitate that is produced when ammonium molybdate is added in excess to phosphoric acid to form the well known ammonium 12-phosphomolybdate $(NH_4)_3[PMo_{12}O_{40}]_{(aq)}$.[9] The composition of such materials was not elucidated until the discovery of the tungstosilicic acids and their salts by *Marignac* in 1864. The analytical composition of the 12:1 heteropolyanion species (HPA) was precisely determined,[10] but for many years the structures of such heteropolyanions remained largely unknown. The first attempt to understand the composition of heteropolyanions was made by *Werner* who tried to explain the structures of 12:1 species on the basis of his highly recognized new theory on coordination chemistry.[11] In 1909, *Werner* suggested that the metal atoms were connected through several oxygen atoms thus anticipating edge and face-sharing polyhedra.[12] This was also expressed as a structural hypothesis by *Miolati* and *Pizzighelli* in 1908 [13] and further developed by *Rosenheim* who conducted a systematic study of heteropolyanions during the first 35 years of the 20th century. In the *Miolati-Rosenheim* (MR) theory, the 12-molybdophosphoric acid was viewed as a derivative of the hypothetical acid $H_7[PO_6]$ through the replacement of the oxygen atoms by Mo_2O_7 groups.[13] The MR structural hypothesis which shed new lights on this initially complicated field of POM chemistry, prevailed until the late 1920s because of the lack of appropriate analytical methods. In 1929, *Pauling* proposed a different structure based on the crystal radii of the metal ions Mo^{6+} and W^{6+} being appropriate for octahedral coordination.[14] The resulting MO_6 octahedra combine by corner sharing with the 36 remaining oxygen ions each taking up a hydrogen ion to stabilize the negative charge. The 12-tungstosilicic acid expressed as $[SiO_4W_{12}O_{18}(OH)_{36}]$ which *Pauling* elaborated later turned out to be incorrect because he did not consider the possibility of edge-sharing between MO_6 octahedra, even if the structure was much closer to reality than models suggested by MR theory. Only four years after *Pauling*'s theory, the correct crystal structure of $H_3[PW_{12}O_{40}]\cdot5H_2O$ was solved by *Keggin* in 1933 using X-ray diffraction methods, (Figure 1.1a).[15] The discovery that 12-tungstophosphoric acid consists of MO_6 octahedra linked by both corner and edge sharing interactions was a first milestone in POM chemistry so that this structure type was named after *Keggin*. Following this discovery, many other fundamental POM motifs, such as the *Wells-Dawson* (Figure 1.1b),[16] *Anderson* (Figure 1.1c),[17] *Lindqvist* (Figure 1.1d),[18] *Waugh* (Figure 1.1e),[19] and *Preyssler* types (Figure 1.1f) [20] were gradually found, and their chemistry and applications were also explored.

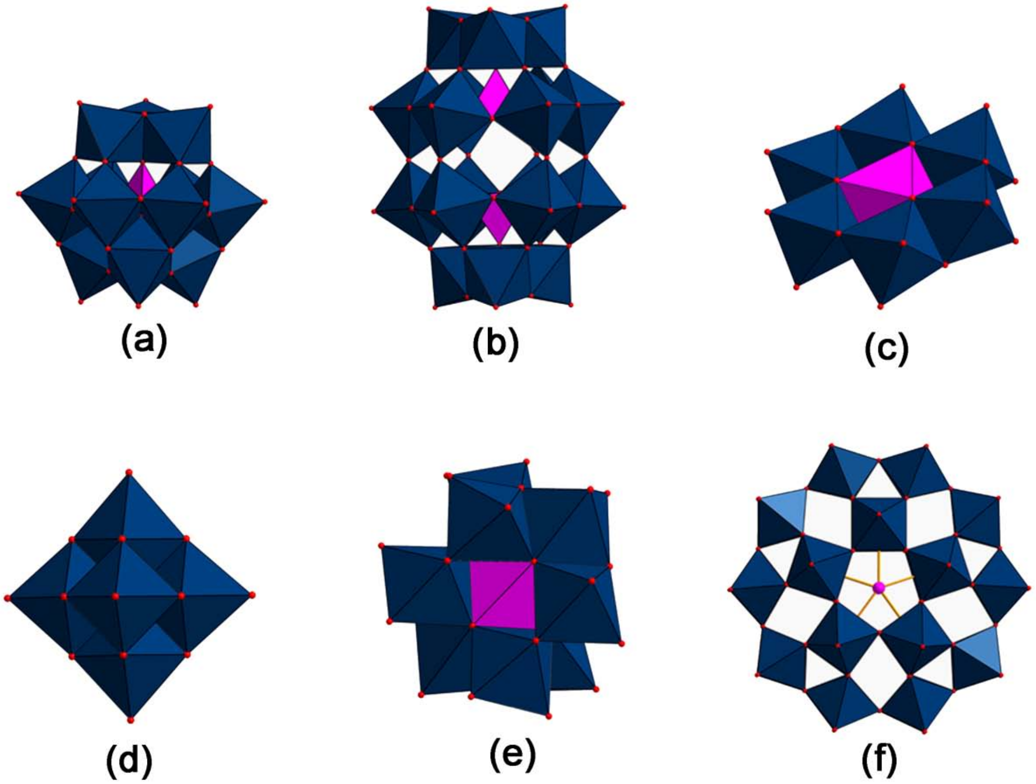

Figure 1.1. Polyhedral representations of basic POM structures: (a) *Keggin*, (b) *Wells-Dawson*, (c) *Anderson*, (d) *Lindqvist*, (e) *Waugh*, (f) *Preyssler*.

Since the early 70’s, many important analytical methods, such as FT-IR, Raman and multinuclear NMR spectroscopy have been extensively used. Meanwhile, the developments of laboratory single-crystal X-ray diffraction techniques has considerably facilitated molecular structure determinations. So far, many remarkable giant polyoxoanions, *e.g.* *Müller*'s classic {Mo_{386}}-POM (Figure 1.2a),[21] *Pope*'s tungstate {W_{148}}-POM (Figure 1.2b),[22] the recently reported {W_{124}}-POM (Figure 1.2c),[23] and *Wang*’s niobate {$Nb_{32}O$}-polyoxoniobate (PON) (Figure 1.2d),[24] have been isolated and then fully characterized to significantly enrich the world of POM chemistry.

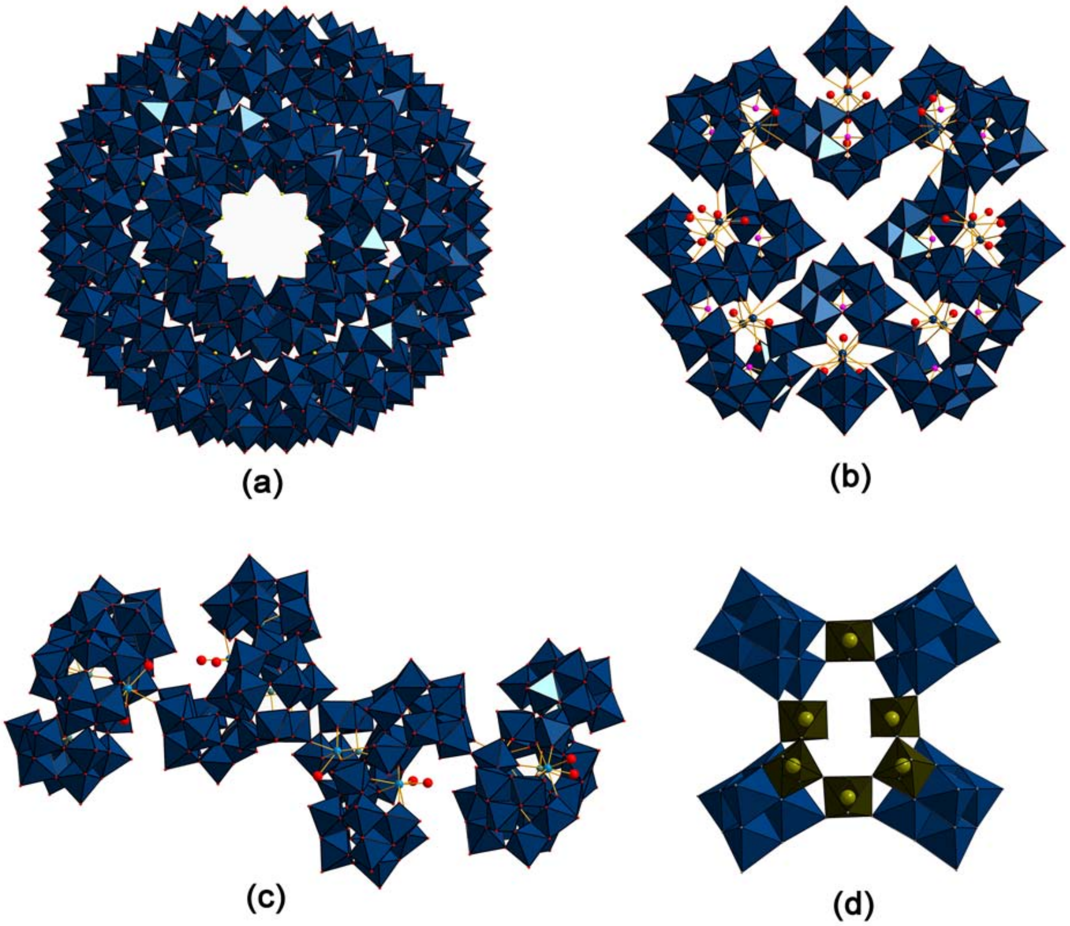

Figure 1.2. Some typical giant polyoxoanion structures in polyhedral representation: (a) {Mo_{386}}-POM, (b) {W_{148}}-POM, (c) {W_{124}}-POM, (d) {$Nb_{32}O$}-PON.

1.2. POM structure types

Polyoxometalates are metal-oxygen clusters which contain highly symmetrical assemblies of MO_X core units, giving rise to a variety of quasi-spherical structures.

Usually, POMs can be classified into two main groups, namely isopolyanions and heteropolyanions (Scheme 1.1):[1]

$[M_mO_y]^p$ Isopolyanion (IPA),

$[X_xM_mO_y]^q$ Heteropolyanion (HPA),

Scheme 1.1. Molecular formula of isopolyanions and heteropolyanions (M = host metal, O = oxygen, X = heteroatom).

Typically the isopolyanionic framework (such as *Lindqvist*-type polyanion $[M_6O_{19}]^{2-}$ or paratungstate $[M_{12}O_{42}]^{12-}$) is composed of one type of metal atom M (termed as the "host atom”), which are often transition metals from group V and VI (Mo, W, V, and Nb). There appears to be a natural limitation to elements suitable for POM formation which is dictated by a combination of ionic radius, charge and the ability to form d_π-p_π M-O bonds. Heteropolyanions clusters usually possess one to two hetero atoms X (eg. Si, P, Ge, Sb, As) which are located in the center of the framework, e.g. P in the *Keggin*-type $[PW_{12}O_{40}]^{3-}$ and Si in the *Wells-Dawson* type polyanion $[Si_2W_{18}O_{62}]^{6-}$. Hitherto, the *Keggin* and *Wells-Dawson* structures are two major structural families of polyoxotungstates, which are both most widely studied structures.

1.2.1. Keggin and lacunary Keggin structures

Keggin-type POMs $[XM_{12}O_{40}]^{q-}$ with tetrahedral T_d symmetry, generally consist of a central XO_4 tetrahedral unit surrounded by 12 MO_6 octahedral units, which are arranged into four groups of three edge sharing M_3O_{13} units called triads (Figure 1.3). Each triad is formed by three edge shared MO_6 octahedra with a central μ_4-oxygen bridge linking to the central tetrahedral XO_4. These four triads are connected to each other via corner sharing oxygen atoms.

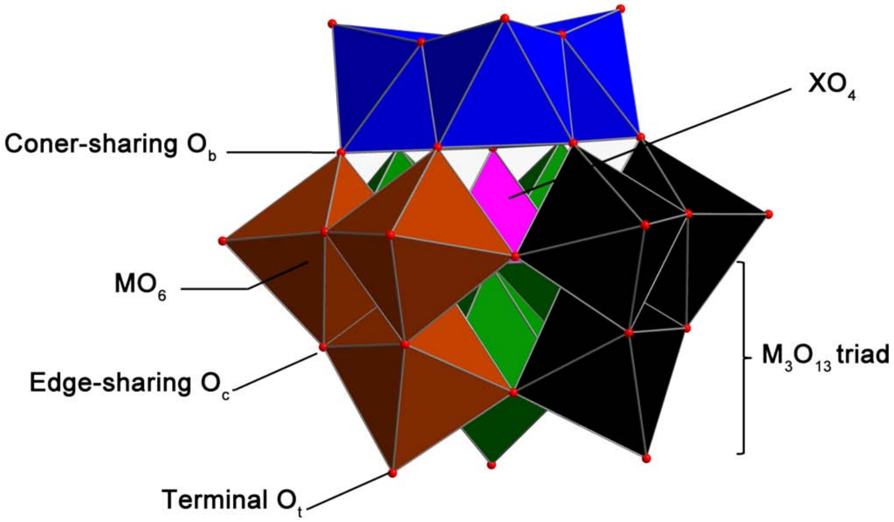

Figure. 1.3. Polyhedral representation of the *Keggin* anion showing the four triads M_3O_{13} in four different colors surrounding the central tetrahedron XO_4 in pink, and assignment of different oxygen types in the *Keggin* anion.

It was later found by *Baker* and *Figgis* that each M_3O_{13} triad of the α-isomer can be rotated by 60º about its 3-fold axis which gives rise to new geometrical isomers: β-isomer (one M_3O_{13} rotated), γ-isomer (two M_3O_{13} rotated), δ-isomer (three M_3O_{13} rotated), and ε-isomer (all four M_3O_{13} rotated), respectively (Figure 1.4).[25] The α-isomer is the most stable and common species of the five isomers. In comparison to the α-isomer (T_d), the β-isomer with lowered symmetry (C_{3v}) has shorter W···W distances and narrowed W-O-W angles between the rotated triad and the rest of the polyanion, resulting in increased Coulomb repulsion and less favorable p_π-d_π interactions. These render the β-isomer less stable than α-isomer. For the same reasons, the γ-isomer (C_{2v} symmetry), δ-isomer (C_{3v} symmetry), and ε-isomer (T_d symmetry) are even less stable.[1] The stability of each isomer is also dependent on the heteroatom: the isomerization from β- to α-isomer for X= Si(IV) or Ge(IV) is known to be slower than that for X= P(V) or As(V).

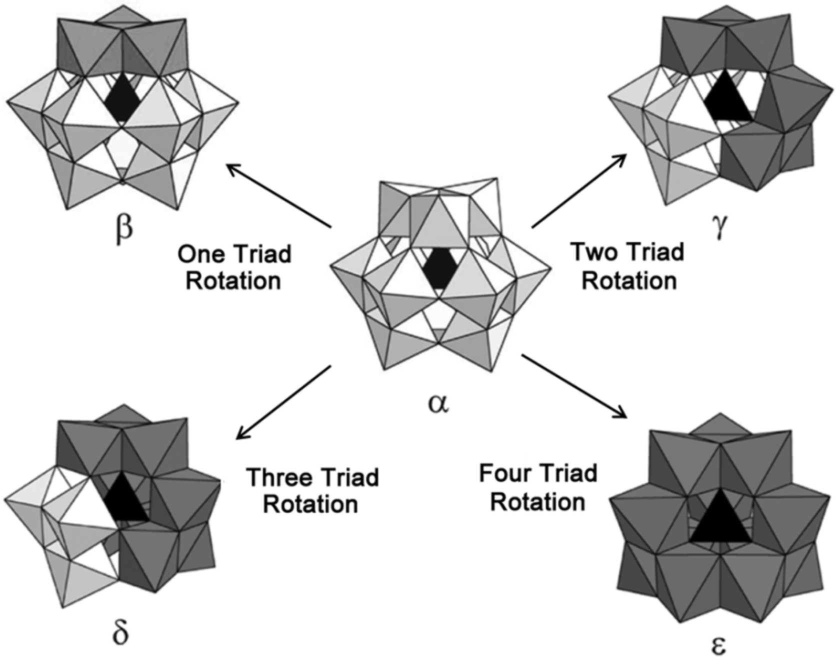

Figure 1.4. The *Baker-Figgis* isomers of the *Keggin* parent *α*-isomer. Rotation of one, two, three or four M_3O_{13} triad by 60^oC produces the *β*-, *γ*-, *δ*-, and *ε*-isomers, respectively.

Usually, the “plenary” *α*- and *β-Keggin* isomers are stable under acidic conditions (lower pH value), but a series of hydrolysis reactions can occur at a higher pH values. A “lacunary” *Keggin* polyanion can be formed when a plenary molecule loses one or more framework atoms (e.g. W) through controlled basic hydrolysis. The common *Keggin*-based lacunary polytungstosilicates as well as their reaction patterns are summarized in Figure 1.5.[1] With the removal of one or more $\{WO_x\}$ units from the parent structure *α-Keggin* $[SiW_{12}O_{40}]^{4-}$, defective POMs (mono-, di-, or tri-lacunary) are formed. These synthetic procedures were well described by *Tézé* and *Hervé*,[26] and were applied for precursor preparation in the course of this thesis. A general *Keggin* silicotungstate hydrolysis reaction is summarized as follows:

$$[SiW_{12}O_{40}]^{4-} + m\ OH^- \rightarrow [SiW_{12-x}O_{40-y}]^{q-} + x\ WO_4 + n\ H_2O$$

(mono-lacunary for x=1; di-lacunary for x=2, tri-lacunary for x=3)

For example, the mono-lacunary $[SiW_{11}O_{39}]^{8-}$ $\{SiW_{11}\}$ is obtained from loss of one $[W{=}O]^{4+}$ unit at *ca.* pH 4.5. Only one mono-lacunary *α*-$[SiW_{11}O_{39}]^{8-}$ isomer with reduced C_s symmetry can be formed from the parent *Keggin* ion (T_d symmetry), whereas there are three β_1-, β_2- and β_3-isomers with C_s, C_1, C_s symmetry, respectively (Figure. 1.5).[27] This is due to a symmetry reduction of the *β-Keggin* isomer {SiW_{12}} from T_d to C_{3v}, so that the four triads are not equivalent any more. Accordingly, mono-lacunary *β-Keggin* species {SiW_{11}} can be prepared by removing one WO_6 octahedron from three different positions (Figure 1.5): the β_3 position is from the rotated, edge-shared 'cap' triad; the β_2 position is from the 'belt' tungsten; β_1 position is from the 'base' corner shared triad. The $[\beta_2\text{-}SiW_{11}O_{39}]^{8-}$ isomer is the only chiral mono-lacunary precursor, and *Hervé* and *Tézé* first pointed out its existence on the basis of polarographic and spectroscopic measurements in 1977.[28] But it was not until 2007 when *Kortz* isolated for the first time single crystals of the lanthanoid substituted sandwich-type mono-lacunary *β₂-Keggin* polyanions $[Ln(\beta_2\text{-}SiW_{11}O_{39})_2]^{13-}$ (Ln = La, Ce, Sm, Eu, Gd, Tb, Yb, Lu). [29]

Moreover, there are two types of tri-lacunary *Keggin* POMs species $[SiW_9O_{34}]^{10-}$ which are assigned as *A*- and *B*-types (Figure 1.6). The *A*-$[SiW_9O_{34}]^{10-}$ type is formed by removing three corner-sharing WO_6 octahedra from three neighboring W_3O_{13} triads. The *B*-$[SiW_9O_{34}]^{10-}$ type is formed by removing an edge-sharing 'cap' W_3O_6. Meanwhile, unlike the *A*-type, there are three linking μ_4-oxygen bridges of the central SiO_4 tetrahedron to three W_3O_{13} triads and one free oxygen pointing out of the lacuna in the *B*-type. Some tri-lacunary polyanions have also been isolated with a central pyramidal geometry and a lone pair on the heteroatom, such as $[Sb^{III}W_9O_{33}]^{9-}$ or $[As^{III}W_9O_{33}]^{9-}$. They exist exclusively in the *B*-type, and are unable to undergo further conversion to the {SbW_{11}} species due to the repulsion exerted by the lone pair of electrons.[30]

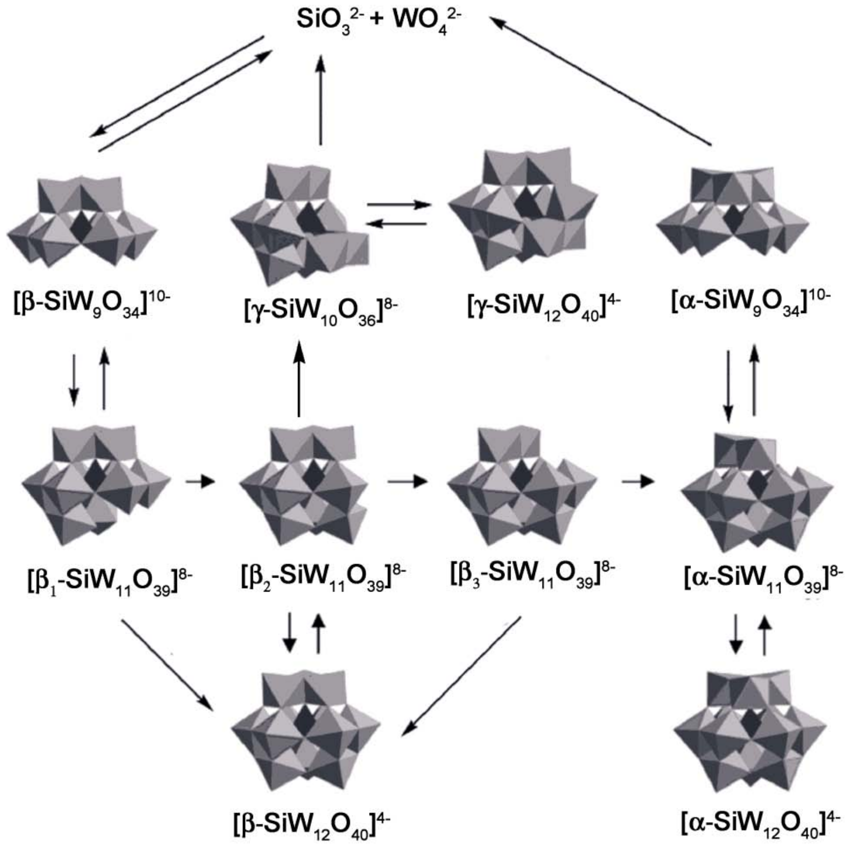

Figure 1.5. General synthetic routes and isomerizations of *Keggin*-based lacunary polysilicotungstates [1].

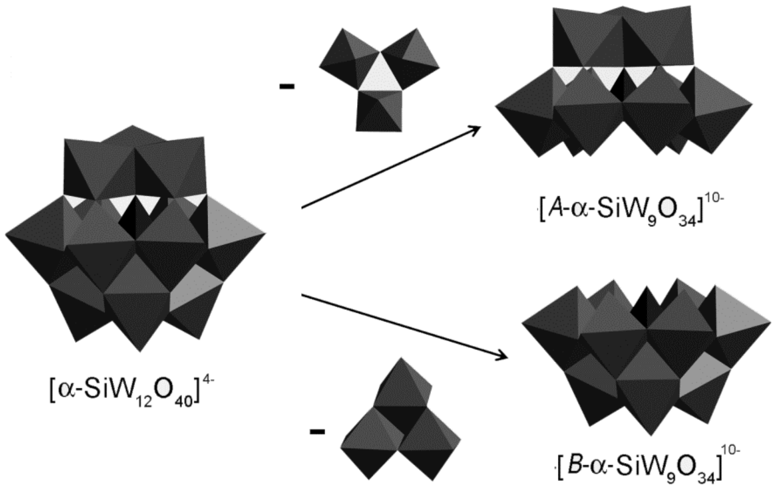

Figure 1.6. Structural illustration of the conversion of the *Keggin* ion $[a\text{-SiW}_{12}O_{40}]^{4-}$ into the tri-lacunary polyanions $[A\text{-}\alpha\text{-SiW}_9O_{34}]^{10-}$ or $[B\text{-}\alpha\text{-SiW}_9O_{34}]^{10-}$.

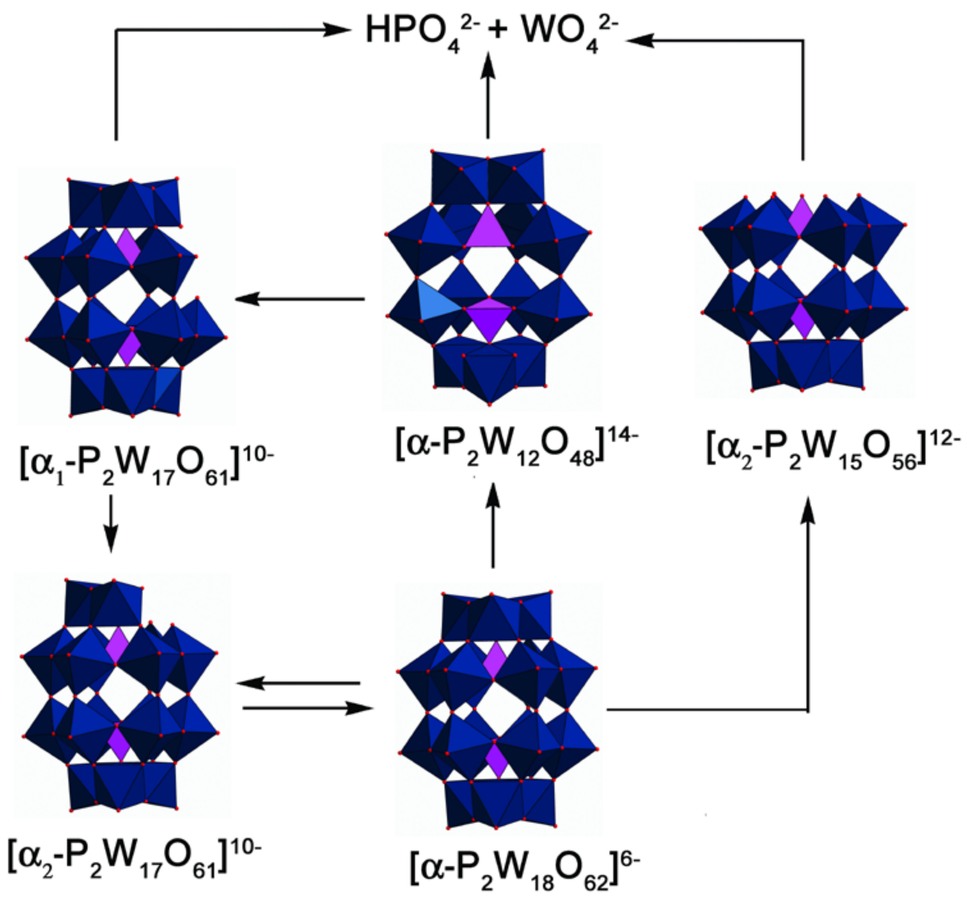

Figure 1.7. General synthetic routes towards the different lacunary *Wells-Dawson* polytungstodiphosphate species.[1]

1.2.2. Wells-Dawson type POMs

The *Wells-Dawson* structure represents another major structural family in POM chemistry with the general formula $[X_2M_{18}O_{62}]^{n-}$ (M= W or Mo; X= As, Sb, P, Si).[16] The polyanion is viewed as a combination of two tri-lacunary *Keggin* *A*-*α*-{XW_9} units by sharing corner oxygen atoms of the lacuna, resulting in a virtual D_{3h} symmetry cluster of the *α*-isomer type. In the case of the *Wells-Dawson* silicotungstate $[Si_2W_{18}O_{62}]^{8-}$, two sets of W atoms and two Si heteroatoms construct this polyanion: the two “cap” M_3O_{13} triads containing six “polar” W and the two belts M_6O_{14} containing twelve “equatorial” W; where the SiO_4 tetrahedra coordinate one caps and one belts each (Figure 1.7). The lacunary *Wells-Dawson* structures can also be prepared by adjusting the alkaline pH value in solution. There are two mono-lacunary isomers derived from the *α-Well-Dawson* structure. The α_2-isomer, $[\alpha_2\text{-}P_2W_{17}O_{61}]^{10-}$, is obtained by removing one WO_6 octahedron from the cap W_3O_{13} triad of the $[\alpha\text{-}P_2W_{17}O_{62}]^{6-}$. The α_1-isomer has a lacunary site in the belt position and can only be prepared by adding WO_6 octahedra to a hexa-lacunary *Well-Dawson* structure $[\alpha\text{-}P_2W_{12}O_{48}]^{14-}$.[31] The hexavacant POM is formed by removing six WO_6 units along the C_3 axis of the $[\alpha\text{-}P_2W_{17}O_{62}]^{6-}$. The common tri-lacunary $[P_2W_{15}O_{56}]^{12-}$ is formed by the removal of one of the cap M_3O_{13} triads from the parent structure. The formation and conversion of these species is shown in Figure 1.7.

1.2.3. Sandwich-type and open Wells-Dawson structures

Lacunary POMs can incorporate transition metals or lanthanide metals in their open sites, which further affords transition-metal substituted POMs (TMSPs) or lanthanoid substituted POMs (LSPs).

Among the transition-metal substituted polyoxometalates, the sandwich-type TMSPs represent the largest subclass and currently attract more and more attention due to their highly tunable structural nature as well as due to their potential applications in diverse fields of catalysis, medicine and electrochemistry.[2-8] The lacunary *Keggin* and *Wells-Dawson* polyanions are frequently used as precursors for self-assembly into these sandwich-type structures. The first sandwich-type polyoxoanion was discovered by *Weakley* et al. in 1973[32]. It is formed between two tri-lacunary *Keggin* moieties $\{PW_9O_{34}\}$ linked by four Co centers to form sandwich-type polyanion $[Co_4(H_2O)_2(B\text{-}\alpha\text{-}PW_9O_{34})_2]^{10-}$, also known as *Weakley* or *Tourné* structures. The most common sandwich-type POMs are composed of a dimeric framework derived from tri-vacant *B-α-Keggin* fragments $[XW_9O_{33}]^{n-}$ or $[XW_9O_{34}]^{n-}$, which can further be divided into two subgroups (see Figure 1.8). [30, 32]

(a). Central heteroatom X with no lone pair and four M center cations:

$\mathbf{[M_4(H_2O)_2(\mathit{B}\text{-}\alpha\text{-}XW_9O_{34})_2]^{n-}}$ X = P^{V}, Si^{IV}, Ga^{III}, Zn^{II}, Ni^{II}, As^{V}, etc;

(b). Central heteroatom X with a lone pair and TM central belt maximally comprising 6 M cations:

$\mathbf{[(M_mM'_{m-6}(\mathit{B}\text{-}\alpha\text{-}XW_9O_{33})_2]^{n-}}$ X =Bi^{III}, As^{III}, Sb^{III}, Te^{IV}, etc

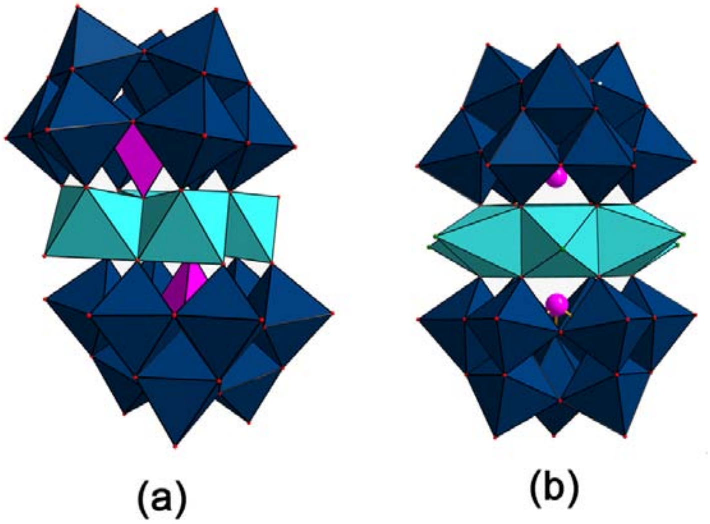

Figure 1.8. Polyhedral representation of two subgroups of sandwich-type POMs based on *Keggin* tri-lacunary moieties.

Since *Weakley* found the first sandwich-type polyoxoanionin in 1973, many mono-, bi- and multi-supported *Keggin* or *Dawson* polyanions have been characterized. During the 1980s to 1990s, sandwich-type polyanions based *Keggin* units were investigated by different research groups. For example, *Knoth* and coworkers first reported the sandwich-type polyanions $[M_3(A\text{-}\alpha\text{-}XW_9O_{34})_2]^{n-}$ (M= Cu^{II}, Co^{II}, Mn^{II}; X= P^{V}) comprising two $\{A\text{-}\alpha\text{-}XW_9O_{34}\}$ units linked by a belt of three metal centers (Figure 1.9a).[33] Meanwhile, the first representative of tri-lacunary *Keggin*-type lanthanoid substituted sandwiched polyoxometalate (LSPs) $[Ce_3O_3(H_2O)_2(A\text{-}\alpha\text{-}XW_9O_{34})_2]^{12-}$ was also reported by *Knoth* (Figure 1.9a).[33b] The synthesis of the so-called “banana” shaped, double-sandwich polyanions $[M_6(B\text{-}\alpha\text{-}XW_6O_{26})(B\text{-}\alpha\text{-}XW_9O_{34})_2]^{n-}$ was introduced in 2003 by *Kortz* and *Nadjo* [34] and later described by *Hill*.[35] This structure can be interpreted as a sandwich-type POM in which two *Keggin* entities, $\{M_3XW_9O_{34}\}$ are bridged via a hexavacant $\{XW_6O_{26}\}$ moiety as depicted in Figure 1.9b.

In 1987, the first sandwiched tri-lacunary *Dawson* POM was synthesized by *Finke* et al.[36] It is formed from two trivacant *Dawson* moieties $[P_2W_{15}O_{56}\}^{12-}$ linked by four Co centers to form $[M_4(H_2O)_2(P_2W_{15}O_{56})_2]^{16-}$ (Figure 1.9c). In the late 1990s and early 2000s, the number of newly synthesized *Dawson* POMs significantly increased. In 2003, *Hervé* and coworkers firstly characterized the open *Wells-Dawson* polyanion $[\alpha\text{-}SiW_{18}O_{66}]^{16-}$

which was built up from two *A*-*α*-$\{SiW_9O_{34}\}$ subunits by the breaking of four of the six corner-sharing oxygen atoms of the lacuna, leading to an “open” pocket between the two subunits with a C_{2v} symmetry.[37] In the course of follow-up reactions, the open *Wells-Dawson* anion can intercalate different transition metal cations into the pocket, resulting in various coordination modes (Figure 1.9d).[38]

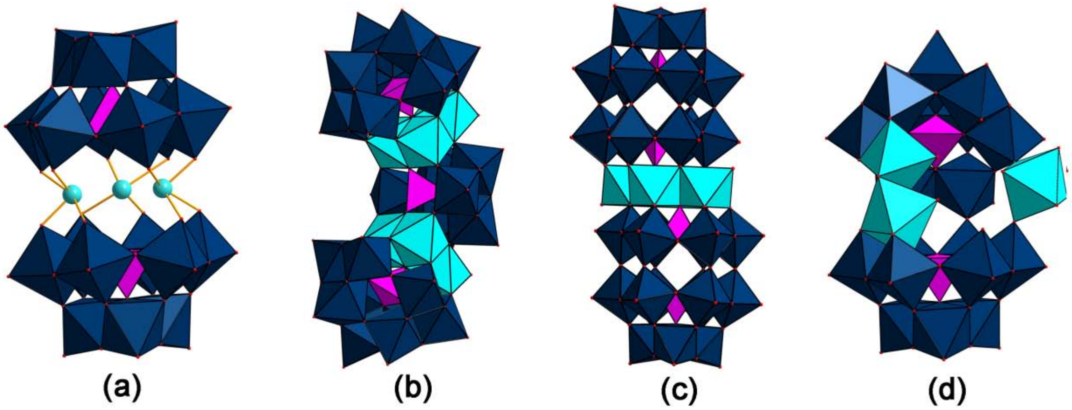

Figure 1.9 Some combined structures of POMs: (a) sandwiched POM based on *A*-*α*-*Keggin* moieties, (b) “banana” shaped double-sandwich structure, (c) sandwich based *Dawson* moieties, (d) TM-substituted open *Wells-Dawson* structure.

During the last few years, the number of newly synthesized POM structures significantly increased due to the developments of new instruments and novel synthetic approaches, which further accelerated the extensive studies of many aspects of the POM chemistry, especially in catalysis, magnetism and photochemistry.

1.3. Applications of POMs

1.3.1. POMs as catalysts in organic synthesis

POMs-based catalysts have been used in several industrial processes since the 1970s (Table 1.1).[4a] The oxidation procedures summarized in Table 1.1 encompass heterogeneous oxidation process of methacrolein to methacrylic acid and ethylene to acetic acid in the gas phase.[39] The remaining processes are acid-catalyzed reactions, such as the homogeneous hydration of olefins, propene and butene to yield alcohols, and biphasic polymerization of tetrahydrofuran to poly-(tetramethylene glycol) and the gas-phase reaction of acetic acid with ethylene to ethyl acetate.[40]

Table 1.1 Industrial processes catalyzed by POM-based catalysts.[4a]

Reaction	Catalyst	Type of catalysis[a]	Date
$CH_2{=}C(CH_3)CHO + O_2 \longrightarrow CH_2{=}C(CH_3)COOH$	Mo-V-P-HPA	Het	1982
$CH_2{=}CH_2 + O_2 \longrightarrow CH_3COOH$	Pd-$H_4SiW_{12}O_{40}/SiO_2$	Het	1997
$CH_2{=}CHCH_3 + H_2O \longrightarrow CH_3CH(OH)CH_3$	$H_4SiW_{12}O_{40}$	Hom	1972
$CH_2{=}C(CH_3)_2 + H_2O \longrightarrow (CH_3)_3COH$	$H_4PMo_{12}O_{40}$	Hom	1984
$CH_3CH{=}CHCH_3 + H_2O \longrightarrow CH_3CH(OH)CH_2CH_3$	$H_4PMo_{12}O_{40}$	Hom	1989
$nTHF + H_2O \longrightarrow HO{\left[(CH_2)_4{-}O\right]}_nH$	$H_4PW_{12}O_{40}$	Bip	1985
$CH_2{=}CH_2 + CH_3COOH \longrightarrow CH_3CH_2OOCCH_3$	$H_4SiW_{12}O_{40}/SiO_2$	Het	2001

[a] hom, homogeneous; het, heterogeneous; bip, biphasic.

POMs-based catalysts have currently attracted much more attention because of their high potential for "Green Chemistry" processes. POMs excel through structural versatility and accessibility, and their unique properties include variable oxidation states, strong Brønsted acidity, high proton mobility, tunable redox potential, high solubility in various solvents and resistance to hydrolytic and oxidative degradations in solutions.[41] All these features have rendered POMs exceptionally promising in acid and oxidation catalysis.[42] *Keggin*-type heteropolyanions (HPA) have been widely used in acid-catalyzed reactions as well as for oxidation reactions both in heterogeneous and homogeneous systems. They display stronger Brønsted acidity than conventional solid acids such as zeolites and mixed oxides.[4a] The acid sites in HPA are more uniform and easier to control than those in other solid acid catalysts. However, some serious problems of HPA catalysts were also put forward: (1) their relative low thermal stability, which limits reaction temperature and regeneration of solid HPA catalysts for acid reactions; (2) the hydrolytic degradation at high pH values is another obvious disadvantage for H_2O_2-assisted oxidation catalysis.[43]

In contrast, transition-metal substituted POMs (TMSPs) are usually oxidatively and hydrolytically stable in the pH region from about 6 to 10,[43] and they are very tolerant towards high temperature applications. Framework metal atoms (W, Mo) of POMs can be substituted with various transition metal including zinc, nickel, cobalt, copper, iron and noble metals.[42] Therefore, various types of transition metal atoms can be introduced as the potential catalytically active sites, which further tunes the catalytic activity and selectivity for acid or oxidation catalysis. [42, 43]

To date, also numerous TMSPs have been applied on H_2O_2 and O_2-based catalytic oxidation systems. Among them, sandwich-type TMSPs based on *tri*-lacunary *Keggin* moieties have received much attention due to their superior catalytic performance for the oxidation of organic substrates with hydrogen peroxide [44] and molecular oxygen [45]. Furthermore, sandwich-type POMs have been considered to be more thermodynamically stable than *Wells-Dawson* and *Keggin*-type polyanions [36, 44e] Apparently, unlike the plenary *Keggin* moieties, these POMs are sufficiently stable not only toward hydrolysis but also against degradation by H_2O_2. *Khenkin* and *Hill* first reported that the Fe_4-containing sandwich-type polyanion $[Fe_4(PW_9O_{34})_2]^{10-}$ catalyzed the selective homogenous epoxidation of alkenes in aqueous acetonitrile at 20°C by H_2O_2.[46] Later *Neumann* examined similar H_2O_2-based epoxidations catalyzed by isostructural but more highly charged sandwich complexes comprising a central, $WZnM_2$ unit (two M ions opposite each other and on the outside of the complex) sandwiched between two *B*-$[XW_9O_{34}]^{12-}$ units (X =Zn^{II}). These compounds were first prepared by *Tourné* and co-workers (Figure 1.8).[47] The zinc-containing polyoxotungstates $[WZnM_2(H_2O)_2(\alpha\text{-}ZnW_9O_{34})_2]^{q-}$ (M = Mn^{II}, Ru^{III}, Zn^{II}, Pd^{II}, Rh^{III}) have been discovered and intensively studied as highly efficient catalysts for biphasic oxidation reactions of alkenes, alcohols, diols, amines, and pyridine derivatives with hydrogen peroxide by *Neumann* (Figure 1.10).[43] In these cases, recycling of the catalyst can be simply carried out by phase separation after the reaction and addition of additional organic solvent, while water is the only by-product of the reaction without organic pollutants. All these remarkable features have made a significant contribution to a thriving “green” economy and related industrial applications.

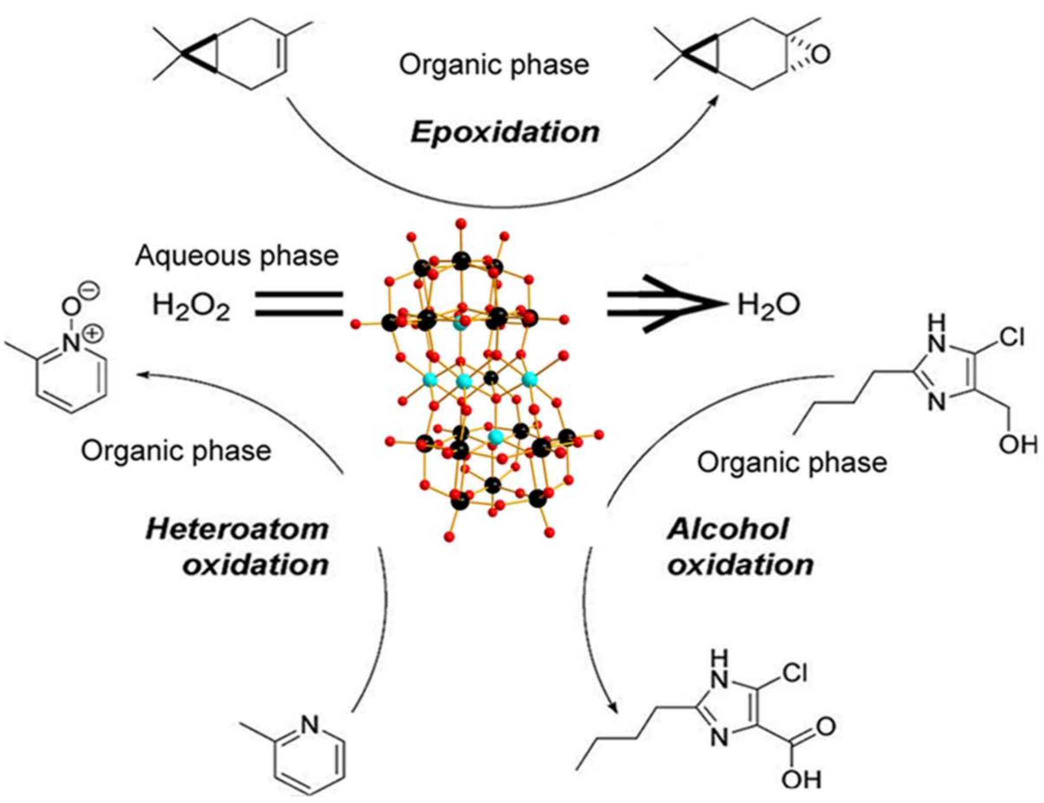

Figure. 1.10. Various oxidations with aqueous H_2O_2 catalyzed by sandwich-type POMs (Figure taken from ref [43]).

Krebs and coworkers synthesized a serie of new manganese(II)-substituted sandwiched POMs, $[(Mn^{II}_2(WO_2)_2(\beta\text{-}BiW_9O_{33})_2]^{10-}$ and $[(Mn^{II}_3(\alpha\text{-}SbW_9O_{33})_2]^{12-}$.[48] These compounds show high catalytic activity for regioselective epoxidation of *R*-(+)-limonene at ambient temperature in a biphasic system. *Hill* and co-workers created a new family of transition-metal substituted polyoxometalates, the so-called “banana” shaped polyoxoanions $[M_6(B\text{-}\alpha\text{-}XW_6O_{26})(B\text{-}\alpha\text{-}XW_9O_{34})_2]^{n-}$ (M=Mn^{2+}, Co^{2+}), which effectively catalyzed the epoxidation of cyclooctene, cyclohexene, and 1-hexene (Figure 1.9b).[35] Recent examples, including new catalytically active *γ-Keggin* sandwich-type Zn(II)-containing silicotungstates $[\{Zn(OH_2)(\mu_3\text{-}OH)\}_2\{Zn\text{-}(OH_2)_2\}_2\{\gamma\text{-}HSiW_{10}O_{36}\}_2]^{8-}$ for the oxidation of secondary alcohols or the thermally induced isomerization of a metastable precursor POM into a zinc-cored silicotungstate with a central hexaprismane motif, have been reported by *Miuzno*.[49] *Finke* and *Droege* synthesized sandwich-type tri-lacunary *Dawson* POMs for the first time (Figure 1.9c),[36] and then *Hill* reported on the sandwich-type *Dawson* POMs $[Fe^{III}_2(NaOH_2)_2(P_2W_{15}O_{56})_2]^{16-}$ and $[Fe^{III}_2(NiOH_2)_2(P_2W_{15}O_{56})_2]^{16-}$ which both exhibited higher activity for the epoxidation of alkenes.[50] In general, all these systems are of high research interest for the development and applications of POMs-based catalysts.

Currently, POMs are not only among the most flexible building blocks for materials development to date, but they also pose many fundamental chemical challenges in catalytic chemistry. POM chemists of our time still need deeper insight to thoroughly resolve remaining key issues, such as limited knowledge of catalytic mechanism and catalysis type (heterogeneous vs. homogeneous) and the identification of short-lived intermediates, in order to finally pave the way for industrial applications.

1.3.2. Magnetism of POMs

POMs are ideal host materials to encapsulate a large number of spin-coupled magnetic centers (3d-transition metals or 4f-lanthanoids) at specific sites of the framework structures.[51] Furthermore, magnetic properties have been widely investigated, particulary in lacunary POMs, which are prone to create magnetic entities either by a single magnetic center or by various magnetic centers connected though μ_2-oxo/hydroxo/aqua bridging groups (magnetic clusters).[51] Owing to the rigidity of these POM ligands, the resulting magnetic POM frameworks are stable in solid state as well as in solution. These magnetic polyoxometalates can be broadly divided into two families: (1) transition-metal spin clusters, and (2) lanthanoid complexes.

The first family of spin-localized POMs is constituted by incorporation of transition metal ions, which are further connected through oxo-bridges into magnetic clusters of variable nuclearities and high symmetries.[51] They are referred to as spin clusters, providing model examples to study key exchange interactions at the molecular level, such as the formation of single-molecule magnets (SMMs). During the last two decades a large number of highly symmetric clusters with intermediate nuclearities, such as dimers, trimers and tetramers, have been widely studied as model systems for the development of magnetic exchange theories.[51] For example, *Coronado* and his coworkers studied sandwich-type tri-lacunary POM $[Co_4(H_2O)_2(PW_9O_{34})_2]^{10-}$ with a tetranuclear rhomb-like Co(II) cluster in 1992, providing the first direct evidence for the Co(II)-Co(II) exchange anisotropy (Figure 1.11a and 1.11d).[52] In 2002, the same research group reported the first angular cobalt trimer $\{Co_3W\}$ cluster in the sandwiched POM polyanion $[Co_3W(H_2O)(ZnW_9O_{34})_2]^{12-}$ obtained by replacement of a Co atom in the short diagonal of the rhomb with a W atom (Fig. 1.11c and 1.11f).[53] Next, they isolated the second trimer triangular $\{NaCo_3\}$ cluster in sandwich-type *Dawson* polyanion $[(NaOH_2)Co_3(H_2O)(P_2W_{15}O_{56})_2]^{17-}$ by replacement of a Co positioned in the longer diagonal of the rhombus by a Na^+ cation (Figure 1.11b and 1.11e).[54] This Co(II) (d^7 ion) shows a high-spin *S=3/2* configuration with an unquenched orbital momentum, when octahedrally coordinated by the weak ligand field of POMs, thus exhibiting a large spin

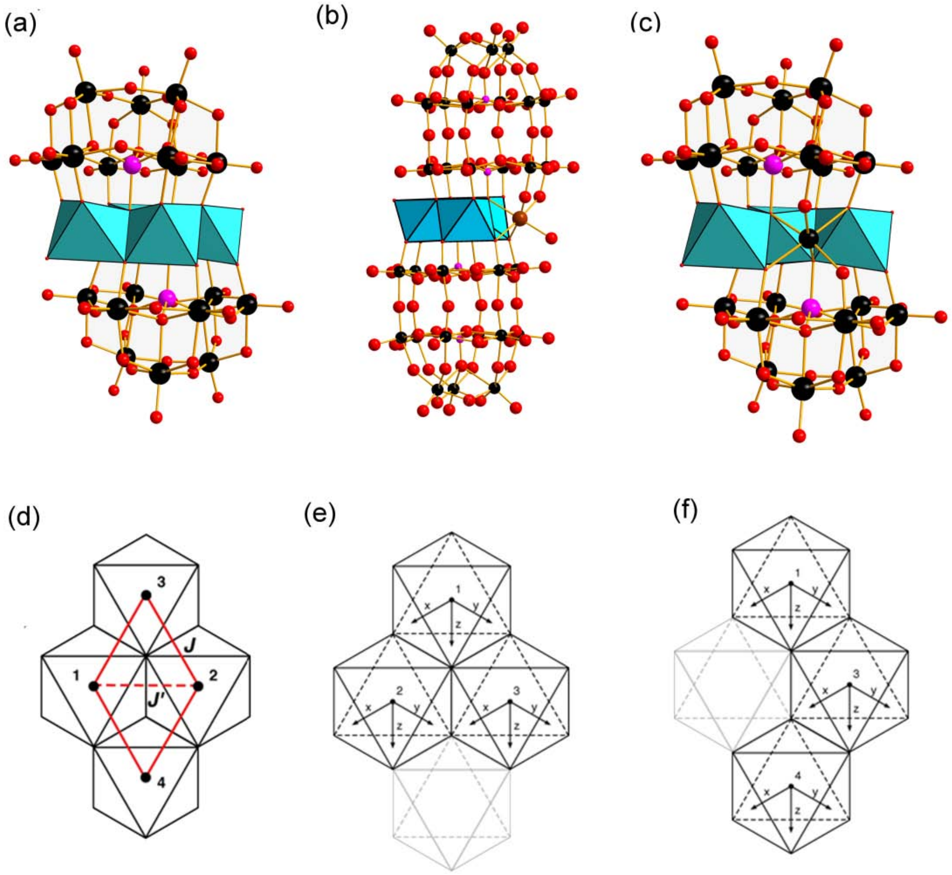

Figure 1.11. Polyhedral representation of the (a) $[Co_4(H_2O)_2(PW_9O_{34})_2]^{10-}$, (b) $[(NaOH_2)Co_3(H_2O)(P_2W_{15}O_{56})_2]^{17-}$ and (c) $[Co_3W(H_2O)(ZnW_9O_{34})_2]^{12-}$ clusters. Orientations of the local anisotropy axes of the (d) $\{Co_4\}$, (e) $\{Co_3Na\}$ and (f) $\{Co_3W\}$.[51]

anisotropy.[52-54] In fact, the first order spin–orbit coupling results in an effective and highly anisotropic spin doublet, $S = 1/2$. Magnetic susceptibility data of these POMs indicate ferromagnetic Co^{II}–Co^{II} interactions within the spin cluster at lower temperature.[52-54]

Moreover, another class of SMMs has also been discovered in the last decade, in which the magnetic moment M resides on a single lanthanoid ion octacoordinated by phthalocyaninato anions to produce a pseudoaxial D_{4d} symmetry.[55] In this case, the energy level splitting of the large total angular momentum J of the Ln^{III} ion caused by an intense spin-orbit coupling together with the anisotropy of the ligand field around the metal ion, may result in a ground high-M_J doublet and, thus, in the presence of an energy barrier for the J reversal, which gives rise to a slow relaxation of the magnetization (Figure 1.12). Meanwhile, lanthanoid substituted polyoxometalates (LSPs) compounds, the sandwich-type *Lindqvist* POM $[Er(W_5O_{18})_2]^{9-}$ [56] and the sandwiched-type mono-lacunuary *Keggin* POMs series $[Ln(\beta_2\text{-}SiW_{11}O_{39})_2]^{13-}$ (Ln(III) = Dy, Ho, Er, and Yb),[57] both with antiprismatic D_{4d} symmetry, also exhibited SMM behavior as inorganic analogues of the bisphthalocyaninato complex (Figure 1.13). [55]

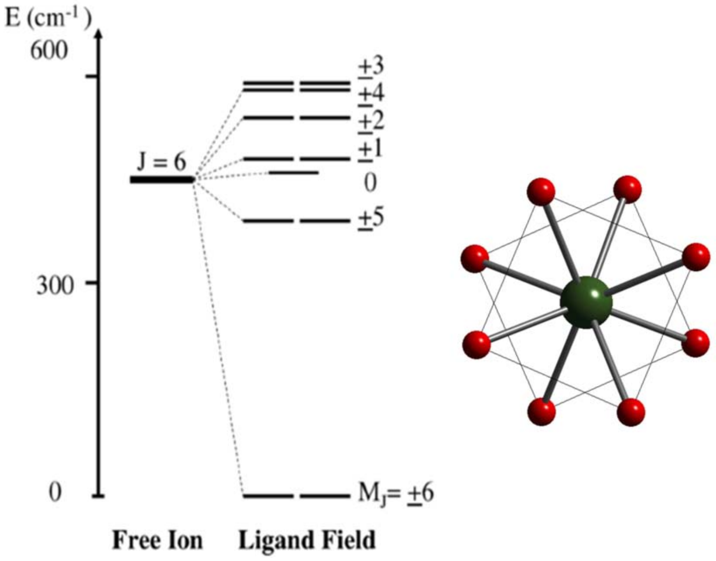

Figure 1.12. Energy level scheme for the ground $J = 6$ multiplet of the terbium phthalocyaninato derivative SMM (Figure taken from ref. [58]).

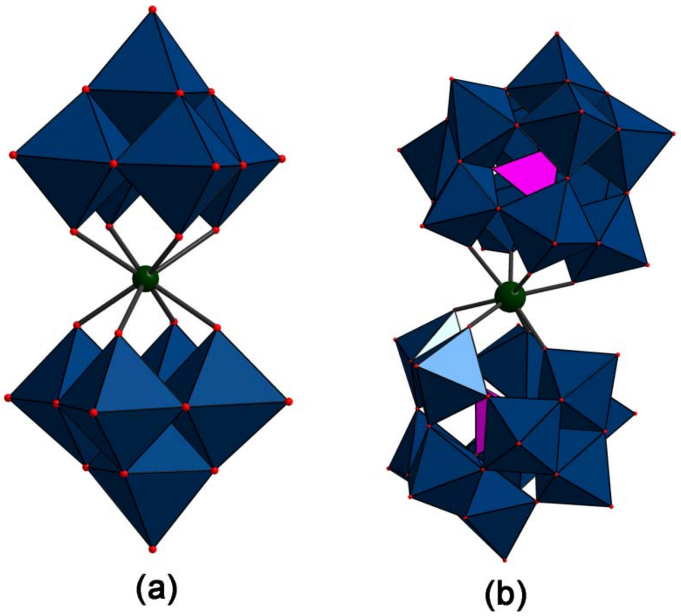

Figure 1.13. Polyhedral representation of $[Er(W_5O_{18})_2]^{9-}$ and $[Ln(\beta_2\text{-}SiW_{11}O_{39})_2]^{13-}$ derivatives.

1.3.3. Photochemistry of POMs

Upon photoexcitation of the oxygen-to-metal (O→M) ligand-to-metal charge-transfer (LMCT) bands of polyoxometalates, electrons can be transferred from the oxygen *2p* orbital (the valence band in the band model) at lower energy electronic states to the metal *d* orbital (the conduction band in the band model) at high-energy electronic states, which simultaneously generates an electron and a hole with *d* and *2p* character, respectively.[6] The fundamental electron transitions in polyoxometalate lattices are described in Figure 1.14. The relaxation processes of the O→M LMCT excitation energy include both the nonradiative recombination of electrons and holes within the energy gap and the intramolecular energy transfer. The latter leads to a charge-transfer emission. This intramolecular energy transfer corresponds to the O→M LMCT energy gap and occurs via radiative recombination and sensitized emission from the heteroatoms or cations (lanthanoid ions). When several energy levels based on the heteroatoms or counter cations act as energy acceptors within the O→M LMCT energy gap, the energy transfer occurs from the charge-transfer states to these levels, followed by the nonradiative or radiative deactivation of the excitation energy.[6]

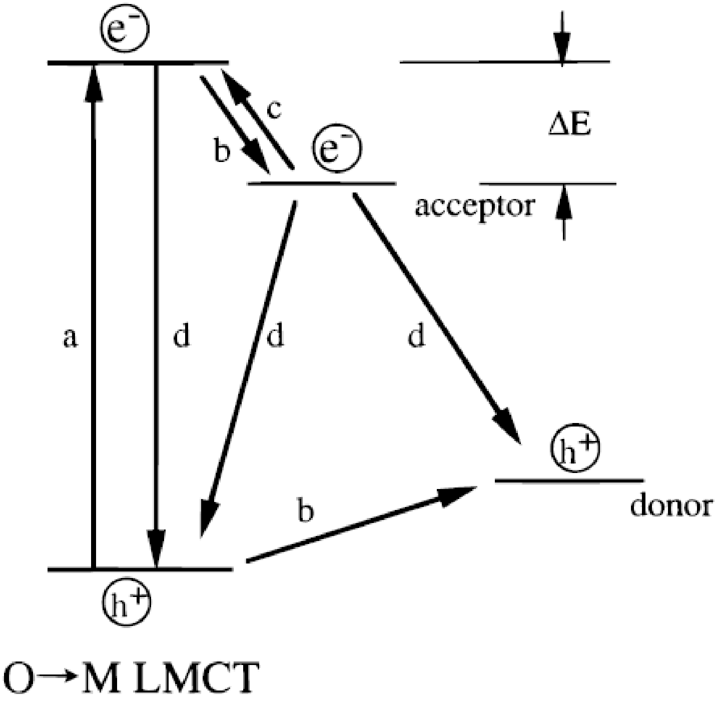

Figure 1.14. Model showing the electron transitions in the polyoxometalates containing electron donors and acceptors: (a) generation of charge carriers; (b) electron and hole trapping; (c) electron release due to stimulation; (d) recombination between electron and hole (electrons: e- ; holes: h+, Figure taken from ref. [6]).

The photoluminescence properties of lanthanoid-substituted polyoxometalates (LSPs) have been widely exploited to date. For example, *Yamase* and co-workers have provided considerable insight into the molecular mechanisms in LSPs compounds.[59] The photoexcitation of the oxygen-to-metal charge transfer (O→M LMCT) bands of the POMs of Mo and W induces Ln^{III} emission due to the intramolecular energy transfer from the O→M excited states to excited energy levels of the lanthanoid(III) ion, thereby sensitizing lanthanoid(III) emission (Figure 1.15).[59a] The majority of these studies is mainly focused on the performance of Eu-POMs, which have provided the majority of examples for luminescent Ln-POM complexes. However, other Ln-POMs (Pr- and Tb-POMs) display rater low emission intensities at room temperature as a result of radiationless deactivation via Ln(IV)-W(V) charge -transfer states for Pr(III) and Tb(III) ions and cross-relaxation based on concentration quenching with a large critical distance for Sm-, Dy-, and Ho-POMs.[60] *Yamase* and co-workers provided deeper insight into

Eu^{III} emission and crystal structure of luminescent POMs such as $[Eu(W_5O_{18})_2]^{9-}$, $[Eu_3(H_2O)_3(SbW_9O_{33})(W_5O_{18})_3]^{18-}$, $[Eu_4(H_2O)_{16}(MoO_4)(Mo_7O_{24})_4]^{14-}$, and $[Eu_2(H_2O)_{12}][Mo_8O_{27}]$ (Figure 1.16a-d) at the molecular level.[59a] Photoexcitation of the O→M LMCT band of the POM ligand affords emission due to the f → f transition within the Ln^{III} ion (Figure 1.16). In the case of Eu-POM compounds, the characteristic emission bands correspond to excited states $^5D_0$ and $^5D_1$ of Eu(III) to the ground state multiplet ^7F_J (J = 0-4). For Tb-POM compounds, the emission bands can be ascribed to the $^5D_4$ excited state of Tb(III) to the ^7F_J (J = 0-6). Moreover, the emission characteristics of the lanthanoid (III) ions are highly dependent on the nature of the POM ligand, on the symmetry and coordination geometry of the lanthanoid center, and on the number of aqua ligands. For example, decrease of the $^5D_0 \rightarrow {}^7F_J$ emission is more pronounced with increasing number of aqua ligands coordinating the Eu^{III} atom due to the weak vibronic coupling of the $^5D_0$ state with vibrational states of the high-frequency O-H oscillators of the aqua ligands.[59] In fact, POM ligands associated to lanthanoid(III) ions are often polydentate, thus minimizing the co-ligation of aqua and similar ligands, which contain high frequency O-H and N-H oscillators that otherwise tend to quench the luminescence.

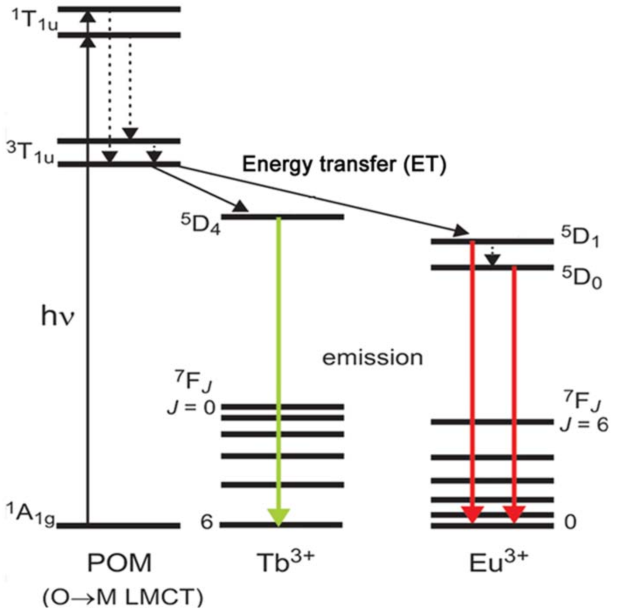

Figure 1.15 Schematic energy level diagram of relaxation processes for the sensitized emission of Tb(III) and Eu(III) in Ln-POM complexes (LSPs) (Figure taken from ref. [60]).

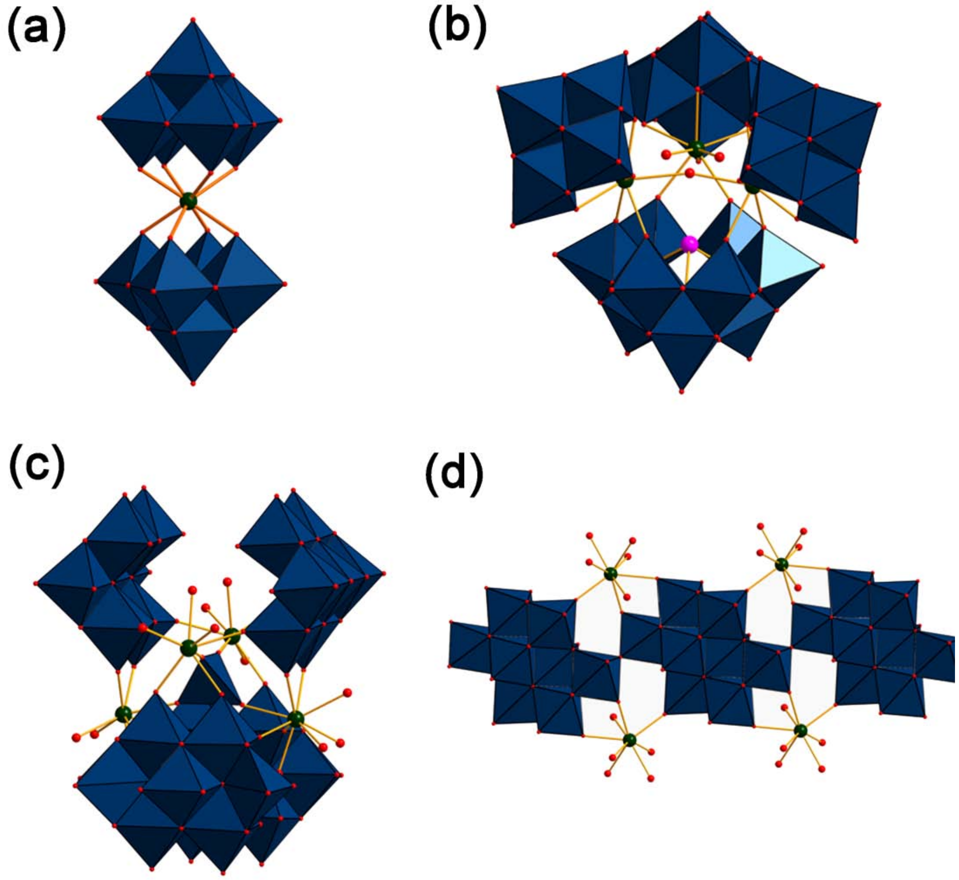

Figure 1.16. Polyhedral representations of (a) $[Eu(W_5O_{18})_2]^{9-}$, (b) $[Eu_3(H_2O)_3(SbW_9O_{33})(W_5O_{18})_3]^{18-}$, (c) $[Eu_4(H_2O)_{16}(MoO_4)(Mo_7O_{24})_4]^{14-}$, (d) $[Eu_2(H_2O)_{12}][Mo_8O_{27}]$.

1.4. Goals and strategy of the present work

1.4.1. Target compounds and properties

This thesis is focused on the synthesis, structural characterization and properties of functional polyoxometalates (POMs). The goal of this project is the development of generally applicable synthetic pathways to POMs with interesting structural features and high potential applications. In parallel, the considerable influence of reaction parameters on target POMs is investigated to further explore the complex relationships between POM structure and applications.

Therefore, the research project is divided into two parts as shown in Figure 1.17: **(1)** systematic structural design of novel lanthanoid-substituted polyoxometalates (LSPs) with versatile topological, photochemical and magnetic properties; **(2)** design and assembly of new transition metal-substituted polyoxometalates (TMSPs) for oxidation catalysis and the deeper investigations of the underlying catalytic mechanisms.

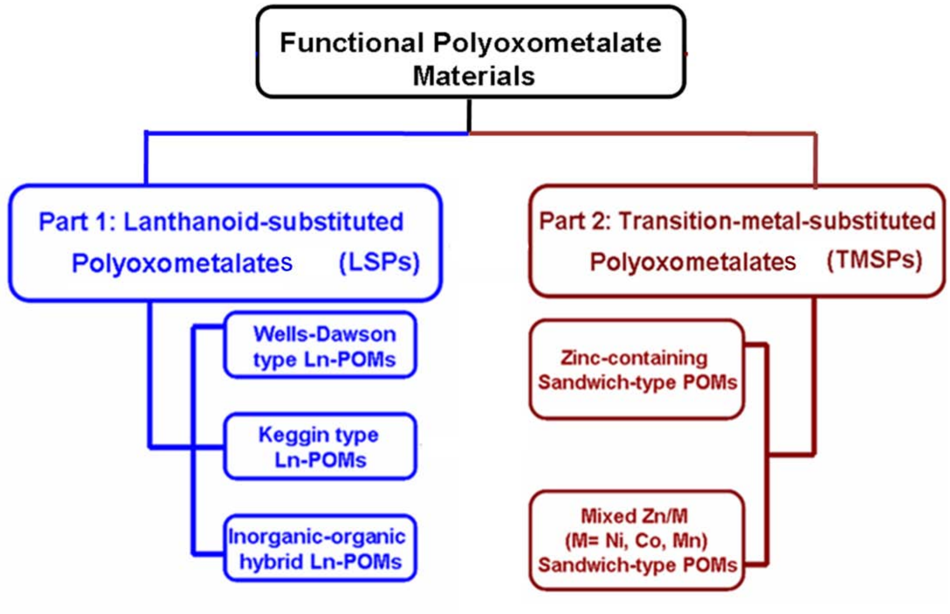

Figure. 1.17. The outline of research aims for functional polyoxometalate materials

1.4.2. Research strategy

Figure 1.18 provides a detailed flow-chart illustrating the overall research strategy.

Part 1 presents solution-based approaches towards new lanthanoid-containing polyoxometalates (LSPs) starting from *Keggin*-type lacunary ligands such as $[SiW_9O_{34}]^{9-}$ or from *Wells-Dawson* type precursors, e.g. $[Si_2W_{18}O_{62}]^{8-}$, with high potential as building blocks for higher architectures (1D-3D). The structure-directing influence of the lanthanoid cation on LSPs is investigated in detail. Moreover, the photoluminescence and magnetic properties of the resulting compounds are explored.

Part 2 establishes tuneable synthetic routes towards a large family of sandwich-type transition metal substituted POMs (TMPs) emerging from lacunary ligands, e.g. $[SbW_9O_{33}]^{9-}$, as efficient oxidation catalysts. For example, the family of novel TM-substituted sandwich-type POMs such as $[Zn_n(H_2O)_n(SbW_9O_{33})_2]^{(18-2n)-}$ (n = 2-6) still remains widely unexplored. Moreover, new POM applications in homogeneous catalysis are explored with special emphasis on alcohol oxidation reactions. The following parameters are investigated in detail: (1) influence of the ***transition metal core*** (geometry, oxidation state), (2) role of the peripheral metal sites of ***POM shell***, (3) isolation of catalytic intermediates and characterization with a wide range of crystallographic and spectroscopic techniques. Finally, this comprehensive strategy of experimental and theoretical approaches sheds new light on the catalytic mechanism of homogeneous oxidation reactions. Experimental approaches and methods for both parts are linked as follows (Fig. 1.18):

(1) Parameter elucidation. Synthetic screening experiments identifying the influence of POM ligands, pH values, counterions, stoichiometry and temperature.

(2) Exploration. **Part 1**: development of new Ln-POMs with structurally flexible building blocks; **Part 2**: development of new sandwich-type Zn-POM classes as oxidation catalysts, i.e. $[\alpha/\beta\text{-}Zn_2Sb_2(ZnW_9O_{34})_2]^{14-}$ by controlling molecular isomerization processes and $[Zn_n(H_2O)_n(SbW_9O_{33})_2]^{(18-2n)-}$ (n = 2-6) by controlling the zinc core size.

(3) Characterization. Thorough structural characterization of all newly obtained POMs by single-crystal and powder X-ray diffraction techniques, spectroscopic methods (FT-IR, Raman, UV/vis), CV, NMR, TG/DSC, XPS, ESI-MS and elemental analyses.

(4) Properties. **Part 1**: evaluation of photoluminescence and magnetic properties of newly synthesized LSPs; **Part 2**: evaluation of selective oxidation catalysis (e.g. alcohol oxidation) performance of TMSPs. Influence of the metal core structures of POMs on the catalytic process is investigated in detail. Together with high-level computational modeling (cooperation with Prof. Dr. Kim Baldridge, Institute of organic chemistry, University of Zurich), the results open up a rational approach to shed new light on the elusive mechanisms behind important POM-based organic transformations.

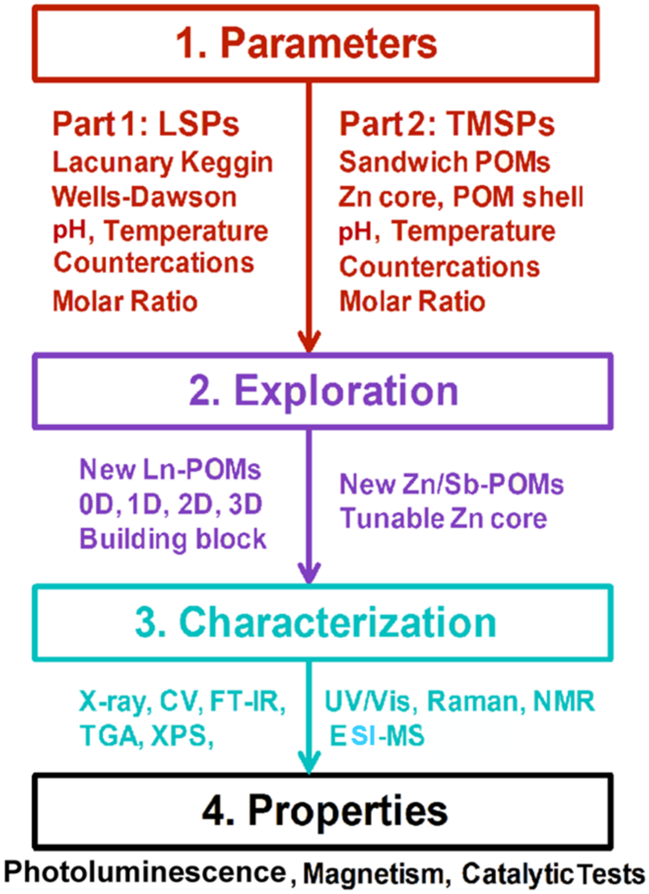

Figure. 1.18. Research flowchart for the construction and implementation of LSPs and TMSPs.

References

[1] Pope, M. T. *Heteropoly and Isopoly Oxometalates*, Springer, Berlin, **1983**

[2]. (a) Pope, M. T.; Müller, A. *Angew. Chem., Int. Ed.,* **1991**, 30, 34–48. (c) Pope, M. T. *Compr. Coord. Chem. II.* **2003**, 4, 635–678. (b) Hill, C. L. *Compr. Coord. Chem. II.* **2003**, 4, 679–759. (c) Cronin, L. *Compr. Coord. Chem. II.* **2003**, 7, 1–56.

[3] (a) *Polyoxometalate Molecular Science* (Eds.: Borras-Almenar, J. J.; Coronado, E.; Müller, A.; Pope, M. T.) Kluwer, Dordrecht, **2004**. (b) *Polyoxometalates: From Platonic Solids to Antiretroviral Activity* (Eds.: Pope, M. T.; Müller, A.) Kluwer, Dordrecht, **1994**. (c) *Chem. Rev.* (Ed.: C. L. Hill), **1998**, 98, 1–389 (*Special Issue on Polyoxometalates*).

[4] (a) Kozhevnikov, I. V. *Catalysis by polyoxometalates*; John Wiley & Sons, Ltd.: Chichester, U. K., **2002**. (b) Okuhara, T.; Mizuno, N.; Misono, M. *Adv. Catal.* **1996**, 41, 113–252. (c) Mizuno, N.; Yamaguchi, K.; Kamata, K. *Coord. Chem. Rev*. **2005**, 249, 1944–1956.

[5] (a) Zhongfeng, L.; Weisheng, L.; Xiaojing, L.; Fengkui, P.; Yingxia, L.; Hao, L. *Magn. Reson. Imaging*. **2007**, 25, 412‒417. (b) B. Hasenknopf, *Frontiers in Bioscience-Landmark* **2005**, 10, 275‒287

[6] Yamase, T. *Chem. Rev*. **1998**, 98, 307–325.

[7] (a) Chen, W.; Li, Y.; Wang, Y.; Wang, E.; Su, Z. *Dalton Trans*. **2007**, 4293‒4301. (b) Ritchie, C.; Speldrich, M.; Gable, R. W.; Sorace, L.; Kögerler, P.; Boskovic, C. *Inorg. Chem*. **2011**, 50, 7004‒7014.

[8] *Polyoxometalate Chemistry: From Topology via Self-Assembly to Applications*. (Eds.: Pope, M. T.; Müller, A.) Kluwer, Dordrecht, **2001**.

[9] (a) Berzelius, J. J. *Poggend. Ann. Phys. Chem.*, **1826**, 6, 369‒392. (b) Berzelius J.J., *Edinburgh New Philosophical Journal*, **1836**, XXI, 223‒228.

[10] Galissard de Marignac J.-C., *Ann. Chim. hys.*, **1864**, 3, 1.

[11] Werner A., *Ber. Dtsch. Chem. Ges.*, **1907**, 40, 4817‒4825.

[12]Werner, A. *Neuere Amschauugen auf dem Gebiete der Anorganischem Chemie*, **1909**.

[13] Miolati, A., Pizzighelli, R. *J. Prakt. Chem.*, **1908**, 77, 417‒456.

[14] Pauling, L. *J. Am. Chem. Soc.*, **1929**, 51, 2868‒2880.

[15] (a) Keggin, J. F. *Nature*, **1933**, 131, 908‒909. (b) Keggin, J. F. *Proc. R. Soc. London, Ser. A* **1934**, 144, 75‒100.

[16] Dawson, B. *Acta Cryst.* **1953**, 6, 113‒126.

[17] Anderson, J. S. *Nature*, **1937**, 140, 850‒851.

[18] (a) Lindqvist, I. *Ark Kemi*, **1952**, 5, 247–250. (b) Lindqvist, I. *Acta Cryst.* **1952**, 5, 667–670.

[19] Waugh, J. C. T.; Schoemaker, D. P.; Pauling, L., *Acta Cryst.*, **1954**, 7, 438–441.

[20] Preyssler, C., *Bull. Soc. Chim.France*, **1970**, 30–36.

[21] Müller, A.; Beckmann, E.; Bögge, H.; Schmidtmann M.; Dress, A. *Angew. Chem., Int. Ed.*, **2002**, 41, 1162–1167.

[22]Wassermann, K.; Dickman, M. H.; Pope, M. T. *Angew. Chem., Int. Ed.* **1997**, 36, 1445–1448.

[23] Hussain, F.; Conrad, F.; Patzke, G. R. *Angew. Chem. Int. Ed.* **2009**, 48, 9088–9091.

[24] Huang, P.; Qin, C.; Su, Z. M.; Xing, Y.; Wang, X. L.; Shao, K. Z.; Lan, Y. Q,; Wang, E. B. *J. Am. Chem. Soc.*, **2012**, 134, 14004–14010.

[25] Baker, L. C. W.; Figgis, J. S. *J. Am. Chem. Soc.* **1970**, 92, 3794–3797.

[26] Tézé, A.; Hervé, G. *Inorganic Syntheses.* **1990**, 27.

[27] Weinstock, I.A.; Cowan, J. J.; Barbuzzi, E. M. G.; Zeng, H.; Hill. C. L. *J Am Chem Soc*. **1999**, 121, 4608–4617.

[28] Tézé, A.; Hervé, G. *J. Inorg. Nucl. Chem.* **1977**, 39, 999–1002.

[29] Bassil, B. S.; Dickman, M. H.; von der Kammer, B.; Kortz, U. *Inorg. Chem*. **2007**, 46, 2452–2458.

[30] Robert, F.; Leyrie, M.; Hervé, G. *Acta Crystallogr.* **1982**, B32, 358–362.

[31] Ginsberg, A. P. *Inorganic syntheses.*Volume 27; Wiley:New York, 1990 (Chapter III: Early Transition Metal Polyoxoanions).

[32] (a) Weakley, T. J. R. *J. Chem. Soc. Dalton Trans* **1973**, 341–346. (b) Weakley, T. J. R.; Evens, H. T.; Showell, J. S.; Tourné, G. F.; Tourné, C. M. *J. Chem. Soc., Chem.Commun*. **1973**, 139–140.

[33] (a) Knoth,W. H.; Domaille, P. J.; Farlee, R. D.; *Organometallics*, **1985**, 4, 62–68. (b) Knoth,W. H.; Domaille, P. J.; Harlow, R. L. *Inorg. Chem.*, **1986**, 25, 1577–1584.

[34] Mbomekalle, I. M.; Keita, B.; Nierlich, M.; Kortz, U.; Berthet, P.; Nadjo, L.; *Inorg. Chem.*, **2003**, 42, 5143–5152.

[35] Ritorto, M. D.; Anderson, T. M.; Neiwert W. A.; Hill, C. L. *Inorg. Chem.*, **2004**, 43, 44–49.

[36] Finke, R. G.; Droege, M. W.; Domaille, P. J. *Inorg. Chem.*, **1987**, 26, 3886–3896.

[37] (a) Laronze, N.; Marrot, J.; Hervé, G. *Chem. Commun*. *2003*, 2360-2361. (b) Laronze, N.; Marrot, J.; Hervé, G. *Inorg. Chem*. **2005**, 44, 1275–1281.

[38] (a) Laronze, N.; Marrot, J.; Hervé, G. *C. R. Chim*. **2006**, 9, 1467–1471. (b) Bi, L.; Kortz, U. *Inorg. Chem*. **2004**, *43*, 7961-7962. (c) Nellutla, S.; Tol, J.; Dalal, N. S.; Bi, L.; Kortz, U.; Keita, B.; Nadjo, L.; Khitrov, G. A.; Marshall, A. G. *Inorg. Chem*. **2005**, 44, 9795–9806.

[39] (a) Kozhevnikov, I. V. *J. Mol. Catal. A: Chem.*, **2007**, *262*, 86-92. (b) Kozhevnikov, I. V. *J. Mol. Catal. A: Chem.*, **2009**, 305, 104-111.

[40] Misono, M. *Catal. Today*, **2005**, 100, 95-100.

[41] (a) Mizuno, N.; Misono, M. *Chem. Rev.*, **1998**, *98*, 199-217. (b) Kozhevnikov, I. V. *Chem. Rev.*, **1998**, *98*, 171-198. (c) Cavani, F. *Catal. Today*, **1998**, 41, 73–86.

[42] (a) Hill, C. L. *Chem. Rev.*, **1998**, 98, 1–2. (b) Mizuno, N.; Yamaguchi, K.; Kamata, K. *Coord. Chem. Rev.*, **2005**, 249, 1944–1956. (c) Hill, C. L. Prosser-McCartha, C. M.; *Coord. Chem. Rev.*, **1995**, 143, 407–435.

[43] Nardello, V.; Aubry, J.; Vos, D. E. D.; Neumann, R.; Adam, W.; Zhang, R.; ten Elshof, J. E. T.; Witte, P. T.; Alsters, P. L. *J. Mol. Catal. A: Chem.*, **2006**, 251: 185–193.

[44] (a) Neumann, R.; Khenkin, A. M. *J. Mol. Catal. A*. **1996**, 114, 169–180. (b) Witte, P. T.; Alsters, P. L.; Walther, J.; Müllner, R.; Pöchlauer, P.; Sloboda-Rozner, D.;

Neumann, R. *Org. Process Res. & Development*. **2004**, 8, 524‒531 (c) Sloboda-Rozner, D.; Alsters, P.; Neumann, R. *J. Am. Chem. Soc.* **2003**, 125, 5280‒5281. (d) Neumann, R.; Khenkin, A. M. *Inorg. Chem.* **1995**, 34, 5753‒5760. (e) Neumann, R. Gara, M, *J. Am. Chem. Soc.* **2004**, 116, 5509‒5510.

[45] (a) Neumann, R.; Dahan, M. *Nature.* **1997**, 388, 353–355. (b) de Visser, S. P.; Kumar, D.; Neumann, R.; Shaik, S. *Angew. Chem. Int. Ed.* **2004**, 43, 5661‒5665.

[46] Khenkin, A.M.; Hill, C. L. *Mendeleev Commun.* **1993**, 4, 140‒142.

[47] Tourné, C. M.; Tourné, G. F.; Zonnevijlle, F. *J. Chem. Soc., Dalton Trans.* **1991**, 143‒151.

[48] Bösing, M.; Nöh, A.; Loose, I.; Krebs, B. *J. Am. Chem. Soc.* **1998**, 120, 7252‒7259.

[49] Kikukawa, Y.; Yamaguchi, K.; Mizuno, N. *Angew. Chem. Int. Ed.* **2010**, 49, 6096‒6100.

[50] Anderson, T. M.; Zhang, X.; Hardcastle, K. I.; Hill, C. L. *Inorg. Chem.* **2002**, 40, 2477‒2488.

[51] Clemete-Juan, J. M.; Coronado, E.; Gaita-Ariño, A. *Chem. Soc. Rev.* **2012**, 41, 7164–7478.

[52] Gomez-Garcia, C. J.; Coronado, E.; Borras-Almenar, J. J.; Aebersold, M.; Gudel, H. U.; Mutkas, H. *Phy. B,* **1992**, 180, 238–244.

[53] Clemete-Juan, J. M.; Coronado, E.; Gaita-Ariño, A.; Gimenez-Saiz, C.; Chaboussant, G.; Gudel, H. U.; Burriel , R. and Mutka, H. *Chem. Eur. J.,* **2002**, 8, 5701–5708.

[54] Clemente-Juan, J. M.; Coronado, E.; Gaita-Ariño, A.; Gimenez-Saiz, C.; Gudel, H. U.; Sieber, A.; Bircher , R.; and Mutka, H. *Inorg. Chem.*, **2005**, 44, 3389–3395.

[55] Ishikawa, N.; Sugita, M.; Ishikawa, T.; Koshihara, S. Y.; and Kaizu, Y. *J. Am. Chem. Soc.,* **2003**, 125, 8694–8695.

[56] AlDamen, M. A.; Clemente-Juan, J. M.; Coronado, E.; Marti-Gastaldo, C. and Gaita-Ariño, A. *J. Am. Chem. Soc.*, **2008**, 130, 8874–8875.

[57] AlDamen, M. A.; Clemente-Juan, J. M.; Coronado, E.; Gaita-Ariño, A.; Marti-Gastaldo, C.; Luis, F.; and Montero, O. *Inorg. Chem.*, **2009**, 48, 3467–3479.

[58] Clemente-Juan, J. M.; Coronado, E.; Gaita-Ariño, A. *Polyoxometalate Chemistry* Volume *8*; World Scientific, **2013** (Chapter IV: Magnetic Polyoxometalates).

[59] (a) Yamase, T.; Kobayashi, T.; Sugeta, M.; Naruke, H. *J. Phys. Chem. A*, **1997**, 101, 5046–5053. (b) Ozeki, T.; Yamase, T. *J. Alloys Compd*. **1993**, 192, 28–29.

[60] Ritche, C.; Baslon, V.; Moore, E. G.; Reber, C.; Boskovic, C. *Inorg. Chem.* **2012**, 51, 1142–1151.

2. Experimental Section

2.1. Materials

$Na_{10}[A\text{-}\alpha\text{-}SiW_9O_{34}]\cdot 23H_2O$[1] and $Na_9[B\text{-}\alpha\text{-}SbW_9O_{33}]\cdot 19.5H_2O$ as precursor materials were prepared according to literature protocols[2], and their purities were confirmed by FT-IR spectroscopy. All other chemicals were commercially purchased and used without further purification.

2.2. Analytical methods

(1) Elemental analyses were performed by Mikroanalytisches Labor Pascher, Remagen, Germany.

(2) Fourier transform infrared (FT-IR) spectra were recorded on a Perkin-Elmer BXII spectrometer with KBr pellets (**Chapter 3**). In **Chapters 4-7**, attenuated total reflectance Fourier-transform infrared (ATR FT-IR) spectra were recorded on a Bruker Optics Vertex 70 Spectrometer and a Platinum ATR accessory with a diamond crystal

(3) Thermogravimetric analyses (TGA) were performed on a Netzsch STA 449 C between 30 and 800 ^{o}C with a heating rate of 5 K min^{-1} in nitrogen atmosphere.

(4) UV/vis spectra were recorded on a Perkin-Elmer Lambda 650S spectrometer.

(5) Raman spectroscopy was performed on a Renishaw Ramascope 1000 with a green SpectraPhysics Argon laser with a wavelength of 524.5 nm and 50 mW capacity.

(6) Powder X-ray diffraction (PXRD) data were recorded on a Philips X'Pert PRO diffractometer, operated at 40 kV and 30 mA (Cu $K_{\alpha 1}$ radiation), in **Chapter 3**. In **Chapters 4-7**, PXRD data were recorded on a STOE STADI P diffractometer in transmission model (flat sample holders, Ge monochromator and Cu $K_{\alpha 1}$ radiation) equipped with a position sensitive detector.

(7) In **Chapter 3**, photoluminescence measurements were performed on a Perkin-Elmer LS 50B spectrometer. In **Chapter 4**, photoluminescence measurements were performed on an Edinburgh Instruments F900 spectrometer.

(8) Magnetic measurements were performed on a SQUID magnetometer (Quantum Design, MPMS-7). The temperature range was 2-300 K with an applied magnetic field of 2 kOe in **Chapter 3**, whereas a temperature of 5-300 K with an applied magnetic field of 1 kOe was used in **Chapter 4**. Corrections were applied for diamagnetic and temperature-independent paramagnetism (TIP) contributions from a combination of core shells of Pascal's constants and the experimentally determined diamagnetic susceptibility of **Gd-1** with $\chi_{\mathrm{dia/TIP}} = -1.54\times10^{-3}$ emu $\mathrm{Oe^{-1}mol^{-1}}$, **Gd-2** with $\chi_{\mathrm{dia/TIP}} = -5.38\times10^{-4}$ emu $\mathrm{Oe^{-1}}$ $\mathrm{mol^{-1}}$, and **Tb-1** with $\chi_{\mathrm{dia/TIP}} = -8.07\times10^{-3}$ emu $\mathrm{Oe^{-1}mol^{-1}}$. [Curie law ($\chi = C/\mathrm{T}$), $\mu_{\mathrm{eff}}{}^2 = 3kC/\mu_{\mathrm{B}}{}^2$ N (k = Boltzmann's constant, μ_{B} = Bohr magneton, and N = Avogadro's number)].

(9) Cyclic voltammetry (CV) measurements were performed using a Metrohm Computrace Voltammetric Analyzer model 757 VA. The system was operated using the 757 VA Computrace software (Metrohm). The three-electrode cell system consisted of a 2 mm glassy carbon working electrode (GCE, modified or unmodified), a saturated Ag/AgCl reference electrode and a Pt wire as counter electrode.

(10) ^{121}Sb-NMR spectra were recorded on a Bruker DRX-500MHZ spectrometer.

(11) X-ray photoelectron spectroscopy (XPS) spectra were recorded on a PHI Quantum 2000 microprobe spectrometer from Physical Electronics Inc. The measurements were taken with a monochromatic Al K_{α} source without any preceding sputter cleaning or other procedures that might alter the surface of the crystals. The C 1s peak at 284.8 eV was set as a reference for all XPS peak positions.

(12) High mass accuracy ESI spectra were recorded on an ultrahigh-resolution ESI-Time-Of-Flight MS (Bruker Daltonik maXis (Bremen, Germany)). Spectra were obtained in negative-ion mode, with the capillary held at 4000 V. The drying gas flow rate was 4.0 L min^{-1} with a temperature of 180 ^{o}C. The nebulizer gas was at a pressure of 0.4 bar. The m/z range detected was from 100 to 2500Da. A calibration tune mix (Agilent Technologies) was sprayed immediately prior to analysis, ensuring a high mass accuracy to assist in the identification of peaks. The flow rate of the solutions was 3μL/min. POMs were dissolved in a H_2O/MeCN mixture (80:20) to enhance peak intensity.

(13) For catalytic activity measurements in **Chapters 4-7**, reaction products were characterized and quantified with a gas chromatograph (Finnigan Trace GC Ultra) equipped with a flame ionization detector and fitted with a ZB-5MS Phenomenex column (30 m length, 0.25 mm internal diameter, 0.25 μm film thickness) using dodecane as internal reference. Products were furthermore identified by GC-MS (Finnigan Trace DSQ GC-MS systems).

References

[1] Tézé, A.; Hervé, G.; Finke, R. G.; Lyon, D. K. *Inorg. Synth*. **1990**, 27, 85–135.

[2] Bösing, M.; Loose, I.; Pohlmann, H.; Krebs, B. *Chem. Eur. J*. **1997**, 8, 1232–1237. IR (KBr disk): 925 (m), 891 (s), 769 (s), 708 cm^{-1} (s).

Part I

Lanthanoid-Substituted Polyoxometalates (LSPs)

3. Lanthanoid-Containing Open Wells-Dawson Silicotungstates: Synthesis, Crystal Structures, and Properties

3.1. Introduction

POMs are versatile inorganic building blocks for the construction of molecular materials. They can also incorporate most lanthanoid (Ln) cations, resulting in a family of lanthanoid-substituted polyoxometalates (**LSPs**) which exhibit interesting Lewis acid catalysis, luminescence and magnetic properties.[1] Gd-POMs, for example, are particularly used as magnetic resonance imaging (MRI) agents.[2] Over the past few decades, the *Keggin* and *Wells-Dawson* families were the two most widely studied polyoxometalate types, which can be represented as $[XM_{12}O_{40}]^{n-}$ and $[X_2M_{18}O_{62}]^{n-}$ (X = P^{V}, Si^{IV}; M = $W^{V,VI}$, $Mo^{V,VI}$, $V^{IV,V}$) respectively.[3] Moreover, the mono-, di- and tri-vacant *Keggin* and *Wells-Dawson* lacunary polyoxoanions are also obtained by the removal of one to three metal centers from the basic POM types. A systematic approach thus has been developed to explore the reactivity of lanthanoid cations with different types of lacunary POMs[4]: (1) Lacunary POMs and large oxophilic lanthanoid cations can be readily combined into high-nuclearity polyoxoanion complexes with unprecedented structures, sizes and new properties and (2) lanthanoid cations are powerful POM linkers due to their high coordination numbers and flexible coordination geometries. Therefore, this synthetic method is generally efficient for constructing polymeric or unusually large POM assemblies. However, to date, the potential of this approach still remains to be explored with lacunary *Keggin*- or *Wells-Dawson*-type POM precursors, as they offer even more flexible coordination chemistry.

This strategy was successfully illustrated by the high-nuclear cerium-containing polyoxotungstoarsenate $[Ln_{16}As_{12}W_{148}O_{524}(H_2O)_{36}]^{76-}$ reported by *Pope* et al., which has long been the largest polyoxotungstate ever observed,[5] followed by *Kortz* et al.'s synthesis of $[Ce_{20}Ge_{10}W_{100}O_{376}(OH)_4(H_2O)_{30}]^{56-}$.[6] The first 1:1 type LSPs-based polymeric structures of $[Ln(\alpha\text{-}SiW_{11}O_{39})_2(H_2O)_3]^{13-}$ (Ln = La^{III}, Ce^{III}) with one-dimensional zigzag chains were isolated in 2000 by *Pope* and co-workers, and three years later,[7] *Mialane* et al. reported several $\{Ln_n(SiW_{11}O_{39})\}$ polyoxoanions with 1D chain or 2D layer structures.[8] The reactivity of the monovacant silicotungstate $[SiW_{11}O_{39}]^{8-}$ with trivalent lanthanoids leading to the formation of 1D inorganic chains or 2D layers has been well investigated by *Peacock*,[9] *Pope*,[10] *Mialane*,[11] *Kortz*,[12] and their respective co-workers. However, no studies on the conversion of the trilacunary *Keggin* polyoxoanion $[SiW_9O_{34}]^{10-}$ into *Wells-Dawson* $[Si_2W_{18}O_{66}]^{16-}$ ions in the presence of lanthanoid cations have been reported. Furthermore, up to now only few 3D inorganic architectures of lanthanoid-containing POMs are known. Two *Keggin*-type monolacunary polyoxotungstoborates $[Ln(H_2O)(BW_{11}O_{39}H)]^{10-}$ (Ln = Ce, Nd) have been recently discovered by *An* and co-workers.[13] In the past 3-4 years, our group has also made great contributions to the new family of large polyoxotungstates by including lanthanoid linkers from the middle and late members of the series,[4] as represented by the $[Cs{\subset}Ln_6As_6W_{63}O_{218}(H_2O)_{14}(OH)_4]^{25-}$ type (Ln = Eu, Gd, Tb, Dy, Ho, Er) and the $[Gd_8As_{12}W_{124}O_{432}(H_2O)_{22}]^{60-}$ polyanion.[4a,b] We finally succeeded in bringing forward the $[Ln_{16}As_{16}W_{164}O_{576}(OH)_8(H_2O)_{42}]^{80-}$ (Ln = Eu, Gd, Tb, Dy, Ho) family displaying the largest number of tungsten centers in a single POM to date.[4c] In the following, the reactivity of the $[A\text{-}\alpha\text{-}SiW_9O_{34}]^{10-}$ precursor with different lanthanoid cations is investigated. New five polymeric Ln-based POMs (Ln = Gd, Tb, Dy, Ho) were successfully obtained by the incorporation of lanthanoid cations into the open *Wells-Dawson* anion $[\alpha\text{-}Si_2W_{18}O_{66}]^{16-}$.[14] The potassium salt of $[Si_2W_{18}O_{66}]^{16-}$ was first characterized by *Hervé* et al.,[15, 16] and it furthermore serves as a precursor for the formation of oligomers $\alpha\text{-}[\{[K(H_2O)_2(\mu\text{-}H_2O)\text{-}[Li(H_2O)_2]\}_2Si_4W_{36}O_{126}(H_2O)_2]^{16-}$ and $\alpha\text{-}[\{[K(H_2O)]\text{-}[K(H_2O)_4]\}_2Si_8W_{36}O_{136}]^{22-}$ through a stepwise self-assembly process.[17] In addition to the K^+ ion present in the pocket position, two transition metal cations (Mn, Co, Ni, Cu) can also be intercalated into the open *Wells-Dawson* anion, resulting in different coordination modes.[17] Later, *Hervé* and co-workers accessed to two dimeric open *Wells-Dawson* polyanions with dinuclear $\{KV_2O(H_2O)_2\}^{5+}$ and tetranuclear $\{Fe_4(OH)_6\}^{6+}$ moieties included between the two $[\alpha\text{-}Si_2W_{18}O_{66}]^{16-}$ subunits through reaction with V^V and Fe^{III} cations.[18] In 2004, *Kortz* et al. obtained a penta-copper substituted polyanion with the copper oxo cluster $\{Cu_5(OH)_4(H_2O)\}^{6+}$ perfectly fitting into the cavity of the open *Wells-Dawson* anion.[19] Two years later, three monosubstituted transition metal derivatives of $\gamma\text{-}[Si_2W_{20}O_{70}]^{12-}$ were also discovered by the same group.[20]

As shown in this present work,[14] the construction of Ln-POM-based coordination polymers was explored from self-assembly processes of the lacunary POM ligand [*A*-*α*-$SiW_9O_{34}]^{10-}$. The novel dimeric polyoxoanions $[Ln_2(H_2O)_7Si_2W_{18}O_{66}]^{10-}$ (Ln = Gd, Ho, Tb) and $[Dy_2(H_2O)_{6.5}(C_2H_4O_2)_{0.5}Si_2W_{18}O_{66}]_n^{10-}$ consist of two lanthanoid cations hosted by the open *Wells-Dawson* units. These polyanions are further linked by Ln^{3+} cations into 3D or 2D architectures. The influence of the cationic radii on the local structure of the POM moiety as well as on the 3D packing motif of the compounds is discussed. The **Tb-** and **Dy-**containing compounds (**Tb-2** and **Dy-2**) exhibit room temperature photoluminescence upon excitation, and the **Ho-**containing compound (**Ho-2**) displays photochromic behavior. The magnetic behavior of **Gd-**containing polyanions (**Gd-1** and **Gd-2**) was found to be paramagnetic between 2 and 300 K in agreement with the spin of non interacting gadolinium centers. All compounds were electrochemically investigated in sodium acetate buffer (pH 4.4) solution as supporting electrolyte.

3.2. Experimental

3.2.1. Synthetic methods

Synthesis of $Na_2CsCaGd_2[Gd_2(H_2O)_7Si_2W_{18}O_{66}]Cl\cdot 27H_2O$ (Gd-1): 0.369 g (0.150 mmol) of $Na_{10}[SiW_9O_{34}]\cdot 23H_2O$[21] was dissolved in 25 ml of sodium acetate buffer (pH 4.4) with stirring. 0.203 g (0.450 mmol) of $Gd(NO_3)_3\cdot 6H_2O$ was slowly added to the reaction mixture. The solution was stirred continuously at 80 ºC for 90 min, followed by cooling to room temperature and filtering. Addition of 1.0 M CsCl solution (0.5 ml) to the colorless filtrate and slow evaporation at room temperature led to the formation of colorless needle-like crystals after about one week. Yield: 21.0 % (based on Na_{10}[*A*-*α*-$SiW_9O_{34}]\cdot 23H_2O$). FT-IR (in cm^{-1}): 1001 (s), 938 (s), 871 (vs), 833 (s), 808 (s), 723 (s), 555 (w), 529 (w). Elemental analysis (%); calcd. (found): W, 55.92 (55.20); Gd, 10.63 (11.00); Cs, 2.25 (3.10); Na, 0.78 (0.63); H, 1.16 (1.13). The number of water molecules has been confirmed by thermogravimetric analysis (Figure 3.19).

Synthesis of $Na_2Cs_3H_2Tb[Tb_2(H_2O)_7Si_2W_{18}O_{66}]\cdot 17H_2O$ (Tb-2): The above synthetic procedure was modified by using 0.196 g (0.450 mmol) of $Tb(NO_3)_3\cdot 5H_2O$ instead of $Gd(NO_3)_3\cdot 6H_2O$. Colorless block shaped crystals were obtained after ca. one week. Yield: 13.8 % (based on Na_{10}[*A*-*α*-$SiW_9O_{34}]\cdot 23H_2O$). FT-IR (in cm^{-1}): 1002 (s), 937 (s), 876 (vs), 818 (s), 718 (s), 547 (w), 524 (w). Elemental analysis (%); calcd. (found): W, 57.28 (54.20); Tb, 8.25 (8.77); Cs, 6.69 (6.74); Na, 0.80 (1.00); H, 0.87 (0.99). The number of water molecules has been confirmed by thermogravimetric analysis (Figure 3.19).

Synthesis of $Na_4Cs_3DyH[Dy_2(H_2O)_{6.5}(C_2H_4O_2)_{0.5}Si_2W_{18}O_{66}]Cl\cdot17H_2O$ (Dy-2): The synthetic procedure was identical to that for **Gd-1**, but 0.197 g (0.450 mmol) $Dy(NO_3)_3\cdot5H_2O$ was used instead of $Gd(NO_3)_3\cdot6H_2O$. Colorless block like crystals were obtained after about one week. Yield: 15.2 % (based on $Na_{10}[A\text{-}\alpha\text{-}SiW_9O_{34}]\cdot23H_2O$). FT-IR (in cm^{-1}): 1002 (s), 940 (s), 882 (vs), 817 (s), 716 (s), 551 (w), 528 (w). Elemental analysis (%); calcd. (found): W, 56.19 (53.30); Dy, 8.27 (8.11); Cs, 6.77 (7.05); Na, 1.56 (1.61); H, 0.85 (0.99); C, 0.20 (0.16). The number of water molecules has been confirmed by thermogravimetric analysis (Figure 3.19).

Synthesis of $Na_4Cs_3Ho[Ho_2(H_2O)_7Si_2W_{18}O_{66}]\cdot18H_2O$ (Ho-2): The above synthetic procedure was performed with 0.200 g (0.450 mmol) $Ho(NO_3)_3\cdot5H_2O$ instead of $Gd(NO_3)_3\cdot6H_2O$. Light pink colored block shaped crystals were obtained after ca. one week. Yield: 12.4 % (based on $Na_{10}[A\text{-}\alpha\text{-}SiW_9O_{34}]\cdot23H_2O$). FT-IR (in cm^{-1}): 1003 (s), 939 (s), 868 (vs), 833 (s), 809 (s), 714 (s), 555 (w), 529 (w). Elemental analysis (%); calcd. (found): W, 56.50 (54.00); Ho, 8.44 (8.68); Cs, 6.81 (6.68); Na, 1.57 (1.58); H, 0.86 (0.98). The number of water molecules has been confirmed by thermogravimetric analysis (Figure 3.19).

Synthesis of $Na_{2.5}Cs_{3.5}GdH_2[Gd_2(H_2O)_7Si_2W_{18}O_{66}](C_2H_3O_2)\cdot16H_2O$ (Gd-2): The synthetic procedure was conducted as described above for **Gd-1** with one alteration: 1.2 ml were added to the colorless filtrate dropwise instead of 0.5 ml of a 1.0 M CsCl solution. Colorless block like crystals were obtained after about one week. Yield: 15.6 % (based on $Na_{10}[A\text{-}\alpha\text{-}SiW_9O_{34}]\cdot23H_2O$). FT-IR (in cm^{-1}): 1002 (s), 934 (s), 886 (vs), 814 (s), 720 (s), 551(w), 529(w). Elemental analysis (%); calcd. (found): W, 56.17 (54.50); Gd, 8.00 (7.68); Cs, 7.30 (7.41); Na, 0.97 (1.09); C, 0.41 (0.40); H,0.86 (0.70). The number of water molecules has been confirmed by thermogravimetric analysis (Figure 3.19).

3.2.2. X-ray crystallography

Data collection of compounds **Gd-1**, **Gd-2**, **Tb-2**, **Dy-2** and **Ho-2** was performed on an Oxford Xcalibur Ruby CCD single-crystal diffractometer (Mo-K_α radiation, λ= 0.71073 Å) at 183(2) K. Routine Lorentz and polarization corrections were applied, and an absorption correction was performed using the program CrysAlis.[22] Direct methods were used to locate the heavy metal atoms (SHELXS-97). The remaining atoms were located from successive Fourier maps (SHELXL-97).[23] All heavy atoms were refined anisotropically except for some disordered alkali-metal countercations and free water molecules. The incorporation of one calcium cation into **Gd-1** was deduced from the crystallographic environment of this specific position. As the calcium content determined from experimental analyses is considerably lower, the selected single crystal probably deviates in this minor detail from the bulk material that is otherwise in good agreement with elemental analysis results for the main constituting elements. Consequently, the experimental PXRD of **Gd-1** (Figure 3.14) displays a less specific match with the theoretical pattern calculated from the X-ray crystallographic data. It is also noteworthy that the PXRD of **Gd-1** displays the lowest crystallinity among the series (Figures 3.14 – 3.18), which is in line with the hypothesis that Ca^{2+} selectively promotes single crystal growth. **Gd-2** contains an obvious site-occupancy disorder of the Cs3, which has been refined on two positions with site occupancies of 0.6 and 0.4. The Tb1 atom in **Tb-2** exhibits disorder over two positions and was refined with site occupancies of 0.8 and 0.2, respectively. The Na1 split positions in **Tb-2** were described with site occupancies of 0.7 and 0.3. The half occupied Cs4 atom in **Tb-2** exhibiting disorder over two positions was refined with site occupancies of 0.3 and 0.2. **Dy-2** also exhibits disorder, namely, of Na2, on two positions with relative occupancies of 0.6 and 0.4, and the Cl1 atom is disordered into two positions with an occupancy of 0.5. In all structures, there is a discrepancy between the formulas determined by elemental analysis and those deduced from the crystallographic atom list. This is due to considerable disorder among the cations and the water molecules, which is a common phenomenon encountered in POM chemistry. Hydrogen atoms were not included in the refinements. The crystallographic data of all polyanions are summarized in Table 10.1 in the Annexes.

3.3. Results and discussion

3.3.1. Synthetic strategy

The silicotungstate precursor $Na_{10}[A\text{-}\alpha\text{-}SiW_9O_{34}]\cdot 23H_2O$ ({α-SiW_9}) was reacted with Ln cations (Ln = Gd^{III}, Ho^{III}, Tb^{III}, Dy^{III}) under optimized reaction conditions. Five polymeric polyanions with two different framework-based structures were successfully isolated in 1.0 M sodium acetate buffer (pH 4.4) at 80 ºC for 90 min by reacting {α-SiW_9} and Ln^{3+} cations in a molar ratio of 1:3.

The new family of open *Wells-Dawson* host anions with lanthanoid guests was characterized with a wide range of analytical methods (FT-IR and UV/Vis spectroscopic techniques, cyclic voltammetry and photoluminescence measurements, TGA, and elemental analysis.) All polyanions were isolated in single crystalline forms as mixed sodium/cesium salts $Na_2CsCaGd_2[Gd_2(H_2O)_7Si_2W_{18}O_{66}]Cl\cdot 27H_2O$ **(Gd-1),** $Na_{2.5}Cs_{3.5}GdH_2[Gd_2(H_2O)_7Si_2W_{18}O_{66}](C_2H_3O_2)\cdot 16H_2O$ **(Gd-2),** $Na_2Cs_3H_2Tb[Tb_2(H_2O)_7Si_2W_{18}O_{66}]\cdot 17H_2O$ **(Tb-2),** $Na_4Cs_3DyH[Dy_2(H_2O)_{6.5}(C_2H_4O_2)_{0.5}Si_2W_{18}O_{66}]Cl\cdot 17H_2O$ **(Dy-2),** and $Na_4Cs_3Ho[Ho_2(H_2O)_7Si_2W_{18}O_{66}]\cdot 18H_2O$ (**Ho-2**). Both **Gd-1** with a 3D inorganic framework and (**Gd-2** to **Ho-2**) with 2D layer networks are consisting of dimeric building blocks. They are connected through W-O-W bonds via two axial oxygen atoms of each individual anion. The W-O-W bonds are bent towards the interior of the polyanion, thereby forming the pocket of the open *Wells-Dawson* ion $[\alpha\text{-}Si_2W_{18}O_{66}]^{16-}$. The multi-lacunary polyanions (**Gd-1** to **Ho-2)** contain two incorporated lanthanoid cations within their structural cavities to form the dimeric building blocks. Meanwhile, these moieties are furthermore linked to external lanthanoid atoms via terminal oxygen atoms of the neighboring polyanion (W=O), thereby forming two different framework types (**Gd-1** and **Gd-2** to **Ho-2**, respectively, Figure 3.1).

In the case of the newly formed $[Ln_2(H_2O)_7Si_2W_{18}O_{66}]^{10-}$ (Ln = Gd^{III} (**Gd-1** and **Gd-2)**, Tb^{III}, Ho^{III}) and $[Dy_2(H_2O)_{6.5}(C_2H_4O_2)_{0.5}Si_2W_{18}O_{66}]^{10-}$ polyanions, two lanthanoid ions occupy the peripheral K^+ pocket position in the $[\alpha\text{-}Si_2W_{18}O_{66}]^{16-}$ host anion that was described by *Hervé* et al.[15, 16] Here, a different synthetic strategy towards the Ln-containing polyanions was employed, starting from the sodium salt of the trivacant

Keggin polyoxoanion $[A\text{-}\alpha\text{-SiW}_9\text{O}_{34}]^{10-}$ ($\{\alpha\text{-SiW}_9\}$) precursor in 1.0 M NaOAc buffer throughout in order to suppress the hydrolysis of the lanthanoid cations by adjusting the pH of the reaction mixture. The structural variety of lanthanoid-containing POMs (LSPs) extending from discrete building blocks to polymeric networks, can be highly affected by a comparable flexibility of synthetic parameters such as the pH value, counter cations, stoichiometry, temperature, etc.[9] Furthermore, many previous studies demonstrate that the $\{\alpha\text{-SiW}_9\}$ polyoxoanion is easily transformed into *Keggin*- or *Dawson*-type polyanions and oligomeric structures in acidic aqueous solution. A literature survey of POM types emerging from the $\{\alpha\text{-SiW}_9\}$ precursor can be found in Table 3.1.

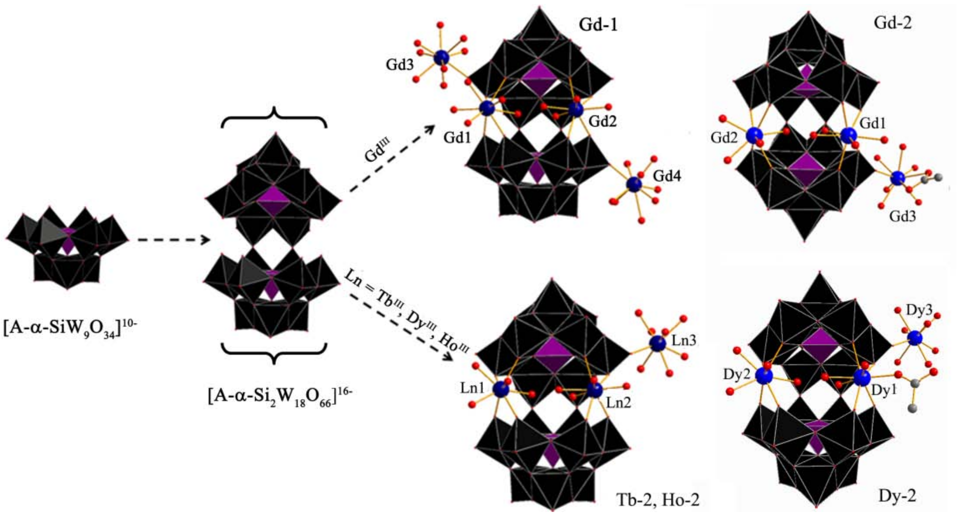

Figure 3.1. Transformation of the $[A\text{-}\alpha\text{-SiW}_9\text{O}_{34}]^{10-}$ precursor into dimeric $[\text{Ln}_2(\text{H}_2\text{O})_7\text{Si}_2\text{W}_{18}\text{O}_{66}]^{10-}$ (Ln = Gd^{III} (**Gd-1** and **Gd-2**), Tb^{III}, Ho^{III}) and $[\text{Dy}_2(\text{H}_2\text{O})_{6.5}(\text{C}_2\text{H}_4\text{O}_2)_{0.5}\text{Si}_2\text{W}_{18}\text{O}_{66}]^{10-}$ polyanions in HOAc/NaOAc buffer (W: black polyhedra; Si: purple polyhedra; Ln: blue; O: red; C: gray).

Thus the results from Table 3.1 indicate throughout that the $\{\alpha\text{-SiW}_9\}$ moiety preferably forms *Dawson*-type polyanions by dimerization or gives rise to oligomeric structures connected through tungsten atoms or alkali metal cations at lower pH values (2.4 > pH > 5.9),[15-20] whereas it is more likely to reassembly into *Keggin*-type polyanions at higher pH values (5.0 > pH > 6.3).[24-26] In the present $\{\alpha\text{-SiW}_9\}/\text{Ln}^{III}$ systems, the transformation from $[\alpha\text{-SiW}_9\text{O}_{34}]^{10-}$ to $[\alpha\text{-Si}_2\text{W}_{18}\text{O}_{66}]^{16-}$ preferably gives rise to the formation of **Gd-1** and **Gd-2** to **Tb-2** under optimized conditions (pH 4.4 and 80 ^{o}C).

Moreover, the crystal structure of the products is obviously influenced by the {α-SiW_9}/ Ln^{III} ratio: the polymeric compounds (**Gd-1** to **Gd-2**) could not be obtained upon its change from 1:3 to 1:2 or 1:1. The countercation is another important synthetic parameter: single crystals of sufficient quality could be obtained, when Cs^+ was replaced with NH_4^+, Na^+, K^+ or Rb^+. This may be assigned to electrostatically superior linker qualities of the larger Cs^+ in connection with the $[Ln_2(H_2O)_7Si_2W_{18}O_{66}]^{10-}$ (Ln = Gd, Ho, Tb, Dy) and $[Dy_2(H_2O)_{6.5}(C_2H_4O_2)_{0.5}Si_2W_{18}O_{66}]^{10-}$ polyoxoanions. Interestingly, **Gd-1** with a 3D inorganic framework structure was isolated by adding a small amount of Cs^+ countercations (0.5 ml, 1.0 M CsCl solution) to the {SiW_9} precursor. The transformation of the 3D POM framework compound **Gd-1** into the 2D POM framework compound **Gd-2** was achieved in aqueous solution by the continuous addition of Cs^+ (1.2 ml). In addition, a mixture of **Gd-1** and **Gd-2** in solution can be deliberately controlled by adjusting the Cs^+ concentration, indicating the existence of an equilibrium between **Gd-1** and **Gd-2**. Whereas neither most alkali cations nor lanthanoid ions bind to the central pocket site of $[Si_2W_{18}O_{66}]^{16-}$, K^+ ions probably play an essential role in maintaining the open *Wells-Dawson* structure of $[\{K(H_2O)_3\}_2\{K(H_2O)_2\}(Si_2W_{18}O_{66})]^{13-}$ with its special coordination sites for different cations.[15-16, 18] There is no doubt that the templating role of the cations during POM formation processes cannot be underestimated, as illustrated by the stabilization effect of Cs^+ for the $[Cs\subset Ln_6As_6W_{63}O_{218}(H_2O)_{14}(OH)_4]^{25-}$ (Ln = Eu, Gd, Tb, Dy, Ho, and Er) series.[4a] Although *Hervé* et al. pointed out that the dimerization of $[NaSi_2W_{18}O_{66}]^{15-}$ cannot be ruled out, their attempt to study the influence of Na^+ on the reactivity of [*A*-α-$SiW_9O_{34}]^{10-}$ led to the formation of monolacunary [*A*-α-$SiW_{11}O_{39}]^{8-}$. This indicates that the affinity of K^+ for the central position is caused by size and solubility differences in comparison with Na^+.

Table 3.1. Product range emerging from the $[A\text{-}\alpha\text{-SiW}_9\text{O}_{34}]^{10-}$ precursor depending on the synthetic conditions.

Type[a]	Compound	pH	T/°C/	time	ref.
I	$\alpha\text{-}[\text{SiW}_9\text{O}_{37}\,\text{M}_3(\text{H}_2\text{O})_3]^{10-}$ (M = Mn, Co, Ni)	5-6	80	1 h	24
I	$[\{\text{Cu(2,2-bipy)}_2\}_2\{\text{SiW}_{12}\text{O}_{40}\}]$	--	160	5 d	25
I	$[\text{Mn(2,2-bipy)}_3]_2[\text{SiW}_{12}\text{O}_{40}]$	--	160	5 d	25
I	$[\text{K}(\text{SiW}_{11}\text{O}_{39})_2]^{15-}$	6.3	80	--	26
II	$\alpha\text{-}[\{\text{K}(\text{H}_2\text{O})_2\}(\text{Si}_2\text{W}_{18}\text{O}_{66})]^{15-}$	5.7	--	30 min	15, 16
II	$[\{\text{M}(\text{H}_2\text{O})\}(\mu\text{-H}_2\text{O})_2\text{K}(\text{Si}_2\text{W}_{18}\text{O}_{66})]^{13-}$ (M = Co, Ni, Cu)	5.9	--	--	16
II	$[\{\text{M}(\text{H}_2\text{O})\}(\mu\text{-H}_2\text{O})_2\text{K}\{\text{M}(\text{H}_2\text{O})_4\}(\text{Si}_2\text{W}_{18}\text{O}_{66})]^{11-}$ (M = Mn, Co, Ni)	5.9	--	--	16
II	$[\{\text{KV}_2\text{O}_3(\text{H}_2\text{O})_2\}(\text{Si}_2\text{W}_{18}\text{O}_{66})]^{11-}$	3.8	--	--	13
II	$[\{\text{Fe}_4(\text{OH})_6\}(\text{Si}_2\text{W}_{18}\text{O}_{66})]^{10-}$	2.9	--	30 min	13
II	$[\text{Cu}_5(\text{OH})_4(\text{H}_2\text{O})_2(A\text{-}\alpha\text{-SiW}_9\text{O}_{33})_2]^{10-}$	4.8	80	30	19
II	$[\text{M}(\text{H}_2\text{O})_2(\text{SiW}_{10}\text{O}_{35})_2]^{10-}$ (M = Mn, Co, Ni)	4.5	50	30	20
II	$[\text{Ln}_2(\text{H}_2\text{O})_7\text{Si}_2\text{W}_{18}\text{O}_{66}]^{10-}$ (Ln = Gd, Tb, Dy, Ho), and $[\text{Dy}_2(\text{H}_2\text{O})_{6.5}(\text{C}_2\text{H}_4\text{O}_2)_{0.5}\text{Si}_2\text{W}_{18}\text{O}_{66}]^{10-}$	4.4	80	90 min	14
III	$\alpha\text{-}[\{[\text{K}(\text{H}_2\text{O})_2](\mu\text{-H}_2\text{O})[\text{Li}(\text{H}_2\text{O})_2]\}_2\text{Si}_4\text{W}_{36}\text{O}_{126}(\text{H}_2\text{O})_4]^{16-}$	2.4	RT	12 h	17
III	$\alpha\text{-}[\{[\text{K}(\text{H}_2\text{O})][\text{K}(\text{H}_2\text{O})_4]\}_2\text{Si}_8\text{W}_{36}\text{O}_{136}]^{22-}$	3.5	RT		17

[a] I: *Keggin*-type; II: *Dawson*-type; III: oligomer

3.3.2. Crystal structures

Although the compounds **Gd-1**, **Tb-2**, **Dy-2**, **Ho-2** and **Gd-2** have the similar dimeric open *Wells-Dawson* polyanion in common, the polymeric structure of **Gd-1** differs from the **Gd-2** to **Ho-2** series (cf. Table 10.1 in the Annexes). In general, two lanthanoid cations are formally replaced with the potassium cations on the exterior pocket sites of the open *Wells-Dawson* parent type $[\{\text{K}(\text{H}_2\text{O})_3\}_2\{\text{K}(\text{H}_2\text{O})_2\}(\text{Si}_2\text{W}_{18}\text{O}_{66})]^{13-}$.[15] The remaining lanthanoid cations as external linkers thus led to the formation of 3D networks (**Gd-1**) or 2D polymeric sheet-like materials (**Gd-2**, **Dy-2**, and **Ho-2**).

The crystal structure of **Gd-1** (Figures 3.2 and 3.3) is comprised of one *Wells-Dawson* anion $A\text{-}\alpha\text{-}[\text{Si}_2\text{W}_{18}\text{O}_{66}]^{16-}$ with four Gd^{3+} cations: the Gd1 and Gd2 cations are located in the peripheral pocket of the $\alpha\text{-}[\text{Si}_2\text{W}_{18}\text{O}_{66}]^{16-}$ anion, whereas the Gd3 and Gd4 cations are

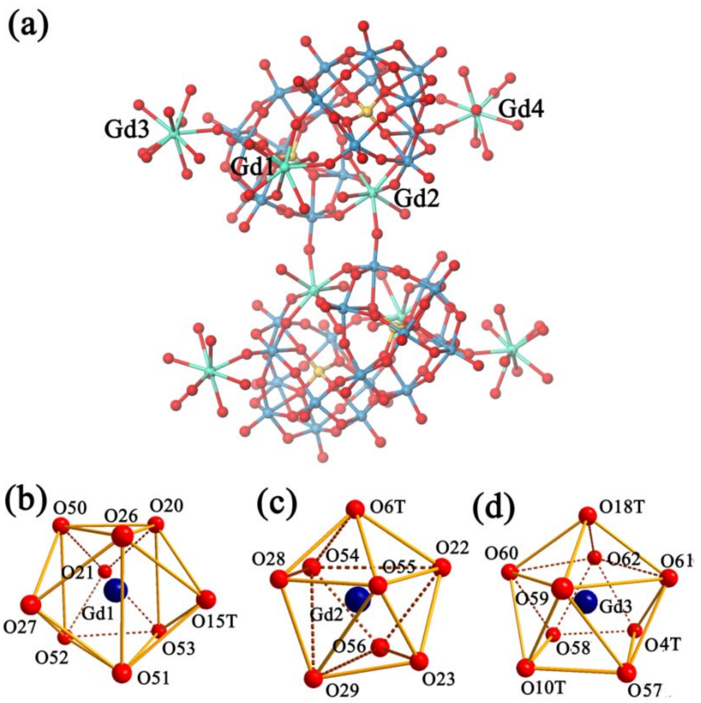

Figure 3.2. (a) Connectivity of the $\{Gd_2[Gd_2(H_2O)_7Si_2W_{18}O_{66}]\}^{4-}$ anion in **Gd-1** (W: blue; Gd: green; Si: yellow; O: red); (b – d) individual Gd geometries of **Gd-1**: (b) tri-capped trigonal prismatic coordination of Gd1, (c) dodecahedral geometry of Gd2, (d) mono-capped square-antiprismatic environment of Gd3.

bound to the terminal oxygen atoms of the tungsten caps contributed by the [*A*-*α*-$SiW_9O_{34}]^{10-}$ $\{SiW_9\}$ precursor. The Gd-Gd distance is 6.338(2) Å in the dimeric *Wells-Dawson* anion $[Gd_2(H_2O)_7Si_2W_{18}O_{66}]^{10-}$ of **Gd-1**. The Gd1 cation is bound to four terminal oxygen atoms (O20, O21, O26 and O27) from two edge-sharing WO_6 octahedra of the *α*-$[Si_2W_{18}O_{66}]^{16-}$ moiety (Gd1-O distance range: 2.372(9) – 2.538(9) Å), to four terminal water ligands (O50, O51, O52 and O53) (Gd1-O distances: 2.438(11) – 2.475(11) Å), and to a terminal oxygen atom (O15T', symmetry code: *1-x, y, 0.5-z*) from another neighbouring $[Gd_2(H_2O)_7Si_2W_{18}O_{66}]^{10-}$ framework (Gd1-O15T' : 2.494(10) Å). The Gd2 cation is also bound to four terminal oxygen atoms (O22, O23, O28 and O29) from pairs of edge-sharing WO_6 octahedra (Gd2-O distances from 2.338(9) to 2.418(10) Å) and to three water molecules (O54, O55 and O56 with Gd2-O ranging from 2.405(13) to 2.456(10) Å). Gd2 is further bound to a terminal oxygen atom (O6T' ; symmetry code: *1-x, -y, -z*) from a neighbouring polyanion (Gd2-O6T' : 2.407(9) Å) via symmetry related Gd-O-W bonds (Gd2-O6T'-W6' and Gd2'-O6T-W6) with an inversion centre, which displays a head-on motif with four metal atoms in the dimeric entity $[Gd_2(H_2O)_7Si_2W_{18}O_{66}]^{10-}$ (Figure 3.2 a).

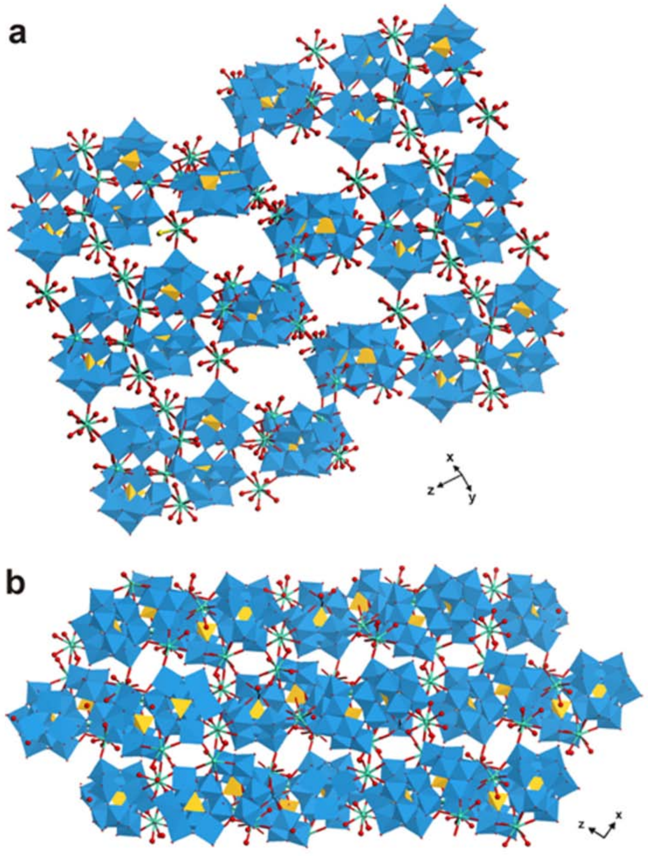

Figure 3.3. Packing motif of the **Gd-1** type. Cations and crystal water molecules are omitted for clarity. (W: blue octahedra; O: red; Si: yellow; Ln: green): (a) polyhedral view of the 3D open framework with 1D channels in **Gd-1**, (b) projection along the *y* axis.

On the other hand, the Gd1 cation of the dimeric polyanion $[Gd_2(H_2O)_7Si_2W_{18}O_{66}]^{10-}$ is coordinated to the terminal oxygen atom of W15, thus connecting six metal centers into a hexameric arrangement with inversion symmetry. The Gd3 atom is coordinated to W4, W10 (*1-x*, *y*, *0.5-z*) and W18 (*0.5+x*, *0.5+y*, *z*) and vice versa via μ-oxo bonds (Gd3-O: 2.366(10) –2.422(9) Å). Gd4 is coordinated to W1 (*0.5-x*, *0.5-y*, *-z*) and W12 of the open *Wells-Dawson* anion via μ-oxo bonds (Gd4-O1T': 2.319(11) Å; Gd4-O12T: 2.316(10) Å), again in a symmetry related pattern with an inversion centre. The coordination sphere of the Gd3 atom is completed by six water molecules, whereas the Gd4 coordination sphere is occupied by seven water molecules. Whilst Gd1, Gd2 and Gd4 are coordinated to two polyanions, Gd3 is attached to three clusters with the highest degree of connectivity. Therefore, each dimeric cluster $[Gd_2(H_2O)_7Si_2W_{18}O_{66}]^{10-}$ is further assembled into a 3D-polymeric material via four Gd cations (Figure 3.3). It is worthwhile to note that this connection mode results in the formation of 1D channels with incorporated crystal water molecules and alkali cations. The dimension of the channels is about 12.7 × 7.1 Å.

From the topological point of view, –Gd1– and –Gd2– can be assigned as the bridging connectors between two $[Gd_2(H_2O)_7Si_2W_{18}O_{66}]^{10-}$ clusters. Consequently, $[Gd_2(H_2O)_7Si_2W_{18}O_{66}]^{10-}$ clusters, Gd3 and Gd4 can be considered as the nodes. In this stylized manner, $[Gd_2(H_2O)_7Si_2W_{18}O_{66}]^{10-}$ clusters are 7-connecting nodes, and Gd3 atoms are 3-connecting nodes. Therefore, the 3D framework can be described as a (3, 7) connecting network (Figure 3.4). To the best of our knowledge, **Gd-1** represents the first 3D inorganic coordination polymer based on lanthanoid-substituted *Wells-Dawson* POMs, and the topology of this framework has never been observed in POM chemistry before.

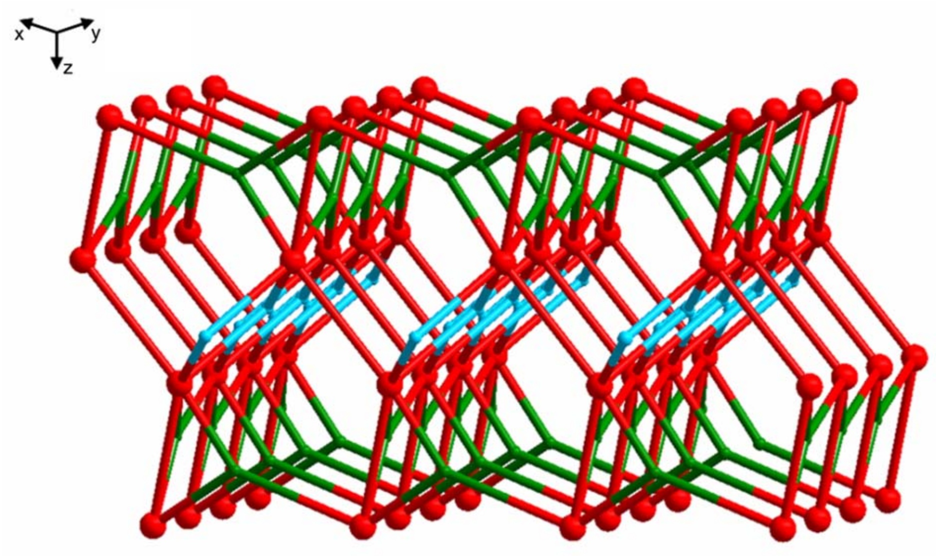

Figure 3.4. View of the topology of **Gd-1** (red nodes: $[Gd_2(H_2O)_7Si_2W_{18}O_{66}]^{10-}$ clusters, green nodes: Gd3 atoms, blue nodes: Gd4 atoms).

Single crystal X-ray diffraction analyses reveal that compounds **Gd-2, Dy-2** and **Ho-2** are isostructural and isomorphous having the same triclinic space group *P-1* in common. Their molecular structures are composed of one *Wells-Dawson* anion *A*-*α*-$[Si_2W_{18}O_{66}]^{16-}$ and three crystallographically independent lanthanoid cations (Ln = Tb, Dy, Ho, Gd). As the four compounds are isomorphous, we only discuss the structure of **Tb-2** in detail as a representative example. In the **Tb-2** polyanions, the Tb1 and Tb2 cations occupy the pocket positions of the $[Si_2W_{18}O_{66}]^{16-}$ host anion with a Tb-Tb distance of 6.265(2) Å (Figure 5a). The Tb1A cation is bound to four terminal oxygen atoms (O22, O23, O28 and O29) from pairs of edge-sharing WO_6 octahedra of the *α*-$[Si_2W_{18}O_{66}]^{16-}$ framework (Tb1A-O distance range: 2.317(11) – 2.411(10) Å), and to four terminal water ligands (O51, O52, O53 and O73, Tb1A-O distances between 2.36(2) and 2.459(14) Å). On the other hand, the Tb2 cation is not only attached to four terminal oxygen atoms (O20, O21, O26 and O27) from the *α*-$[Si_2W_{18}O_{66}]^{16-}$ framework (Tb2-O distance range: 2.292(10) – 2.398(10) Å) and three terminal water ligands (O49, O50 and O69, Tb2-O distances 2.387(11) – 2.472(12) Å), but also bridged to another single polyanion which is connected to the adjacent cluster via symmetry related Tb-O-W bonds (Tb2-O6T'-W6'and Tb2'-O6T-W6; symmetry code of O6T', W6' and Tb2': *1-x,-y, -z* with Tb2-O6T' 2.341(9) Å), thereby forming a similar head-on species of four metal centres via an inversion center as has been observed in **Gd-1** (Figure 3.5a).

The Tb3 cations are coordinated to three terminal oxygen atoms O4T, (O18T', symmetry code: *x, 1+y, z*) and (O17T', symmetry code: *-x, -y, 1-z*) of the dimeric $[Tb_2(H_2O)_7Si_2W_{18}O_{66}]^{10-}$ polyanions (Tb3-O: 2.321(11) – 2.371(10) Å) and to five water molecules (O55-O59 with Tb3-O distances ranging from 2.383(13) to 2.425(12) Å). Tb3 is bound to W4, W18 (*x, 1+y, z*) and W17 (*-x, -y, 1-z*) from different three clusters by via μ-oxo bridges, thus connecting the 1D polyanion chains into a 2D sheet-like polymeric material with voids for alkali cations and crystal water molecules (Figure 3.6). Additionally, from the viewpoint of topology, the $[Tb_2(H_2O)_7Si_2W_{18}O_{66}]^{10-}$ clusters represent 4-connecting nodes, Tb2 atoms can be assigned as bridging connector ligands between two clusters, and the Tb3 atoms are also representing 3-connecting nodes (Figure 3.7). Therefore, the 2D architecture displays a 2D (3,4) - binodal topological network.

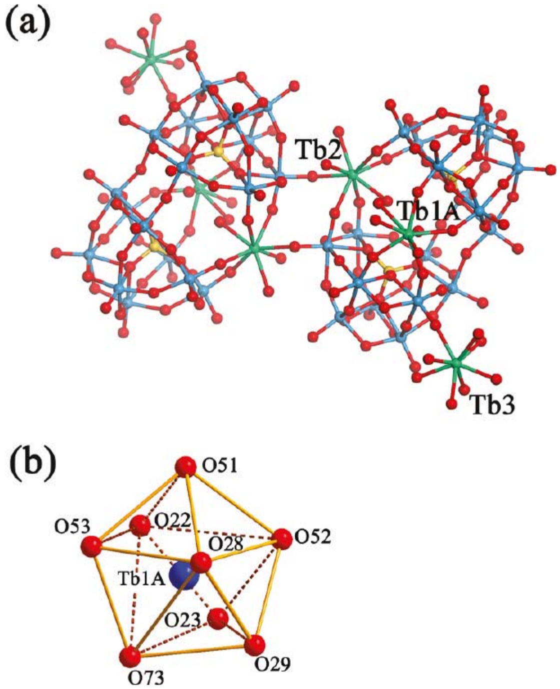

Figure 3.5. (a) Ball-and-stick representation of the $\{Tb[Tb_2(H_2O)_7Si_2W_{18}O_{66}]\}^{7-}$ anion in **Tb-2** (W: blue; Tb: green; Si: yellow; O: red), (b) dodecahedral coordination environment of Tb1A in **Tb-2**. Only the major position of the disordered Tb1 (Tb1A) is shown for clarity.

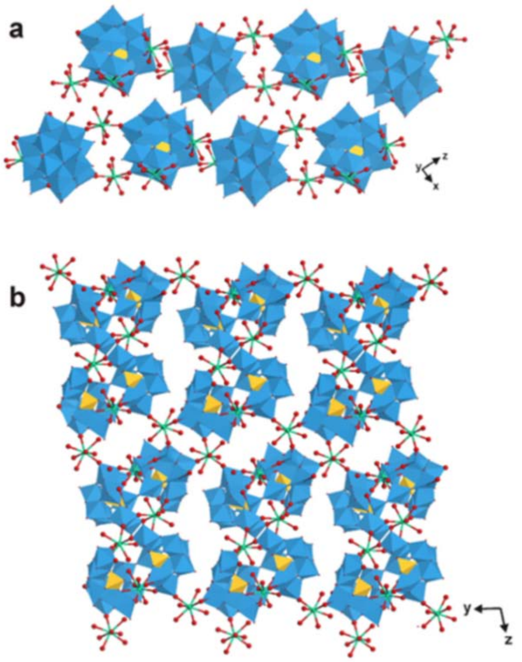

Figure 3.6. Packing motif of the **Tb-2** type. Cations and crystal water molecules are omitted for clarity (W: blue; O: red; Si: yellow; Ln: green): (a) polyhedral view of 1D chains in the *xz* plane, (b) 2D sheet projection along the *x* axis.

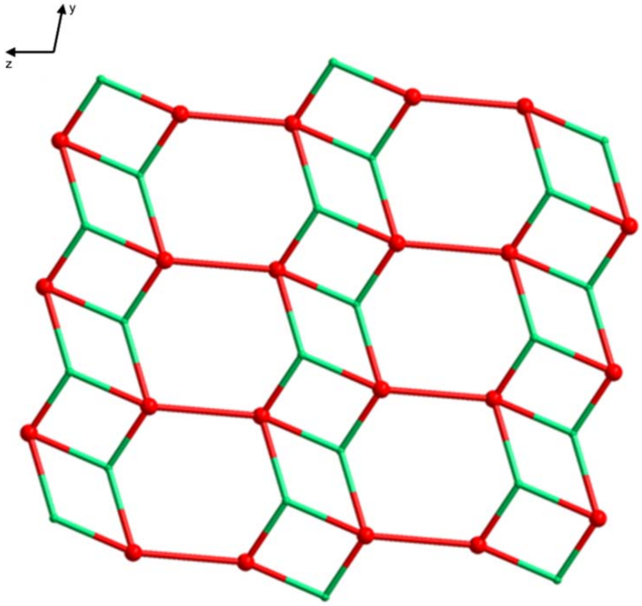

Figure 3.7. Topological view of **Tb-2** projection along the *x* axis (red nodes: $[Tb_2(H_2O)_7Si_2W_{18}O_{66}]^{10-}$ clusters, green nodes: Tb3 atoms).

Furthermore, it is noteworthy that there is a slight structural difference between the (**Tb-2**, **Dy-2** and **Ho-2**) series and **Gd-2**: (1) A half-occupied acetate oxygen and a half-occupied water molecule are bound to the Dy1 ion in **Dy-2**, whereas the analogous bonding sites of the Ln1 ions in **Tb-2** and **Ho-2** are occupied by one terminal water molecule (Figure 3.1). (2) Moreover, the Ln^{III} cations in **Tb-2**, **Dy-2** and **Ho-2** are eight-coordinate with an almost ideal dodecahedral coordination geometry (Figure 3.5). In **Gd-2**, the Gd1 and Gd2 cations in the external pocket of α-$[Si_2W_{18}O_{66}]^{16-}$ anion, are eight-coordinate with an almost ideal dodecahedron and a distorted square anti-prismatic coordination geometry, respectively. Gd3 adopts a distorted nine-coordinate mono-capped square antiprism with three terminal oxygen atoms from three neighboring $[Gd_2(H_2O)_7Si_2W_{18}O_{66}]^{10-}$ polyanions and four water molecules. The remaining two coordination sites are occupied by two oxygen atoms of the bidentate acetate ligand (cf. Figure 3.8 and discussion below). All these polyanions can be viewed as “inversion pairs” in analogy to K_{16}-α-$[Si_2W_{18}O_{66}]$.[11] Actually, the lanthanoid cations not only occupy the external pockets position of α-$[Si_2W_{18}O_{66}]^{16-}$ host anion, but also they act as external linkers, leading to the formation of novel polymeric materials. Therefore, the double role of Ln^{3+} differs from the role of K^+ in previous structures.

It is well known that the trivalent lanthanoid ions usually possess variable higher coordination numbers: eight (dodecahedral, square anti-prismatic or bi-capped trigonal prismatic), and nine (tri-capped trigonal prismatic, mono-capped square antiprismatic).[27] Lanthanide coordination geometries of comparable extension in POM chemistry have also been widely described, such as for cerium containing polyoxotungstates {$Ce_{16}W_{148}$} with two, five or no aqua ligands per Ce atom[6] and for {$Ce_{20}W_{100}$} with one or two aqua ligands, respectively.[7] The same trend was observed for the large gadolinium containing polyoxotungstate {Gd_8W_{124}} reported previously by our group.[4b] The lanthanoid ions in the present new series (**Gd-1** to **Ho-2**) display four different coordination environments with three to seven terminal aqua ligands, respectively. The coordination polyhedron of Gd1 in **Gd-1** can be described as a nine-coordinated tri-capped trigonal prism (D_{3h}), and the capping oxygen atoms are located in the centre of three rectangular faces (Figure 3.2 b). The trigonal faces are constituted by O50-O26-O20 and O52-O51-O53 in the tri-capped trigonal prism with three eclipsing pairs (O50 and O52, O26 and O51, O20 and O53). Three oxygen atoms (O21, O27 and O15T) as the three capping atoms of the rectangular faces are approximately trigonal coplanar with an average angle between capping oxygen atoms and Gd1 of 119.9(2)^o in comparison to 120^o for an ideal tri-capped trigonal prism. The dihedral angles between the plane, which are defined by the capping atoms and Gd1 and the two trigonal planes, are 1.0(4)^o and 0.9(3)^o respectively. The dihedral angle between the two trigonal planes is 1.5(4)^o, thereby rendering an ideal tri-capped trigonal prismatic geometry.[28] Bond angles between Gd1 and two eclipsing oxygen atoms of opposite trigonal planes are 90.8(4)^o for O50-Gd1-O52, 90.7(4)^o for O26-Gd1-O51 and 92.6(4)^o for O20-Gd1-O53. The coordination geometry around Gd2 can be best described as an eight-coordinated dodecahedron with an idealized D_{2d} symmetry, and two interpenetrating trapezoids are orthogonal to each other (Figure 3.2 c).[29] Regarding Gd2, two trapezoids are defined as the near-planar arrangements of O54-O56-O55-O6T and O22-O23-O29-O28 with average deviations from their least-squares planes of 0.7938 and 0.0212 Å, respectively. The degrees of non-planarity (ϕ) are 2.8(3)^o and 1.6(4)^o, respectively. The dihedral angle between the two trapezoids is 89.4(2)^o. The coordination spheres of both Gd3 and Gd4 are quite close to mono-capped square antiprisms with idealized C_{4v} symmetry. In the case of Gd3, the two approximately antiparallel squares are composed of O61-O62-O60-O59 and O58-O4T-O57-O10T, respectively, with a dihedral angle of 2.9(3)° (Figure 3.2 d).[30] The capping atom (O18T) is located above the open square plane of O61-O62-O60-O59. The base diagonals are somewhat different, 3.693(2) and 4.113(2) Å for O4T-O10T and O57-O58, respectively. This is because that O57-O10T (3.012(2) Å) and O4T-O57 (2.712(2) Å) are longer than the other two distances in the square, 2.640(2) and 2.703(2) Å for O4T-O58 and O58-O10T, respectively.

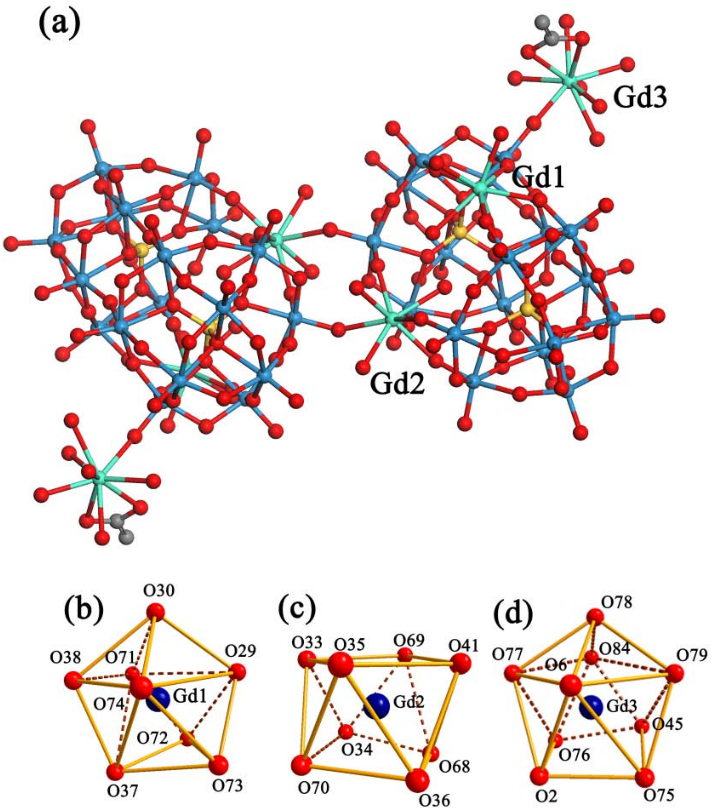

Figure 3.8. (a) Ball-and-stick representation of the Gd[Gd$_2$(H$_2$O)$_7$Si$_2$W$_{18}$O$_{66}$]}$^{7-}$ anion in **Gd-2** (W: blue; Tb: green; Si: yellow; O: red; C: gray); (b – d) individual Gd geometries of **Gd-2**: (b) dodecahedral coordination environment of Gd1, (c) square-antiprismatic geometry of Gd2, (d) monocapped square-antiprismatic environment of Gd3 in **Gd-2**.

The coordination geometries of Gd1 and Gd2 in **Gd-2** are both eight-coordinated, adopting an almost ideal dodecahedron (*D$_{2d}$*) and a slightly distorted square antiprism (*D$_{4d}$*), respectively (Figure 3.8b and Figure 3.8d). In the case of Gd1 cation, the two ϕ

values for two body-diagonals of the trapezoids, defined as O74-O73-O72-O71 and O38-O37-O29-O30, are 3.8(3)^o and 1.1(3)°. The dihedral angle between the trapezoids is 88.8(2)°. In the case of Gd2, two groups of oxygen atoms, namely (O33, O35, O67 and O69) and (O34, O70, O36 and O68) constitute the two bottom planes of a square antiprism, and the average deviations from their least-squares planes are 0.1119 and 0.1096 Å, respectively. The dihedral angle for the two bottom planes is 5.1(2)^o. The Gd3 cation is located in a distorted monocapped square antiprism (Figure 3.8c) with O78 atom from one acetate ligand at the capped position. The two antiparallel squares are constituted of O77-O6-O79-O84 and O76-O2-O75-O45, with average deviations of 0.2410 and 0.1527 Å, respectively. The dihedral angle between the two bottom squares is 6.2(3)^o. As for **Tb-2, Dy-2** and **Ho-2**, the coordination environment of all the lanthanoids can be described as an almost undistorted eight-coordinate dodecahedron (D_{2d}). As shown in Figure 3.5b as a representative example, the Tb1 cation displays a near-perfect dodecahedral coordination geometry with the dihedral angle between the two trapezoids being 88.9(2)^o. It has been suggested that larger lanthanoids are prone to have higher coordination numbers and display more flexible coordination geometries compared to smaller lanthanoids: the electrostatic stability of the crystal structure decreases with the lanthanoid radius owing to the increasing ligand repulsion in the coordination sphere.[31] Moreover, the average Ln-O distances in all the compounds tentatively indicate the presence of a lanthanoid contraction effect with 2.42(2) Å for **Gd-1**, 2.41(1) Å for **Gd-2**, 2.39(3) Å for **Tb-2**, 2.36(2) Å for **Dy-2**, and 2.34(2) Å for **Ho-2**.

Bond valence sum calculations (BVS) indicate that Si site is present in the +4 oxidation state, Ln sites display a +3 oxidation state and all W sites have an oxidation number of +6, which is in agreement with the initial valencies from the starting materials.[32] Meanwhile, no protonation of the oxygen atoms of the dimeric {α-$Si_2W_{18}O_{66}$} moiety was observed. However, to balance the charge -10 for the polyanions $[Ln_2(H_2O)_7Si_2W_{18}O_{66}]_n^{10-}$ (Ln = Gd^{III} (**Gd-1** and **Gd-2)**, Tb^{III}, Ho^{III}) and $[Dy_2(H_2O)_{6.5}(C_2H_4O_2)_{0.5}Si_2W_{18}O_{66}]_n^{10-}$ by their countercations in the solid state, we added two protons in **Tb-2**, one proton in **Dy-2** and two protons in **Gd-2**, respectively, as the products were isolated from acidic aqueous solution (pH 4.4). These protons cannot be located crystallographically and are assumed to be delocalized over the entire structure, which is a common phenomenon in POM chemistry.[33]

3.3.3. Analytical characterizations and properties

3.3.3.1. FT-IR spectroscopy

The FT-IR spectra of all compounds (**Gd-1** and **Gd-2, Tb-2**, **Dy-2**, **Ho-2)** display four characteristic ν_{as}(Si-O$_a$), terminal ν_{as}(W-O$_t$), corner-sharing ν_{as}(W-O$_b$) and edge-sharing ν_{as}(W-O$_c$) asymmetrical vibration peaks of the common open *Wells-Dawson* anion *A-α-*$[Si_2W_{18}O_{66}]^{16-}$ (Figure 3.9). In the IR spectrum of **Gd-1**, the peaks at 1001 cm^{-1} can be attributed to ν_{as}(Si-O$_a$) and the characteristic bands at 938, 871, 833, 808 and 723 cm^{-1} are assigned to ν_{as}(W-O$_t$), ν_{as}(W-O$_b$) and ν_{as}(W-O$_c$). The characteristic features in the IR spectrum of **Gd-2** at 1002, 934, 886, 814 and 720 cm^{-1} arise from ν_{as}(Si-O$_a$), ν_{as}(W=O$_d$), ν_{as}(W-O$_b$) and ν_{as}(W-O$_c$), respectively. The peaks in the IR spectrum of **Tb-2** at 1002, 937, 876, 818 and 718 cm^{-1} can be assigned to ν_{as}(Si-O$_a$), ν_{as}(W=O$_d$), ν_{as}(W-O$_b$) and ν_{as}(W-O$_c$). In the IR spectrum of **Dy-2**, the peaks at 1002, 940, 882, 817 and 716 cm^{-1} are attributed as follows: ν_{as}(Si-O$_a$), ν_{as}(W=O$_d$), ν_{as}(W-O$_b$) and ν_{as}(W-O$_c$). Likewise, the characteristic vibrations in IR spectrum of **Ho-2** at 1003, 939, 868, 833, 809 and 714 cm^{-1} arise from ν_{as}(Si-O$_a$), ν_{as}(W=O$_d$), ν_{as}(W-O$_b$) and ν_{as}(W-O$_c$). Moreover, the gradual blue shift of the ν_{as}(W-O$_c$) vibration indicated the influence of the lanthanoid contraction on the FT-IR spectra.

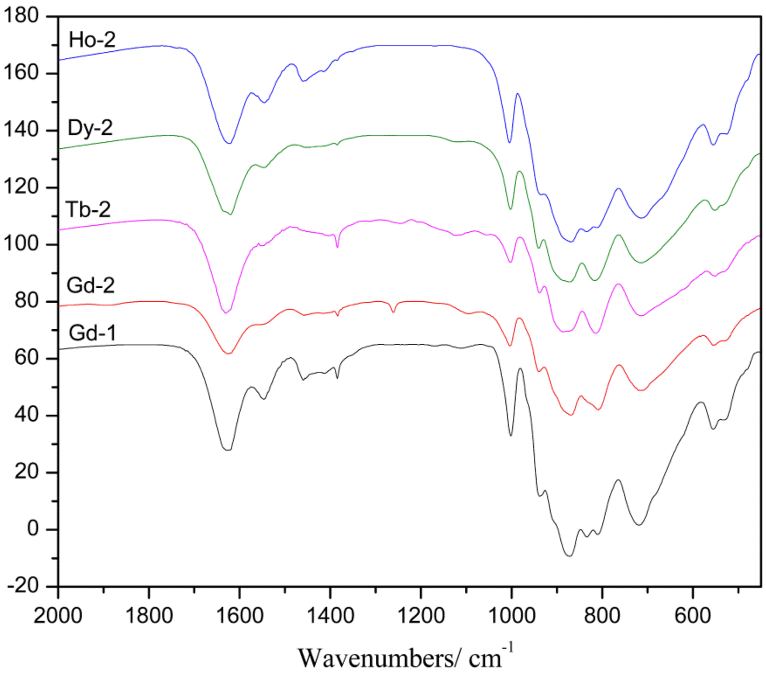

Figure 3.9. FT-IR spectra of the polyanions **Gd-1** and **Gd-2**, **Tb-2**, **Dy-2**, **Ho-2** recorded in KBr.

3.3.3.2. UV/Vis spectroscopy

The UV/Vis spectra of all compounds were recorded in aqueous solution in the 600-190 nm range (Figure3.10). The UV spectra of (**Gd-1** and **Gd-2, Tb-2**, **Dy-2**, **Ho-2)** revealed two characteristic absorption bands at 202-205 and 250 nm throughout. The absorption band at higher energies can be assigned to the p_π-d_π charge-transfer transitions of the O_t→W bonds, whereas the latter low energy absorption band is due to the p_π-d_π charge-transfer transitions of the $O_{b(c)}$→W bonds. However, the UV spectra of **Gd-2**, **Dy-2** and **Ho-2** exhibit only the higher energy absorption band located at 194-200 nm that can be assigned to the p_π-d_π charge-transfer transitions of the O_t→W bonds.[34a] The blue shift of the absorption bands at higher energies might point out the influence of the different lanthanoid cations on the local geometry of the $[Ln_2(H_2O)_7Si_2W_{18}O_{66}]^{10-}$ (Ln = Gd, Ho, Tb) and $[Dy_2(H_2O)_{6.5}(C_2H_4O_2)_{0.5}Si_2W_{18}O_{66}]^{10-}$ polyanions. Similar phenomena have been already observed in previous related studies on the reaction of Ln cations with monovacant *Keggin*-type polyoxometalates.[34] Moreover, the absorption bands of the trivalent lanthanides in aqueous solution were not observed, probably due to concealing by the strong (O→W) charge transfer bands. Therefore, the solid state absorption spectra of all samples were also recorded in the 400-850 nm range. In the case of **Tb-2**, two weak absorption bands around 466 and 498 nm correspond to the $^7F_6 \rightarrow ^5D_3$ and $^7F_6 \rightarrow ^5D_4$ transitions of the Tb^{3+} ion (Figure 3.11). For **Dy-2**, three weak absorption bands appear in the visible range at 428, 453, and 475 nm which can be assigned to the $^6H_{15/2} \rightarrow ^4F_{9/2}$, $^6H_{15/2} \rightarrow ^4I_{15/2}$, $^6H_{15/2} \rightarrow ^4G_{11/2}$ transitions of Dy^{3+}, respectively. Two stronger bands at 757 and 806 nm in the near-infrared region correspond to the $^6H_{15/2} \rightarrow ^6F_{3/2}$ and $^6H_{15/2} \rightarrow ^6F_{5/2}$ transitions of the Dy^{3+} ion, respectively (Figure 3.12).[35] For **Ho-2**, seven absorption bands at 418, 451, 468, 474, 486, 537 and 642 nm can be ascribed to the $^5I_8 \rightarrow ^5G_5$, $^5I_8 \rightarrow (^5F_1, ^5G_6)$, $^5I_8 \rightarrow ^3K_8$, $^5I_8 \rightarrow ^5F_2$, $^5I_8 \rightarrow ^5F_3$, $^5I_8 \rightarrow (^5F_4, ^5S_2)$ and $^5I_8 \rightarrow ^5F_5$ transitions of the Ho^{3+} ion (Figure 3.13), respectively. However, only the $^5I_8 \rightarrow (^5F_1, ^5G_6)$ and $^5I_8 \rightarrow (^5F_4, ^5S_2)$ transitions mainly contribute to the color of this compound.[36] More interestingly, a rapid color shift between light yellow and pink was observed when the **Ho-2** sample was illuminated under incandescent light or daylight. This phenomenon could be ascribed to the light source dependent color of the Ho^{3+} centers, which is a promising feature for the preparation of photochromic inorganic materials.[35, 36]

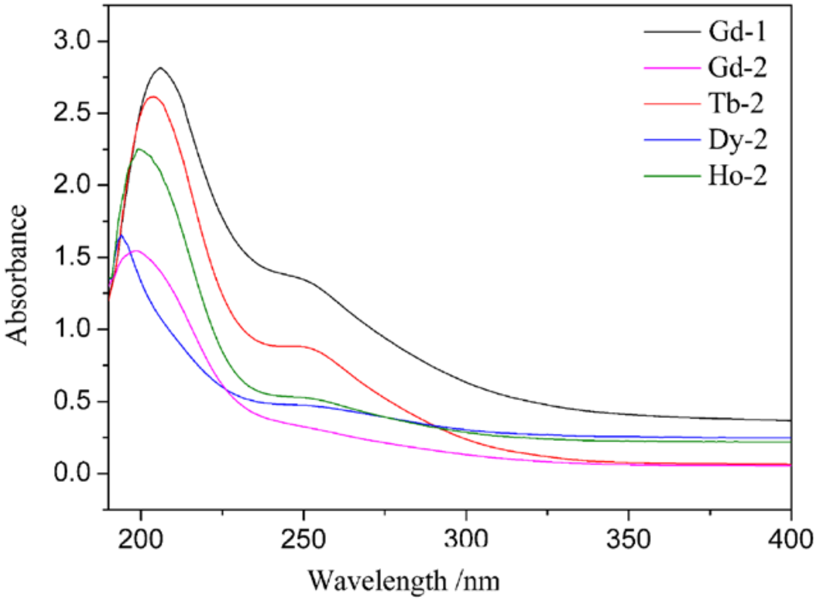

Figure 3.10. UV/Vis spectra of the polyanions **Gd-1** and **Gd-2**, **Tb-2**, **Dy-2**, **Ho-2** recorded in aqueous solution.

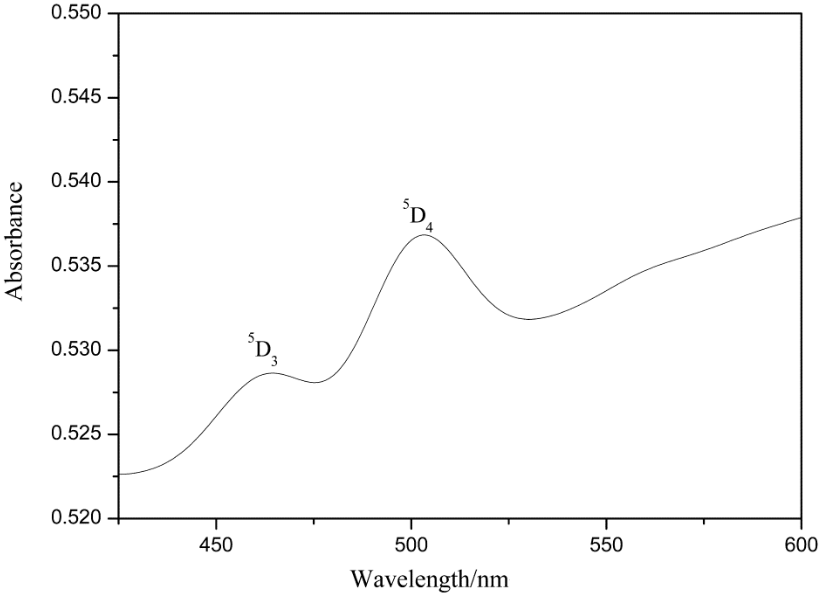

Figure 3.11. Solid state UV/Vis spectrum of **Tb-2** (400 - 600 nm range)

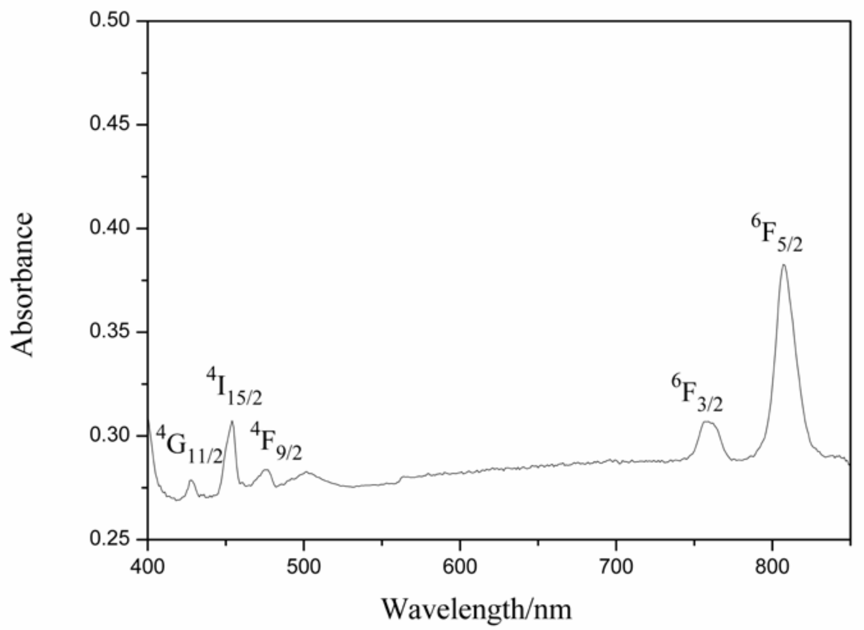

Figure 3.12. Solid state UV/Vis spectrum of **Dy-2** (400 - 850 nm range).

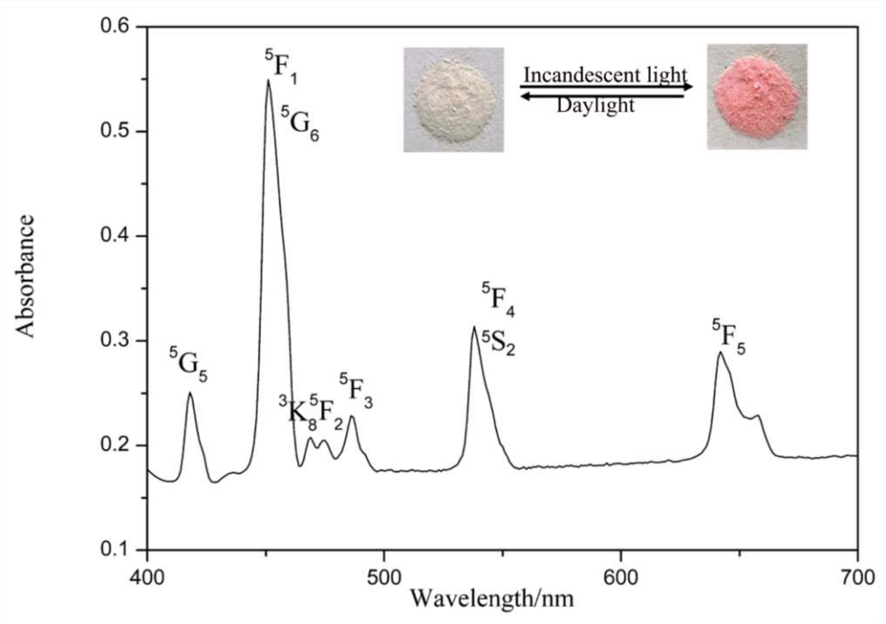

Figure 3.13. Solid state UV-Vis spectrum of **Ho-2** measured in the 300 – 700 nm range. Inset: color change of **Ho-2** upon irradiation from different light sources.

3.3.3.3. PXRD and TGA characterizations

The PXRD patterns for **Gd-1** and **Gd-2**, **Tb-2**, **Dy-2**, **Ho-2** samples are shown below (Figure 3.14-3.18). The diffraction peaks of both calculated and experimental patterns match almost perfectly, and intensity differences are due to sample preparation and texture effects. The PXRD patterns for **Gd-Ho-2** series are quite similar, emphasizing the isostructural nature of the four compounds. These conclusions are in agreement with the results obtained from single crystal X-ray structure determination.

TGA measurements were recorded under nitrogen flow in the temperature range from 30 to 800 ^{o}C. The TGA curves of all the compounds (Figure 3.19) exhibit one weight loss process in the temperature range of 30 - 300 ^{o}C, respectively. For **Gd-1**, the observed weight loss of 10.0 % (calcd. 10.2 %) corresponds to the release of crystal water molecules and adsorbed water molecules. The corresponding values are 5.2 % (calcd. 5.3 %) for **Tb-2**, 6.7% (calcd. 7.6 %) for **Ho-2**. For **Dy-2,** one weight loss step of 7.6 % corresponds to the loss of water molecules and 0.5 formula units of the acetate ligand (calcd. 7.9 %). For **Gd-2**, one weight loss step of 7.8 % (calcd 7.9 %) can be assigned to the loss of water molecules and one acetate ligand. The structural similarities of the compounds were further underscored by the related shapes of the TGA curves.

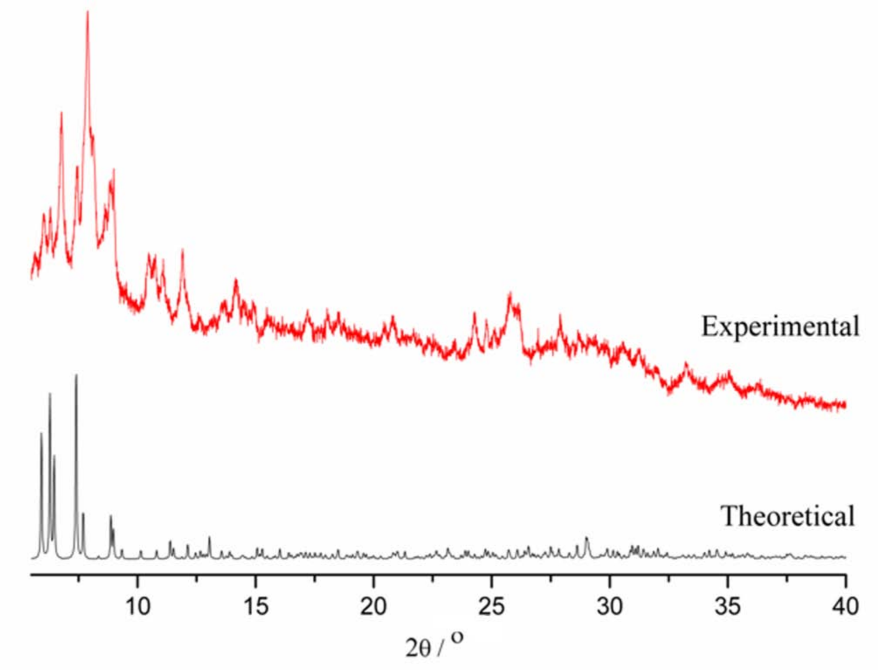

Figure 3.14. Powder X-ray diffraction pattern of bulk **Gd-1** (top) compared to the theoretical pattern calculated from single crystal X-ray diffraction data (bottom).

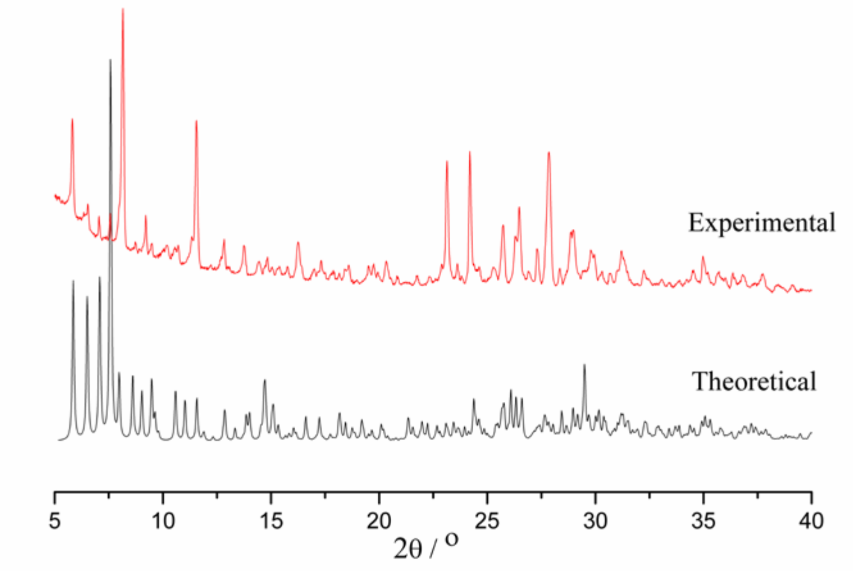

Figure 3.15. Powder X-ray diffraction pattern of bulk **Tb-2** (top) compared to the theoretical pattern calculated from single crystal X-ray diffraction data (bottom).

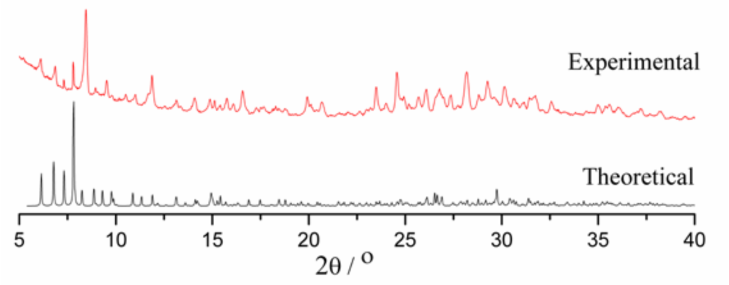

Figure 3.16. Powder X-ray diffraction pattern of bulk **Ho-2** (top) compared to the theoretical pattern calculated from single crystal X-ray diffraction data (bottom).

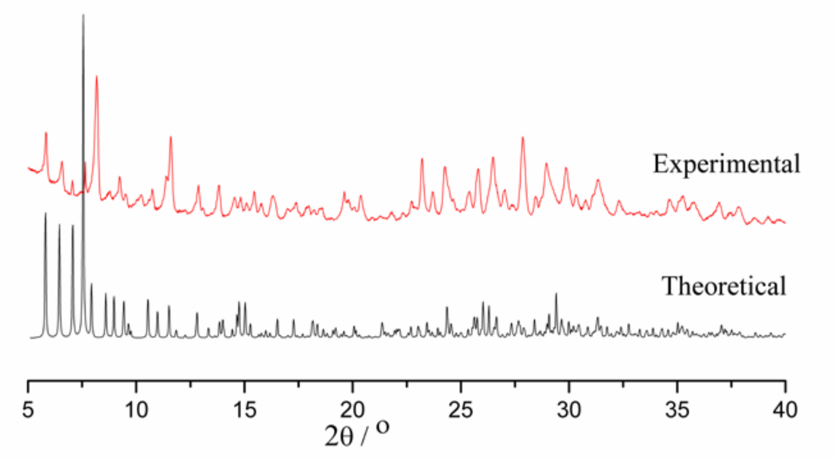

Figure 3.17. Powder X-ray diffraction pattern of bulk **Dy-2** (top) compared to the theoretical pattern calculated from single crystal X-ray diffraction data (bottom).

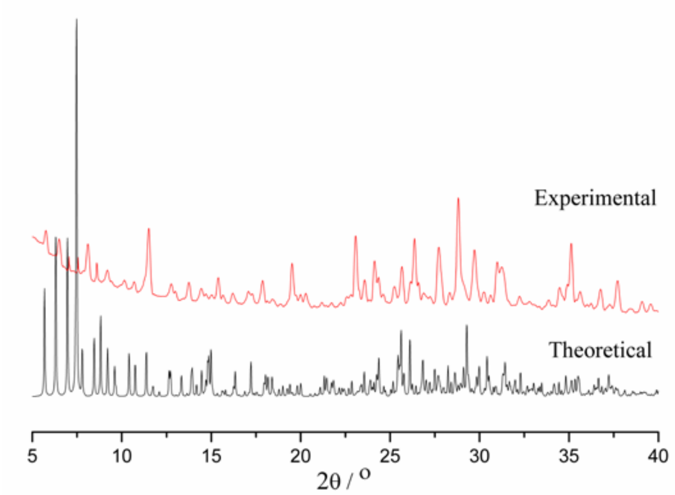

Figure 3.18. Powder X-ray diffraction pattern of bulk **Gd-2** (top) compared to the theoretical pattern calculated from single crystal X-ray diffraction data (bottom).

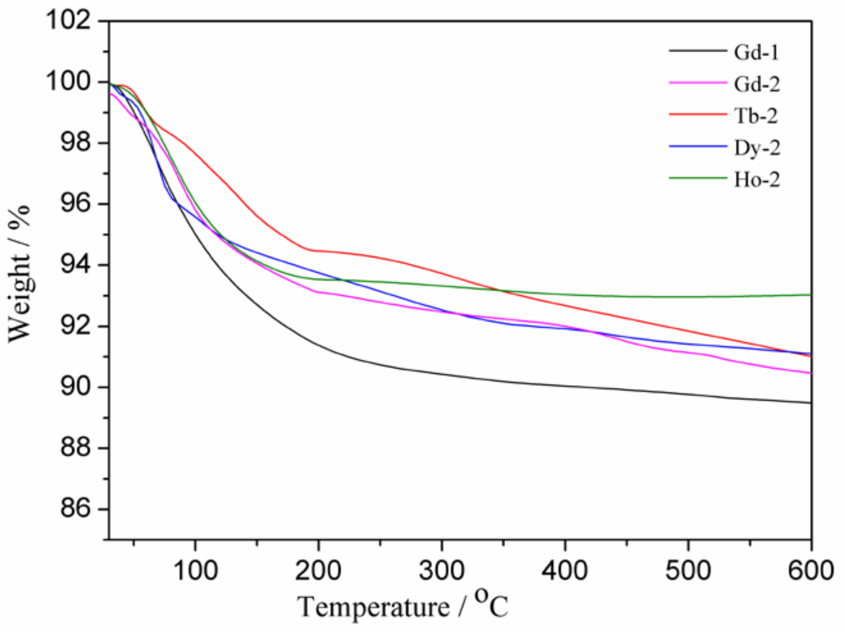

Figure 3.19. Thermogravimetric curves of the compounds **Gd-1** and **Gd-2**, **Tb-2**, **Dy-2**, **Ho-2**.

3.3.3.4. Photoluminescence properties

The photoluminescence (PL) spectra of **Gd-1** and **Gd-2**, **Tb-2**, **Dy-2**, **Ho-2** were investigated at room temperature upon photoexcitation. However, the results of PL measurements reveal that only **Tb-2** and **Dy-2** exhibit significant photoluminescence phenomena (Figure 3.20). The terbium compound **Tb-2** exhibits green photoluminescence under excitation at 255 nm. The emission spectrum displays four characteristic emission bands of Tb^{3+} at 487, 532, 579 and 624 nm, assigned to the transition of the $^5D_4$ excited state to the corresponding ground state ^7F_J (J = 6, 5, 4, 3) of the Tb^{3+} ion.[37] The $^5D_4\rightarrow{}^7F_6$ transition is a magnetic-dipole transition, and its intensity varies with the strength of the ligand field experienced by the Tb^{3+} ion. The strongest emission band $^5D_4\rightarrow{}^7F_5$ is an electric-dipole transition that is exceptionally sensitive to local coordination environments for the terbium ions, and the intensity of the $^5D_4\rightarrow{}^7F_5$

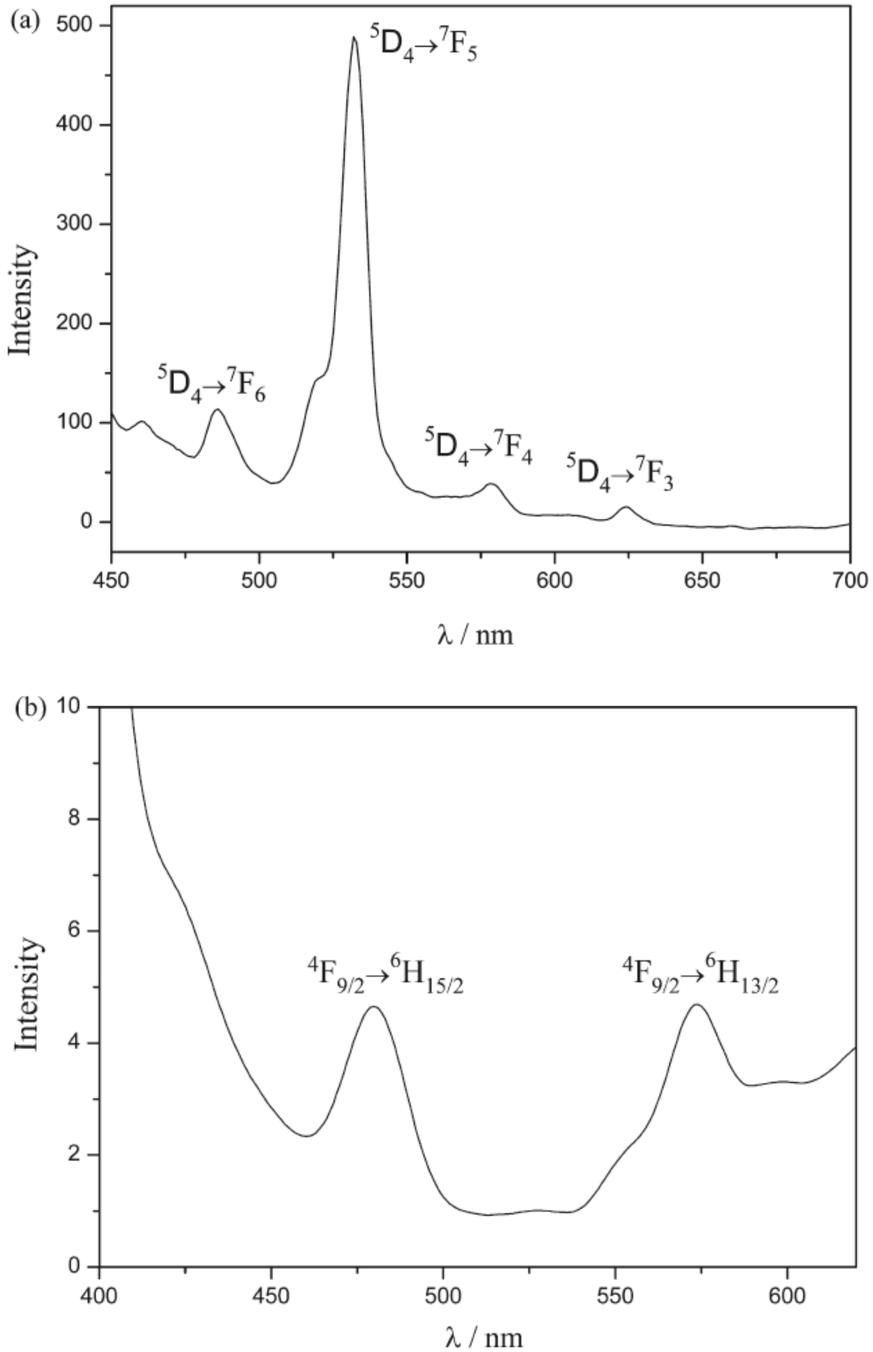

Figure 3.20. Photoluminescence spectra of **Tb-2** (a) and **Dy-2** (b) at room temperature (excitation wavelengths at 255 and 350 nm).

transition increases with decreasing site symmetry of the Tb^{3+} ion. Therefore, the intensity ratio of the $I(^5D_4 \rightarrow {}^7F_5)$ to $I(^5D_4 \rightarrow {}^7F_6)$ transitions is widely used to quantify coordination state and site symmetry of the rare earth ions.[37] In this case, the intensity ratio $I(^5D_4\rightarrow{}^7F_5)$ to $I(^5D_4\rightarrow{}^7F_6)$ is about 3.1, which further confirms the closely related low symmetry coordination environments of the three Tb^{3+} ions. The dysprosium-containing POM **Dy-2** displays two characteristic $^4F_{9/2}\rightarrow{}^6H_{15/2}$ and $^4F_{9/2}\rightarrow{}^6H_{13/2}$ transitions upon excitation at 350 nm with blue (around 479 nm) and yellow (around 574 nm) emissions, respectively.[38] The $^4F_{9/2}\rightarrow{}^6H_{13/2}$ transition due to a hypersensitive transition with ΔJ=2, is strongly influenced by the chemical environment of Dy^{3+}. In general, the low luminescence intensity of the Dy^{3+} ion can be caused by the small energy gap between the excited level $^4F_{9/2}$ and the sublevels of the ground term $^6H_{3/2}$, $^6H_{5/2}$ and $^6H_{5/2}$ in terms of effective radiationless deactivation in the excited state.[50]

3.3.3.5. Magnetic properties

The magnetic susceptibility of **Gd-1** and **Gd-2** was investigated on a polycrystalline sample in the temperature range of 2-300 K in a 2 kOe applied magnetic field. The molar magnetic susceptibility χ_m per Gd-ion and $1/\chi_m$ vs. T plots are shown in Figure 3.21. For both compounds **Gd-1** and **Gd-2**, $1/\chi_m$ vs. T plots display characteristic paramagnetic behavior over the entire temperature range with Curie constant values of $C_{\text{Gd-1}}$ = 8.00 emu K Oe^{-1} mol^{-1} and $C_{\text{Gd-2}}$ = 8.20 K Oe^{-1} mol^{-1}, respectively. The experimental effective magnetic moments μ_{eff} per gadolinium ion of 8.03 μ_B for **Gd-1** and 8.13 μ_B for **Gd-2** are in good agreement with the expected value of 7.94 μ_B for a free Gd^{3+} ion. Furthermore, the refined spin values S for **Gd-1** and **Gd-2** of 3.54 and 3.58 respectively, agree well with the theoretical spin value ($S=7/2$) for non-interacting gadolinium centers. All these above results indicate that a spin-spin coupling through O-W-O bridges can be negligible due to large Gd−Gd distances in both **Gd-1** and **Gd-2**. Related phenomena were also observed in previous studies on other Gd-containing polyoxometalates.[4c]

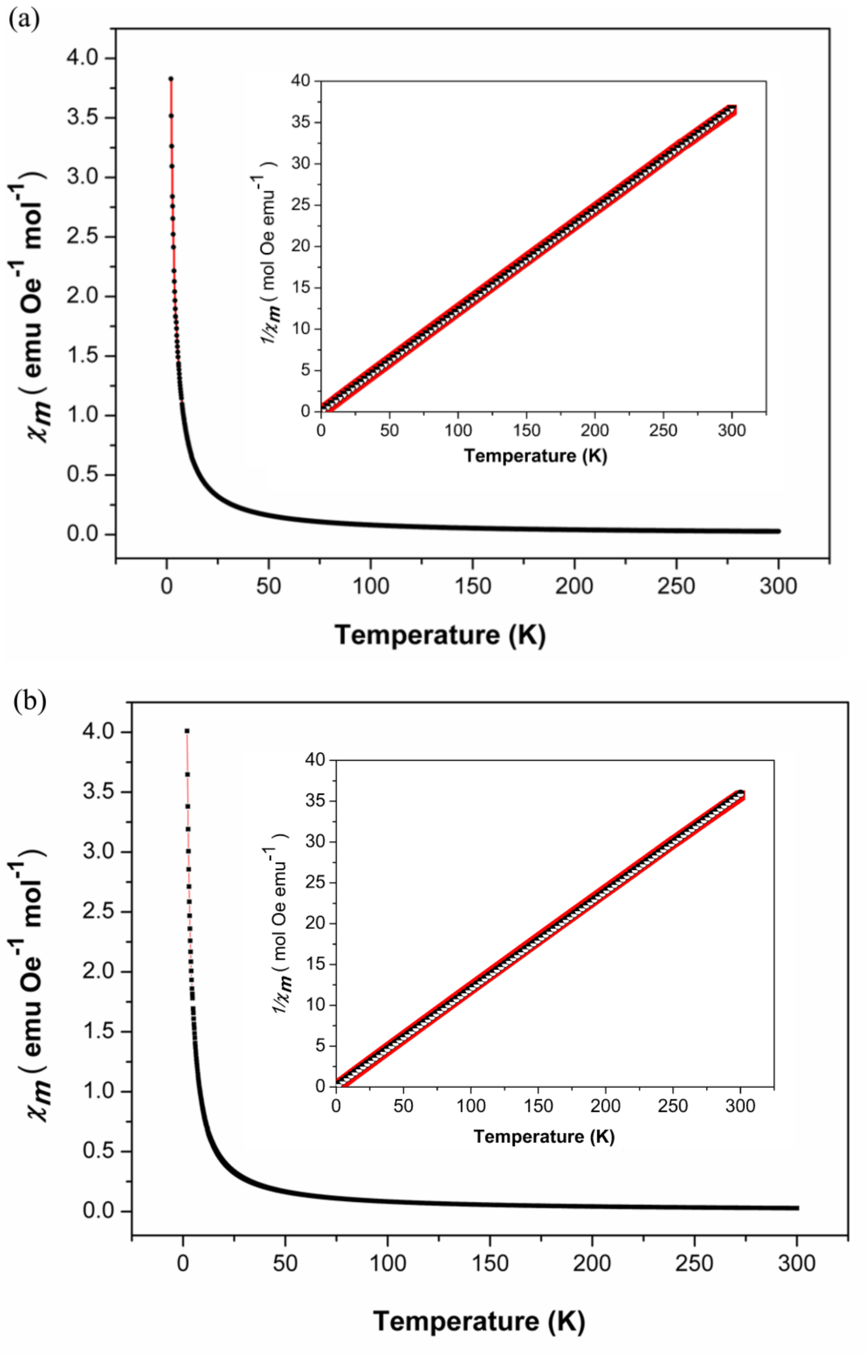

Figure 3.21. Temperature dependence of the magnetic susceptibility χ_m and $1/\chi_m$ (inset) from 2 to 300 K for (a) **Gd-1** and (b) **Gd-2**.

3.3.3.6. Electrochemical characterization

In order to the explore electrochemical behavior of the newly synthesized compounds, cyclovoltammetric (CV) measurements were investigated in a sodium acetate buffer solution (pH 4.4) as supporting electrolyte (Figure 3.22). Cyclic voltammograms indicate that all compounds show a similar electrochemical behavior mainly due to the presence of the *Wells-Dawson* anion A-α-$[Si_2W_{18}O_{66}]^{16-}$ in their crystal structures. Therefore, the following discussion is focused on **Gd-1** as a representative example. CVs display two reduction waves (I, II) of **Gd-1** at -0.657 V (E_{pc1}), and -0.901 V (E_{pc2}), respectively, in two separate steps, which can be assigned to the reduction of W centers. During the reoxidation process, one oxidation peak I' occurs at -0.562 V (E_{pa1}) corresponding to the first reduction wave E_{pc1}. The peak potential difference between E_{pa1} and E_{pc1} is 95 mV for this redox couple (I-I'), corresponding to a reversible one-electron redox process.[40] However, the reoxidation wave associated with the second reduction process is more complicated, and a splitting of the reoxidation pattern of W-waves into two waves occurs at -0.806 V (II', E_{pa2}) and -0.682V (III', E_{pa3}). These results might indicate that a strong irreversible electron transfer process takes place during the second redox step. Related observations have also been encountered in the electrochemical behavior of dilacunary $[\gamma\text{-}SiW_{10}O_{36}]^{8-}$ and the transition-metal substituted decatungstosilicate $[M(H_2O)_2(\gamma\text{-}Si_2W_{20}O_{70})]^{10-}$ (M = Mn^{2+}, Co^{2+}, Ni^{2+}).[20, 21] Furthermore, no redox processes of lanthanoid cations were detected in the potential range from -1.0 to +1.0 V, which is in line with previous studies of lanthanide substituted Dawson-type arsenotungstates (α_2-$[Ln(As_2W_{17}O_{61})_2]^{17-}$ and $\{[(\alpha_2\text{-}As_2W_{17}O_{61})Ln(H_2O)_2]_2\}^{14-}$).[41] CVs of **Gd-1** at different scan rates were also recorded, with the observation of a gradual variation of the peak potentials when changing from 100 to 300 mV s^{-1}: (1) the cathodic peak potentials were shifted towards negative values whereas the corresponding anodic peak potentials were shifted into the opposite direction with the increase of scan rate. (2) In addition, the peak currents are proportional to the scan rate (v), which indicates that the redox process is surface-controlled with a fast exchange rate of electrons.

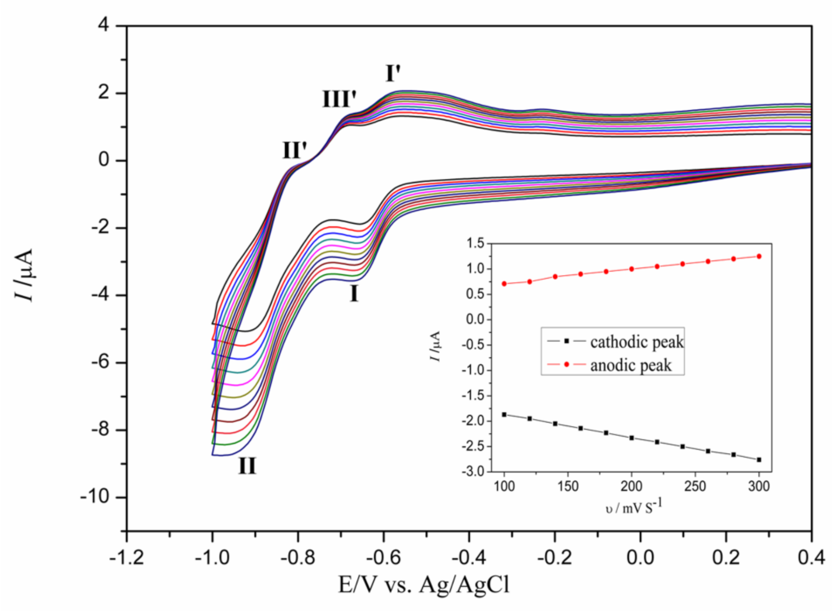

Figure 3.22. Cyclic voltammograms of 0.2 mM **Gd-1** in 1.0 M CH_3COONa/CH_3COOH buffer (pH 4.4) at different scan rates (from inner to outer plot: 100, 120, 140, 160, 180, 200, 220, 240, 260, 300 mV/s). The inset shows plots of the anodic and the cathodic peaks currents of I-I' against the scan rates.

3.4. Conclusions

A new family of lanthanide-containing silicotungstates based on the open *Wells-Dawson* anion *A*-α-$[Si_2W_{18}O_{66}]^{16-}$ has been successfully constructed from the $[A\text{-}\alpha\text{-}SiW_9O_{34}]^{10-}$ precursor with Ln(III) cations in buffer solutions. This new polyoxotungstate series is the first example of lanthanoids embedded in the open *Wells-Dawson* silicotungstate anion $[\alpha\text{-}Si_2W_{18}O_{66}]^{16-}$. All compounds $[Ln_2(H_2O)_7Si_2W_{18}O_{66}]^{10-}$ (Ln = Gd, Ho, Tb) and $[Dy_2(H_2O)_{6.5}(C_2H_4O_2)_{0.5}Si_2W_{18}O_{66}]_n^{10-}$ were fully characterized with a wide range of analytical techniques including single crystal X-ray diffraction as well as spectroscopic techniques, such as FT-IR, UV/Vis and photoluminescence spectroscopy, and furthermore by electrochemistry and thermogravimetric analysis. The lanthanoid-containing *Wells-Dawson* type polyoxoanions $[Ln_2(H_2O)_7Si_2W_{18}O_{66}]^{10-}$ (Ln = Gd^{III} (**Gd-1** and **Gd-2)**, Tb^{III}, Ho^{III}) and $[Dy_2(H_2O)_{6.5}(C_2H_4O_2)_{0.5}Si_2W_{18}O_{66}]^{10-}$ are linked by Ln^{3+} cations to form 3D architectures for **Gd-1** or 2D frameworks for the isostructural compounds **Tb-2**, **Dy-2, Ho-2** and **Gd-2.** The structure-directing influence of the lanthanoid cation on the local structure of the dimeric building blocks and on the crystal packing motifs is investigated in detail. The individual coordination environments of the lanthanoid cations also differ between the two new 3D and 2D compound types with size dependence of the lanthanoid cation. Their electrochemical behavior was studied by cyclic voltammetry in sodium acetate buffer (pH 4.4) as supporting electrolyte. The **Tb-2** and **Dy-2** compounds exhibit both room temperature photoluminescence and the **Ho-2** compound displays an interesting photochromic behavior. The magnetic behavior of **Gd-1** and **Gd-2** between 2 and 300 K was found to be paramagnetic due to the non-interacting gadolinium centers.

All in all, our recent work provides new insights to explore controllable assemblies and structural transformations of Ln-POM-based coordination polymers with fascinating structural features and potential applications.

References

[1] (a) Howell, R. C.; Perez, F. G.; Jain, S.; W.; Horrocks, D., Jr.; Rheingold, A. L.; Francesconi, L. C. *Angew. Chem., Int. Ed*. **2001**, 40, 4031–4034. (b) Yamase, T.; Naruke, H.; Sasaki, Y. *J. Chem. Soc., Dalton Trans*. **1990**, 1687–1696. (c) Niu, J. Y.; Guo, D. J.; Wang, J. P.; Zhao, J. W. *Cryst. Growth Des*. **2004**, 4, 241–247. (d) Niu, J. Y.; Wei, M. L.;Wang, J. P.; Dang, D. B. *Eur. J. Inorg. Chem*. **2004**, 160–170. (e) Mialane, P.; Dolbecq, A.; Sécheresse, F. *Chem. Commun*. **2006**, 3477–3485.

[2] Zhongfeng, L.; Weisheng, L.; Xiaojing, L.; Fengkui, P.; Yingxia, L.; Hao, L. *Magn. Reson. Imaging*. **2007**, 25, 412–417.

[3] Contant, R.; Herve, G. Rev. *Inorg. Chem*. **2002**, 22, 63–105.

[4] (a) Hussain, F.; Spingler, B.; Conrad, F.; Speldrich, M.; Kögerler, P.; Boskovic, C.; Patzke, G. R. *Dalton Trans.* **2009**, 4223–4225. (b) Hussain, F.; Conrad, F.; Patzke, G. R. *Angew. Chem. Int. Ed*. **2009**, 48, 9088–9091. (c) Hussain, F.; Patzke, G. R. *CrystEngComm* **2011**, 13, 530–536. (d) Hussain, F.; Gable, R. W.; Speldrich, M.; Kögerler, P.; Boskovic, C. *Chem. Commun*. **2009**, 328–330.

[5] Wassermann, K.; Dickman, M. H.; Pope, M. T. *Angew. Chem., Int. Ed.* **1997**, 36, 1445–1448.

[6] Bassil, B. S.; Dickman, M. H.; Römer, I.; Kammer, B. von der.; Kortz, U. *Angew. Chem., Int. Ed.* **2007**, 46, 6192–6195.

[7] Sadakane, M.; Dickman, M. H.; Pope, M. T. *Angew. Chem., Int. Ed.* **2000**, 39, 2914–2916.

[8] Mialane, P.; Lisnard, L.; Mallard, A.; Marrot, J.; Antic-Fidancev, E.; Aschehoug, P.; Vivien, D.; Sécheresse, F. *Inorg. Chem.* **2003**, 42, 2102–2108.

[9] Peacock, R. D.; Weakley, T. J. R. *J. Chem. Soc A.* **1971**, 1836–1839.

[10] Sadakane, M.; Dickman, M. H.; Pope, M. T. *Angew. Chem., Int. Ed.* **2000**, 39, 2914-2916.

[11] Mialane, P.; Lisnard, L.; Mallard, A.; Marrot, J.; Antic-Fidancev, E.; Aschehoug, P.; Vivien, D.; Sécheresse, F. *Inorg. Chem.* **2003**, 42, 2102–2108.

[12] Bassil, B. S.; Dickman, M. H.; von der Kammer, B.; Kortz, U. *Inorg. Chem.* **2007**, 46, 2452–2458.

[13] An, H. Y.; Han, Z. B.; Xu, T. Q. *Inorg. Chem.* **2010**, 49, 11403–11414.

[14] Ni, L.; Hussain, F.; Springler, B.; Weyeneth, S.; Patzke, G. R. *Inorg. Chem.* **2011**, 50, 4944–4955.

[15] Laronze, N.; Marrot, J.; Hervé, G. *Chem. Commun.* **2003**, 2360–2361.

[16] Laronze, N.; Marrot, J.; Hervé, G. *Inorg. Chem.* **2005**, 44, 1275–1281.

[17] Laronze, N.; Haouas, M.; Marrot, J.; Taulelle, F.; Hervé, G. *Angew. Chem. Int. Ed.* **2006**, 45, 145–148.

[18] Laronze, N.; Marrot, J.; Hervé, G. *C. R. Chimie* **2006**, 9, 1467–1471.

[19] (a) Bi, L.; Kortz, U. *Inorg. Chem.* **2004**, 43, 7961–7962. (b) Nellutla, S.; Tol, J.; Dalal, N. S.; Bi, L.; Kortz, U.; Keita, B.; Nadjo, L.; Khitrov, G.A.; Marshall, A.G. *Inorg. Chem.* **2005**, 44, 9795–9806.

[20] Bassil, B. S.; Dickman, M. H.; Reicke, M.; Kortz, U.; Keita, B.; Nadjo, L. *Dalton Trans.* **2006**, 4253–4259.

[21] Tézé, A.; Hervé, G.; Finke, R. G.; Lyon, D. K. *Inorg. Synth*. **1990**, 27, 85–135.

[22] Oxford Diffraction, CrysAlis CCD and CrysAlis RED, Oxford Diffraction Ltd., Abingdon, UK, **2005**.

[23] Sheldrick, G. M. SHELX97, Program for Crystal Structure Analysis; Release 97-2; University of Göttingen; Göttingen, Germany, **1997**.

[24] Liu, J. F.; Ortega, F.; Sethuraman, P.; Katsoulis, D. E.; Costello, C. E.; Pope, M. T. *J. Chem. Soc., Dalton Trans*. **1992**, 1901–1906.

[25] Chatterjee, R.; Ali, M.; Drew, M. G. B.; Nethaji, M.; Mondal, S.; Mukherjee, M. *Transition Met Chem*. **2009**, 34, 1–5.

[26] Laronze, N.; Marrot, J.; Hervé, G. *Inorg. Chem*. **2003**, 42, 5857–5862.

[27] Helm, L.; Merbach, A. E. *Coord. Chem. Rev.* **1999**, 187, 151–181.

[28] Favas, M. C.; Kepert, D. L. Prog. *Inorg. Chem*. **1981**, 28, 309–367.

[29] (a) Porai-Koshits, M. A.; Aslanov, L. A. Zh. *Strukt. Khim*. **1972**, 13. 266–276. (b) Hoard, J. L.; Silverton, J. V. *Inorg. Chem*. **1963**, 2, 235-242. (c) Kepert, D. L. *J. Chem. Soc*. **1965**, 4736–4744. (d) Lippard, S. J.; Russ, B. J. *Inorg. Chem*. **1968**, 7, 1686–1688. (e) Muetterties, E. L. *Inorg. Chem.* **1973**, 12, 1963–1966.

[30] (a) Corbett, J. D. Struct. *Bonding* **1997**, 87, 157–193. (b) Fässler, T. F.; Hoffmann, R. *Angew. Chem., Int. Ed*. **1999**, 38, 543–546.

[31] Karraker, D. G. *J. Chem. Educ*. **1970**, 47, 424–430.

[32] (a) Brown, I. D.; Altermatt, D. *Acta Crystalllogr Sect. B*. **1985**, 41, 244–247. (b) Trzesowska, A.; Kruszynski, R.; Bartczak, T. J. *Acta Crystallogr. Sect. B*. **2004**, 60, 174–178.

[33] (a) Mialance, P.; Dolbecq, A.; Lisnard, L.; Mallard, A.; Marrot, J.; Sécheresse, F. *Angew. Chem., Int. Ed*. **2002**, 41. 2398–2401. (b) An, H.Y.; Wang, E. B.; Xiao, D. R.; Li, Y. G.; Su. Z. M.; Xu, L. *Angew. Chem., Int. Ed*. **2006**, 45. 904–908. (c) Du, D.

Y.; Qin, J. S.; Li, S. L.; Lan, Y. Q.; Wang, X. L.; Su, Z. M. *Aus. J. Chem.* **2010**, 63, 1398–1395.

[34] (a) Niu, J. Y.; Wang, K. H,; Chen, H. N.; Zhao, J. W.; Ma, P. T.; Wang, J. P.; Li, M. X.; Bai, Y.; Dang, D. B. *Cryst. Growth. Des*. **2009**, 9, 4362–4372. (b) Niu, J. Y.; Zhao, J. W.; Wang, J. P. *Inorg. Chem. Commun*. **2004**, 7, 876–879.

[35] (a) Binnemans. K.; Görller-Walrand, C. *Chem. Phy. Lett*. **1995**, 235, 163–174. (b) Carnall, W. T.; Goodman, G. L.; Rajnak, K.; Rana, R. S; A systematic analysis of the spectra of the lanthanides doped into single crystal LaF3, *Argonne National Laboratory Report NL-88-8 Argonne*, IL, **1988**.

[36] (a) Yamase, T. *Chem. Rev*. **1998**, 98, 307–325. (b) Papaconstantinou, E. *Chem. Soc. Rev*. **1989**, 18, 1–31.

[37] (a) Xia, J.; Zhao, B.; Wang, H.-S.; Shi, W.; Ma, Y.; Song, H.B.;Cheng, P.; Liao, D. Z.; Yan, S. P. *Inorg. Chem*. **2007**, 46, 3450–3458. (b) Lill, D. T.; Bettencourt-Dias, A.; Cahill, C. L. *Inorg. Chem*. **2007**, 46, 3960–3965.

[38] (a) Xu, Q. H.; Li, L. S.; Liu, X. S.; Xu, R. R. *Chem. Mater*. **2002**, 14, 549–555. (b) Yan, B.; Bai, Y. Y. *J. Fluoresc*. **2005**, 15, 605–611.

[39] (a) Kuang, J. Y.; Liu, Y. L.; Zhang, J. X. *J. Solid State Chem*. **2006**, 179, 266–269. (b) Meshova, S. B.; Kiriyaka, A. V.; Tsvirko, M. P.; Gorodnyuk, V. P. *J. Anal. Chem*. **2008**, 63, 840–843.

[40] Sadakane, M.; Steckhan, E. *Chem. Rev*. **1998**, 98, 219–237.

[41] (a) Xi, X. D.; Wang, G.; Liu, B. F.; Dong, S. *J. Electrochim. Acta*. **1995**, 40, 1025–1029. (b) Liu, L. Z.; Li, F. Y.; Xu, L.; Liu, X. Z; Gao, G. G. *J. Solid State Chem*. **2010**, 183, 350–355.

4. Trilacunary Keggin-type POMs as Versatile Building Blocks for Lanthanoid Silicotungstates

4.1. Introduction

In the field of POM chemistry, exploring the reactivity of lacunary POMs with lanthanide cations is an important area, not only because they can offer "building blocks" to be organized into novel larger aggregates and extended high-dimensional frameworks, but they can also bring forward many potential applications in areas ranging from photochemistry over medicinal chemistry to molecular magnetism and catalysis.[1-6] However, the complex influence of synthetic parameters on the POM structure emerging from a given reaction still remains to be fully mastered and explored for predictive POM design.

A number of very large POM aggregates based on lacunary POMs and lanthanides have been synthesized and structurally characterized by *Pope, Müller, Yamase and Kortz* et al.[7-10] There is some evidence suggesting the selective influence of specific lanthanoid cations on the formation of such high nuclear POMs[11], for example, their preference for Ce-linkers: $[Ce_{16}As_{12}(H_2O)_{36}W_{148}O_{524}]^{76-}$ and $[Ce_{20}Ge_{10}W_{100}O_{376}(OH)_4(H_2O)_{30}]^{56-}$ have been the largest polyoxotungstate representatives for many years.[7, 8] The main target of preceding studies on Ln-POMs (LSPs) in our group was the construction of large polyoxotungstates with an exceptionally high number of tungsten centers, such as $[Ln_{16}As_{16}W_{164}O_{576}(OH)_8(H_2O)_{42}]^{80-}$ (Ln = Eu, Gd, Tb, Dy, Ho),[12] and $[Gd_8As_{12}W_{124}O_{432}(H_2O)_{22}]^{60-}$.[13] Recently, small Ln-sandwich complexes of $[\beta\text{-}SiW_9O_{34}]^{10-}$ also showed a distinct selectivity for Eu^{III} and Gd^{III} cores.[14] As shown in the previous **Chapter 3**, Gd^{III} forms two structurally and topologically different 2D and 3D members of the above-mentioned $\{LnSi_2W_{18}O_{66}\}$ series, whilst Dy^{III} and Ho^{III} were only found in a single 2D type.[15] In the following, these individual structure-directing properties of the lanthanide cations are explored for targeted POM synthesis. The challenge of synthetic control over POMs for the lanthanoid-assisted conversion of the versatile $[A\text{-}\alpha\text{-}SiW_9O_{34}]^{10-}$ precursor into the newly obtained polyanions $\{LnSi_2W_{18}O_{66}\}$ [Ln = Eu^{III} (**Eu-1** and **Eu-2**), Tb^{III} (**Tb-1**)] and $[Eu(\alpha\text{-}SiW_{11}O_{39})_2]^{13-}$ (**Eu-3**) is illustrated in the present chapter.[16] Starting from the above investigations into the open *Wells-Dawson* series {$LnSi_2W_{18}O_{66}$} [Ln = Gd^{III}, Tb^{III}, Dy^{III}, Ho^{III}], [15] the subtle interplay of lanthanide radii vs. synthetic fine-tuning is illustrated for the reaction of the lacunary {SiW_9O_{34}} POM building block with Eu as a mid lanthanide. A systematic method for the construction of {$LnSi_2W_{18}O_{66}$}-based motifs is developed along structural and preparative lines. First, their 2D and 3D architectures are expanded by newly introducing Eu^{III} as a mid-lanthanoid to the series (**Eu-1** and **Eu-2**). Secondly, the astonishing influence of countercations on the synthetic protocol is illustrated: Even a very slight change of Cs^+ concentration can bring forward a new 3D representative of the {$LnSi_2W_{18}O_{66}$}-type (**Tb-1**). These results shed new light on the concurrence between structure-directing additives and templating strategies via lanthanoid cations. Interestingly, the transformation of the $[A\text{-}\alpha\text{-}SiW_9O_{34}]^{10-}$ {SiW_9} into the sandwich-type geometry of $[Eu(\alpha\text{-}SiW_{11}O_{39})_2]^{13-}$ (**Eu-3**) was furthermore obtained through step-wise alterations of the overall ionic strength for Eu-based protocols.

As discussed in the preceding chapter, the open *Wells-Dawson* host polyanion $[\alpha\text{-}Si_2W_{18}O_{66}]^{16-}$ has a cavity, which is able to take up various guest cations, such as K^+,[17] transition metal cations[18] or larger clusters, e.g. $\{KV_2O_3(H_2O)_2\}^{5+}$, $\{Fe_4(OH)_6\}^{6+}$ or $\{Cu_5(OH)_4(H_2O)\}^{6+}$.[19 20] Although the pocket structure of {$Si_2W_{18}O_{66}$} is a key building block for controlling POM construction,[21] control over the manifold alternative transformation pathways of its {SiW_9O_{34}} precursor remains challenging[22, 23] (Figure 4.1). A survey of representative transformation conditions for {SiW_9O_{34}} (Table 4.1) shows that its flexible conversion processes have been explored and implemented rather empirically.[24] In fact, anions and cations seemingly regarded as innocent "spectator" often play a crucial role on the resulting POM structure[25, 26]. This has been illustrated for the K^+/Cs^+-assisted transformation of $[A\text{-}\alpha\text{-}SiW_9O_{34}]^{10-}$ into $Cs_{15}[K(SiW_{11}O_{39})_2]\cdot 39H_2O$.[18]

Regarding lanthanide sandwich-type POMs, the mono-lacunary {$XW_{11}O_{39}$} (X = Si, P, B) unit[27] has been widely used to construct this growing group containing a variety of hosts, e.g. lanthanoids,[28, 29, 23] UO_2^{2+},[30] mixed 3d-4f[31] or hybrid cores[32], thus giving rise to a rich POM-based materials chemistry.[33] Meanwhile, acetate-bridged $[(SiW_{11}O_{39}Ln)_2(\mu\text{-}CH_3COO)_2]^{12-}$ (Ln = Gd, Yb) POMs[34] and related {$\alpha\text{-}PW_{11}O_{39}$} compounds[35] have been reported, as well as the 1D linkage of $[\alpha\text{-SiW}_{11}O_{39}]^{8-}$ by Eu^{III} into wire-like $Na_{0.5}Cs_{4.5}[Eu(\alpha\text{-SiW}_{11}O_{39})(H_2O)_2]\cdot 23H_2O$.[36] Further $[Ln^{III}(\alpha\text{-PW}_{11}O_{39})_2]^{11-}$ compounds have been recently characterized as well,[37] and $\{Ln(PW_{11})_2\}$ POMs were enantioselectively resolved through the reaction with proline.[38] As for lanthanoid containing sandwiched POMs with the $\{SiW_{11}O_{39}\}$ building block, the $[Ln(\beta_2\text{-SiW}_{11}O_{39})_2]^{13-}$ (Ln = La, Ce, Sm, Eu, Gd, Tb, Yb, Lu) series[28a] has been already well characterized by *Kortz*'s group, and its Tb - Yb species were investigated for single-molecule-magnet behavior.[28b] However, the more stable α-isomers of the Ln-members, $[Ln(\alpha\text{-SiW}_{11}O_{39})_2]^{13-}$, have not been isolated in single crystalline form to date, although NMR studies on the $[Ln(SiW_{11}O_{39})_2]^{13-}$ series already identified higher symmetric solution structures as more preferable for the earlier lanthanides.[39] Therefore, all these synthetic gaps needs to be closed, given that the luminescent $[Eu(SiW_{11}O_{39})_2]^{13-}$ is an attractive component for organic-inorganic hybrid multilayers,[40] ultrathin films,[41] self-organized microporous structures,[42] liquid crystals[43] and related materials

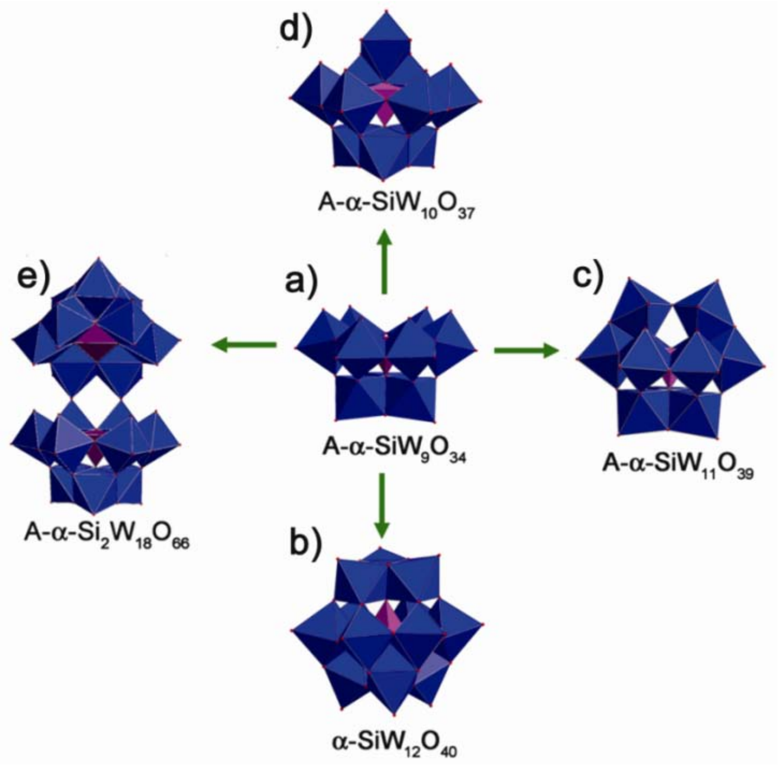

Figure 4.1. Transformation of $\{A\text{-}\alpha\text{-SiW}_9O_{34}\}$ (a) into different POM building blocks (b - e).

In this work, the efficiency of direct structure control via lanthanoid cations is compared to the influence of "spectator" counterions and synthetic parameters on the transformation of $[A\text{-}\alpha\text{-SiW}_9O_{34}]^{10-}$ into the new Eu- and Tb-POMs $\{LnSi_2W_{18}O_{66}\}$ (Ln = Eu, Tb) (**Eu-1**, **Eu-2**, **Tb-1**) and $[Eu(\alpha\text{-SiW}_{11}O_{39})_2]^{13-}$ (**Eu-3**). Moreover, key structural, photoluminescent, electrochemical, magnetic and electrochemical properties of the produced materials were investigated.

Table 4.1. Summary of synthetic conditions for transformations between the $[A\text{-}\alpha\text{-SiW}_9O_{34}]^{10-}$ precursor (Figure 1a) and different POM units.

Compounds	**pH**	**T / °C**	**time**	**Countercations**	**Molar ratio of TM or RE cations and precursor**
$\alpha\text{-}[SiW_9O_{37}M_3(H_2O)_3]^{10-}$ (M = Mn, Co, Ni)[44] (Figure 4.1d)	5-6	80	1 h	K, Na	$M^{2+}/[SiW_9O_{34}]^{10-} \approx 3$
$[Fe_4(\mu\text{-O})_2(\mu\text{-OH})_2(SiW_{10}O_{37})_2]^{14-}$ [45] (Figure 4.1d)	9.2	80	1.5 h	K, Na	$Fe^{3+}/[SiW_9O_{34}]^{10-} = 8.5$
$[\{M(2,2\text{-bipy})_2\}_2\{SiW_{12}O_{40}\}]$ (M = Mn, Cu) [46] (Figure 4.1b)	--	160	5 d	--	$M^{2+}/[SiW_9O_{34}]^{10-} = 5.0$
$[K(SiW_{11}O_{39})_2]^{15-}$ [22] (Figure 4.1c)	6.3	80	--	Cs	--
$\alpha\text{-}[\{K(H_2O)_2\}(Si_2W_{18}O_{66})]^{15-}$ [17, 18] (Figure 4.1e)	5.7	--	30 min	K	--
$[\{M(H_2O)\}(\mu\text{-}H_2O)_2K(Si_2W_{18}O_{66})]^{13-}$ (M = Co, Ni, Cu) [18] (Figure 1e)	5.9	--	--	K	$M^{2+}/[SiW_9O_{34}]^{10-} = 0.5$
$[\{M(H_2O)\}(\mu\text{-}H_2O)_2K\{M(H_2O)_4\}(Si_2W_{18}O_{66})]^{11-}$ (M = Mn, Co, Ni) [18] (Figure 4.1e)	5.9	--	--	K	$M^{2+}/[SiW_9O_{34}]^{10-} = 1.0$
$[\{KV_2O_3(H_2O)_2\}(Si_2W_{18}O_{66})]^{11-}$ [19] (Figure 4.1e)	3.8	--	--	K	$V^{5+}/[SiW_9O_{34}]^{10-} = 2.0$
$[\{Fe_4(OH)_6\}(Si_2W_{18}O_{66})]^{10-}$ [19] (Figure 4.1e)	2.9	--	30 min	K, Na	$Fe^{3+}/[SiW_9O_{34}]^{10-} = 6.0$
$[Cu_5(OH)_4(H_2O)_2(A\text{-}\alpha\text{-SiW}_9O_{33})_2]^{10-}$ [20a] (Figure 4.1e)	4.8	80	30 min	K	$Cu^{2+}/[SiW_9O_{34}]^{10-} = 2.8$
$[Ln_2(H_2O)_7Si_2W_{18}O_{66}]^{10-}$ (Ln = Gd, Tb, Dy, Ho) [15] (Figure 4.1e)	4.4	80	90 min	Cs, Na	$Ln^{3+}/[SiW_9O_{34}]^{10-} = 3.0$
Eu-1, **Eu-2**, **Tb-1** (Ln = Eu, Tb) [16] (Figure 4.1e)	4.4	80	90 min	Cs, Na	$Ln^{3+}/[SiW_9O_{34}]^{10-} = 3.0$
Eu-3 [16] (Figure 4.1c)	4.4	80	90 min	Cs, Na	$Eu^{3+}/[SiW_9O_{34}]^{10-} = 2.0$

4.2. Experimental

4.2.1. Synthetic methods

Synthesis of $CsNa_2Eu_2H_3[Eu_2(H_2O)_7(\alpha\text{-}Si_2W_{18}O_{66})]Cl_2\cdot30H_2O$ (Eu-1): 0.369 g (0.150 mmol) of $Na_{10}[SiW_9O_{34}]\cdot23H_2O$ [47] was dissolved in 25 ml of sodium acetate buffer (pH 4.4) with stirring. 0.201 g (0.450 mmol) of $Eu(NO_3)_3\cdot6H_2O$ was slowly added to the reaction mixture. The solution was stirred continuously at 80 ºC for 90 min, followed by cooling to room temperature and filtration. Addition of 1.0 M CsCl solution (0.5 ml) to the colorless filtrate and slow evaporation at room temperature led to the formation of colorless needle-like crystals after ca. one week. Yield: 0.093 g, 21 % (based on W). FT-IR (in cm^{-1}): 1002 (s), 933 (s), 864 (vs), 790 (s), 696 (s), 638 (s), 543 (w), 522 (w). Elemental analysis (%); calcd. (found): W, 55.63 (53.60); Eu, 10.22 (10.20); Cs, 2.23 (2.53); Na, 0.77 (0.78), Si, 0.94 (0.93); H, 1.30 (1.69). TGA measurements (Figure 4.17) display a weight loss of 11.6 % in the temperature range of 30–220 ^oC resulting from coordination and solvent water molecules (expected 11.2 %).

Synthesis of $Na_3Cs_3EuH_4[Eu_2(H_2O)_7(\alpha\text{-}Si_2W_{18}O_{66})](C_2H_3O_2)Cl_2\cdot28H_2O$ (Eu-2): The synthesis was performed as described above for **Eu-1** with one alteration: instead of 0.5 ml of a 1.0 M CsCl solution, 1.5 ml were added dropwise to the colorless filtrate. Colorless block-shaped crystals were obtained after about one week. Yield: 0.081 g, 18 % (based on W). FT-IR (in cm^{-1}): 1004 (s), 943 (s), 876 (vs), 824 (s), 758 (s), 709(s), 551(w), 472(w). Elemental analysis (%); calcd. (found): W, 54.16 (54.20); Eu, 7.46 (7.01); Cs, 6.52 (7.39); Na, 1.12 (1.84);. TGA measurements (Figure 4.17) display a weight loss of 9.8 % in the temperature range of 30–220 ^oC resulting from loss of coordination and solvent water molecules (expected 10.3 %).

Synthesis of $Na_7Cs_3H_4[Eu(\alpha\text{-}SiW_{11}O_{39})_2]Cl\cdot31H_2O$ (Eu-3): The above synthetic procedure was modified by using 0.073 g (0.20 mmol) $EuCl_3\cdot6H_2O$ instead of $Eu(NO_3)_3\cdot6H_2O$. Addition of 1.0 M CsCl solution (0.75 ml) to the colorless filtrate and slow evaporation at room temperature led to the formation of colorless block-shaped crystals after ca. one week. Yield: 0.240 g, 48 % (based on W). FT-IR (in cm^{-1}): 1002 (s), 936 (s), 873 (vs), 755 (s), 677 (s), 607(s), 517(w), 466 (w). Elemental analysis (%); calcd.

(found): W, 60.7 (59.6); Eu, 2.28 (2.23); Cs, 5.98 (6.58); Na, 2.41 (3.25). H, 0.99 (1.48). TGA measurements (Figure 4.17) display a weight loss of 9.6 % in the temperature range of 30–220 ^{o}C resulting from loss of coordination and solvent water molecules (expected 8.9 %).

Synthesis of $Na_2CsTb_2H_2[Tb_2(H_2O)_7(\alpha\text{-}Si_2W_{18}O_{66})]Cl\cdot32H_2O$ (Tb-1): The synthetic procedure was conducted as described above for Eu-1 with two alterations: first, 0.196 g (0.450 mmol) of $Tb(NO_3)_3\cdot5H_2O$ instead of $Eu(NO_3)_3\cdot6H_2O$ was used as a lanthanoid precursor; secondly, lower Cs^+ concentrations (0.2 - max. 0.5 ml of 1.0 M CsCl) were employed instead of 0.5 ml 1M CsCl. Colorless needle-like crystals were obtained after ca. one week. Yield: 0.076 g, 17 % (based on W). FT-IR (in cm^{-1}): 1003 (s), 939 (s), 868 (vs), 833 (s), 809 (s), 714 (s), 555 (w), 529 (w). Elemental analysis (%); calcd. (found): W, 55.44 (54.17); Tb, 10.65 (9.41); Cs, 2.22 (3.88); Na, 0.77 (0.62); H, 1.21 (1.53). TGA measurements (Figure 4.17) display a weight loss of 10.9 % in the temperature range of 30–220 ^{o}C resulting from loss of coordination and solvent water molecules (expected 11.7 %).

4.2.2. X-ray crystallography

Data collection of compounds **Eu-1**, **Eu-2**, **Eu-3**, and **Tb-1** was performed on an Oxford Xcalibur Ruby CCD single-crystal diffractometer (Mo-K_α radiation, λ= 0.71073 Å) at 183(2) K. Routine Lorentz and polarization corrections were applied, and an absorption correction was performed using the program CrysAlis.[48] Direct methods were used to locate the heavy metal atoms (SHELXS-97). The remaining atoms were located from successive Fourier maps (SHELXL-97).[49] Hydrogen atoms were not included in the refinement processes. All heavy atoms were refined anisotropically. **Eu-2** contains an obvious site-occupancy disorder for the Cs3 atom, which has been refined on two positions with site occupancies of 0.5 and 0.5. The Tb3 atom in **Tb-1** exhibits disorder over two positions that were refined with site occupancies of 0.8 and 0.2, respectively. In all of the structures, there is a discrepancy between the formulae determined by elemental analysis and those deduced from the crystallographic atom list. This is due to low crystal quality and considerable disorder among the cations, which is a common phenomenon encountered in polyoxometalate chemistry. Crystallographic data of all polyanions are summarized in Table 10. 2 (Annexes).

4.3. Results and discussion

4.3.1. Synthetic parameters

Table 4.1 summarizes synthetic conditions, related products and transformations of [*A*-α-$SiW_9O_{34}]^{10-}$ into different POM building blocks (Figure 4.1). It has been established that the trivacant *Keggin* [*A*-α-$SiW_9O_{34}]^{10-}$ is a versatile inorganic precursor to construct transition metal and lanthanide containing POMs with diverse structural motifs and properties.[17-20, 44-46] However, the reaction between [*A*-α-$SiW_9O_{34}]^{10-}$ and Ln precursors in aqueous solution are highly affected by the reaction parameters such as pH values, counterions, stoichiometry, temperature etc.[27] Furthermore, the {α-SiW_9} polyoxoanion can be easily transformed into *Keggin*- or *Dawson*-type polyanions in acidic aqueous media (Figure 4.1). Starting from previous studies on Ln-derivatives of the open *Wells-Dawson* silicotungstate $[Ln_2(H_2O)_2SiW_{18}O_{66}]^{10-}$ (Ln = Gd, Tb, Dy, Ho),[15] the influence of different Ln cations on their structural diversity is investigated further in the following. For this purpose, the [*A*-α-$SiW_9O_{34}]^{10-}$ precursor was used to react with $Eu(NO_3)_3$ ({α-SiW_9}/Eu^{3+} molar ratio 1:3) in NaOAc buffer solution (pH 4.4) at 80 ^{o}C. The polymeric compound **Eu-1** with a 3D inorganic framework structure was obtained at lower Cs^+ concentrations (0.5 ml of 1.0 M CsCl), whereas **Eu-2** with a 2D framework motif was formed with excess Cs^+ (1.5 ml of 1.0 M CsCl). **Tb-1** with a 3D framework structure was accessed with related strategies, whereas **Tb-2** with a 2D network structure was obtained at higher Cs^+ concentrations compared to previous studies.[15] Therefore, the equilibrium between (**Eu-1** and **Eu-2**), (**Tb-1** and **Tb-2**) can be adjusted via the Cs^+ concentration as an efficient and straightforward control parameter. The new protocol permits control over 2D/3D equilibria between **Ln-1** and **Ln-2** type compounds (Ln = Eu, Gd, Tb), whereas **Dy-2** and **Ho-2** exclusively afforded 2D frameworks as outlined in the preceding chapter.[15] By replacing the $Eu(NO_3)_3$ precursor with $EuCl_3$ and modifying the {α-SiW_9}/Eu^{III} to 3:4, we succeeded in isolating mono-lacunary *Keggin* sandwich-type polyanion $[Eu(\alpha\text{-}SiW_{11}O_{39})_2]^{13-}$ (**Eu-3**) with a 0D structural motif. Interestingly, the preceding studies in **Chapter 3**[15] and this present work[16] demonstrated that the Ln^{III} radii are a decisive factor for the construction of various dimensional architectures of POMs. However, the role of other synthetic parameters may not be underestimated and requires equally careful explorations.

4.3.2. Structural motifs

The single crystal X-ray diffraction analyses revealed that **Eu-1** and **Tb-1** crystallize in the space group *C*2/*c*, while **Eu-2** and **Eu-3** display a triclinic structure (*P*-1, cf. Table 10.2 in Annexes). Compounds **Eu-1**, **Eu-2** and **Tb-1** all consist of an open *Wells-Dawson* polyoxoanion $[\alpha\text{-}Si_2W_{18}O_{66}]^{16-}$ containing two trivalent lanthanoid cations at the exterior pocket sites. The remaining lanthanoid cations as external linkers coordinate to the neighboring polyanions, either leading into 3D frameworks (**Tb-1** and **Eu-1**) or 2D sheet-like structures (**Eu-2**). As **Eu-1** and **Tb-1** are essentially isomorphous and isostructural, only the structure of **Eu-1** is discussed in detail as a representative example.

Eu-1 exhibits a 3D open framework constructed from the *Wells-Dawson* host anion *A*-*α*-$[Si_2W_{18}O_{66}]^{16-}$ and four Eu^{3+} cations. The Eu1 and Eu2 cations are incorporated into the peripheral pocket sites, whereas the external Eu3 and Eu4 linker cations connect neighboring $[Eu_2(H_2O)_7Si_2W_{18}O_{66}]^{10-}$ subunits via Eu-O-W bridges (Figure 4.2a, 4.2b). The Eu1 cation is eight-coordinated in a distorted dodecahedral coordination geometry (idealized symmetry is D_{2d}, Figure 4.2c). Eu1 is connected to four terminal oxygen atoms (O29, O30, O37 and O38) of the $\alpha\text{-}[Si_2W_{18}O_{66}]^{16-}$ framework [Eu1-O: 2.339(9) – 2.450(10) Å], to three water molecules [O67, O68 and O69; Eu1-O: 2.414(14) – 2.453(10) Å], and to a terminal oxygen atom [O47a, symmetry code: a, *-x, 1-y, -z*] from a neighboring $[Eu_2(H_2O)_7Si_2W_{18}O_{66}]^{10-}$ moiety [Eu1-O: 2.408(9) Å] via a Eu1-O47a-W16a bridging bond. In the case of Eu1, two interpenetrating trapezoids are defined as the two orthogonal O38-O37-O29-O30 and O69-O47a-O67-O68 planes with a dihedral angle of 89.6(2)°. The Eu2 cation is coordinated to four terminal oxygen atoms (O31, O32, O35 and O36) of the $\alpha\text{-}[Si_2W_{18}O_{66}]^{16-}$ framework [Eu2-O: 2.366(9) – 2.539(10) Å], to four water molecules [O70, O71, O72 and O73; Eu2-O: 2.442(10) – 2.510(11) Å], and furthermore to a terminal oxygen atom [O18b, symmetry code: b, *-x, y, -0.5-z*] of a neighboring polyanion $[Eu_2(H_2O)_7Si_2W_{18}O_{66}]^{10-}$ via Eu2-O18b-W5b. The Eu-Eu distance between Eu1 and Eu2 within the open *Wells-Dawson* anion is 6.341(2) Å. The cations Eu3 and Eu4 as external linkers are connected to three or two neighboring polyanions, respectively. Eu3 is coordinated to W6 (*0.5-x, 0.5+y, -z-0.5*), W18 (*0.5+x, 0.5+y, z*) and W2 via terminal oxygen bonds [Eu3-O: 2.373(9) – 2.420(10) Å] and to six crystal water molecules. Eu4 is surrounded by seven water molecules, and it is furthermore coordinated to W8 (*0.5-x, 0.5-y, -z*) and W10 via terminal oxygen bonds [Eu3-O: 2.999(10) and 2.318(11) Å].

For both Eu2 and Eu3 in **Eu-1**, the coordination geometries can be described as a nine-coordinate distorted tricapped trigonal prism (idealized symmetry is D_{3h}), and the capping oxygen atoms are located in the center of three rectangular faces (Figure 4.2c). However, both Eu1 and Eu4 cations display a dodecahedral coordination environment (Figure 4.2b). For Eu2, two trigonal planes of this tricapped trigonal prism are defined by O35-O71-O32 and O72-O70-O73, with O35 eclipsing O72, O71 eclipsing O70, and O32 eclipsing O73. The three capping oxygen atoms of the rectangular face (O31, O36, and O18b) lead to a 119.9(3)° angle towards Eu2, which is close to the ideal value of 120°. As bond angles between Eu2 and two eclipsing oxygen atoms of opposite trigonal planes for O71-Eu2-O70, O35-Eu2-O72 and O32-Eu2-O73 are 90.8(3), 91.8(3) and 91.4(3), respectively, and the dihedral angle between the two trigonal planes is 1.9(4)°, thereby giving rise to the overall geometry close to an ideal tricapped trigonal prism.[50] Eu1, Eu2 and Eu4 are linked to two $[Eu_2(H_2O)_7Si_2W_{18}O_{66}]^{10-}$ clusters, whereas Eu3 is coordinated to three polyanions. Finally, each dimeric cluster $[Eu_2(H_2O)_7Si_2W_{18}O_{66}]^{10-}$ is further linked into a 3D polymeric network via four Eu^{3+} linkers (Figure 4.3).

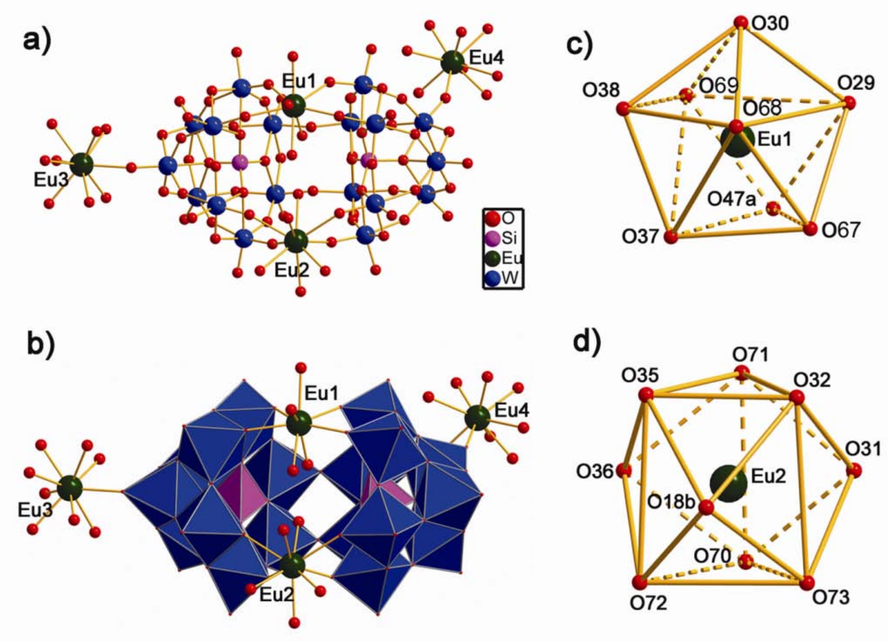

Figure 4.2. (a) Ball-and-stick representation of the molecular structure of **Eu-1**, (b) polyhedral representation of the molecular structure of **Eu-1**, (c) dodecahedral coordination environment of Eu1 in **Eu-1**, (d) tricapped trigonal-prismatic coordination geometry of Eu2 in Eu-1 (W: blue; Eu: green; Si: pink; O: red; WO_6 octahedra: blue; SiO_4 tetrahedra: pink.)

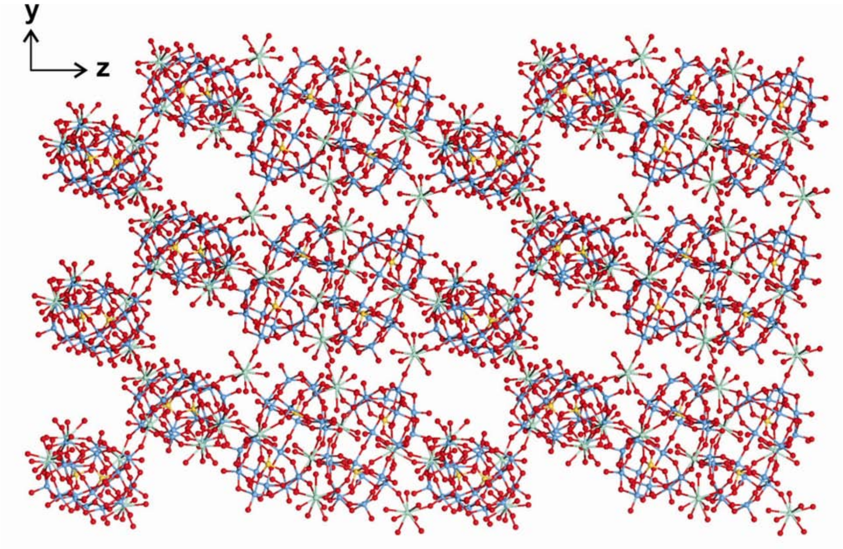

Figure 4.3. Packing motif of Eu-1 perpendicular to *x*. Cations and crystal water molecules are omitted for clarity (W: blue; Eu: green; Si: pink; O: red).

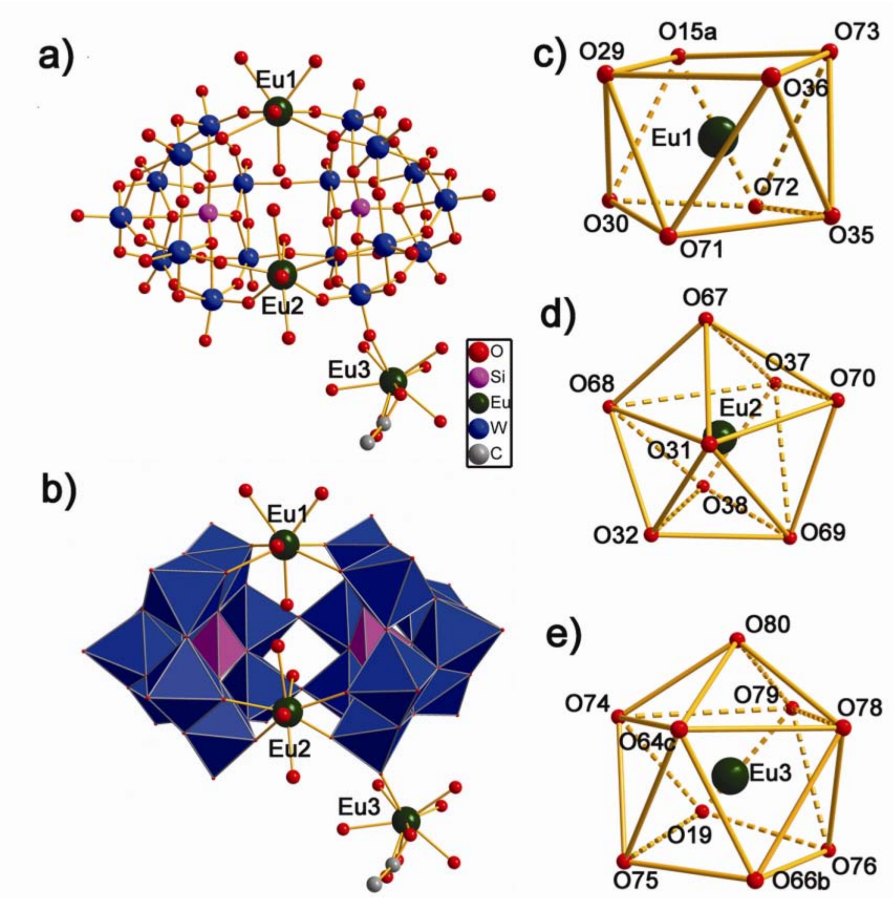

Figure 4.4. (a) Ball-and-stick representation of the molecular structure of **Eu-2**, (b) polyhedral representation of the molecular structure of **Eu-2**, (c) square-antiprismatic geometry of Eu1 in **Eu-2**, (d) dodecahedral coordination geometry of Eu2 in **Eu-2**, (e) monocapped square-antiprismatic coordination geometry of Eu3 in Eu-2 (W: blue; Eu: green; Si: pink; O: red; C: grey; WO_6 octahedra: blue; SiO_4 tetrahedra: pink.)

However, **Eu-2** also consists of one *Wells-Dawson* anion *A*-*α*-$[Si_2W_{18}O_{66}]^{16-}$ which is connected to three crystallographic different europium cations. The Eu1 and Eu2 cations are located in the peripheral pocket positions of the $[Si_2W_{18}O_{66}]^{16-}$ host anion at a Eu-Eu distance of 6.213(2) Å. Eu3 is attached to a terminal oxygen atom of the tungstate shell via O=W bond (Figures 4.4a-b). The distorted square antiprismatic coordination of Eu1 (idealized symmetry is D_{4d}, Figure 4.4c) consists of four terminal oxygen atoms of the $[Si_2W_{18}O_{66}]^{16-}$ anion [O29, O30, O35, O36; Eu1-O: 2.335(8) – 2.424(9) Å], three terminal water molecules [O71, O72 and O73; Eu1-O: 2.391(11) – 2.454(12) Å] and another terminal oxygen atom of an adjacent cluster connected via a symmetry-related

Eu-O-W bond [Eu1-O15a-W4a, symmetry code: a, *2-x,-y, 1-z*; Eu1-O15a: 2.368(9) Å]. The bottom planes of the square antiprism around Eu1 [(O15a, O29, O36, O73) and (O72, O30, O71, O35)] deviate only by 0.356 and 0.109 Å from the ideal geometry. The dihedral angle between these bottom planes is 5.3(3)^{o}, and Eu1 is located at distances of 1.192(1) and 1.308(2) Å, respectively. The eightfold coordination of Eu2 can be described with a slightly distorted dodecahedron (idealized symmetry is D_{2d}) constituted by four terminal oxygen atoms of the α-$[Si_2W_{18}O_{66}]^{16-}$ framework [O31, O32, O37, O38; Eu2-O: 2.351(9) – 2.394(9) Å] and four terminal water molecules [O67, O68, O69 and O70, Eu2-O: 2.408(11) – 2.510(12) Å, Figure 4.4c]. Eu3 is surrounded by a distorted monocapped square antiprism (idealized C_{4v} symmetry, Figure 4.4e). The coordination environment consists of three terminal oxygen atoms O19, O66b (symmetry code: b, *x, 1+y, z*), and O64c (symmetry code: c, *1-x, -y, -z*) of the $[Eu_2(H_2O)_7Si_2W_{18}O_{66}]^{10-}$ polyanions [Eu3-O: 2.350(10) – 2.422(9) Å], four aqua ligands [O74, O75, O76 and O78, Eu3-O: 2.452(12) – 2.518(14) Å] and two oxygen atoms contributed by an acetate ligand [O79 and O80, Eu3-O: 2.543(12) and 2.546(15) Å]. The antiparallel squares are constituted by (O79-O74-O64c-O78 and O19-O75-O66b-O76) with dihedral angle of 6.1(3)^{o}, and the capping atom (O80) is located above the top square plane.[51] The lengths of their base diagonals (O76-O75 and O19-O66b) are quite close (3.924(2) and 4.055(2) Å). Linkage of two and three polyanions by Eu1 and Eu3 via Eu-O-W bridges, respectively, leads to the interesting 2D sheet-like structure of **Eu-2** (Figure 4.5).

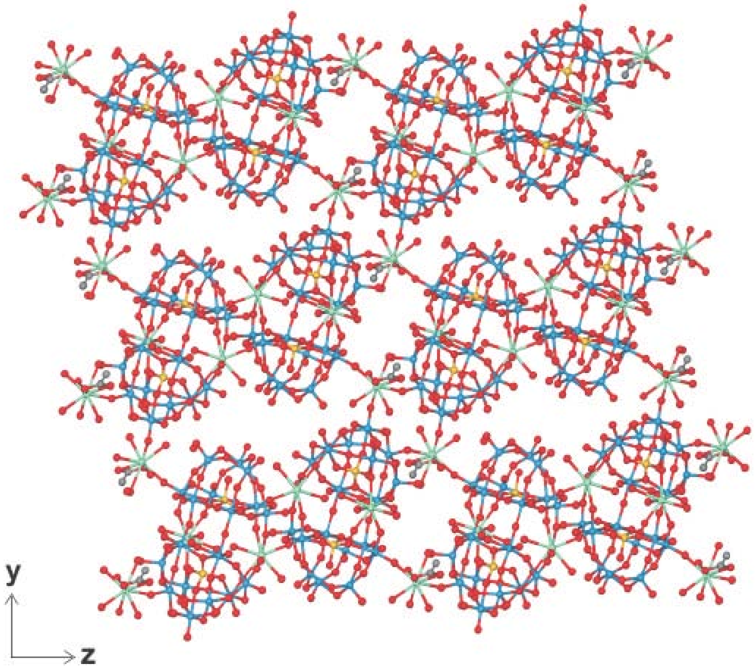

Figure 4.5. Packing motif of **Eu-2** perpendicular to *x* (monovalent cations and crystal water molecules are omitted for clarity; W: blue; Eu: green; Si: yellow; O: red; C: grey).

The compound **Eu-3** is composed of two α-$[SiW_{11}O_{39}]^{8-}$ moieties sandwiching a Eu^{3+} cation that is linked to each of the monolacunary *Keggin* fragments via four Eu-O-W bonds with C_2 symmetry (Figure 4.6). The α-$[SiW_{11}O_{39}]^{8-}$ polyanions coordinate the central Eu1 cation via four oxygen atoms [(O53, O20, O56 and O24), Eu-O: 2.402(8) – 2.431(9) Å] of the edge-sharing belt region and four further oxygen atoms [(O23, O41, O45 and O51), Eu-O: 2.370(9) – 2.396(8) Å] of the corner-sharing polyanion base in a distorted square antiprismatic geometry (Figure 4.7a). Consequently, the Eu^{3+} cation can interact more strongly with corner-shared oxygen than that with edge-shared oxygen. Eu-O bond lengths of **Eu-3** are in the range 2.370(9) – 2.431(9) Å [average 2.400(9) Å] for Eu1, which is in good agreement with an average Eu-O bond length 2.40(3) Å of the $[Eu(\beta\text{-}SiW_{11}O_{39})_2]^{13-}$ polyanion.[28a] **Eu-3** crystallizes in the centrosymmetric space group *P*-1 containing the two enantiomers as a racemic mixture in the asymmetric unit (**A-** and **B-**configurations, cf. Figures 4.6 – 4.8). In analogy to **Eu-3**, the asymmetric units of the isostructural polyanions $[M^{IV}(\alpha\text{-}PW_{11}O_{39})_2]^{11-}$ (M = Zr^{4+}, Hf^{4+}), $[Ce(\alpha\text{-}PW_{11}O_{39})_2]^{10-}$,

$[Pr(\alpha\text{-}GeW_{11}O_{39})_2]^{13-}$ and $[Eu(\beta\text{-}SiW_{11}O_{39})_2]^{13-}$ also contain two different configurations in achiral space groups.[52, 28a]

As shown in Figure 4.7b, we can observe the side view of **Eu-3** as a function of the "twist angle" θ [$\angle\theta$ (upper plane: O56-O23-O51-O24) – Eu – O(bottom plane: O20-O41-O45-O53)]. A twist angle of 45^o gives rise to a molecule with an ideal square-antiprismatic structure, while 0^o indicates a cubic conformation.[52] *Francesconi* et al. first investigated coordination geometries and twist angles of $[Ln^{III}(\alpha\text{-}PW_{11}O_{39})_2]^{11-}$ by introducing ^{183}W NMR spectroscopy in aqueous solutions.[39] The effect of Ln^{3+} species on the molecular configuration in the solid state has furthermore been characterized for $[Ln^{III}(\beta\text{-}SiW_{11}O_{39})_2]^{13-}$ and $[Ce^{III/IV}(\alpha\text{-}PW_{11}O_{39})_2]^{11-/10-}$ by *Kortz* and *Naruke*, respectively.[28a, 52c] In the present case of **Eu-3**, the twist angle θ of 39.4^o (**A**-form, Figure 4.7b) slightly deviates from the ideal value of 45^o due to a distorted square-antiprismatic coordination geometry of EuO_8 in **Eu-3**.

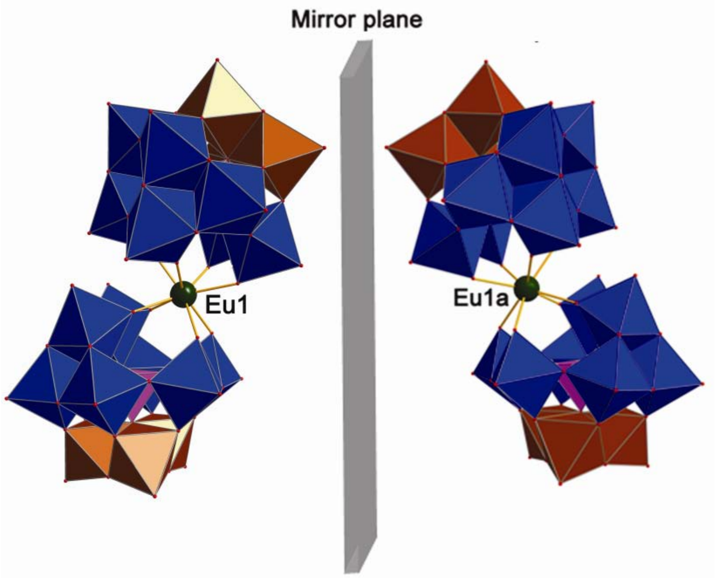

Figure 4.6. Combined polyhedral and ball-and-stick representation of the two $[Eu(SiW_{11}O_{39})]^{13-}$ enantiomers (left: **A**-configuration, right: **B**-configuration; rotated triad shown in brown for clarity; Eu: green; WO_6 octahedra: blue; SiO_4 tetrahedra: pink; symmetry code: a, *-x, 1-y, 1-z*).

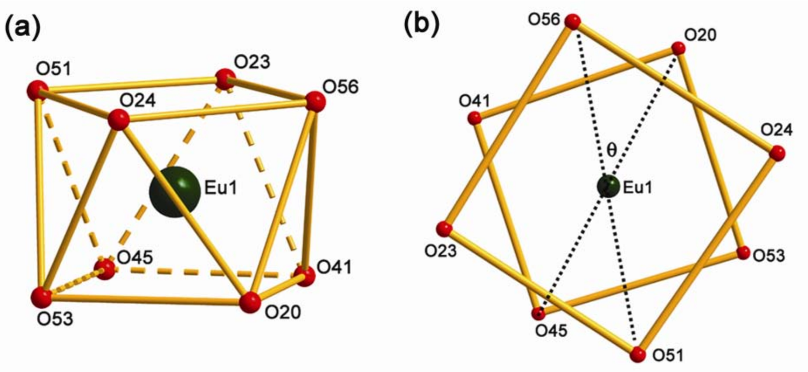

Figure 4.7. (a) Square-antiprismatic geometry of Eu1 in **Eu-3**, (b) side view of **Eu-3** (**A** configuration) and twist angle θ.

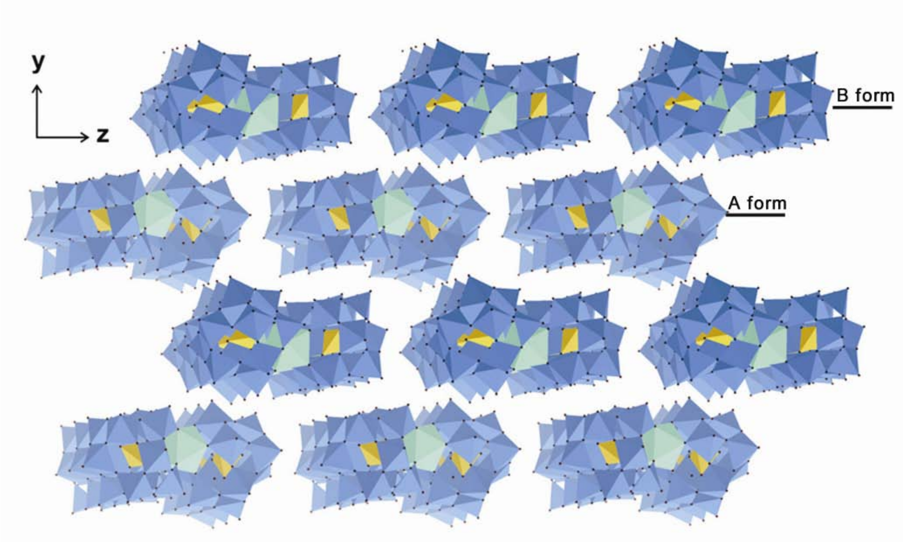

Figure 4.8. Polyhedral view of the packing motif of **Eu-3** along *x* (EuO_8 polyhedra: light green; WO_6 octahedra: blue; SiO_4 tetrahedra: yellow).

Bond-valence-sum calculations[53] (BVS) revealed that the oxidation states of all metal and oxygen atoms in **Eu-1**, **Eu-2**, **Eu-3**, and **Tb-1** polyanions are consistent with their formal values, and we did not observe the oxygen protonation of all the polyoxoanions. In order to balance the charge of the above-mentioned polyoxoanions, $[Ln_2(H_2O)_7Si_2W_{18}O_{66}]^{10-}$ [Ln = Eu, Tb] and $Eu(\alpha\text{-}SiW_{11}O_{39})_2]^{13-}$, three protons were added to **Eu-1**, four protons to **Eu-2**, four protons to **Eu-3**, and two protons in **Tb-1**, respectively, because the products were isolated in an acidic aqueous solution. These protons cannot be located crystallographically and are assumed to be delocalized over the entire structure, which is a commonly observed phenomenon in POM chemistry.[54]

4.3.3. Analytical characterizations and properties

4.3.3.1. FT-IR spectroscopy

The FT-IR spectra of all compounds (**Eu-1**, **Eu-2**, **Eu-3**, and **Tb-1)** exhibit characteristic stretching vibrations which are corresponding to other $[Si_2W_{18}O_{66}]^{16-}$ or $[SiW_{11}O_{39}]^{13-}$ containing species (cf. Figure 4.9).[28a, 18] Four characteristic bands assigned to $\nu_{as}(Si\text{-}O_a)$, terminal $\nu_{as}(W\text{-}O_t)$, corner-sharing $\nu_{as}(W\text{-}O_b)$ and edge-sharing $\nu_{as}(W\text{-}O_c)$ asymmetrical vibration peaks are observed at 1002, 933, 864, 790 and 696 cm^{-1} for **Eu-1**, at 1004, 943, 876, 824, 758 and 709 cm^{-1} for **Eu-2**, at 1003, 940, 873, 755 and 677 cm^{-1} for **Eu-3**, and at 1002, 937, 858, 797 and 665 cm^{-1} for **Tb-1**, respectively. All in all, FT-IR spectra are consistent with single-crystal structure determinations for all compounds.

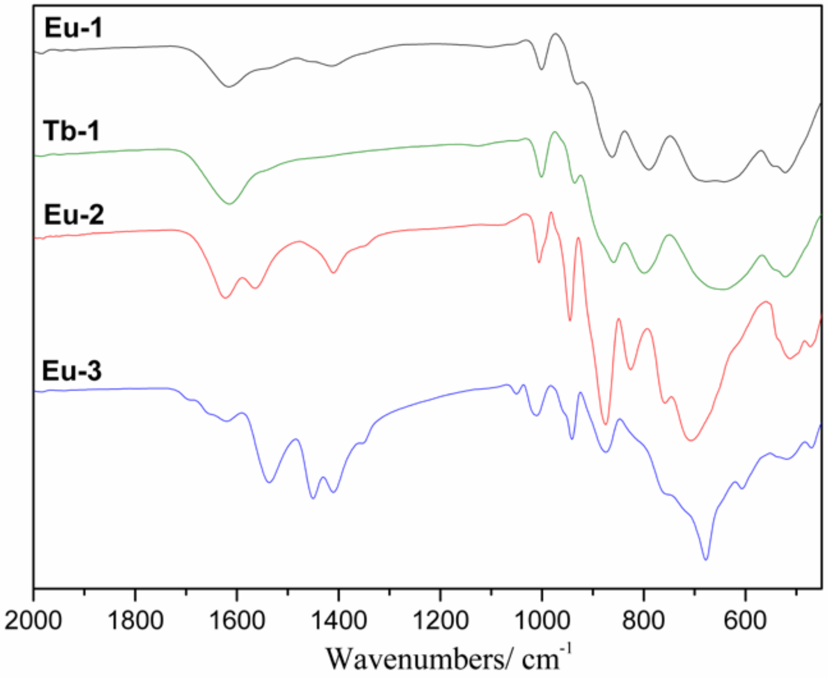

Figure 4.9. FT-IR spectra of the polyanions **Eu-1**, **Eu-2**, **Eu-3**, and **Tb-1** recorded in KBr.

4.3.3.2. UV/Vis spectroscopy

The UV/Vis spectra of **Eu-1**, **Eu-2**, **Eu-3**, and **Tb-1** were recorded in an aqueous solution in the 600-200 nm range (Figure 4.10). The spectra of **Eu-1**, **Eu-2** and **Eu-3** have two characteristic absorption bands at 200-205 and 250 nm in common. The absorption band at higher energies can be ascribed to the p_{π}-d_{π} charge-transfer transitions of the O_t-W bonds, whereas the lower-energy absorption band arises from p_{π}-d_{π} charge-transfer transitions of the $O_{b,c}$-W bonds. However, the UV spectra of **Tb-1** show only the higher-energy absorption band centered at 203 nm that can be assigned to the pπ-dπ charge-transfer transitions of the O_t-W bonds.[35] Moreover, the typical absorption bands of trivalent lanthanides in aqueous solution were not observed, probably due to the concealment by strong charge-transfer bands (O→W). Meanwhile, the solid-state absorption spectra over the 200-600 nm range were also investigated (Figures 4.11 and 4.12). In addition to the above strong absorption bands (O_t-W or $O_{b,c}$-W), **Eu-3** displays four weak absorption bands centred at 537, 465, 395, 386, 380 and 374 nm which can be assigned to $^7F_0$-$^5D_1$, $^7F_0$-$^5D_2$, $^7F_0$-$^5L^6$, $^7F_0$-$^5G_2$, $^7F_0$-$^5L_7$, $^7F_0$-$^5G_{3,4,5,6}$ transitions of the Eu^{3+} ion, respectively, whereas only the $^7F_0$-$^5L_6$ transitions around at 393 nm could be recorded for **Eu-1**, and **Eu-2** (Figure 4.11). For **Tb-1**, two weak absorption bands around 462 and 499 nm correspond to $^7F_6$-$^5D_4$ and $^7F_6$-$^5D_3$ transitions of Tb^{3+} (Figure 4.12).[55]

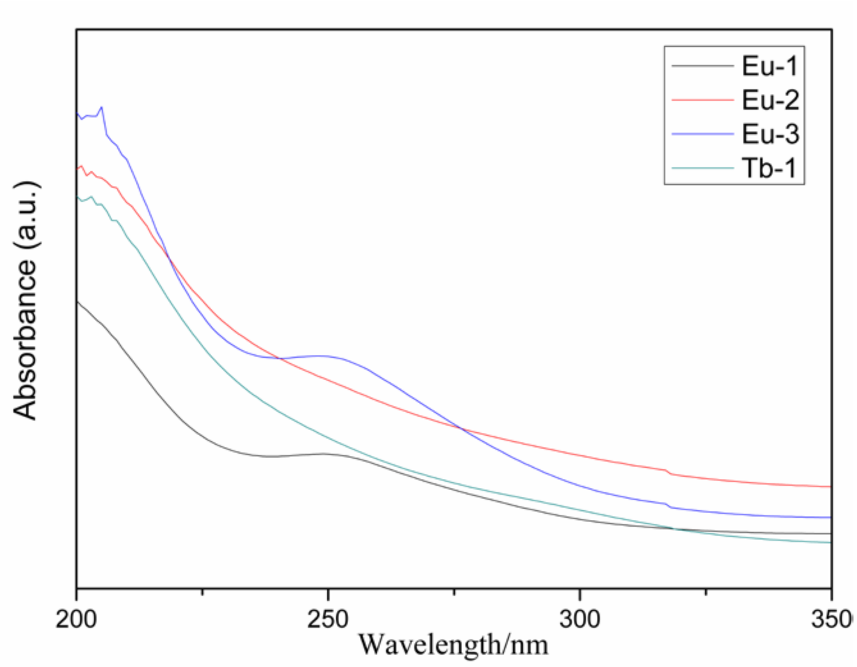

Figure 4.10. UV/Vis spectra of the polyanions **Eu-1**, **Eu-2**, **Eu-3**, and **Tb-1** recorded in aqueous solution.

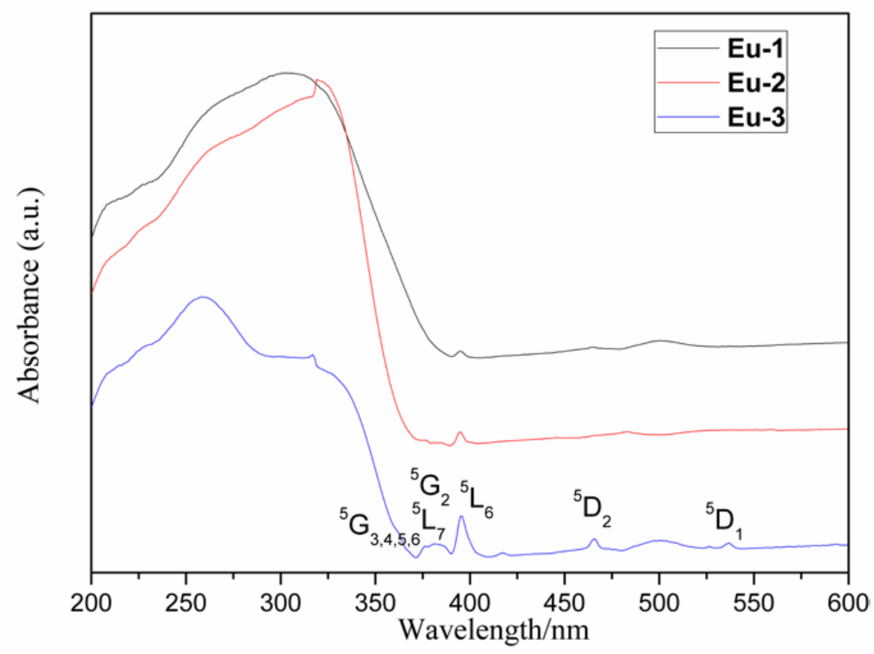

Figure 4.11. Solid state UV/Vis spectra of **Eu-1, Eu-2** and **Eu-3**.

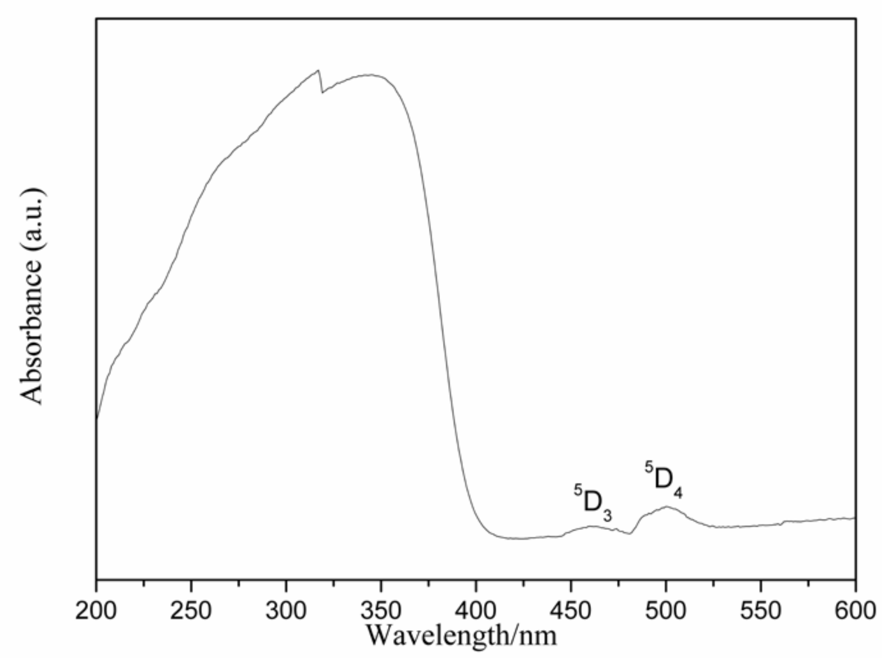

Figure 4.12. Solid state UV/Vis spectra of **Tb-1**.

4.3.3.3. PXRD and TGA characterizations

The phase purity of **Eu-1**, **Eu-2**, **Eu-3**, and **Tb-1** samples was checked by bulk powder X-ray diffraction measurements (Figures 4.13–4.16). The PXRD patterns for **Eu-Tb-1** series are similar, indicating the isostructural character of the all compounds. The experimental diffraction patterns are in line with the calculated ones, thus confirming the results of single crystal X-ray structure determination. Intensity differences are due to sample preparation and texture effects.

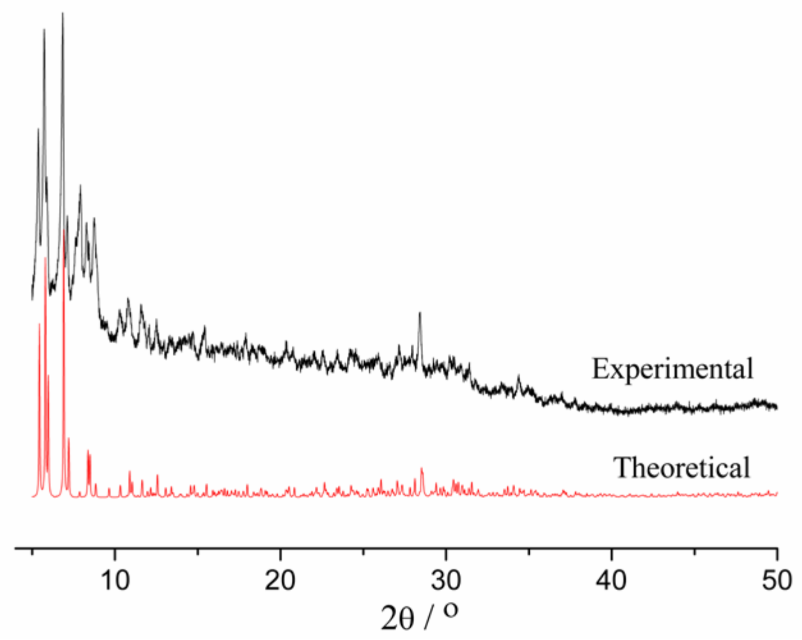

Figure 4.13. Powder X-ray diffraction pattern of bulk **Eu-1** (top) compared to the theoretical pattern calculated from single crystal X-ray diffraction data (bottom).

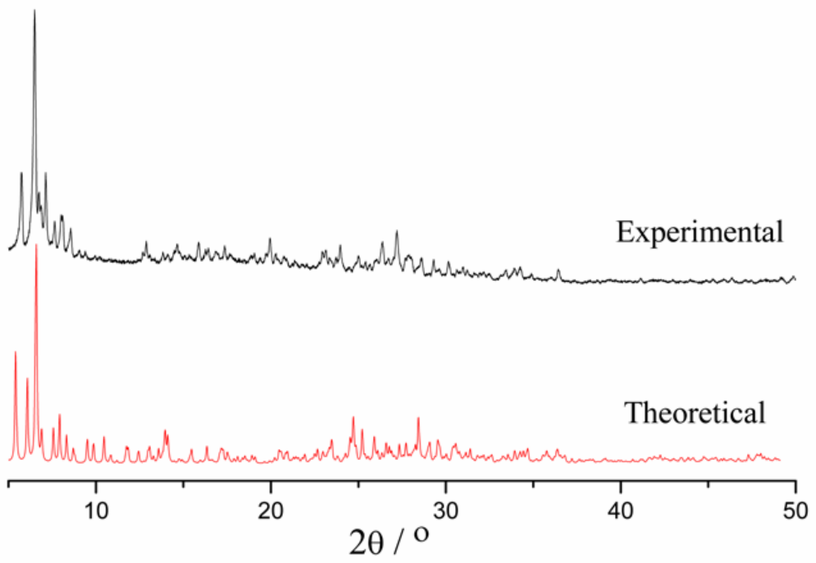

Figure 4.14. Powder X-ray diffraction pattern of bulk **Eu-2** (top) compared to the theoretical pattern calculated from single crystal X-ray diffraction data (bottom).

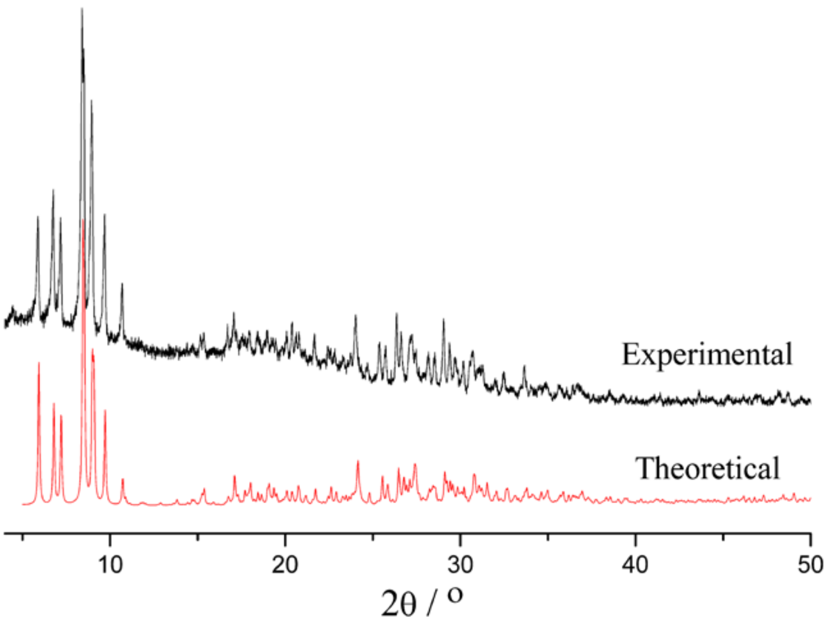

Figure 4.15. Powder X-ray diffraction pattern of bulk **Eu-3** (top) compared to the theoretical pattern calculated from single crystal X-ray diffraction data (bottom).

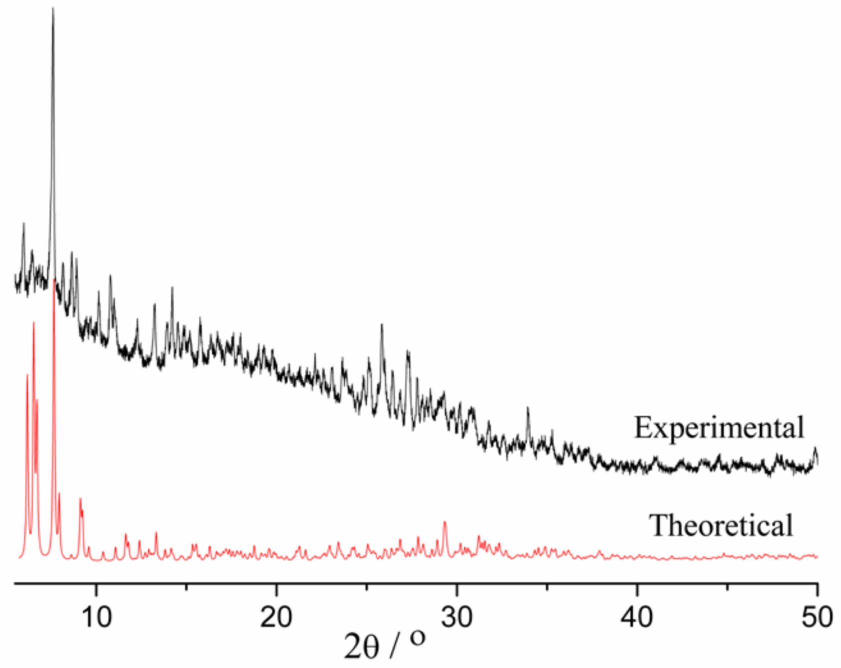

Figure 4.16. Powder X-ray diffraction pattern of bulk **Tb-1** (top) compared to the theoretical pattern calculated from single crystal X-ray diffraction data (bottom).

TGA measurements on **Eu-1**, **Eu-2**, **Eu-3**, and **Tb-1** samples were performed under nitrogen flow in the temperature range of 30-600 ^{o}C. The TGA curves of all compounds (Figure 4.17) exhibit one weight loss step in the temperature range of 30-300 ^{o}C, respectively. The observed weight loss in the 30-220 ^{o}C range for **Eu-1** is 11.6% (calcd. 11.2 %), corresponding to the release of crystal water molecules and adsorbed water molecules. The corresponding values are 9.8 % in the 30-200 ^{o}C range (calcd. 10.3 %) for **Eu-2**, 9.6 % (calcd. 8.9 %) in the 30-150 ^{o}C range for **Eu-3**, 10.9 % in the 30-210 ^{o}C range (calcd. 11.7 %) for **Tb-1**.

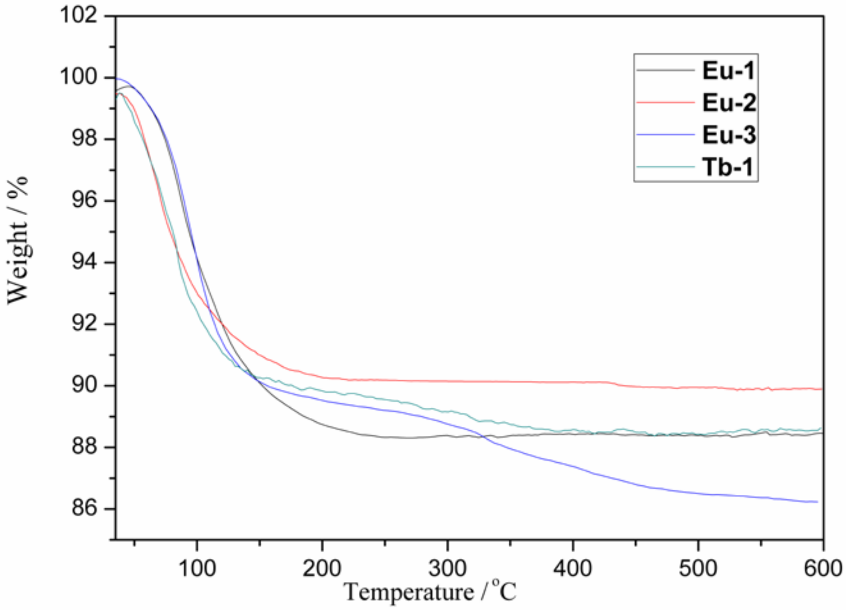

Figure 17. Thermogravimetric measurements of **Eu-1**, **Eu-2**, **Eu-3**, and **Tb-1**.

4.3.3.4. Photoluminescencent properties

As lanthanoid compounds play a key role in lighting and colour conversion technologies (e.g. lasers, light-emitting diodes or plasma displays),[56] the solid state photoluminescence properties of **Eu-1**, **Eu-2**, **Eu-3** and **Tb-1** were recorded at room temperature. All four compounds exhibit characteristic emission spectra of the Ln^{3+} f-f-transitions under photoexcitation of the O→W LMCT bands of the polyoxometalates (Figures 4.18). The terbium compound **Tb-1** displays green photoluminescence upon excitation at 255 nm. The emission spectrum exhibits four characteristic peaks of Tb^{3+}, which can be ascribed to the $^5D_4 \rightarrow ^7F_6$ (490 nm), $^5D_4 \rightarrow ^7F_5$ (548 nm), $^5D_4 \rightarrow ^7F_4$ (590 nm) and $^5D_4 \rightarrow ^7F_3$ (619 nm) transitions, in agreement with preceding studies (Figure 4.18d).[57] As shown in Figure 18a-c, the europium compounds of **Eu-1**, **Eu-2**, and **Eu-3** show four representative characteristic emission bands centered at 593, 618, 653 and 701 nm corresponding to the $^5D_0 \rightarrow ^7F_1$, $^5D_0 \rightarrow ^7F_2$, $^5D_0 \rightarrow ^7F_3$, $^5D_0 \rightarrow ^7F_4$ transitions, respectively, in line with previous reports.[36, 58] The $^5D_0 \rightarrow ^7F_2$ transitions exhibit the highest intensity in the four transitions for all compounds, and the absence of $^5D_0 \rightarrow ^7F_0$ may be due to symmetry-forbidden transitions. The $^5D_0 \rightarrow ^7F_{2,4}$ transition are eclectic-dipole transitions that are hypersensitive to the coordination environment of Eu^{3+} ions, whereas the $^5D_0 \rightarrow ^7F_1$ transitions are magnetic-dipole transitions that are insensitive to their local environments and vary in intensity with the ligand field strength acting on the Eu^{3+} ion.[58, 59] Stronger interactions of rare-earth complexes with their local chemical surroundings decrease their symmetry, thereby enhancing the intensity of electric-dipolar transitions.[57] As the intensity of the $^5D_0 \rightarrow ^7F_2$ transition increases upon lower site symmetry of the Eu^{3+} ion, the $^5D_0 \rightarrow ^7F_2$ / $^5D_0 \rightarrow ^7F_1$ intensity ratio is often used to quantify coordination states and site symmetries of rare earth ions.[58, 60] The relative intensity ratios of the $^5D_0 \rightarrow ^7F_2$ / $^5D_0 \rightarrow ^7F_1$ transition of **Eu-1** and **Eu-2** are around 3.7 and 3.4, respectively, which are much larger than around 1.4 in **Eu-3**. This result is good agreement with previous reports that the relative intensities of the $^5D_0 \rightarrow ^7F_J$ (J=0-4) emission for $K_{13}[Eu_2(SiW_{11}O_{39})_2].3H_2O$ at 300 K.[61] This indicates that the Eu^{3+} ions in **Eu-1** and **Eu-2** display a coordination environment with lower symmetry than that in **Eu-3**. Moreover, the presence of the aqua ligands coordinating to Eu^{III} centres in **Eu-1** and **Eu-2** also can result in a dramatic increase in the magnitude of the hypersensitive of $^5D_0 \rightarrow ^7F_2$ transitions, compared to the absence of aqua ligands in **Eu-3**.[3, 62] All these results are in good agreement with the crystallographic results. The excitation spectra for **Eu-1**, **Eu-2** and **Eu-3** were also recorded at room temperature by monitoring the emission for the most intense $^5D_0 \rightarrow ^7F_2$ transition at 618 nm, respectively (Figure 4.19a-c). All the spectra display characteristic broad bands corresponding to the transitions of the ligand-to-metal charge transfer O→W (LMCT) bands of POM ligands at $\lambda < 300$ nm and f-f lines of Eu^{3+} ion. A strong $^7F_0$-$^5L^6$ transition line at about 393 nm was recorded as a constant photon flux in excitation curves.[62] Compared to the emission spectra under the O→W LMCT band excitation, the emission spectra under photoexcitation of the $^7F_0$-$^5L^6$ transition (393 nm) show no obvious change (Figure 4.19d-f).[62] Therefore, the photoexcitation of O→W LMCT bands of polyoxometalates result in an effective intramolecular energy transfer from O→W LMCT triplet states of POM ligands to Eu^{3+} ions, following by the typical emission $^5D_0 \rightarrow {}^7F_J$ (J=0-4).[3] The ligand-metal energy transfer mechanisms behind the luminescence of lanthanoid complexes have been widely investigated.[63] We can observe efficient luminescence properties when the triplet state energy of the ligand is greater than or equal to the energy gap (ΔE) between the excited state and ground state of the metal ion.[64] According to the above results, we propose that the energy gap (ΔE) of the Eu^{3+} ion may be smaller than that of the Tb^{3+} ion, i.e. the ligand-to-metal charge transfer (LMCT) of the Eu^{3+} ion is more effective in comparison with the Tb^{3+} ion.

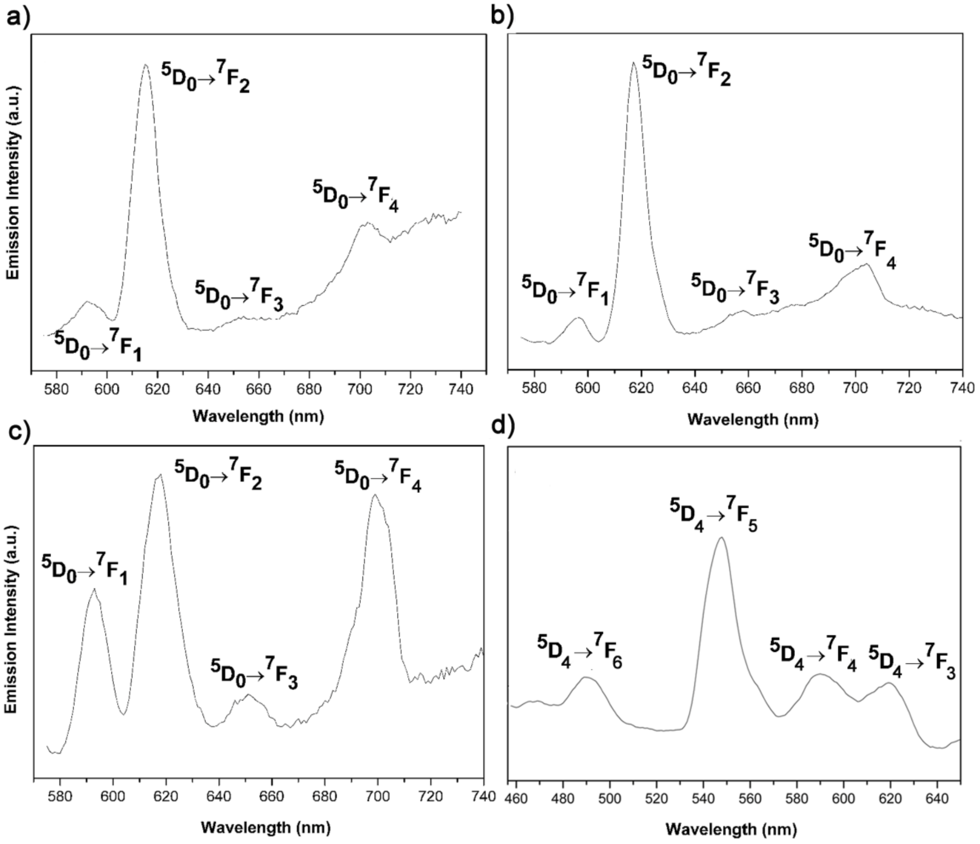

Figure 4.18. Photoluminescence spectra of (a) **Eu-1**, (b) **Eu-2**, (c) **Eu-3,** (d) **Tb-1** at room temperature (excitation wavelengths: 250 nm for **Eu-1**, 275 nm for **Eu-2**, 275 nm for **Eu-3** and 255 nm for **Tb-1**, respectively).

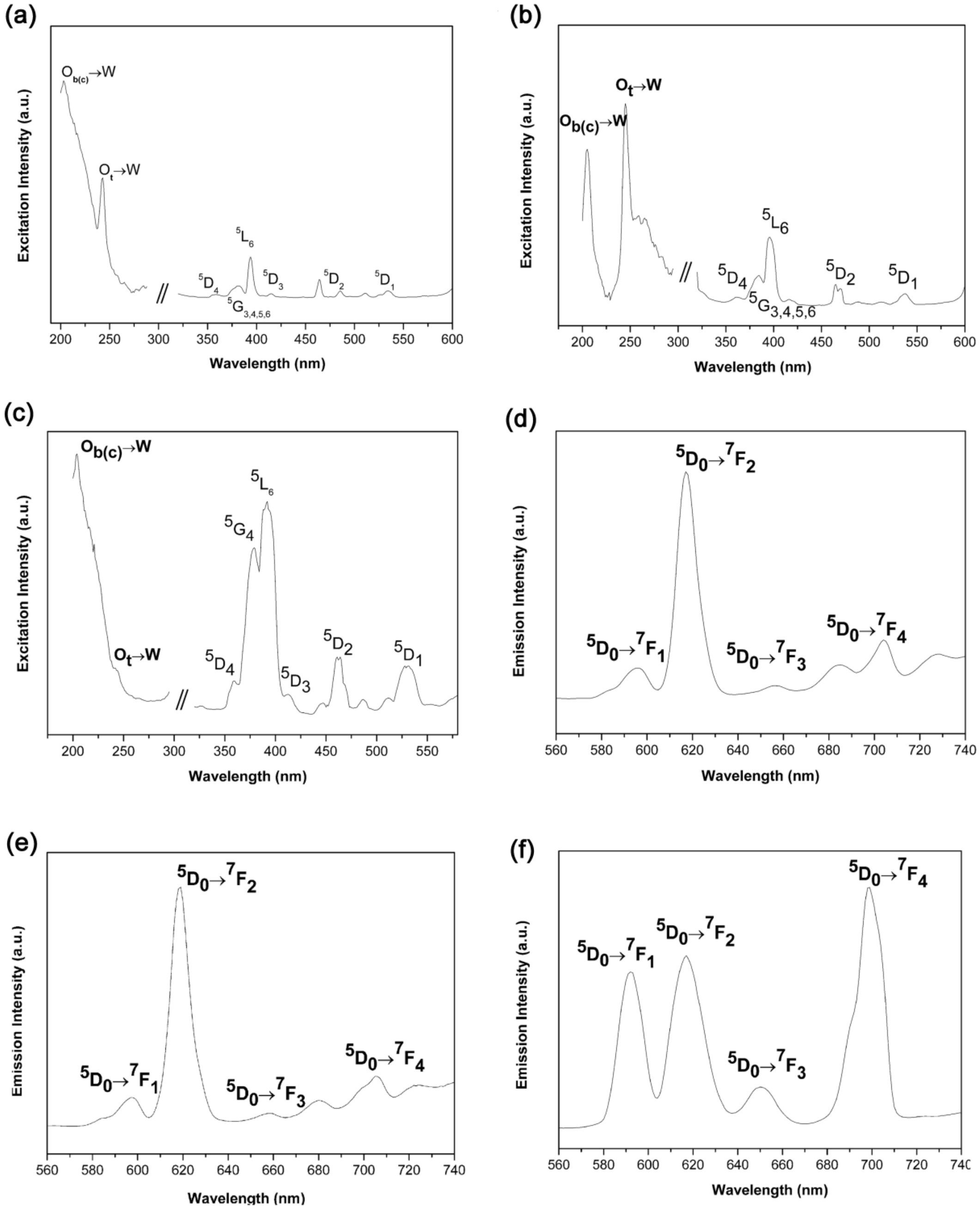

Figure 4.19. Excitation spectra of (a) **Eu-1**, (b) **Eu-2**, (c) **Eu-3** at room temperature for the $^5D_0\rightarrow{}^7F_2$ transitions at 618 nm (// cut-off for double frequency scattering peak around 310 nm); Photoluminescence spectra of (d) **Eu-1**, (e) **Eu-2** and (f) **Eu-3** (λ_{ex} = 393 nm).

4.3.3.5. Magnetic properties

The magnetic susceptibilities of **Eu-1**, **Eu-2**, **Eu-3** and **Tb-1** were measured on a polycrystalline sample in an applied magnetic field of 1 kOe over the temperature range of 5-300 K. Magnetic properties of **Eu-1**, **Eu-2**, and **Eu-3** could not be investigated due to the non-magnetic ground term $^7F_0$ of the Eu^{3+} ion. Despite the low-temperature limit, χ_m of the magnetic susceptibility is nonzero owing to the term $\chi(0)$ arising from the coupling between the $^7F_0$ and the first excited states $^7F_1$ through Zeeman perturbation observed for some europium compounds.[65] In contrast, **Tb-1** exhibits characteristic paramagnetic behavior over the entire temperature range. The χ_m value slowly increases from 0.043 emu Oe^{-1} mol^{-1} at 300 K to 0.467 emu Oe^{-1} mol^{-1} at 25 K, and then exponentially increases to the maximum of 1.639 emu Oe^{-1} mol^{-1} at 5 K (Figure 4.20). The $1/\chi_m$ plot follows the Curie law ($\chi = C/T$) with the extracted Curie constant $C_{\mathbf{Tb-1}}$ = 11.80 emu K Oe^{-1} mol^{-1} (Figure 4.20). The effective magnetic moment μ_{eff} per terbium ion of 9.76 for **Tb-1** is consistent with the expected spin-only value 9.72 for the four Tb^{3+} ions Furthermore, the refined spin value S of 1.50 for **Tb-1** is in good agreement with the spin of non-interacting terbium centers (S = 3/2). Therefore, the magnetic spin-spin interactions between the Tb ions linked via O-W-O bridges are negligible owing to large Tb−Tb distances in **Tb-1**.

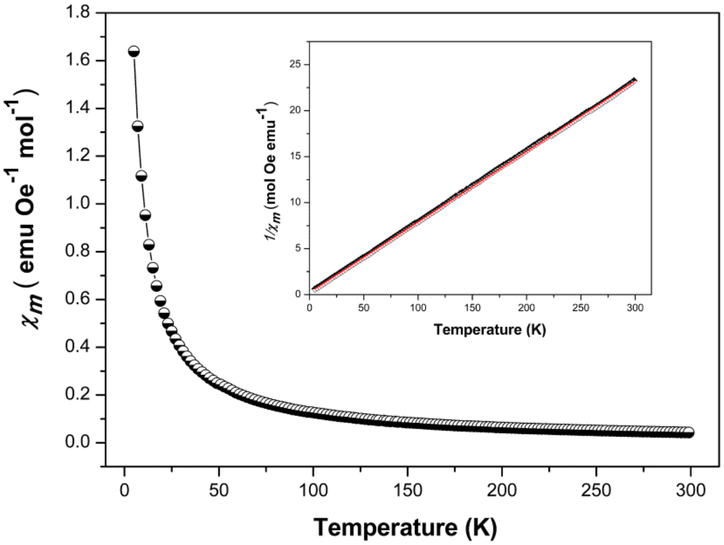

Figure 4.20. Temperature dependent magnetic susceptibility χ_m and $1/\chi_m$ (inset) of **Tb-1** in the 5 - 300 K range.

4.3.3.6. Electrochemical characterization

The electrochemical properties of the title compounds **Eu-1**, **Eu-2**, **Eu-3** and **Tb-1** were studied by cyclic voltammetry analysis (CV) in sodium acetate buffer solution (pH 4.4) as the supporting electrolyte (Figure 4.21). The electrochemical behavior of **Eu-1**, **Eu-2**, **Eu-3** and **Tb-1** was investigated in the potential range of +1.0 to -1.0 V. As the CV curves of **Eu-1**, **Eu-2**, **Eu-3** and **Tb-1** are quite similar, **Eu-2** is discussed in the following as a representative example. Interestingly, the reduction wave I of **Eu-2** in the negative potential region occurs only at -0.893 V (E_{pc1}) in a single step (Figure 4.21), whereas two separated reduction waves of $[Ln_2(H_2O)_7Si_2W_{18}O_{66}]^{10-}$ (Ln = Gd, Tb, Dy, Ho) were observed in two steps, respectively.[15] Interestingly, the second reduction step of the tungsten centers is absent for the europium compounds. However, the reoxidation process of tungsten associated with this reduction process is split into two waves (I' and II') located at -0.823 V (E_{pa1}) and -0.708 V (E_{pa2}). Related behavior was reported for the preceding studies into this compound family as mentioned above.[15] Moreover, no redox processes of the lanthanoid cations were detected in the potential range from -1.0 to +1.0 V. This phenomenon was also observed for structurally related lanthanoid-substituted Dawson-type arsenotungstates (α_2-$[Ln\text{-}(As_2W_{17}O_{61})_2]^{17-}$ and $\{[(\alpha_2\text{-}As_2W_{17}O_{61})Ln(H_2O)_2]_2\}^{14-}$).[66] As can be seen from Figure 4.21, the cathodic peak potentials shift towards the negative direction with an increase of the scan rate, whilst the corresponding anodic peak potentials shift towards the positive direction. In addition, the peak currents are proportional to the scan rate (υ), which indicates that the redox process is surface-controlled with a fast exchange rate of electrons.

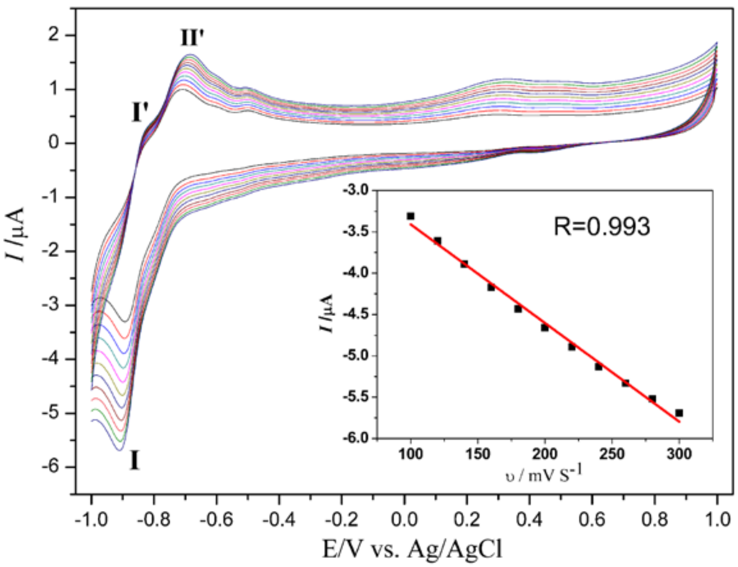

Figure 4.21. Cyclic voltammograms of 0.1 mM **Eu-2** in a pH 4.4 (1.0 M CH_3COONa/CH_3COOH) buffer at different scan rates (from inner to outer plots: 100, 120, 140, 160, 180, 200, 220, 240, 260, and 300 mVs^{-1}). Inset: representation of the cathodic peak currents I_{pc} of reduced peak I against the scan rates.

4.4. Conclusions

Three new lanthanide substituted polyoxotungstates with open *Wells-Dawson* fragments were obtained. $[Ln_2(H_2O)_7SiW_{18}O_{66}]^{10-}$ [Ln = Eu^{III} (**Eu-1** and **Eu-2**), Tb^{III} (**Tb-1**)] and a new sandwich-type polyoxometalate with *Keggin*-type monolacunary anions $[Eu(\alpha\text{-}SiW_{11}O_{39})_2]^{13-}$ **(Eu-3)** emerged from adjusted one-pot reactions of the trilacunary *Keggin* precursor $Na_{10}[SiW_9O_{34}]\cdot 23H_2O$ with lanthanide salts. All compounds were fully characterized by inductively coupled plasma (ICP) and thermogravimetric analyses, FT-IR and UV/Vis spectroscopic techniques, as well as powder X-ray diffraction (PXRD) and single-crystal X-ray diffraction. The versatile tri-lacunary $\{SiW_9O_{34}\}$ building block could be converted into open *Wells-Dawson* $\{Si_2W_{18}O_{66}\}$ polyanions or mono-lacunary *Keggin* $\{SiW_{11}O_{39}\}$ anions through control of reaction parameters (pH, countercations, stoichiometry, temperature and time). Furthermore, the POM dimensional diversity can be easily adjusted by lanthanoid cations, ranging from 3D open frameworks of **Eu-1** and **Tb-1** over the 2D sheet-like networks of **Eu-2** to 0D moieties of **Eu-3**. Electrochemical properties of all compounds were studied through CV in a sodium acetate buffer (pH 4.4). **Eu-1**, **Eu-2**, **Eu-3** and **Tb-1** exhibit room temperature photoluminescence upon excitation. The magnetic susceptibility of **Tb-1** was studied in the temperature range between 5 and 300 K indicating paramagnetic behavior due to the spins of non-interacting terbium centers.

References

[1] Katsoulis, D. E. *Chem. Rev*. **1998**, 98, 359–387.

[2] (a) Clemente-Juan, J. M.; Coronado, E. *Coord. Chem. Rev*. **1999**, 361–394 (and references cited therein). (b) Ritchie, C.; Ferguson, A.; Nojiri, H.; Mirras, H. N.; Song, Y. F.; Long, D. L.; Burkholder, E.; Murrie, M.; Kögeler, P.; Brechin, E. K.; Cronin, L. *Angew. Chem. Int. Ed.* **2008**, 47, 5609–5612.

[3] Yamase, T. *Chem. Rev*. **1998**, 98, 307–325.

[4] (a) Mizuno, N.; Misono, M. *Chem. Rev*. **1998**, 98, 199–218. (b) Nardello, V.; Aubry, J.-M.; De Vos, D. E.; Neumann, R.; Adam, W.; Zhang, R.; ten Elshof, J. E.; Witte, P. T.; Alsters, P. L. *J. Mol. Catal. A* **2006**, 251, 185–193.

[5] Malaestan, I. L.; Ellern, A.; Baca, S.; Kögerler, P. *Chem. Commun*. **2012**, 48, 1499–1501.

[6] (a) Chen, W.; Li, Y.; Wang, Y.; Wang, E.; Su, Z. *Dalton Trans*. **2007**, 4293–4301. (b) Ritchie, C.; Speldrich, M.; Gable, R. W.; Sorace, L.; Kögerler, P.; Boskovic, C. *Inorg. Chem*. **2011**, 50, 7004–7014. (c) Sadakane, M.; Dickmann, M. H.; Pope, M. T. *Angew. Chem. Int. Ed.* **2000**, 39, 2914–2916. (d) Hussain, F.; Spingler, B.; Conrad, F.; Speldrich, M.; Kögerler, P.; Boskovic, C.; Patzke, G. R. *Dalton Trans*. **2009**, 23, 4423–4425. (e) El Moll, H.; Nohra, B.; Mialane, P.; Marrot, J.; Dupre, N.; Riflade, B.; Malacria, M.; Thorimbert, S.; Hasenknopf, B.; Lacôte, E.; Aparicio, P. A.; Lopez, X.; Poblet, J. M.; Dolbecq, A. *Chem. Eur. J.* **2011**, 17, 14129–14138.

[7] Wassermann, K.; Dickman, M. H.; Pope, M. T. Angew. Chem., **1997**, 109, 1513–1516; Angew. Chem., Int. Ed. 1997, 36, 1445–1448.

[8] Bassil, B. S.; Dickman, M. H.; Römer, I.; Kammer, B. von der.; Kortz, U. Angew. Chem., Int. Ed. Engl. 2007, 46, 6192–6195.

[9] Cronin, L.; Beuggholt, C.; Krickemeyer, E.; Schmidtmann, M.; Bögge, H.; Kögerler, P.; Kim, T.; Luong K.; Müller, A. *Angew. Chem., Int. Ed.*, **2002**, 41, 2805–2808.

[10] Fukaya, K.; Yamase, T. *Angew. Chem., Int. Ed.*, **2003**, 42, 654–658.

[11] Qin, C.; Song, X.-Z.; Su, S.-Q.; Dang, S.; Feng, J.; Song, S.-Y.; Hao, Z.-M.; Zhang, H.-J. *Dalton Trans*. **2012**, 41, 2399–2407.

[12] Hussain, F.; Patzke, G. R. *CrystEngComm* **2011**, 13, 530–536.

[13] Hussain, F.; Conrad, F.; Patzke, G. R. *Angew. Chem. Int. Ed.* **2009**, 48, 9088–9091.

[14] Khoshnavazi, R.; Bahrami, L.; Gholamyan, S. *J. Mol. Struct*. **2011**, 990, 57–62.

[15] Ni, L.; Hussain, F.; Springler, B.; Weyeneth, S.; and Patzke, G. R. *Inorg. Chem*. **2011**, 50, 4944–4955.

[16] Ni, L.; Springler, B.; Weyeneth, S.; and Patzke, G. R. *Eur. J. Inorg. Chem.* **2013**, 1681–1692.

[17] Laronze, N.; Marrot, J.; Hervé, G. *Chem. Commun*. **2003**, 2360–2361.

[18] Laronze, N.; Marrot, J.; Hervé, G. *Inorg. Chem*. **2005**, 44, 1275–1281.

[19] Laronze, N.; Marrot, J.; Hervé, G. *C. R. Chimie* **2006**, 9, 1467–1471.

[20] (a) Bi, L.-H.; Kortz, U.; *Inorg. Chem*. **2004**, 43, 7961–7962. (b) Netlulla, S.; van Tol, J.; Dalal, N. S.; Bi, L.-H.; Kortz, U.; Keita, B.; Nadjo, L.; Khitrov, G. A.; Marshall, A. G. *Inorg. Chem*. **2005**, 44, 9795–9806.

[21] Laronze, N.; Haouas, M.; Marrot, J.; Taulelle, F.; Hervé, G. *Angew. Chem. Int. Ed*. **2006**, 45, 139–142.

[22] Laronze, N.; Marrot, J.; Hervé, G. *Inorg. Chem*. **2003**, 42, 5857–5862.

[23] Zhang, S.; Zhao, J.; Ma, P.; Chen, H.; Niu, J.; Wang, J. *Cryst. Growth Des*. **2012**, 12, 1263–1272.

[24] R. Khoshnavazi, L. Bahrami, H. Davoodi, *Inorg. Chim. Acta* **2012**, 382, 158–161.

[25] S.-J. Li, S.-X. Liu, N.-N. Ma, Y.-Q. Qiu, J. Miao, C.-C. Li, Q. Tang, L. Xu, *CrystEngComm* **2012**, 14, 1397–1404.

[26] (a) P. Yin, D. Li, T. Liu, *Isr. J. Chem*. **2011**, 51, 191–204. (b) D.-L. Long, E. Burkholder, L. Cronin, *Chem. Soc. Rev*. **2007**, 36, 105–121. (c) M. Hutin, D.-L. Long, L. Cronin, *Isr. J. Chem*. **2011**, 51, 205–214.

[27] R. D. Peacock, T. J. R. Weakley, *J. Chem. Soc. (A)* **1971**, 1836–1839.

[28] (a) B. S. Bassil, M. H. Dickmann, B. von der Kammer, U. Kortz, *Inorg. Chem*. **2007**, 46, 2452–2458. (b) M. A. AlDamen, S. Cardona-Serra, J. M. Clemente-Juan, E. Coronado, A. Gaita-Arino, C. Martí-Gastaido, F. Luis, O. Montero, *Inorg. Chem*. **2009**, 48, 3467–3479.

[29] H. An, Z. Han, T. Xu, *Inorg. Chem*. **2010**, 49, 11403–11414.

[30] M. N. Sokolova, G. B. Andreev, A. B. Yusov, *Inorg. Chem. Commun*. **2011**, 14, 466–469.

[31] (a) W.-D. Wang, X.-X. Li, W.-H. Fang, G.-Y. Yang, *J. Cluster Sci*. **2011**, 22, 87–95. (b) B. Nohra, P. Mialane, A. Dolbecq, E. Rivière, J. Marrot, F. Sécheresse, *Chem. Commun*. **2009**, 2703–2705.

[32] D.-Y. Du, J.-S. Qin, G. Yuan, Y.-Q. Lan, X.-L. Wang, K.-Z. Shao, Z.-M. Su, *Solid State Sci*. **2011**, 13, 1115–1121.

[33] E. Wang, B. Li, B. Zhang, Z. Wang, *Transition Met. Chem*. **1997**, 22, 58–60.

[34] P. Mialane, A. Dolbecq, E. Rivière, J. Marrot, F. Sécheresse, *Eur. J. Inorg. Chem*. **2004**, 33–36.

[35] J. Niu, K. Wang, H. Chen, J. Zhao, P. Ma, J. Wang, M. Li, Y. Bai, D. Dang, *Cryst. Growth Des*. **2009**, 9, 4362–4372.

[36] P. Mialane, L. Lisnard, A. Mallard, J. Marrot, E. Antic-Fidancev, P. Aschehoug, D. Vivien, F. Sécheresse, *Inorg. Chem*. **2003**, 42, 2102–2108.

[37] J. Iijima, H. Naruke, *Inorg. Chim. Acta* **2011**, 379, 95–99.

[38] H. Naruke, J. Iijima, T. Sanji, *Inorg. Chem*. **2011**, 50, 7535–7539.

[39] J. Bartis, S. Sukal, M. Dankova, E. Kraft, R. Kronzon, M. Blumenstein, L. C. Francesconi, *Dalton Trans*. **1997**, 1937–1944.

[40] S. Zhai, Y. Chen, S. Wang, J. Jiang, S. Dong, J. Li, *Talanta* **2004**, 63, 927–931.

[41] L. Xu, H. Zhang, E. Wang, A. Wu, Z. Li, *Mater. Lett*. **2002**, 54, 452–457.

[42] H. Sun, H. Li, W. Bu, M. Xu, L. Wu, *J. Phys. Chem. B* **2006**, 110, 24847–24854.

[43] S. Yin, H. Sun, Y. Yan, W. Li, L. Wu, *J. Phys. Chem. B* **2009**, 113, 2355–2364.

[44] J. Liu, F. Ortéga, P. Sthuraman, D. E. Katsoulis, C. E. Costello, M. T. Pope, *J. Chem. Soc. Dalton Trans*. **1992**, 1902–1906.

[45] X. Zhao, Y.-G. Li, Y.-H. Wang, E.-B. Wang, *Trans. Met. Chem*. **2008**, 33, 323–330.

[46] R. Chattherjee, M. Ali, M. G. B. Drew, M. Nethaji, S. Mondal, M. Mukherjee, *Trans. Met. Chem*. **2009**, 34, 1–5.

[47] A. Tezé, G. Hervé, R. G. Finke, D. K. Lyon, *Inorg. Synth*. **1990**, 27, 85–96.

[48] CrysAlis Pro; Oxford Diffraction Ltd.: Abingdon, U.K., **2007**.

[49] G. M. Sheldrick, *Acta Crystallogr*. **2008**, A64, 112–122.

[50] M. C. Favas, D. L. Kepert, Prog. *Inorg. Chem*. **1981**, 28, 309–367.

[51] (a) J. D. Corbett, *Struct. Bonding (Berlin)* **1997**, 87, 157–193. (b) T. F. Fässler, R. Hoffmann, *Angew. Chem., Int. Ed.* **1999**, 38, 543–546.

[52] (a) C. N. Kato, A. Shinohara, K. Hayshi, K. Nomiya, *Inorg. Chem.* **2006**, 45, 8108–8119. (b) C. Zhang, R. C. Howell, K. B. Scotland, F. D. Perez, L. Todaro, L. C. Francesconi, *Inorg. Chem.* **2004**, 43, 7691–7701. (c) J. lijima, E, Ishikawa, Y, Nakamura, H, Naruke, *Inorg. Chim. Acta*. **2010**, 363, 1500–1506. (d) N. Jing, L. Xu, F. Li, G. Gao, L. Fan, *Inorg. Chem. Commun.* **2008**, 11, 24–27.

[53] (a) I. D. Brown, D. Altermatt, *Acta Crystalllogr., Sect. B* **1985**, 41, 244–247. (b) A. Trzesowska, R. Kruszynski, T. Bartczak, *J. Acta Crystallogr., Sect. B* **2004**, 60, 174–178.

[54] (a) P. Mialane, A. Dolbecq, L. Lisnard, A. Mallard, J. Marrot, F. Sécheresse, *Angew. Chem., Int. Ed.* **2002**, 41, 2398–2401. (b) H. Y. An, E. B. Wang, D. R. Xiao, Y. G. Li, Z. M. Su, L. Xu, *Angew. Chem., Int. Ed.* **2006**, 45, 904–908. (c) D. Y. Du, J. S. Qin, S. L. Li, Y. Q. Lan, X. L. Wang, Z. M. Su, *Aust. J. Chem.* **2010**, 63, 1398–1395.

[55] K. Binnemans, C. Görller-Walrand, *Chem. Phys. Lett*. **1995**, 235, 163–174.

[56] L. Armelao, S. Quici, F. Barigelletti, G. Accorsi, G. Bottaro, M. Cavazzini, E. Tondello, *Coord. Chem. Rev*. **2010**, 254, 487–505.

[57] (a) J. Xia, B. Zhao, H.-S. Wang, W. Shi, Y. Ma, H.-B. Song, P. Cheng, D.-Z. Liao, S.-P. Yan, *Inorg. Chem*. **2007**, 46, 3450–3458.(b) D. T. de Lill, A. de Bettencourt-Dias, C. L. Cahill, *Inorg. Chem*. **2007**, 46, 3960–3965.

[58] Q. Xu, L. Li, X. Liu, R. Xu, *Chem. Mater*. **2002**, 14, 549–555.

[59] F. S. Richardson, *Chem. Rev*. **1982**, 82, 541–552.

[60] X. Wang, Y. Guo, Y. Li, E. Wang, C. Hu, N. Hu, *Inorg. Chem*. **2003**, 42, 4135–4140.

[61] (a) G. Blasse, G. J. Dirksen, *J. Inorg. Nucl. Chem.* **1981**, 43, 2847–2853. (b) T. Yamase, H, Naruke, Y. J. Sasaki, *J. Chem. Soc., Dalton Trans*. **1990**, 1687–1696. (c) R. Ballardini, E. Chiorboli, and V. Balzani, *Inorg. Chim. Acta*, **1984**, 95, 323–327.

[62] T. Yamase, T. Kobayashi, M. Sugeta, H. Naruke. *J. Phys. Chem. A* **1997**, 101, 5046–5053.

[63] (a) R. M. Supkowski, J. P. Bolender, W. D. Smith, L. E. L. Reynolds, W. DeW. Horrocks Jr., *Coord. Chem. Rev*. **1999**, 185–186, 307–319. (b) A. Beeby, S. Faulkner, D. Parker, J. A. Gareth Williams, *J. Chem. Soc. Perkin Trans*. **2001**, 2, 1268–1273.

[64] (a) C. Benelli, D. Gatteschi, *Chem. Rev*. **2002**, 102, 2369–2387; (b) R. L. Carlin, Magnetochemistry, Springer-Verlag: Berlin, **1986**.

[65] S. Dasgupta, R. K. Mukherjee, S. Mroczkowski, D. Ghosh, *J. Phys. C: Solid State Phys.***1988**, 21, 3339–3349.

[66] (a) X. D. Xi, G. Wang, B. F. Liu, S. Dong, *J. Electrochim. Acta*, **1995**, 40, 1025–1029. (b) L. Z. Liu, F. Y. Li, L. Xu, X. Z. Liu, G. G. Gao, *J. Solid State Chem.* **2010**, 183, 350–355.

Part II

Transition Metal-Substituted Polyoxometalates (TMSPs)

5. New Catalytic and Computational Perspectives for Polyoxometalate Design: Alcohol Oxidation with Zn/Sb Polyoxotungstates

5.1. Introduction

Transition metal-substituted Polyoxometalates (TMSPs) are an important class of heteropolyoxometalates, which have currently attracted growing attention on the interface between molecular design and nanomaterials science.[1-6] Their endless structural motifs give rise to widespread applications, and the development of POMs-based catalysts for some forefront topics, such as water splitting[7, 8] or key organic transformations[9-17] in sustainable energy research and green chemistry. Therefore, POMs are not only among the most flexible building blocks for materials development, but they also pose fundamental chemical challenges. Many TMSPs are exceptionally promising in the area of acid and oxidation catalysis due to their unique properties, such as variable oxidation states, activation of oxidants, strong Brønsted acidity, and tunable redox potential.[3] POM-mediated alcohol oxidation has attracted worldwide academic and industrial interest for decades. Within the class of TMSPs, the sandwich-type TMSPs are a large compound class of current research interest, e.g. as versatile catalysts for water oxidation or organic processes.[7, 8] Generally, their lacunary $[MW_{9-11}O_{33-39}]^{n-}$ (M = main group element) building blocks are a rich source for new materials.[7d] However, considerably less of them contain central transition metal heteroatoms (M = Fe, Co, Ni, Cu, Mn, Zn).[18] $\{ZnW_9O_{34}\}$-containing POMs, for example, have great potential for materials design. Their sandwich-type derivatives, e.g. sandwich-type $[WZnM_2(ZnW_9O_{34})_2]^{n-}$ (M = Zn, Mn, Ru, Pd, Pt, Rh) compounds,[13a-e] display outstanding catalytic activity in key organic transformations, such as "green" alcohol oxidation,[13d] oxidative aromatization[19a] or cyclization of acetylacetone.[19b]

However, even after many years of detailed topical investigations, POM chemists still need deeper insight to understand the complex reaction and interconversion pathways[20, 21] of POMs in order to fully tap their design options. This serious methodological gap between the outstanding application potential of the ever growing POM family *vs.* limited mechanistic knowledge calls for computational approaches towards POMs.[22-24]

Currently, the demanding combination of experimental and theoretical approaches to understand POM reactivity is being eagerly pursued.[25-27] Although alcohol oxidation with TMSPs-based catalysts is a representative and industrially important area, most of the catalytic mechanisms involved are derived solely from spectroscopic data and other analytical evidences [28] with no clear-cut crystallographic data for reactive intermediates at hand. A major issue resides in the difficulties associated with the isolation of crystalline POM intermediates and catalytically active species.[29] However, this would be indispensable for clarifying and controlling homogeneous catalytic mechanisms. Whereas ample spectroscopic data for intermediate peroxocomplexes of POMs have been collected over almost two decades, [30, 31] these species have never been crystallographically characterized, nor verified with high-level theoretical methods. In the process of addressing the open questions concerning the catalytic mechanism, a direct all-round strategy for POM catalyst development is offered and new Zn/Sb-POMs catalysts open up new reaction pathways beyond the established models for the catalytic cycle.[32]

(a) Synthetic control: First of all, a convenient and controlled method to access two new Zn/Sb-polyoxotungstate forms is discovered. Starting from two new polyoxotungstates, α-/β-$[Zn_2Sb_2(ZnW_9O_{34})_2]^{14-}$, as highly efficient catalysts for the selective oxidation of various alcohols with H_2O_2, ammonium cations are implemented as a straightforward structure directing additive to selectively access the different catalyst forms. Crystallographic studies reveal a variety of solid state motifs depending on the countercations employed. This amplifies the versatile trilacunary $[ZnW_9O_{34}]^{12-}$ moiety as an important building block for main group metal-containing sandwich POMs.[13a-e, 33]

(b) Catalytic cycles: The catalytic alcohol oxidation performance of both α-/β-$[Zn_2Sb^{III}_2(ZnW_9O_{34})_2]^{14-}$ isomers is compared. Most importantly, the first crystallographic evidence is obtained ever for POM reactive species involved in alcohol oxidation processes, i.e. the high-valent Sb(V) containing α-/β-$[Zn_2Sb^{V}_2(ZnW_9O_{34})_2]^{12-}$ compounds. A wide range of spectroscopic and analytical methods confirms their structure.

(c) Computational studies: Insights into isomerization behavior and catalytic activity of POMs are correlated with theoretical predictions. Additional perspective is gained in high-level modelling of larger functional POMs in solvent environments, and newly found Sb(V)-species are verified.[22a, 27a] As such, the theoretical elucidation of POM isomerization processes are extended from classical *Keggin*[34] or *Wells-Dawson* types[20] and gas phase methods,[35] towards larger functional POMs in aqueous media. The complementary experimental and theoretical approach results in innovative insights into the catalytic alcohol oxidation cycle, with strategies for catalyst design by steering the reaction pathways through chemical tuning of the POM metal belt.

5.2. Experimental

5.2.1. Synthetic methods

Synthesis of α-NH_4-[Zn_2Sb_2] (1a) 0.377 g (0.132 mmol) of $Na_9[B\text{-}\alpha\text{-}SbW_9O_{33}]\cdot 19.5H_2O$[36] was dissolved in 25 ml of water and heated to 85 ºC under stirring. After 20 min, 0.098 g (0.45 mmol) of $Zn(OAc)_2\cdot 2H_2O$ was added in individual portions. The solution underwent a color change to light yellow at pH values around 6.0 ~ 6.5. The mixture was left stirring for 90 min at 85 ºC, cooled to room temperature and filtered. Addition of 20~30 drops NH_4Cl solution (1.0 M) to the yellow filtrate, followed by slow evaporation of the solution afforded yellow needle shaped crystals after about 10 d. Yield: 0.061 g, 16.3 % based on W. TGA showed a weight loss of 7.2 % in the 30 - 110 ^{o}C temperature range, corresponding to the loss of coordinating and solvent water molecules (expected 7.6 %). FT-IR (cm^{-1}): 3406(vs), 1624(m), 1400(s), 918(vs), 858(vs), 738(s), 435(m). Raman (cm^{-1}): 946(vs), 882(s), 769(s), 699(m), 436(w), 353(w). Elemental analysis calcd. (found): W 58.61 (57.50); Zn 6.95 (6.57); Sb 4.31 (4.26); N 2.48 (2.40); H 1.57 (1.53).

Synthesis of β-Na-[Zn_2Sb_2] (2a) The synthetic method (method A) used for **2a** is similar to the one described above for the synthesis of α-NH_4-[Zn_2Sb_2] (**1a**) except for a reduced amount of ammonium countercations, i.e. 5~10 drops instead of 20~30 drops. Light yellow colored plate-like crystals were obtained after about two weeks. Yield: 0.036 g, 9.1 % based on W. TGA showed a weight loss of 13.8 % in the 30 - 140 ^{o}C range, corresponding to the loss of coordinating and solvent water molecules (expected 13.7 %). FT-IR (cm^{-1}): 3420(vs), 1623(m), 920(vs), 861(vs), 755(s), 432(m). Raman (cm^{-1}): 948(vs), 890(s), 852(s), 799(s), 699(m), 373(w). Elemental analysis calcd. (found): W

54.67 (54.80); Zn 4.32 (4.56); Sb 4.02 (4.03); Na 5.30 (5.46); H 1.53 (1.59). Method B: β-Na-[Zn_2Sb_2] (**2a**) also can be isolated in the absence of 1.0 M NH_4Cl solution with lower yield (2-3 %).

Isomerization reactions The spontaneous isomerization reaction of β-Na-[Zn_2Sb_2] (**2a**) (from method A) into α-NH_4-[Zn_2Sb_2] (**1a**) in aqueous solution is observed after 2~3 weeks through isolation of both isomers from aqueous solution. Moreover, β-Na-[Zn_2Sb_2] (**2a**) (from method B) partially isomerizes into yellow block-shaped crystals of $Na_{12}(H_3O)_2[Zn_2Sb_2(ZnW_9O_{34})_2]\cdot 62H_2O$ (**1b**) within about 3 weeks after β-Na-[Zn_2Sb_2] (**2a**) (from method B) was isolated from aqueous solution. Yield for α-Na-[Zn_2Sb_2] (**1b**): 0.019 g (4.5 % based on W). FT-IR (KBr pellet, cm^{-1}): 3410(vs), 1623(m), 920(vs), 857(vs), 738(s), 437(m). Raman (cm^{-1}): 944(vs), 872(s), 761(s), 693(m), 441(w), 352(w). Elemental analysis calcd. (found): W 52.25 (54.02); Zn 4.13 (4.57); Sb 3.84 (4.10); Na 4.35 (4.59); H 2.26 (2.11).

Transformation of β-Na-[Zn_2Sb_2] (2a) into β-NH_4-[Zn_2Sb_2] (2b) 0.013 g (2.14 μmol) of β-Na-[Zn_2Sb_2] (**2b**) was dissolved in 10 mL of water and heated to 85 ºC. Next, 1.5 mL NH_4Cl solution (1.0 M) was added drop-wise under vigorous stirring and the mixture was kept at 85 ºC for 30 min. The mixture was filtered and cooled down to room temperature. Slow evaporation of the solution afforded yellow single crystals of β-NH_4-[Zn_2Sb_2] (**2b**) suitable for X-ray crystallography. FT-IR (cm^{-1}): 3420(vs), 1623(m), 1400(s), 920(vs), 861(vs), 755(s), 432(m). Raman (cm^{-1}): 944(vs), 872(s), 761(s), 693(m), 441(w), 352(w). Elemental analysis calcd. (found): W 61.60 (57.80); Zn 4.87 (4.33); Sb 4.53 (4.18); N 3.65 (3.36); H 1.50 (1.28).

Isolation of α-[$Zn_2Sb^V_2(OH)_2$] (3) First, crystalline α-NH_4-[Zn_2Sb_2] (**1a**) was isolated from aqueous solution after about 10 d. Evaporation was continued until the solution level was reduced by 50 %. Next, 3 mL of 30 % H_2O_2 were introduced dropwise into a mixture of crystals and saturated solution. The mixture was left stirring for 30 min at 85 ºC and α-NH_4-[Zn_2Sb_2] (**1a**) crystals were re-dissolved in the aqueous solution through interaction with H_2O_2. The solution underwent a color change from light yellow to colorless at pH values around 5.1 ~ 5.5. Slow evaporation at room temperature after filtration afforded colorless crystalline α-[$Zn_2Sb^V_2(OH)_2$] (**3**) within two weeks. FT-IR (cm^{-1}): 3415(vs), 1618(vs), 1401(vs), 939(vs), 881(vs), 743(s), 439(m). Raman (cm^{-1}): 955(vs), 894(s), 870(s), 784(s), 727(m), 459(w), 408(w). Elemental analysis calcd. (found): W 58.29 (56.70); Zn 4.60 (4.77); Sb 4.28 (4.74); Na 1.61(1.83); N 1.97 (1.88); H 1.59 (1.36).

Isolation of *β*-[$Zn_2Sb^V_2(OH)_2$] (4) First, crystalline β-Na-[Zn_2Sb_2] (**2a**) was isolated from aqueous solution after about two weeks. Evaporation was continued until the solution level was reduced to ca. 33 %. Next, 3 mL of 30 % H_2O_2 were added dropwise to a mixture of crystals and saturated solution. The mixture was left stirring for 30 min at 85 ºC and β-Na-[Zn_2Sb_2] (**2a**) crystals were re-dissolved in the aqueous solution through interaction with H_2O_2. The solution underwent a color change from light yellow to colorless at pH values around 5.5 ~ 6.0. Slow evaporation at room temperature after filtration afforded colorless crystalline β-[$Zn_2Sb^V_2(OH)_2$] (**4**) within two weeks. FT-IR (cm^{-1}): 3415(vs), 1618(vs), 1465(m), 1402(m), 941(m), 886(s), 730(s), 622(s), 478(m). Raman (cm^{-1}): 956(vs), 900(s), 860(s), 827(s), 708(m), 474(w), 365(w). Elemental analysis calcd. (found): W 59.91 (58.00); Zn 4.73 (4.69); Sb 4.40 (4.29); Na 0.83 (0.63); N 2.53 (2.46); H 1.49 (1.33).

5.2.2. Catalytic alcohol oxidation

Catalyst, solvent, substrate, and 30 % aqueous H_2O_2 were successively placed into a 10 ml round-bottom flask, and the reaction mixture was stirred at 85 °C. Detailed reaction conditions are given in the caption of Table 5.2. All yields reported in the following are based on alcohol conversion. Reaction products were characterized and quantified with a gas chromatograph (Finnigan Trace GC Ultra) equipped with a flame ionization detector and fitted with a ZB-5MS Phenomenex column (30 m length, 0.25 mm internal diameter, 0.25 μm film thickness) using dodecane as internal reference. Products were furthermore identified by GC-MS (Finnigan Trace DSQ GC-MS systems). After the oxidation of cyclohexanol with ***α*-NH_4-[Zn_2Sb_2] (1a)** and ***β*-Na-[Zn_2Sb_2] (2a)** (conditions see Table 5.2) was completed, the catalyst was recycled by evaporation of the aqueous phase. FT-IR spectra of used ***α*-NH_4-[Zn_2Sb_2] (1a)** and ***β*-Na-Zn_2Sb_2 (2a)** correspond to those of the pristine catalysts, suggesting that the POM framework was preserved after the oxidation process. XPS data (Figure 5.21) show the conversion of Sb(III) to Sb(V) after the catalytic reaction. Table 5.3 shows the catalytic activity in the oxidation of cyclohexanol based on ***α*-NH$_4$-[Zn$_2$Sb$_2$] (1a)** and ***β*-Na-Zn$_2$Sb$_2$ (2a)** for different cycles.

5.2.3. X-ray crystallography

Data collections of all compounds were performed on an Oxford Xcalibur Ruby CCD single-crystal diffractometer (MoK$_\alpha$ radiation, λ= 0.71073 Å) at 183(2) K. Routine Lorentz and polarization corrections were applied, and an absorption correction was performed using the program *CrysAlis* (multi-scan).[37] The structural analysis was performed using the *Win-GX for Windows* software.[38] Direct methods were used to locate heavy metal atoms (SHELXS-97). The remaining atoms were located from successive Fourier maps (SHELXL-97).[39] The Na5 and Na8 atoms in **(2a)** are disordered and their site occupancies were fixed at 0.50. Three W atoms in **(2a)**, W6, W8 and W9, are each disordered over two positions with occupancies of 0.90 and 0.10, respectively. The same disorder for atoms W6, W8 and W9 atoms was observed in **(2b)**. Six tungsten atoms in **(4)**, i.e. W6, W8, W9, W10, W14 and W18, are disordered over two positions with occupancies of 0.90 and 0.10, respectively. Such tungsten disorder has been previously observed in related polyanions.[33b] Hydrogen atoms were not included in the refinements. Heavy metal atoms (Sb, Zn, W and Na) were refined anisotropically and oxygen atoms were refined isotropically. The lighter atoms in POMs are generally difficult to refine anisotropically due to the presence of manifold heavy metal atoms.[40] Crystal data and structure refinement details for all compounds are summarized in Table 10.3 - 10.4 (Annexes).

5.2.4. Computational methods (cooperation with Prof. Kim Baldridge)

The conformational analyses of the molecular systems described in this study, including structural and orbital arrangements as well as property calculations, were carried out using the GAMESS[41] and GAUSSIAN09[42] software packages. Structural computations of all compounds were performed using the BP86 density functional method[43,44] in combination with the Def2-TZVPP basis set.[45] Full geometry optimizations in water environment were performed and uniquely characterized via second derivative (Hessian) analysis to determine the number of imaginary frequencies (0=minima; 1=transition state), and effects of zero point energy. Effects of solvation were taken into account using the COSMO method,[46, 47] using a dielectric for water and solvent radii from Klamt.[48] Ionization potentials were determined via ΔSCF ($E_{neu}-E_{cat}$) method. Visualization and analysis of structural and property results were obtained using QMView[49] and WEBMO.

5.3. Results and discussion

5.3.1. Controlled access to new Zn/Sb-POMs

To the best of our knowledge, Zn/Sb-combinations have seldom been reported for the $[MW_{9-11}O_{33-39}]^{n-}$ lacunary POM family hitherto. In the following a newly discovered family of Zn/Sb-polytungstoantimonates α-/β-$[Zn_2Sb_2(ZnW_9O_{34})_2]^{14-}$ **(α-/β-$[Zn_2Sb^{III}_2]$)** is investigated as highly efficient catalysts for the selective oxidation of various alcohols with H_2O_2 (Figure 5.1). These new POMs bring forward innovative control options over the complex solution chemistry of POMs via combined experimental and theoretical approaches.

The isomeric zinc-containing polytungstoantimonate anions $[Zn_2Sb_2(B\text{-}\alpha\text{-}ZnW_9O_{34})_2]^{14-}$ and $[Zn_2Sb_2(B\text{-}\beta\text{-}ZnW_9O_{34})_2]^{14-}$ are selectively obtained from the trilacunary precursor $Na_9[B\text{-}\alpha\text{-}SbW_9O_{33}]\cdot 19.5H_2O$[36] in the presence of zinc acetate using initial NH_4^+ concentration as an efficient and straightforward control parameter (Figure 5.1a). Yellow rod-shaped crystals of (**α-NH_4-$[Zn_2Sb_2]$ (1a)**) were formed with excess NH_4Cl, whereas light yellow quadrilateral crystals of the β-isomer were obtained as the sodium salt (**β-Na-$[Zn_2Sb_2]$ (2a)**) at lower NH_4^+ concentrations (5~10 drops, 1.0 M NH_4Cl) or in the absence of NH_4^+ (Figure 5.1b). The compositions of **(1a)** and **(2a)** were determined as $(NH_4)_{10}[Zn(H_2O)_6]_2[Zn_2Sb_2(B\text{-}\alpha\text{-}ZnW_9O_{34})_2]\cdot 12H_2O$ and $Na_{14}[Zn_2Sb_2(B\text{-}\beta\text{-}ZnW_9O_{34})_2]\cdot 46H_2O$, respectively, from X-ray crystallography data in combination with elemental and thermogravimetric analyses (Table 10.3 in the Annexes and Figure 5.9). For both **(1a)** and **(2a)** (Figure 5.1b), the TM central belt that sandwiched between two $[B\text{-}\alpha/\beta\text{-}ZnW_9O_{34}]^{12-}$ trivacant *Keggin* subunits contains four coplanar Zn^{II} and Sb^{III} cations. Recently, a bismuth containing analogue $[Zn_2Bi_2(\beta\text{-}ZnW_9O_{34})_2]^{14-}$ has been

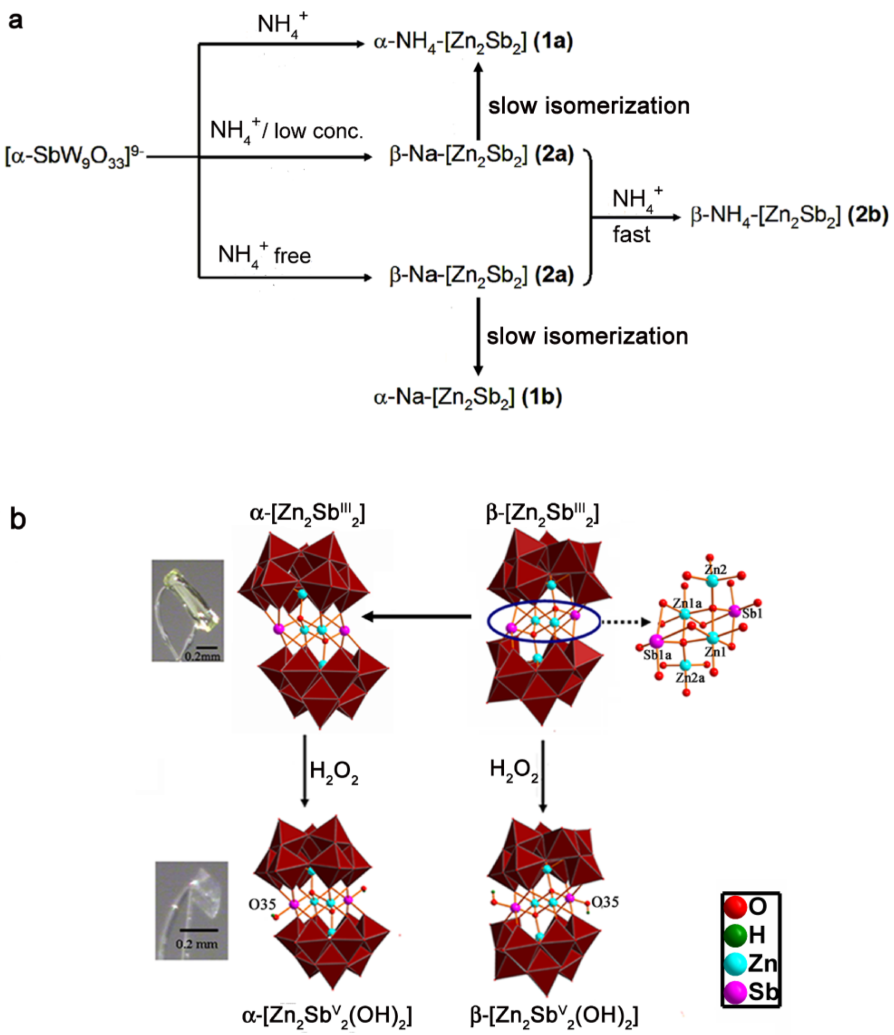

Figure 5.1. (a) Isomerization and NH_4^+ induced transformation scheme of the **[*α*-Zn_2Sb_2]** and **[*β*-Zn_2Sb_2]** polyanions, (b) Combined polyhedral/ball-and-stick representations of the $[\alpha/\beta\text{-}Zn_2Sb_2(ZnW_9O_{34})_2]^{14-}$ and their high-valent species $[\alpha/\beta\text{-}Zn_2Sb^{V}_2(OH)_2(ZnW_9O_{34})_2]^{12-}$ (symmetry codes: *a*, *-x*, *1-y*,*- z;* Zn = blue, O = red, Sb = pink, Zn/Sb = light purple, H = green; photographs: crystal color and morphology).

reported.[33b] **(1a)** and **(2a)**, however, are the first representative examples of sandwich-type POMs hosting a novel core $[Zn_2Sb_2(O)_{14}]^{18-}$. The Zn2 and Zn2a heteroatoms are located in the central position of each tri-lacunary $[ZnW_9O_{34}]^{12-}$ ligand (Figure 5.1b) and adopt a tetrahedral $Zn(\mu_4\text{-}O)_4$ coordination geometry (Zn-O distances: 1.934(14)-1.945(9) Å for **(1a)**; 1.929(8)-1.983(8) Å for **(2a)**). The $[Zn_2Sb_2(O)_{14}]^{18-}$ core consists of Zn1 and Zn1a atoms, two Sb atoms and six interconnecting oxygen atoms. These two zinc atoms exhibit a distorted Zn(μ_2-O)$_2$(μ_3-O)$_2$(μ_4-O)$_2$ octahedral environment with Zn-O distances: 2.072(10) - 2.134(9) Å for **(1a)**, 2.056(8) - 2.165(7) Å for **(2a)**. The Sb atoms display a distorted square-pyramidal coordination with planar Sb-O distances (2.073(10) - 2.380(10) Å for **(1a)**, 2.007(8) - 2.482(7) for (**2a)**) longer than axial Sb-O bonds (1.973(12) Å for **(1a)**, 1.9647(7) Å for **(2a)**). The bond valence sum (BVS)[50] values of zinc (2.04 and 2.15 for **(1a)**, 2.02 and 2.14 for **(2a)**), antimony (3.08 for **(1a)**, 3.04 for **(2a)**) and tungsten atoms (5.88 - 6.00 for **(1a)** and 5.82-6.03 for **(2a)**) are in line with their respective oxidation states of +2, +3 and +6 (Table 10.5 in the Annexes).

5.3.2. Isomerization and computational studies

The two novel isomers **(1a)** and **(2a)** display flexible isomerization and interconversion processes with ***β*-Na-[Zn$_2$Sb$_2$] (2a)** playing a central role (Figure 5.1a and Experimental). In NH_4^+/Na^+-containing solutions, spontaneous isomerization of the *β*-isomer **(2a)** into the *α*-form **(*α*-NH$_4$-[Zn$_2$Sb$_2$] (1a))** very slowly sets in. Likewise, ***β*-Na-[Zn$_2$Sb$_2$] (2a)** equilibrates with ***α*-Na-[Zn$_2$Sb$_2$] (1b)** in the absence of NH_4^+ ions. Furthermore, ***β*-Na-[Zn$_2$Sb$_2$] (2a)** can undergo a cation exchange into ***β*-NH$_4$-[Zn$_2$Sb$_2$] (2b)** upon addition of NH_4^+. The isomerization of **(2a)** into **(1a)** or **(1b)**, respectively, is thermodynamically favored. Initially, the *α*- or *β*-form can be selectively accessed by adjusting the initial NH_4^+ concentration.

Computational studies of polyanions **(1a)** and **(2a)** at the BP86/Def2-TZVPP level of theory agree well with the experimental observations (cf. bond length comparisons in Figure 10.1 and Table 10. 7 - 10. 8 in the Annexes). Calculated energetics of **(1a)** and **(2a)** show a relative energy difference of ~1.0 kcal/mol, with **(1a)** being the lower energy form. This energy difference is commensurate with what one would expect given the described experimental isomerization process. The fully optimized structural results were found to be in excellent agreement with the crystallographically determined values. Moreover, crystal structure details for **(1b)** and **(2b)** are also provided in Table 10.3 in the Annexe .

5.3.3. Isolation of high valent Sb(V)-species

Next, the reactivity of catalysts **(1a)** and **(2a)** with hydrogen peroxide was investigated. The Sb(V)-containing derivatives of **(1a)** and **(2a)**, $Na_4(NH_4)_8[Zn_2Sb^V_2(OH)_2(B\text{-}\alpha\text{-}ZnW_9O_{34})_2]\cdot 28H_2O$ **(3)** and $Na_2(NH_4)_{10}[Zn_2Sb_2(OH)_2(B\text{-}\beta\text{-}ZnW_9O_{34})_2]\cdot 20H_2O$ **(4)**, were obtained in single crystalline form through treatment with H_2O_2 at 85 °C (crystallographic details cf. Table 10.4 in the Annexes). Decolorization of the yellow solution indicates the oxidation of Sb(III) centers in **(1a)** and **(2a)** to Sb(V), probably through attack of H_2O_2. Whereas the basic POM frameworks of **(1a)** and **(2a)** remain unchanged, the coordination geometry of Sb in **α-[$Zn_2Sb^V_2(OH)_2$]** **(3)** and **β-[$Zn_2Sb^V_2(OH)_2$]** **(4)** is extended from five-coordinated square-pyramidal to six-coordinated octahedral (Figure 5.1b, Sb-O distances: 1.970(7)-2.063(7) Å for **(3)**, 1.944(9)-2.030(8) Å for **(4)**). BVS values for Sb1 (4.63), Zn1 (2.16), Zn2 (2.29), W (5.88-5.98) in **(3)** and 1.99, 2.23 (Zn1, Zn2), 4.95 (Sb1), as well as an average of 5.94 for W in **(4)** correspond to Zn(II), Sb(V) and W(VI) in both compounds. Furthermore, BVS values of 0.91 and 0.87 in **(3)** and **(4)**, respectively, clearly identify O35 as hydroxo ligand (Table 10. 6 in the Annexes).

5.3.4. Electrophilic attack at the Sb atom

The formation of high-valent hydroxo species **(3)** and **(4)** was furthermore verified with computational methods (Table 10. 9 - 10. 10 in the Annexes). The energetic preference for α-species **(3)** over the β-form **(4)** is larger than the respective difference between **(1a)** and **(2a)** (~10 kcal/mol) and the ionization potential for **α-[$Zn_2Sb^V_2(OH)_2$]** **(3)** is also predicted to be 0.6-0.7 eV higher than for **(1a)** and **(2a)**. Calculated electrophilic HOMO density plots for **(1a)** and **(2a)** show the highest probability for an electrophilic attack at the vicinity of the Sb(III) atoms, which are probable targets for two hydroxyl radicals arising from the homolytic cleavage of H_2O_2 that subsequently oxidize Sb(III) to Sb(V) to form the hydroxometal species **(3)** or **(4)** and hydroxyl ions (Figure 5.2 and equation 5.1).

$$\alpha/\beta\text{-}[Zn_2Sb^{III}_2(ZnW_9O_{34})_2]^{14-} + 2H^+ + 2H_2O_2 \rightarrow \alpha/\beta\text{-}[Zn_2Sb^V_2(OH)_2(ZnW_9O_{34})_2]^{12-} + 2H_2O \qquad \textbf{(5.1)}$$

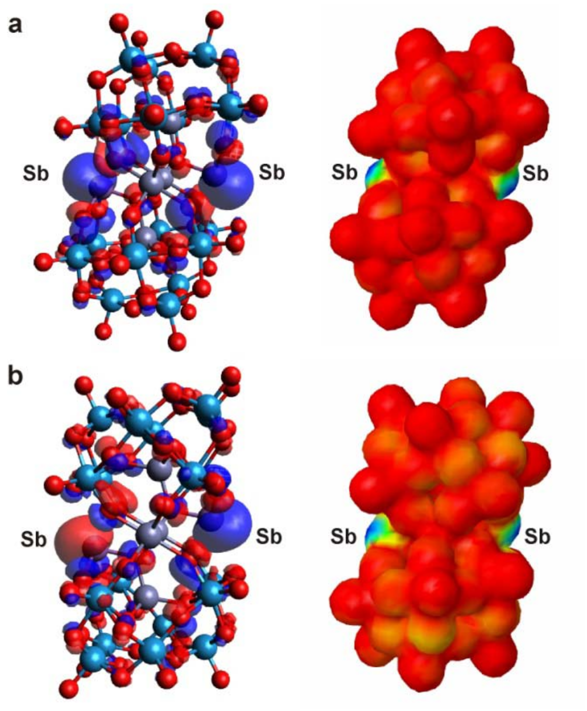

Figure 5.2. BP86/Def-TZVPP calculated HOMO (left, contour level 0.02) (a) for α-$[Zn_2Sb_2(ZnW_9O_{34})_2]^{14-}$ and (b) for β-$[Zn_2Sb_2(ZnW_9O_{34})_2]^{14-}$ together with electrophilic density plots (contour level 0.05; blue/red = highest/lowest probability of electrophilic attack).

5.3.5. Analytical characterizations

5.3.5.1. PXRD and TGA characterizations.

The PXRD patterns for {**(1a)**, **(1b)**, **(2a)**, **(2b)**, **(3)** and **(4)**} are presented in Figure 5.3 - 5.8. The diffraction peaks of both calculated patterns from single-crystal X-ray diffraction data and experimental patterns match very well. The phase purity of all compounds obtained in this study was confirmed with PXRD measurements. For all patterns, intensity differences may be due to preferred orientation of the powder samples.

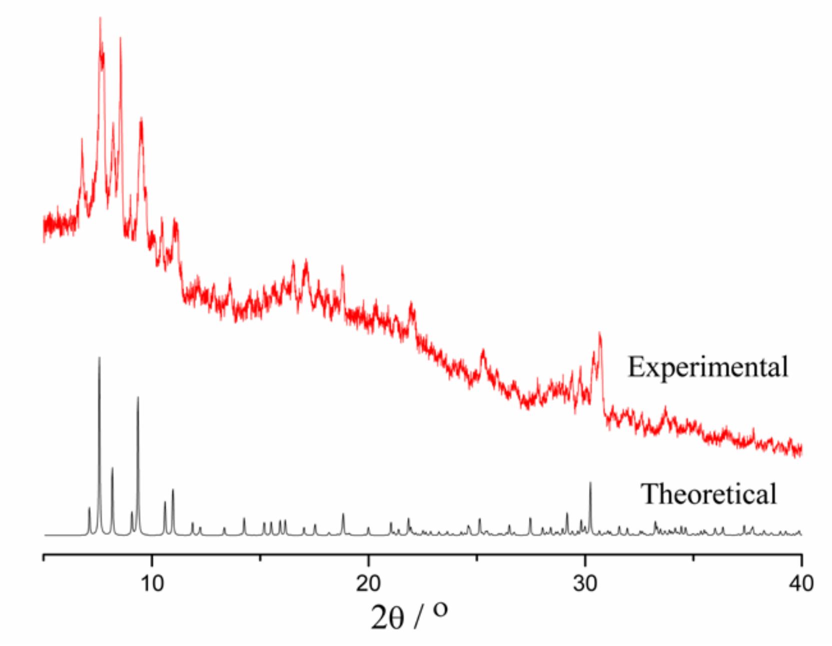

Figure 5.3. Powder X-ray diffraction pattern of bulk ***α*-NH$_4$-[Zn$_2$Sb$_2$] (1a)** *vs*. calculated pattern.

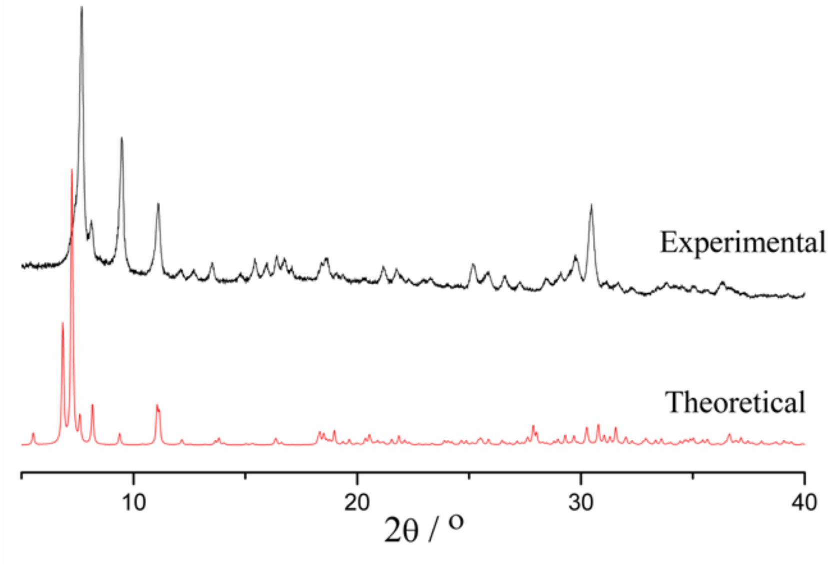

Figure 5.4. Powder X-ray diffraction pattern of bulk ***α*-Na-[Zn$_2$Sb$_2$] (1b)** *vs.* calculated pattern.

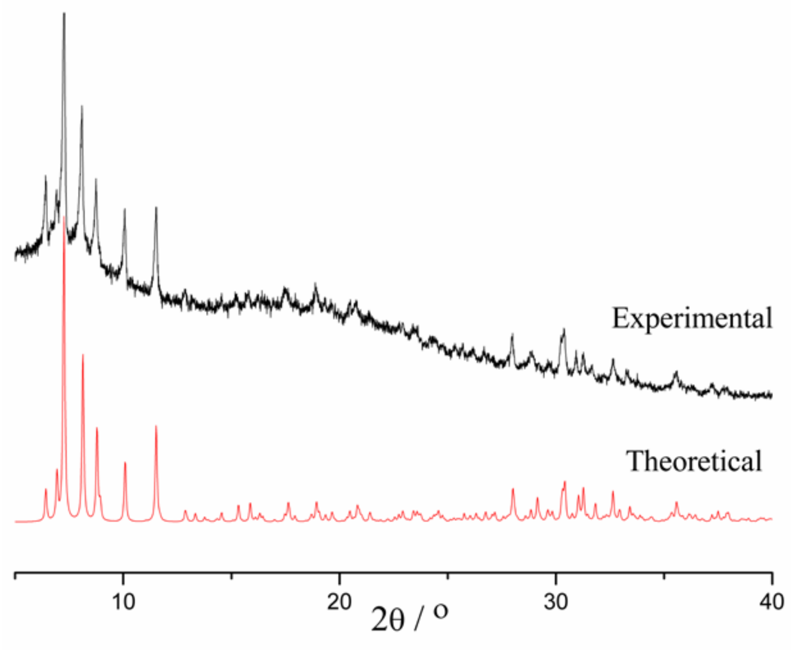

Figure 5.5. Powder X-ray diffraction pattern of bulk ***β*-Na-[Zn$_2$Sb$_2$] (2a)** *vs*. calculated pattern.

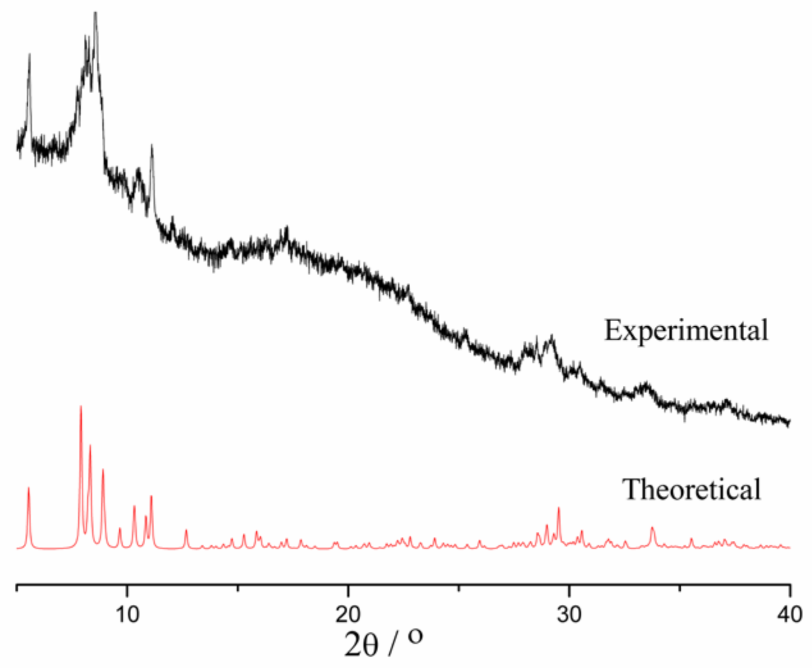

Figure 5.6. Powder X-ray diffraction pattern of bulk ***β*-NH$_4$-[Zn$_2$Sb$_2$] (2b)** *vs.* calculated pattern.

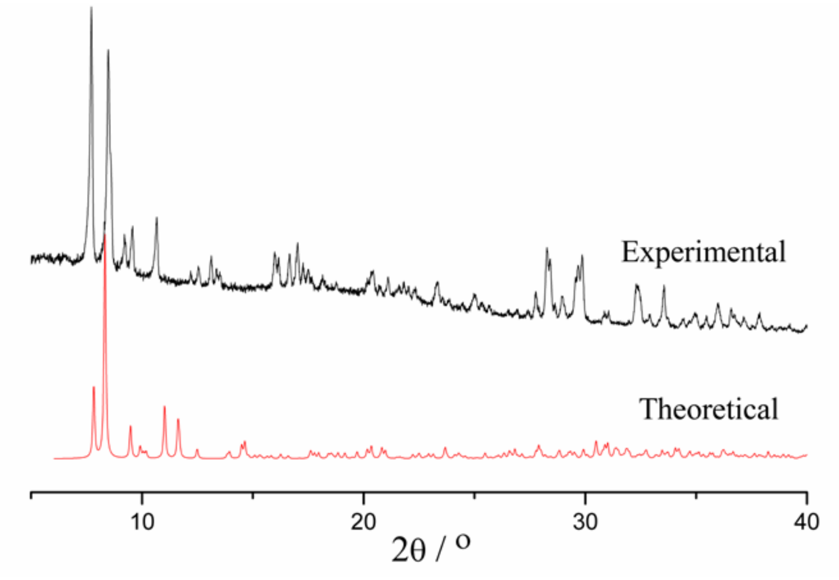

Figure 5.7. Powder X-ray diffraction pattern of bulk ***α*-[$Zn_2Sb^V{}_2(OH)_2$] (3)** vs. calculated pattern.

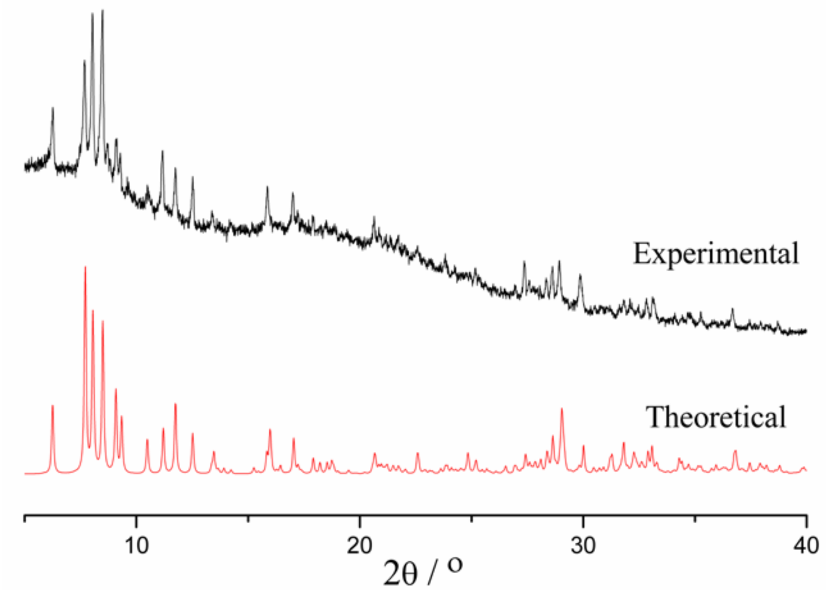

Figure 5.8. X-ray powder diffraction pattern of bulk ***β*-[$Zn_2Sb^V{}_2(OH)_2$] (4)** vs. calculated pattern.

Here two isomers ***α*-NH_4-[Zn_2Sb_2] (1a)** and ***β*-Na-[Zn_2Sb_2] (2a)** as representative examples are investigated by using TGA measurements under a nitrogen flow in the temperature range from 30 to 600 ^oC. The TGA curves of both compounds (Figure 5.9) display one weight loss step in the all temperature range, respectively. The observed weight losses 7.2 % (**1a**, calcd. 7.6 %) and 13.8 % (**2a**, calcd. 13.7 %) correspond to the release of crystal water molecules and adsorbed water molecules.

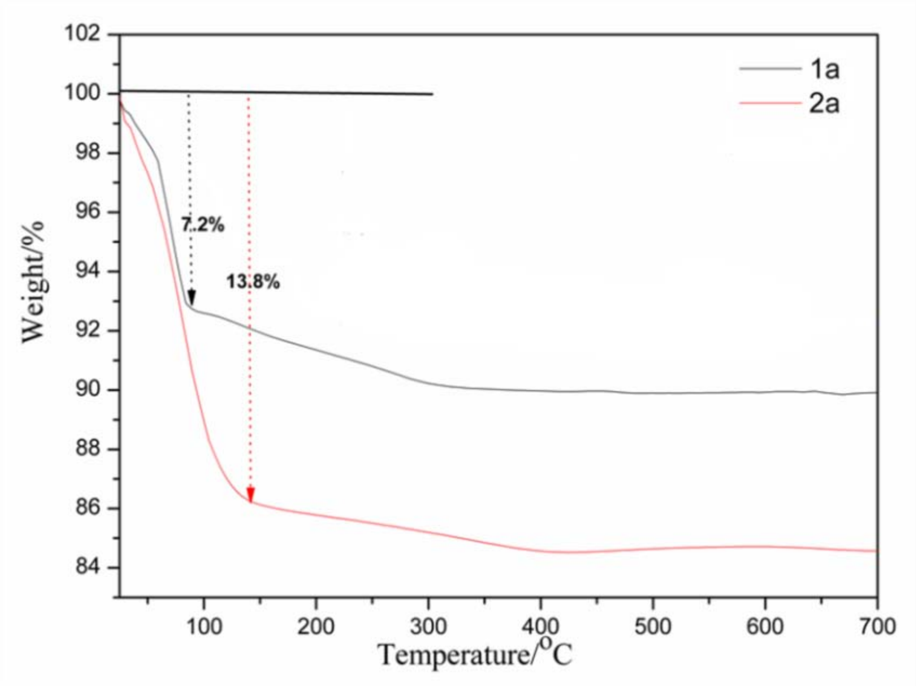

Figure 5.9. Thermogravimetric curves of ***α*-NH$_4$-[Zn$_2$Sb$_2$] (1a)** and ***β*-Na-[Zn$_2$Sb$_2$] (2a)**.

5.3.5.2. Electrochemical characterization

Cyclic voltammograms (CVs) of aqueous solutions of **(1a)** and **(2a)** are strongly pH-dependent (Figures 5.10 a-b). The redox signals become weaker and finally disappear with higher solution pH due to protonation effects.[51] The quasi-reversible peak (I-I’) between -0.5 and -1.0 V at pH 4.0 corresponds to the redox processes of the W(VI) centers. The irreversible oxidation peak (II’) around 0.27 V is assigned to the oxidation of metallic Sb(0) to oxygenic Sb^{3+}.[52] The CV curves of **(3)** and **(4)** are similar to **(1a)** and **(2a)**; however, cyclovoltammetric determination of the Sb(III)/Sb(V) redox couple is very difficult owing to the electro-inactivity of Sb(V), which hinders the electron transfer (Figure 5.10 c-d).[53]

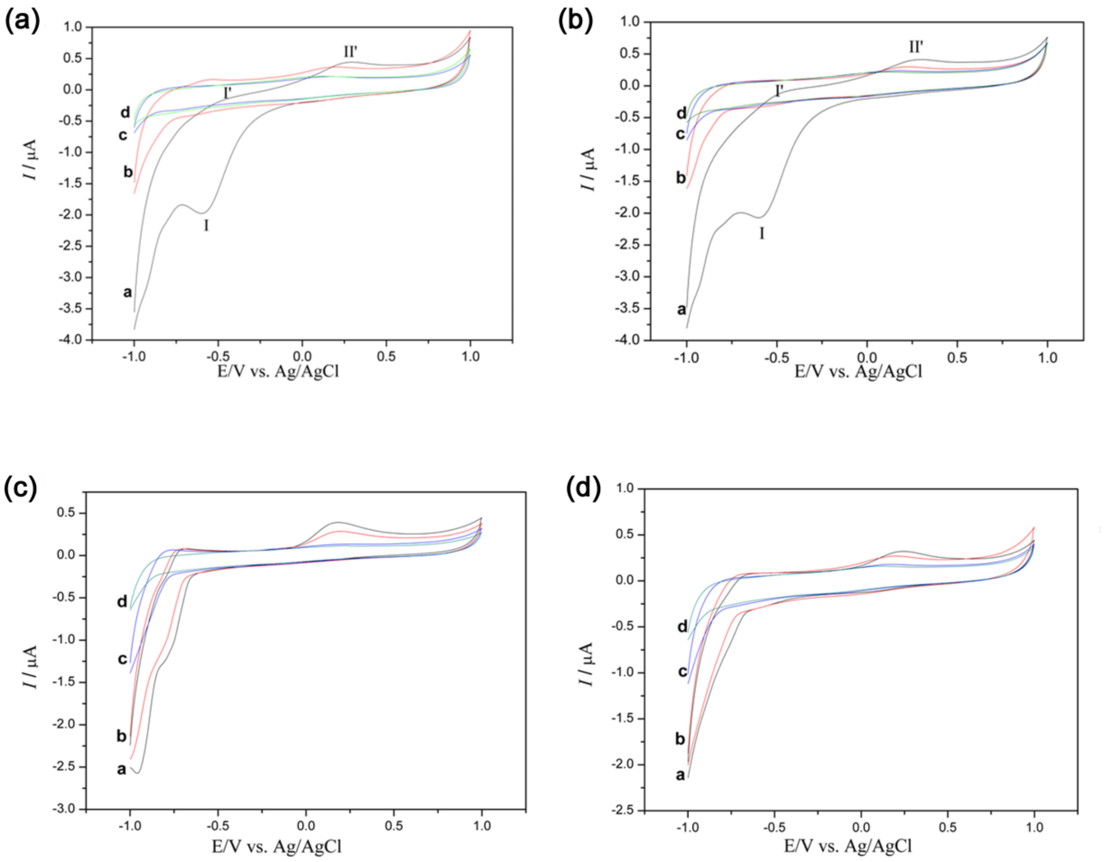

Figure 5.10. Cyclic voltammograms of 0.1 mM (a) **α-NH_4-[Zn_2Sb_2] (1a)**; (b) **β-Na-[Zn_2Sb_2] (2a)**, (c) **α-[$Zn_2Sb^V{}_2(OH)_2$] (3)**, (d) **β-[$Zn_2Sb^V{}_2(OH)_2$] (4)** in 0.5 M CH_3COONa/CH_3COOH) buffer solution (scan rate 25 mV/s, GCE working electrode, Ag/AgCl reference electrode); pH = 4.0, **a**; pH = 5.0, **b**; pH = 6.0, **c**; pH = 7.0, **d**.

5.3.5.3. FT-IR and Raman spectroscopy

FT-IR and Raman spectra of **(1a)** and **(2a)** in the solid state are closely related, and the characteristic peaks are assigned to W-O vibrations (Figures 5.11, 5.12, and detailed assignment in Table 5.1).

Moreover, POM stability in aqueous media can be confirmed by FT-IR spectroscopy. Solid state and solution FT-IR spectra for **(1a)** or **(3)** are practically identical (Figure 5.13), indicating the stability of the entire POM building-block in solution. Solid state and solution FT-IR spectra of the Sb(V) containing compound **(3)** agree well with the Sb(III) precursor **(1a)**, which also underlines the oxidative stability of the POM motif (Figure 5.13).

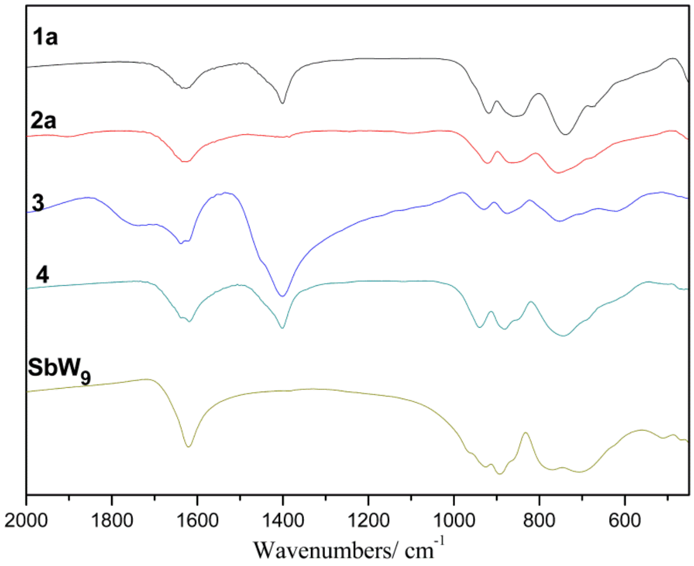

Figure 5.11. FT-IR spectra of the compounds ***α*-NH$_4$-[Zn$_2$Sb$_2$] (1a)**, ***β*-Na-[Zn$_2$Sb$_2$] (2a)**, ***α*-Zn$_2$Sb$^V{}_2$(OH)$_2$] (3)**, ***β*-[Zn$_2$Sb$^V{}_2$(OH)$_2$] (4)** and Na$_9$[*B*-*α*-SbW$_9$O$_{33}$]·19.5H$_2$O **{SbW$_9$}** precursor (KBr pellets).

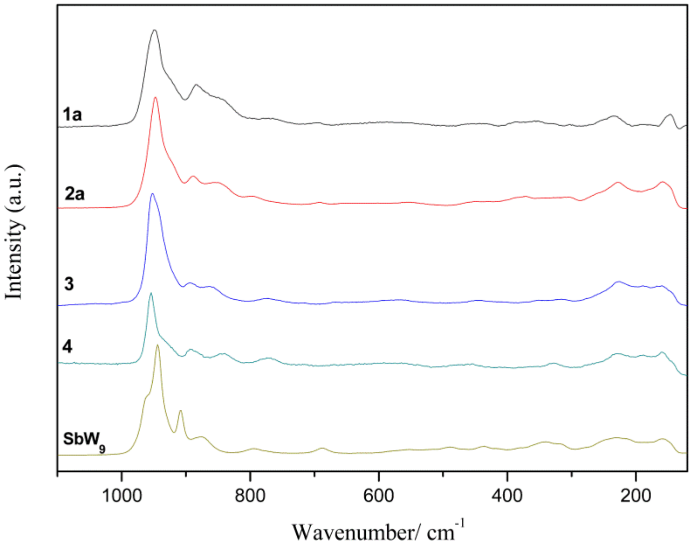

Figure 5.12. Raman spectra of the compounds ***α*-NH$_4$-[Zn$_2$Sb$_2$] (1a)**, ***β*-Na-[Zn$_2$Sb$_2$] (2a)**, ***α*-Zn$_2$Sb$^V{}_2$(OH)$_2$] (3)**, ***β*-[Zn$_2$Sb$^V{}_2$(OH)$_2$] (4)** and Na$_9$[*B*-*α*-SbW$_9$O$_{33}$]·19.5H$_2$O **{SbW$_9$}** precursor (KBr pellets).

Table 5.1. Vibrational features (IR and Raman) for **α-NH_4-[Zn_2Sb_2] (1a)**, **β-Na-[Zn_2Sb_2] (2a), α-[$Zn_2Sb^V{}_2(OH)_2$] (3)**, **β-[$Zn_2Sb^V{}_2(OH)_2$] (4)** and Na_9[*B*-α-SbW_9O_{33}]·19.5H_2O **{SbW_9}** precursor.

Label		**Band assignments**[a] **(cm^{-1})**					
		δ(HOH)	δ(NH_4)	ν(W=O_d)	ν_{as}(W-O_b)	ν_{as}(W-O_c)	δ(W-$O_{b,c}$-W)
{SbW_9}	IR	1617		959, 922	893	770, 710	
	Raman			961, 943	905, 873	795, 688	438, 338
(1a)	IR	1624	1400	918	858	738	
	Raman			946	882	769, 699	436, 353
(2a)	IR	1624		920	861	755	
	Raman			948	890, 852	799	373
(3)	IR	1617	1401	939	881	743	
	Raman			955	894, 870	784, 727	459, 408
(4)	IR	1618	1402	941	886	730	
	Raman			956	900, 860, 827	708	474, 365

[a]. W=O_d, terminal; W-O_b, corner-sharing; W-O_c, edge-sharing.

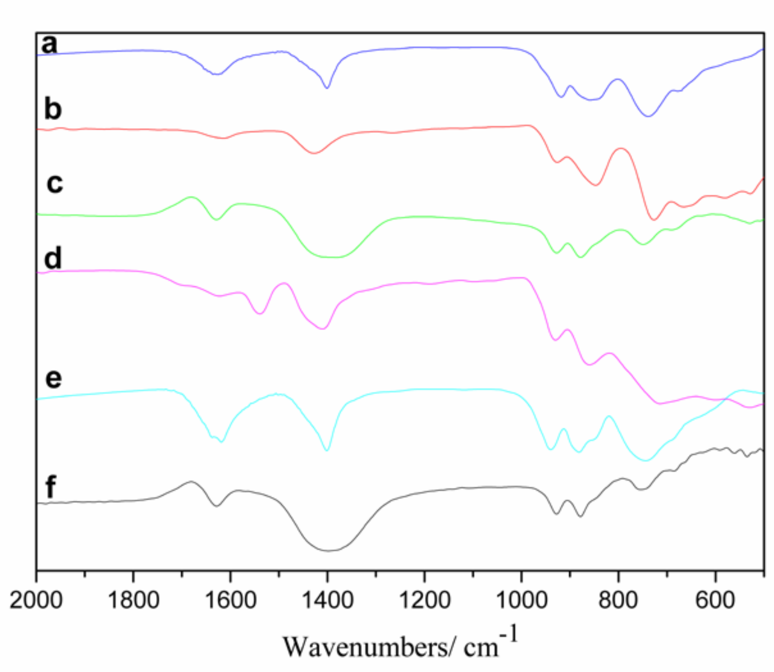

Figure 5.13. FT-IR spectra of (a) ***α*-NH$_4$-[Zn$_2$Sb$_2$] (1a)** in solid state; (b) ***α*-NH$_4$-[Zn$_2$Sb$_2$] (1a)** in aqueous solution; (c) ***α*-NH$_4$-[Zn$_2$Sb$_2$] (1a)** after treatment with 30% H_2O_2 **(d)** ***α*-NH$_4$-[Zn$_2$Sb$_2$] (1a)** after the oxidation of cyclohexanol; (e) ***α*-[Zn$_2$Sb$^V_2$(OH)$_2$] (3)** in solid state; (f) ***α*-[Zn$_2$Sb$^V_2$(OH)$_2$] (3)** in aqueous solution.

5.3.5.4. UV/Vis spectroscopy

UV/Vis diffuse reflectance spectra of **(1a)**, **(2a)** in the range between 190 and 600 nm (Figure. 5.14) display three absorption bands centered at 210 nm, 260 nm and 365 nm. Two absorption bands at higher energies arise from p_π-d_π charge-transfer transitions of the $O_{b(c)}$→W bonds,[54] whereas another low energy bands are likely due to O→Zn charge transfer or W-O-Sb intervalence band transfer in the visible region.[33a] Solid state UV/Vis spectra of compounds **(1a)** and **(2a)** show visible-light absorption (Figure 5.14) with band gap values of 2.78 (2.65) and 2.88 (2.71) eV, respectively, are in relatively good agreement with computationally predicted values shown in parentheses.

Meanwhile, the UV/Vis spectra of POMs **(3)** and **(4)** exhibit a considerable blue shift with respect to **(1a)** and **(2a)** in line with the observed color change (Figure 5.14).

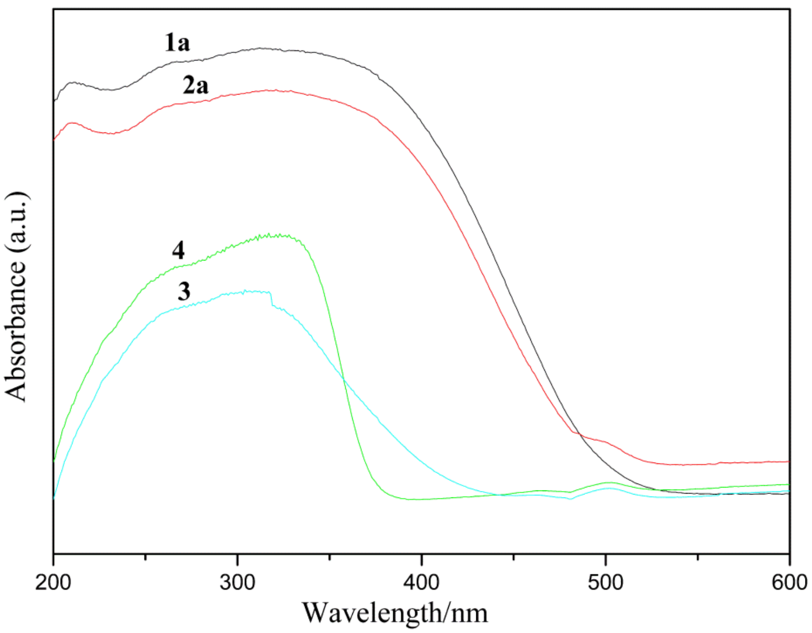

Figure 5.14. Solid state UV/Vis spectra of the compounds ***α*-NH$_4$-[Zn$_2$Sb$_2$] (1a)**, ***β*-Na-[Zn$_2$Sb$_2$] (2a)**, ***α*-[Zn$_2$Sb$^V{}_2$(OH)$_2$] (3)** and ***β*-[Zn$_2$Sb$^V{}_2$(OH)$_2$] (4)**.

5.3.5.5. Negative ion electrospray ionization mass spectra (ESI-MS)

The ESI-MS spectra of compounds **(1a)** and **(2a)** in a mixture of deionized water and acetonitrile (80:20) are very similar and show the presence of the intact $\{Zn_2Sb_2(ZnW_9O_{34})_2\}$ cluster with various amounts of associated cations and water molecules. Two main distributions of peaks arise from quadruply and quintuply charged species (Figures 5.15 and 5.16). However, ESI-MS investigations of compounds **(3)** and **(4)** show that three main distributions of peaks arise from quadruply, quintuply and sextuply charged species. All of the main peaks can be assigned to the expected $\{Zn_2Sb_2(OH)_2(ZnW_9O_{34})_2\}$ cluster polyanion with different cations and charges (Figures 5.17 and 5.18).

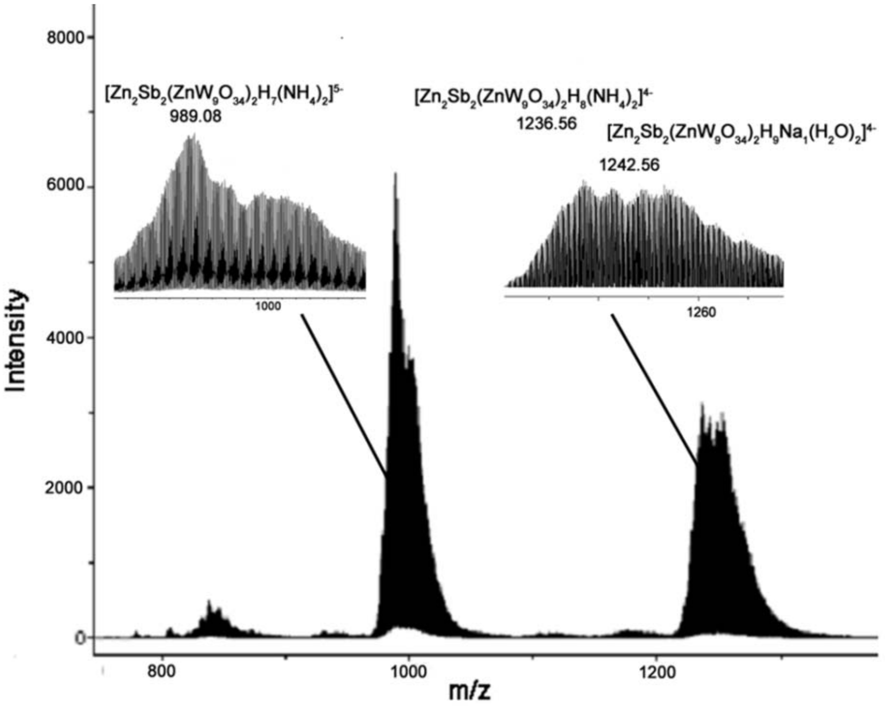

Figure 5.15. Negative ion electrospray ionization mass spectra (ESI-MS) of ***α*-NH$_4$-[Zn$_2$Sb$_2$] (1a)** in H_2O/MeCN (80:20) solution.

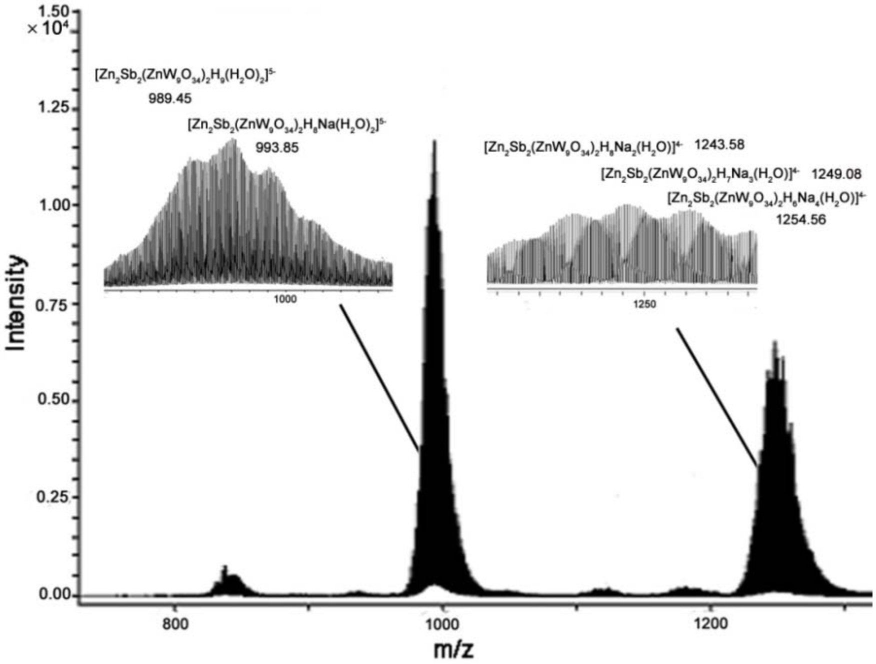

Figure 5.16. Negative ion electrospray ionization mass spectra (ESI-MS) of ***β*-Na-[Zn$_2$Sb$_2$] (2a)** in H_2O/MeCN (80:20) solution.

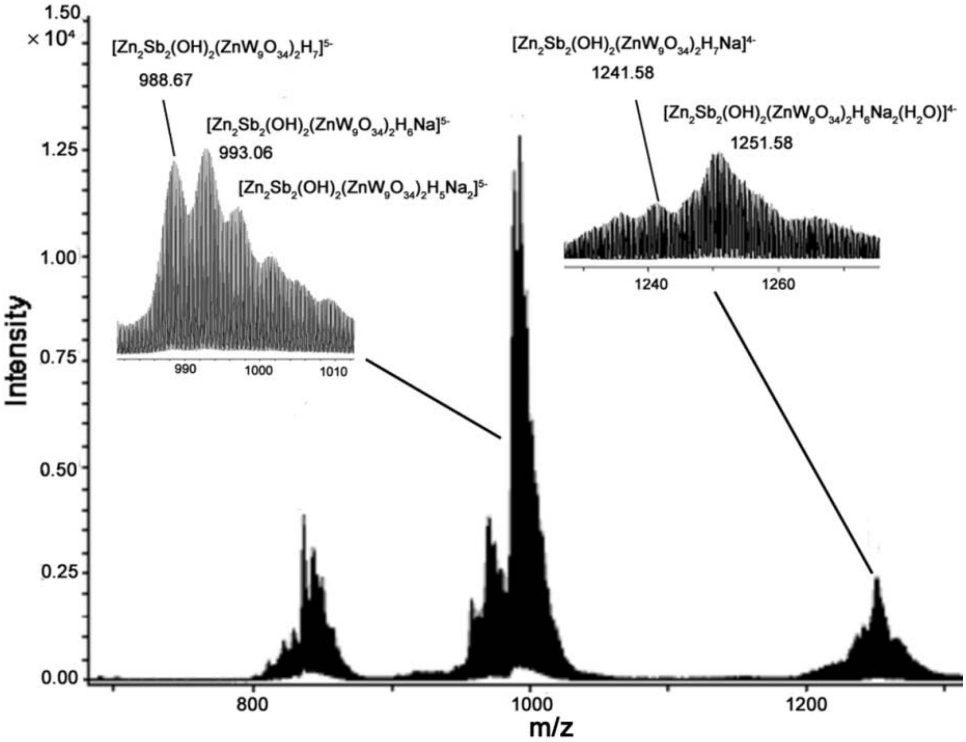

Figure 5.17. Negative ion electrospray ionization mass spectra (ESI-MS) of ***α*-[Zn$_2$Sb$^V_2$(OH)$_2$] (3)** in H_2O/MeCN (80:20) solution.

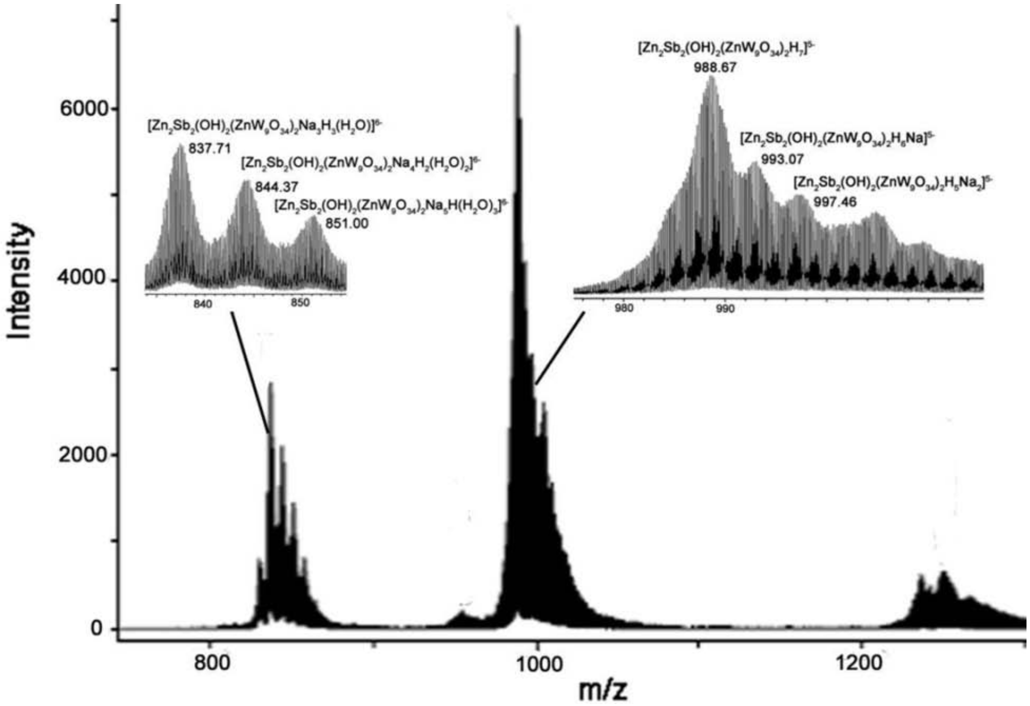

Figure 5.18. Negative ion electrospray ionization mass spectra (ESI-MS) of ***β*-[Zn$_2$Sb$^V_2$(OH)$_2$] (4)** in H_2O/MeCN (80:20) solution.

5.3.5.6. X-ray photoelectron spectroscopy (XPS) and ^{121}Sb NMR characterizations

X-ray photoelectron spectroscopy (XPS) was employed to confirm the Sb(V) valence state for the Sb $3d_{3/2}$ peak in **(3)** and **(4)**, as the Sb $3d_{5/2}$ peak could not be used due to overlapping with the O1s peak in Sb/O containing compounds (Figure 5.19a). In addition, Sb 4d is almost entirely masked by the W 4f line of much higher intensity, and is therefore not available for analysis. The peak at 540.5 eV is assigned to the $3d_{3/2}$ state of Sb(V) in **(3)**, while the peak at 539.7 eV is corresponding to the $3d_{3/2}$ state of Sb(III) in **(1a)**.[55] The slight shift for binding energy of the Sb $3d_{3/2}$ is due to the different binding sites of the Sb(III) and Sb(V) cations in **(3)** and **(1a)** (Figure 5.19a). The Zn 2p spectra exhibit one doublet with bonding energies of 1021.2 and 1044.5 eV corresponding to Zn $2p_{3/2}$ and Zn $2p_{1/2}$ (Figure 5.19b), and no changes of the Zn 2p peaks with respect to reference data were observed in **(3)** and **(1a)**.

As shown in Figure 5.20, ^{121}Sb NMR spectra furthermore support the existence of α-$[Zn_2Sb^V_2(OH)_2(ZnW_9O_{34})_2]^{12-}$ polyanion in solution. A solution of **(3)** in CH_3CN displays a strong, broad resonance at 220 ppm (relative to SbF_6^-, $W_{1/2}$ = 3600 Hz, Figure 5.20). However, no such signal was detected for Sb(III) containing ***α*-NH$_4$-[Zn$_2$Sb$_2$] (1a)**, consistent with previous reports.[56]

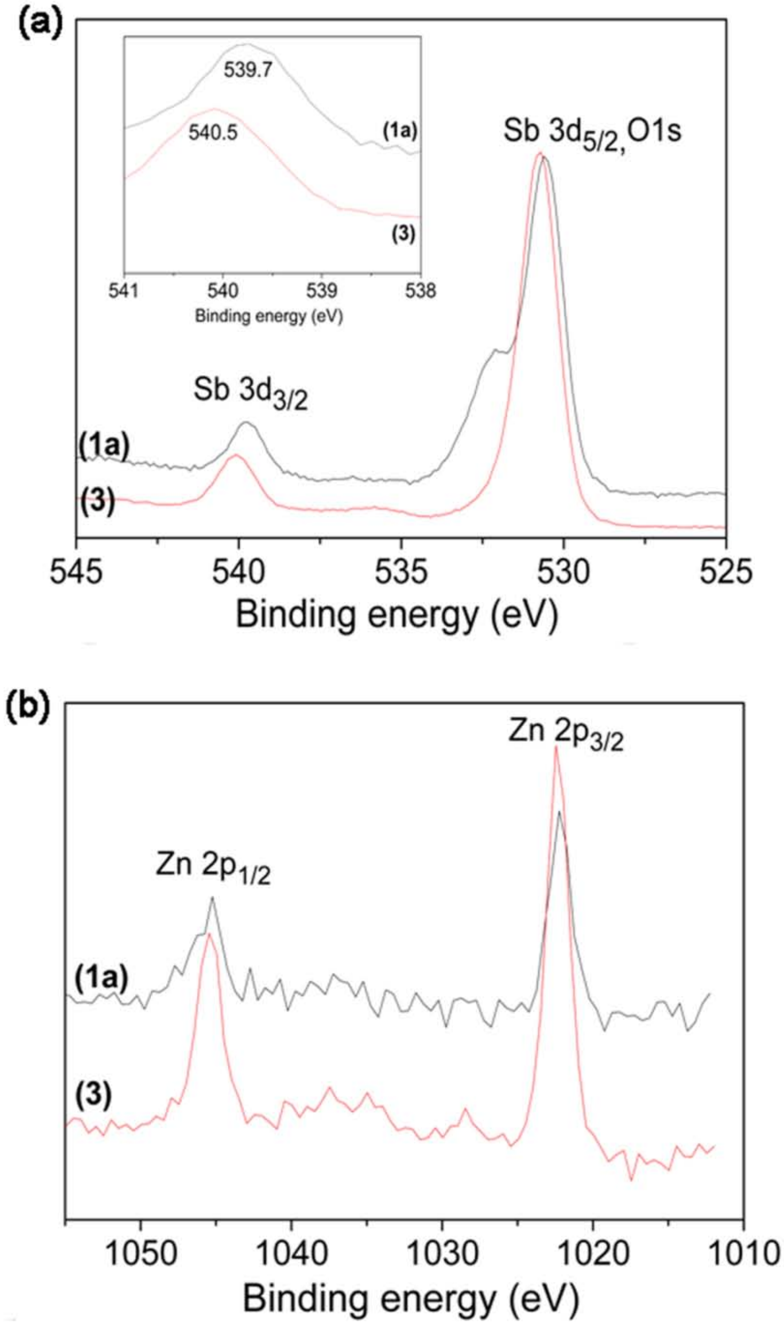

Figure 5.19. XPS spectra of **α-NH$_4$-[Zn$_2$Sb$_2$] (1a)** and **α-[Zn$_2$Sb$^{V}_2$(OH)$_2$] (3)**: (a) Sb 3d levels (inset: Sb 3d$_{3/2}$ peak), (b) Zn 2p levels,

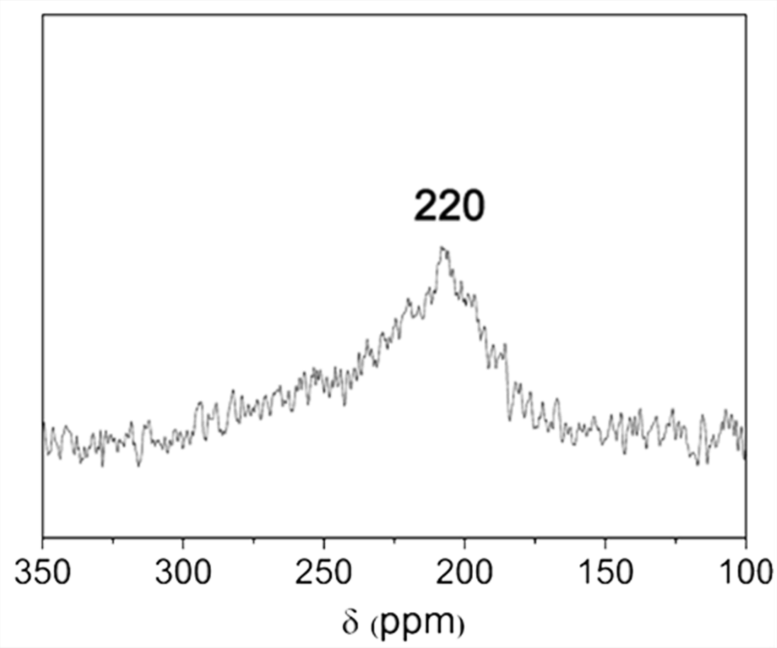

Figure 5.20. ^{121}Sb NMR spectrum of ***α*-[Zn$_2$Sb$^V_2$(OH)$_2$] (3)** in CH$_3$CN recorded at 119.721 MHz.

5.3.6. Catalytic performance

Next, activity of the isomers ***α*-NH$_4$-[Zn$_2$Sb$_2$] (1a)** and ***β*-Na-[Zn$_2$Sb$_2$] (2a)** for alcohol oxidation catalysis with H_2O_2 was investigated. They both exhibit promising catalytic activities for the oxidation of various alcohol types to the corresponding ketones or aldehydes in Table 5.2[57] Liquid cyclic alcohols (cyclopentanol, cyclohexanol and cyclooctanol) are easily converted into the corresponding cyclic ketones in high yields. However, solid cyclic alcohols, such as 2-adamantanol, are less active due to insufficient homogeneous interaction.[31b] Dissolution of 2-adamantanol in 1,2-dichloroethane partially affords the corresponding ketone 2-adamantanone, which could be further oxidized to 4-oxahomodamatan-5-one through Baeyer-Villiger oxidation due to ring strain effects. Secondary benzylic alcohol (1-phenylethanol) and propargylic alcohol (1-phenyl-2-propyn-1-ol) were also efficiently oxidized. 2-ethyl-1,3-hexanediol as a representative linear secondary aliphatic alcohol was completely oxidized to yield the 3-keto alcohol (2-ethyl-3-oxo-1-hexanol), whereas the efficient oxidation of 2-hexanol to the corresponding 2-hexanone turned out more difficult. Moreover, we observed no reactivity in the oxidation of primary alcohols. Only benzyl alcohol as an aromatic

All in all, results for catalysts **(1a)** and **(2a)** give the following order of relative activity in alcohol oxidation: benzylic > propargylic, cyclic, acyclic 1,3-diols > allylic, primary aromatic > secondary acyclic >> primary acyclic. Reference experiments in the absence of catalyst under identical conditions (Table 5.2) also confirm the high efficiency of catalysts **(1a)** and **(2a)**. Their overall alcohol oxidation performance ranks equal with industrially attractive and recently discovered polyoxometalate catalysts, such as $Na_{12}[WZnZn_2(H_2O)_2(ZnW_9O_{34})_2]$[13a] or $TBA_8[\{Zn(OH)_2(\mu_3\text{-}OH)\}_2\{\gamma\text{-}HSiW_{10}O_{36}\}_2]\cdot 9H_2O$.[16]

Table 5.2. Oxidation of various alcohols with α-NH_4-$[Zn_2Sb_2]$ **(1a)** and β-Na-$[Zn_2Sb_2]$ **(2a)**.[a]

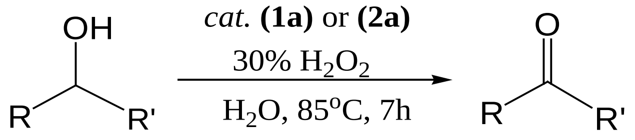

Substrate	Alcohol conv.(mol %)[b]			Product selectivity (mol %)[b]		
	(1a)	**(2a)**	No catalyst		**(1a)**	**(2a)**
cyclopentanol	98	99	0	cyclopentanone	100	100
cyclohexanol	>99	>99	6	cyclohexanone	100	100
cyclooctanol	90	92	5	cyclooctanone	100	100
2-adamantanol[d]	54	75	21	2-adamantanone	80	50
benzyl alcohol	83	82	0	benzaldehyde	60	60
1-phenylethanol[c]	>99	96	14	acetophenone	100	100
1-phenyl-2-propyn-1-ol[c]	88	92	7	1-phenyl-2-propyn-1-one	100	100
2-ethyl-1,3-hexanediol	>99	>99	0	2-ethyl-3-oxo-1-hexanol	100	100
2-hexanol	23	36	0	2-hexanone	100	100
1-hexen-3-ol	85	90	0	1-hexen-3-one	100	100

[a] Reaction conditions: 0.25 mmol substrate, 1.25 mmol (30 %) H_2O_2, 1.0 μmol catalyst, 0.50 mL H_2O, 85 °C, 7 h. [b] Organic products were identified and quantified by GC-MS and GC with calibrations using pure corresponding standards and dodecane as an internal standard. [c] 1-phenylethanol and 1-phenyl-2-propyn-1-ol: 2 molar excess was sufficient. [d] 0.5 mL 1,2-dichloroethane added instead of H_2O. Product distributions were not significantly affected by carrying out the reactions in N_2 atmosphere.

5.3.7. Catalyst recycling

Biphasic homogeneous catalysis processes are generally very advantageous for practical and industrial applications due to facile catalyst removal and recycling. After the alcohol oxidation was thoroughly completed, the newly synthesized POMs catalysts *α/β*-[Zn_2Sb_2] **(1a/2a)** can simply be recycled via the aqueous phase by phase separation. These catalysts retrieved from initial fresh catalysts **(1a)** and **(2a)** still maintain their high catalytic activity over five cycles as shown by the respective cyclohexanone yields of 98 % and 94 % (Table 5.3).

Table 5.3. Oxidation of cyclohexanol for different cycles starting from ***α*-NH_4-[Zn_2Sb_2] (1a)** and ***β*-Na-[Zn_2Sb_2] (2a)** before cycle 1.[a]

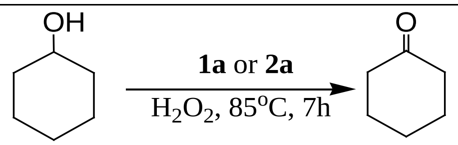

Cycle	Product (Yield / %)	
	1a[a]	**2a**[a]
1	cyclohexanone (98)	cyclohexanone (99)
2	cyclohexanone (98)	cyclohexanone (99)
3	cyclohexanone (97)	cyclohexanone (96)
4	cyclohexanone (98)	cyclohexanone (91)
5	cyclohexanone (98)	cyclohexanone (94)

[a] Reaction conditions: 0.25 mmol of substrate, 1.25 mmol (30 %) of H_2O_2, 1.0 μmol of catalyst **(1a)** and **(2a)**, 0.50 mL of H_2O, 85 ^oC, 7 h. Yield (%) were determined by GC analyses by using pure corresponding samples as calibration standards and dodecane as an internal standard.

Moreover, the recovered catalyst after use of ***α*-NH_4-[Zn_2Sb_2] (1a)** or ***α*-[$Zn_2Sb^V_2(OH)_2$] (3)** has a white color after one catalytic cycle, which is line with the color of the Sb(V)-containing derivative **(3)**. However, it is difficult to distinguish the presence of **(1a)** or **(3)** in the white-colored recycled catalyst with FT-IR methods due to closely related spectra of both compounds (Figure 5.13).

Therefore, XPS methods were used to confirm the valence state of Sb atom in the recycled catalysts. Comparison of the Sb $3d_{3/2}$ XPS regions for recycled samples of **(1a)** and **(3)** which were regenerated after alcohol oxidation (Figure 5.21 a) demonstrates identical oxidation states for both compounds. Furthermore, both recycled **(1a)** and **(3)** contain high valent Sb(V) owing to the characteristic peak positions for the $3d_{3/2}$ state of Sb(V) at 540.5 eV and 540.2 eV, respectively (Figure 5.21 a).[55] This finding is further corroborated by comparing the valence band spectra (Figure 5.21 b), which show the onset of the density of states at about 1.7 eV for Sb^{III} (reference: Sb_2O_3), while that of Sb^{V} (recycled catalysts and reference $KSb(OH)_6$) lies at about 3.1 - 3.4 eV.

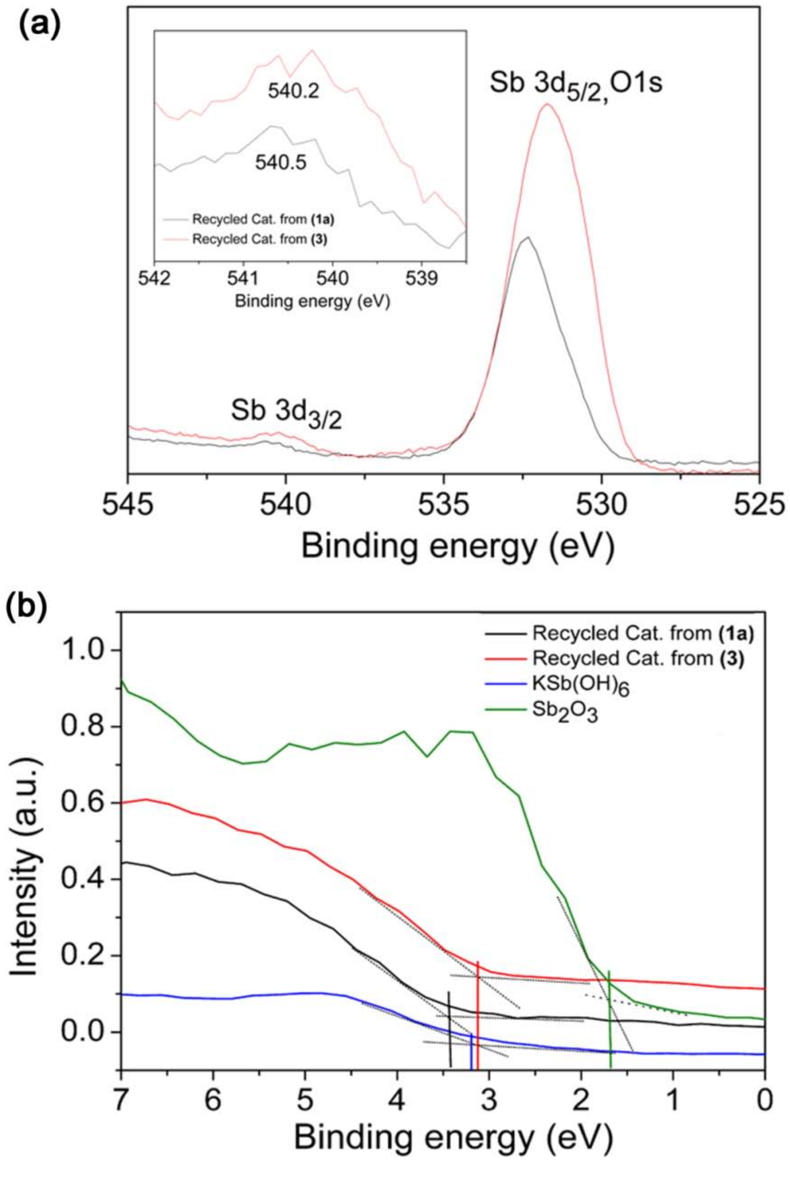

Figure 5.21. XPS spectra of the catalysts recycled from initial fresh **(1a)** and **(3)**: (a) Sb 3d levels (inset: Sb $3d_{3/2}$ peak), (b) valence band region together with $KSb(OH)_6$ and Sb_2O_3 references.

5.3.8. Kinetic studies and stoichiometric reactions

In order to gain further insight into the catalytic mechanism, kinetic studies for cyclohexanol oxidation with hydrogen peroxide catalyzed by compounds **(1a)**, **(2a)** and **(3)** were performed (Figure 5.22). Both **(1a)** and **(2a)** displayed sigmoidal curves, whereas an exponential curve was obtained for **(3)** (Figure 5.22 a). While an induction period of approximately 60 min precedes the oxidation of cyclohexanol for the isomeric catalysts **(1a)** and **(2a)**, **(3)** shows a clean first order reaction over a wider range time of 200 min without any induction period (Figure 5.22 b). This indicates a transformation of pre-catalysts **(1a)** or **(2a)** with H_2O_2 to form the catalytically reactive species **(3)** or **(4)**, consistent with the above-mentioned crystal structures of **(3)** and **(4)**, which were isolated from the reaction of **(1a)** and **(2a)** with H_2O_2.

Next, stoichiometric oxidation reactions with **(3)** were investigated (Figure 5.23). Under stoichiometric conditions (Figure 5.23, series (1): [cyclohexanol]/[**(3)**]= 2:1), no significant initial oxidation of cyclohexanol was observed with $\boldsymbol{\alpha}$-$\mathbf{[Zn_2Sb^{V}_2(OH)_2]}$ **(3)** (cyclohexanone yield, about 3 %), showing that **(3)** is inactive in absence of hydrogen peroxide. However, treatment of species **(3)** with hydrogen peroxide dramatically enhances the catalytic efficiency. The cyclohexanone yield can be improved from around 9 % to 93 % with increasing amounts of hydrogen peroxide from 0.25 to 10 equiv. relative to cyclohexanol (Figure 5.23). Furthermore, it is obvious that this oxidation reaction process is independent of the H_2O_2 concentration in the absence of **(3)** or **(4)** (Figure 5.23, series (2)).

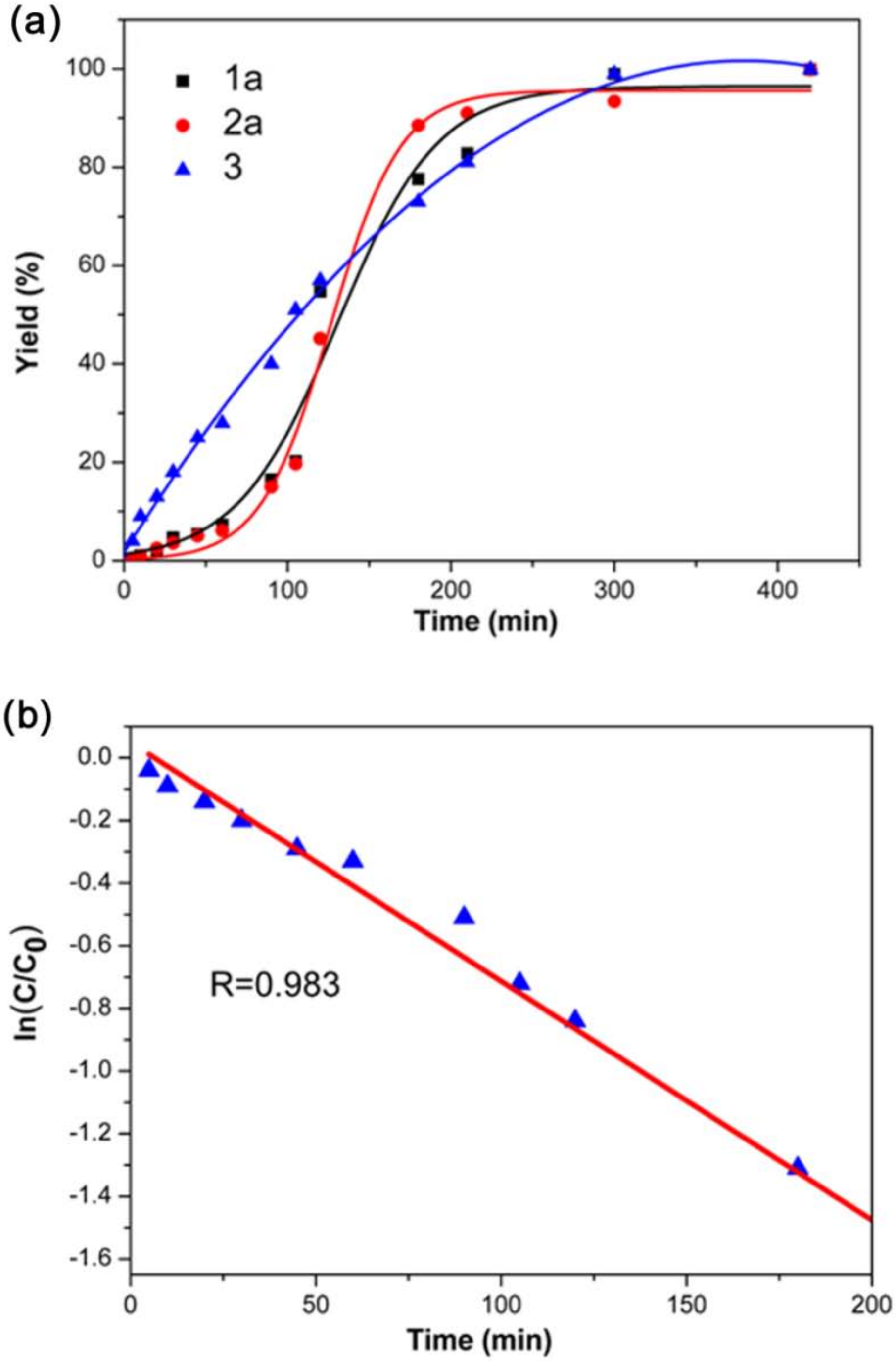

Figure 5.22. (a) Kinetic profiles for the oxidation of cyclohexanol catalyzed by **α-NH$_4$-[Zn$_2$Sb$^{III}_2$] (1a), β-Na-[Zn$_2$Sb$^{III}_2$] (2a)** and **α-[Zn$_2$Sb$^{V}_2$(OH)$_2$] (3)**, (b) Kinetic profile for **α-[Zn$_2$Sb$^{V}_2$(OH)$_2$] (3)** of the first 200 min as a first order plot. (reaction conditions: 1.0 μmol catalyst: 0.25 mmol alcohol, 1.25 mmol H_2O_2 (30 %), T = 85 °C, yield (%) = [cyclohexanone] / initial [cyclohexanol] × 100%, C_0 = initial [cyclohexanol], C = initial [cyclohexanol]-[cyclohexanone]).

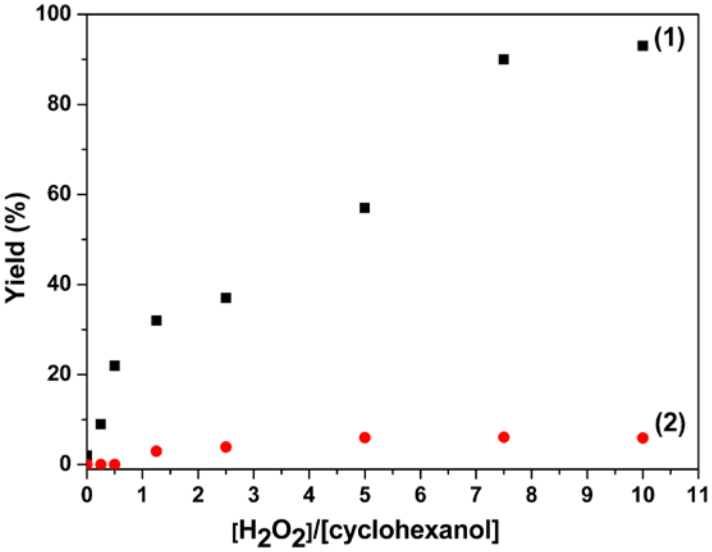

Figure 5.23. Dependence of the stoichiometric oxidation of cyclohexanol on the [H_2O_2] / [cyclohexanol] ratio. Conditions: (1) 0.125 mmol cyclohexanol, 0.0625 mmol **α-[$Zn_2Sb^V{}_2(OH)_2$] (3)**, (0-1.25 mmol) H_2O_2, 1 mL H_2O, 85 °C, 7 h; (2) 0.125 mmol cyclohexanol, (0-1.25 mmol) H_2O_2, 1 mL H_2O, 85 °C, 7 h.

5.3.9. Catalytic mechanism

Based on these results, a new catalytic mechanism for alcohol oxidation with hydrogen peroxide initially catalyzed by **(1a)** or **(2a)** (Scheme 5.1) is proposed. First, **(1a)** or **(2a)** reacts with hydrogen peroxide to form the high-valent Sb(V)-containing derivatives **(3)** or **(4)**, and the induction period observed in the catalytic oxidation points to an irreversible step. Next, **(3)** or **(4)**, respectively, are involved in the catalytic cycle as active catalyst and react further with hydrogen peroxide to probably form some reactive intermediate. Finally, the Sb(V) catalyst **(3)** or **(4)** can be recycled for new runs, again leading to the corresponding alcohol oxidation products.

The conversion of the Sb(III)-POM **(1a)** into a Sb(V) species **(3)** after catalysis and the persistence of Sb(V) in recycled catalysts (Figure 5.21) provide further strong evidence that the catalytic cycle is initiated and maintained by high valent Sb(V) compounds **(3)** or **(4)**. Despite intense efforts, we have not been able to further monitor and directly isolate any competent intermediate from **(3)** or **(4)** with H_2O_2 in the catalytic cycle. Such intermediates are probably very short lived, i.e. beyond the detection timescale of conventional FT-IR, Raman and NMR spectroscopy. As a consequence, they have never been identified for POM-assisted oxidations. Catalytic intermediate isolation thus poses a major physicochemical challenge in its own right, which we will tackle as long-term goal with advanced time-resolved spectroscopy methods.

Therefore, the present investigation sheds new light on the type of catalytic cycles involved in POM-assisted alcohol oxidation through combined kinetic, crystallographic and computational methods. The structural evidence of high-valent Sb(V) species involved in the catalytic cycle is backed by high level theoretical calculations in solution, and Sb as a newly introduced main group atom in the POM metal belt has been identified as a novel type of reactive center in the important class of sandwich-type POMs. This renders our easily accessible Zn/Sb-POMs unique “hands-on” model systems for the complementary development of structure-activity relationships. The influence of key POM tailoring parameters (e.g. composition of the metal belt and variations of the POM shell around the active Sb centers) can now be computationally as well as experimentally tracked. Such guidelines are essential for forefront POM applications in general, including water oxidation catalysts for alternative energy technologies. Further mechanistic studies of the catalytic cycle are now required to re-evaluate the established models. Future studies will include time-resolved FT-IR and UV/vis investigations for the first identification of the short-lived "genuine" active intermediate in POM alcohol oxidation. Application-oriented investigations are now in progress, with immobilization of the low-cost Zn/Sb-catalysts on abundant natural and synthetic polymer matrices as the next step.

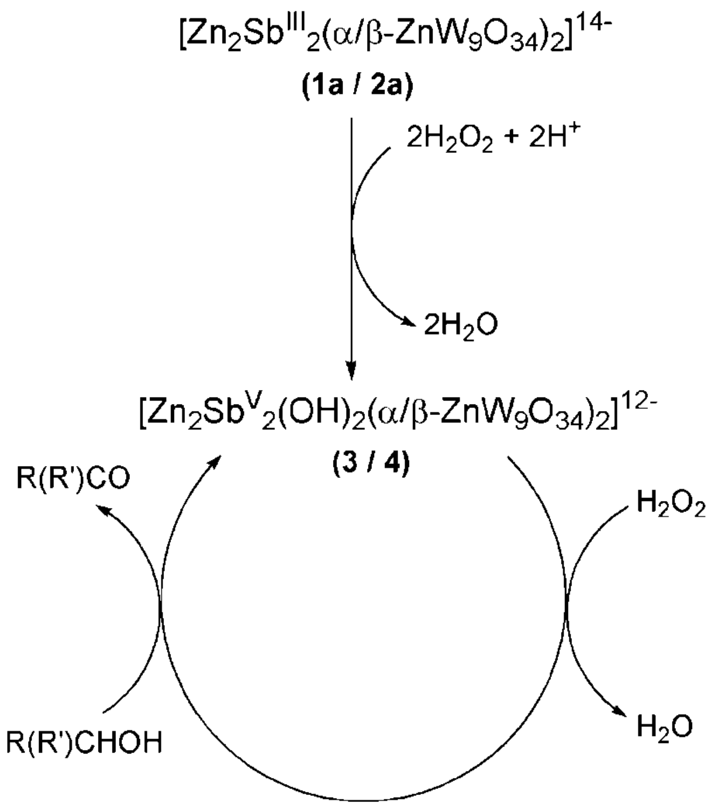

Scheme 5.1. Proposed catalytic scheme for alcohol oxidation with catalysts (**1a** and **3**) or (**2a** and **4**).

5.4 Conclusion.

In conclusion, new Zn-polytungstoantimonate isomeric catalysts for alcohol oxidation are introduced together with their fully characterized high-valent Sb(V)-containing derivatives that play a key role in initiating and maintaining the catalytic cycle.

The novel two *α/β*-isomers of the $[Zn_2Sb^{III}_2(B\text{-}\alpha\text{-}ZnW_9O_{34})_2]^{14-}$ polyanion {**(1a)** and **(2a**)} emerge from an efficient and selective preparative strategy using NH_4^+ as a straightforward structure-directing agent. The observed spontaneous isomerization of *β*- into *α*-isomer is consistent with high level theoretical studies in solution environments. For the first time, important high-valent Sb(V)-species *α/β*-$[Zn_2Sb^{V}_2(OH)_2(B\text{-}\alpha\text{-}ZnW_9O_{34})_2]^{12-}$ involved in the catalytic cycle are characterized with single crystal X-ray diffraction methods together with various analytical techniques, and they are verified with high level computational methods.

Complementary crystallographic and analytical evidence together with computational results shed new light on the still unknown pathways of POM-catalyzed alcohol oxidation The $[Zn_2Sb_2(ZnW_9O_{34})_2]^{14-}$ polyanion can be steered into a variety of structural motifs with ammonium cations as a versatile structure directing agent. High-level BP86/Def2-TZVPP computational methods (collaboration with Prof. Kim Baldridge) provide new insight into relative stabilities of the polyoxometalate isomers and the corresponding high-valent Sb(V)-species. Their reactivity is correlated with the proposed catalytic cycle through electrophilicity plots, and this multidisciplinary approach reveals structure-reactivity relationships among economic Zn/Sb-POM catalysts. The introduction of Sb centers as a main group element into sandwich-type POM catalysts alters their catalytic reaction pathway by shifting the reactivity to the tuneable "metal belt" region of the POM catalyst. This opens up innovative and economical design options through replacement of noble metals in POM catalysts with abundant catalytically active elements. As a consequence, the new Zn/Sb-POM catalysts are synthetic and theoretical model systems for tailoring low-cost catalytic POMs towards key industrial processes and urgent energy applications.

References

[1] (a) Pope, M. T. Heteropoly and Isopoly Oxometalates, Springer, Berlin, 1983. (b) Pope, M. T.; Müller, A. *Angew. Chem., Int. Ed.* **1991**, 30, 34–48. (c) Pope, M. T. *Compr. Coord. Chem*. II. **2003**, 4, 635–678. (d) *Polyoxometalate Molecular Science* (Eds.: Borras-Almenar, J. J.; Coronado, E.; Müller, A.; Pope, M. T.) Kluwer, Dordrecht, **2004**. (e) *Polyoxometalate Chemistry: From Topology via Self-Assembly to Applications.* (Eds.: Pope, M. T.; Müller, A.) Kluwer, Dordrecht, **2001**. (f) *Polyoxometalates: From Platonic Solids to Antiretroviral Activity* (Eds.: Pope, M. T.; Müller, A.) Kluwer, Dordrecht, **1994**.

[2] Long, D.-L.; Tsunashima, R.; Cronin. L. *Angew. Chem. Int. Ed*. **2010**, 49, 1736–1758.

[3] Kozhevnikov, I. V. *Catalysis by polyoxometalates;* John Wiley & Sons, Ltd.: Chichester, U. K., **2002**.

[4] Okuhara, T.; Mizuno, N.; Misono, M. *Adv. Catal*. **1996**, 41, 113–252.

[5] Dolbecq, A.; Dumas, E.; Mayer, C. R.; Mialane, P. *Chem. Rev.* **2010**, 110, 6009–6048.

[6] (a) Hasenknopf, B.; Micoine, K.; Lacôte, E.; Thorimbert, S.; Malacria, M.; Thouvenot, R. *Eur. J. Inorg. Chem.* **2008**, 32, 5001–5013. (b) Chen, L.; Zhu, K.; Bi, L.H.; Suchopar, A.; Reicke, M.; Mathys, G.; Jaensch, H.; Kortz, U.; Richards, R. M. *Inorg. Chem.* **2007**, 46, 8457–8459. (c) Bosco, M.; Rat. S.; Dupre, N.; Hasenknopf, B.; Lacôte, E.; Malacria, M.; Remy, P.; Kovensky, J.; Thorimbert, S.; Wadouachi, A. *ChemSusChem* **2010**, 3, 1249–1252.

[7] (a) Yin, Q.; Tan, J. M.; Besson, C.; Geletiij, Y. M.; Musaev, D. G.; Kuznetsov, A. E.; Luo, Z.; Hardcastle, K. I; Hill, C. L. *Science* **2010**, 328, 342–345. (b) Stracke, J. J.; Finke, R. G. *J. Am. Chem. Soc.* **2011**, 133, 14872–14875. (c) Nohra, B.; El Moll, H.; Albelo, L. M. R.; Mialane, P.; Marrot, J.; Mellot-Draznierks, C.; O'Keeffe, M.; Biboum, R. N.; Lemaire, J.; Keita, B.; Nadjo, L.; Dolbecq, A. *J. Am. Chem. Soc.* **2011**, 133, 13363–13374. (d) Zhang, Z.; Lin, Q.; Zheng, S.-T.; Bu X.; Feng, P. *Chem. Commun.*, **2011**, 47, 3918–3920.

[8] Puntoriero, F.; La Ganga, G.; Sartorel, A.; Carraro, M.; Scorrano, G.; Bonchio, M.; Campagna, S. *Chem. Commun.* **2010**, 46, 4725–4727.

[9] Witte, P. T.; Alsters, P. L.; Walther, J.; Müllner, R.; Pöchlauer, P.; Sloboda-Rozner, D.; Neumann, R. *Org. Process Res. & Development.* **2004**, 8, 524–531.

[10] Kamata, K.; Yonehara, K.; Nakagawa, Y.; Uehara, K.; Mizuno, N. *Nature Chem.* **2010**, 2, 478–483.

[11] Mizuno, N.; Yamaguchi, K.; Kamata, K. *Coord. Chem. Rev.* **2005**, 249, 1944–1956.

[12] Kamata, K.; Yonehare, K.; Sumida, Y.; Yamaguchi, K.; Hikichi, S.; Mizuno, N. *Science* **2003**, 300, 964–966.

[13] (a) Sloboda-Rozner, D.; Alsters, P.; Neumann, R. *J. Am. Chem. Soc.* **2003**, 125, 5280–5281. (b) Neumann, R.; Khenkin, A. M. *Inorg. Chem.* **1995**, 34, 5753–5760. (c) Neumann, R.; Mohammad, G. *J. Am. Chem. Soc.* **1995**, 117, 5066–5074. (d) Sloboda-Rozner, D.; Witte, P.; Alsters, P. L.; Neumann, R. *Adv. Synth. Catal.* **2004**, 346, 339–345. (e) Neumann, R.; Khenkin, A. M. *J. Mol. Catal. A.* **1996**, 114, 169–

180. (f) Morris, A. M.; Anderson, O. P.; Finke, R. G. *Inorg. Chem.* **2009**, 48, 4411–4420.

[14] Ben-Daniel, R.; Weiner, L.; Neumann, R. *J. Am. Chem. Soc.* **2002**, 124, 8788–8789.

[15] Bösing, M.; Nöh, A.; Loose, I.; Krebs, B. *J. Am. Chem. Soc*. **1998**, 120, 7252–7259.

[16] Kikukawa, Y.; Yamaguchi, K.; Mizuno, N. *Angew. Chem. Int. Ed.* **2010**, 49, 6096–6100.

[17] Neumann, R.; Dahan, M. *Nature.* **1997**, 388, 353–355.

[18] (a) Wasfi, S. H.; Rheingold, A. L.; Kokoszka, G. F.; Goldstein, A. S. *Inorg. Chem*., **1987**, 26, 2934–2939. (b) Tourne, C. M.; Tourne, G. F.; Zonnevijlle, F. *J. Chem. Soc. Dalton Trans*., **1991**, 143–155. (c) Limanski, E. M.; Piepenbrink, M.; Droste, E.; Burgemeister, K.; Krebs, B. *J. Cluster Sci*., **2002**, 13, 369–379. (d) Wang, J. P.; Ma, P. T.; Shen, Y.; Niu, J. Y. *Cryst. Growth Des*., **2007**, 7, 603–605.

[19] (a) Shi, L.-X.; Zhao, W.-F.; Xu, X.; Tang, J.; Wu, C.-D. *Inorg. Chem*., **2011**, 50, 12387–12389. (b) Shi,L.-X.; Zhang, X.-W.; Wu, C.-D. *Dalton Trans*., **2011**, 40, 779–781.

[20] Anderson, T. M.; Hill, C. L. *Inorg. Chem*. **2002**, 41, 4252–4258.

[21] Assran, A. S.; Mal, S. S.; Izarova, N. V.; Banerjee, A.; Suchopar, A.; Sadakane, M.; Kortz U. *Dalton Trans*. **2011**, 40, 2920–2925.

[22] (a) Lopez, X.; Miró, P.; Carbó, J. J.; Rodríguez-Fortea, A.; Bo, C.; Poblet, J. M. *Theor. Chem. Acc.* **2011**, 128, 393–404. (b) Henry M. *J. Cluster Sci*. **2002**, 13, 437–458. (c) Bridgeman, A. J.; Cavigliasso, G. *Faraday Discuss*. **2003**, 124, 239–258. (d) Poblet, J. M.; López, X.; Bo, C. *Chem. Soc. Rev*. **2003**, 32, 297–308. (e) Li, J. *J. Cluster Sci.* **2002**, 13, 137–163. (e) Si, Y.-L.; Chen, W.-L.; Wang, E.-B. *Molecular Phys*. **2009**, 107, 53–58.

[23] (a) Vilà-Nadal, L.; Rodríguez-Fortea, A.; Poblet, J. M. *Eur. J. Inorg. Chem*. **2009**, 5125–5133. (b) Miró, P.; Poblet, J.; Bonet Avalos, J.; Bo, C. *Can. J. Chem*. **2009**, 87, 1296–1301. (c) Kumar, D.; Derat, E.; Khenkin, A. M.; Neumann, R.; Shaik, S. *J. Am. Chem. Soc*. **2005**, 127, 17712–17718. (d) Zhang, F.-Q.; Zhang, X.-M.; Fang, R.-Q.;

Wu, H.-S. *Dalton Trans*. **2010**, 39, 8256–8260. (e) Derat, E.; Kumar, D. Neumann, R.; Shaik, S. *Inorg. Chem*. **2006**, 45, 8655–8663.

[24] (a) Si, Y.-L.; Chen, W.-L.; Wang, E.-B. *Intern. J. Quantum Chem*. **2009**, 109, 1560–1565. (b) Guo, Y.-R.; Pan, Q.-J.; Wei, Y.-D.; Li, Z.-H.; Li, X. *J. Mol. Struct. (Theochem)* **2004**, 676, 55–64. (c) Bridgeman, A. J. *Chem. Eur. J*. **2006**, 12, 2094–2012. (d) Bonhomme, F.; Larentzos, J. P.; Alam, T. M.; Maginn, E. J.; Nyman, M. *Inorg. Chem*. **2005**, 44, 1774–1785.

[25] Antonova, N. S.; Carbó, J. J.; Kortz, U.; Kholdeeva, O. A.; Poblet, J. M. *J. Am. Chem. Soc*. **2010**, 132, 7488–7497.

[26] Khenkin, A. M.; Kumar, D.; Shaik, S.; Neumann R. *J. Am. Chem. Soc*. **2006**, 128, 15451–15460.

[27] (a) McGlone, T.; Vilà-Nadal, L.; Miras, H. N.; Long, D.-L.; Poblet, J. M.; Cronin, L. *Dalton Trans*. **2010**, 39, 11599–11604. (b) Uehara, K.; Mizuno, N. *J. Am. Chem. Soc*. **2011**, 133, 1622–1625. (c) Derat, E.; Lacôte, E.; Hasenknopf, B.; Thorimbert, S.; Malacria, M. *J. Phys. Chem. A* **2008**, 112, 13002–13005.

[28] Kholdeeva, O. A.; Maksimov, G. M.; Maksimovskaya, R. I.; Vanina, M. P.; Trubitsina, T. A.; Naumov, D. Yu.; Kolesov, B. A.; Antonova, N. S.; Carbó, J. J.; Poblet, J. M. *Inorg. Chem*. **2006**, 45, 7224–7234.

[29] Khenkin, A. M.; Shimon, L. J. W.; Neumann, R. *Eur. J. Inorg. Chem*. **2001**, 789–794.

[30] Mal, S. S.; Nsouli, N. H.; Carraro, M.; Sartorel, A.; Scorrano, G.; Oelrich, H.; Walder, L.; Bonchio, M.; Kortz, U. *Inorg. Chem*. **2010**, 49, 7–9.

[31] Carraro, M.; Nsouli, N.; Oelrich, H.; Sartorel, A.; Sorarù, A.; Mal, S. S.; Scorrano, G.; Walder, L.; Kortz, U.; Bonchio, M. *Chem. Eur. J*. **2011**, 17, 8371–8378.

[32] Ni, L.; Patscheider, J.; Baldridge, K. K.; Patzke, G. R. *Chem. Eur. J*. **2012**, 18, 13293–13298.

[33] (a) Tourné, C. M.; Tourné, G. F.; Zonnevijlle, F. *J. Chem. Soc., Dalton Trans.* **1991**, 143–155. (b) Liu, Y.; Liu, B.; Xue, G.; Hu, H.; Fu, F.; Wang, J. *Dalton Trans*. **2007**, 3634–3630.

[34] Lopez, X.; Maestre, J. M.; Bo. C.; Poblet, J.-M. *J. Am. Chem. Soc*. **2001**, 123, 9571–9576.

[35] Baffert, C.; Boas, J. F.; Bond, A. M.; Kögerler, P.; Long, D.-L.; Pilbrow, J. R.; Cronin, L. *Chem. Eur. J.* **2006**, 12, 8472–8483.

[36] Bösing, M.; Loose, I.; Pohlmann, H.; Krebs, B. *Chem. Eur. J*. **1997**, 8, 1232–1237. IR (KBr disk): 925 (m), 891 (s), 769 (s), 708 cm^{-1} (s).

[37] Oxford Diffraction, CrysAlis CCD and CrysAlis RED, Oxford Diffraction Ltd., Abingdon, UK, **2005**.

[38] Farrugia, L. J. *J. Appl. Crystallogr.* **1999**, 32, 837–838.

[39] Sheldrick, G. M. SHELX97, *Programs for Crystal Structure Analysis*; Release 97-2; University of Göttingen, Göttingen: Germany, **1997**.

[40] (a) Sadakane, M.; Dickman, M. H.; Pope, M. T. *Inorg. Chem*. **2001**, 40, 2751–2755. (b) du Peloux, C.; Dolbecq, A.; Mialane, P.; Marrot, J.; Rivière, E.; Sécheresse, F. *Inorg. Chem.* **2002**, 41, 7100–7104. (c) Gaunt, A. J.; May, L.; Collison, D.; Fox, D. *Inorg. Chem*. **2003**, 42, 5049–5051. (d) Lei, C.; Mao, J.-G.; Sun, Y.-Q.; Song, J.-L. *Inorg. Chem.* **2004**, 43, 1964–1968. (e) Mazeaud, A.; Dromzee, Y.; Thouvenot, R. *Inorg. Chem*. **2000**, 39, 4735–4740. (f) Juraja, S.; Vu, T.; Richardt, P. J. S.; Bond, A. M.; Cardwell, T. J.; Cashion, J. D.; Fallon, G. D.; Lazarev, G.; Moubaraki, B.; Murray, K. S.; Wedd, A. G. *Inorg. Chem*. **2002**, 41, 1072–1078. (g) Dolbecq, A.; Cadot, E.; Eisner, D.; Sécheresse, F. *Inorg. Chem*. **1999**, 38, 4217–4223. (h) Villanneau, R.; Proust, A.; Robert, F.; Viellet, P.; Gouzerh, P. *Inorg. Chem*. **1999**, 38, 4981–4985. (i) Volkmer, D.; Bredenkötter, B.; Tellenbröker, J.; Kögerler, P.; Kurth, D. G.; Lehmann, P.; Schnablegger, H.; Schwahn, D.; Piepenbrink, M.; Krebs, B. *J. Am. Chem. Soc.* **2002**, 124, 10489–10496.

[41] Schmidt, M.; Baldridge, K. K.; Boatz, J. A.; Elbert, S.; Gordon, M.; Jenson, J. H.; Koeski, S.; Matsunaga, N.; Nguyen, K. A.; Su, S. J.; Windus, T. L.; Dupuis, M.; Montgomery, J. A. *J. Comp. Chem.* **1993**, 14, 1347–1363.

[42] Gaussian 09. Gaussian, Inc., Wallingford CT, **2009**.

[43] Becke, A. D. *Phys. Rev. A* **1988**, 38, 3098–3100.

[44] Perdew, J. P. *Phys. Rev. B.* **1986**, 33, 8822–8824.

[45] Weigend, F.; Ahlrichs, R. *PhysChemChemPhys*., **2005**, 7, 3297–3351.

[46] Klamt, A.; Schürmann, G. *J. Chem. Soc. Perkin Trans.* **1993**, 2, 799–805.

[47] Baldridge, K.; Klamt, A. *J. Chem. Phys.* **1997,** 106, 6622–6633.

[48] Klamt, A.; Jonas, V.; Bürger, T.; Lohrenz, C. W. *J. Phys. Chem.* **1997**, 102, 5074–5085.

[49] Baldridge, K. K.; Greenberg, J. P. *J. Mol. Graphics*. **1995**, 13, 63–66.

[50] Brown, I. D.; Altermatt, D. *Acta Crystallogr., Sect. B.* **1985**, 41, 244–247.

[51] Keita, B.; Nadjo, L. *Electrochemistry of Polyoxometalates. Encyclopedia of Electrochemistry*; Bard, A. J., Stratmann, M., Eds.; Wiley-VCH: Weinheim, Germany, **2006**, 7, 607–700.

[52] Hara, M.; Inukai, J.; Yoshimoto, S.; Itaya, K. *J. Phys. Chem. B*. **2004**, 108,17441–17447.

[53] Toghill, K. E.; Lu, M.; Compton, R. G. *Int. J. Electrochem. Sci.* **2011**, 6, 3057–3076.

[54] Tao, J.; Shi, J.-X.; Tong, M.-L.; Zhang X.-X.; and Chen, X.-M. *Inorg. Chem*., **2001**, 40, 6328–6330.

[55] Garbassi, F. *Surf. Interf. Anal.* **1980**, 2, 165–169.

[56] Kidd, R. G.; Matthew, R. W. *J. Inorg. Nucl. Chem.* **1975**, 37, 661–663.

[57] (a) Sheldon, R. A.; Arends, I. W. C. E.; Dijisman, D. *Catal. Today*. **2000**, *57*,157–166; (b) Mallat, T.; Baiker, A. *Chem. Rev*. **2004**, 104, 3037–3058; (c) Matsumoto, T; Ueno, M.; Wang, N.; Kobayashi, S. *Chem. Asian J.* **2008**, 3,196–214.

6. 1D- and 2D-Architectures via Self-Assembly of the Novel Sandwich-type Polyoxometalate $[Zn_2Sb_2(\alpha\text{-}B\text{-}ZnW_9O_{34})_2]^{14-}$

6.1. Introduction

As POMs cross the border between molecular architectures and the nanoscale, controlling POM synthesis remains a critical challenge that extends from single molecular structures (0D) to various dimensional architectures (1D, 2D, 3D) of POM chemistry.[1,2] In this chapter, a multiscale approach towards new polymeric zinc-containing polytungstoantimonates is presented which proceedings from 0D POM building blocks mentioned in the preceding chapter over 1D polymeric chains to higher dimensional networks.

To the best of our knowledge, Zn/Sb-combinations have rarely been reported for the $[MW_{9-11}O_{33-39}]^{n-}$ lacunary POM family. New structural motifs of Zn-POMs are in the focus of ongoing research activities, as illustrated by the development of *Keggin*-type POM $[\{Zn(OH_2)(\mu_3\text{-}OH)\}_2\{Zn(OH_2)_2\}_2\{\gamma\text{-}HSiW_{10}O_{36}\}_2]^{8-}$ as a powerful catalyst for alcohol oxidation,[3] as well as by new hexa-sandwiched Zn-POMs[4] or compounds with $[\{Zn_2W(O)O_3\}_2]^{4+}$ hexaprismane cores.[5] Furthermore, $[WZn\{Co(H_2O)\}_2(ZnW_9O_{34})_2]^{12-}$ with 1D polymeric chains has been found to catalyze the selective oxidation of styrene to benzaldehyde.[6] The $[M_2(H_2O)_2Bi_2(\beta\text{-}B\text{-}MW_9O_{34})_2]^{14-}$ (M = Co, Zn) POMs are further new examples, but their catalytic and isomerization properties remain to be investigated.[7]

As outlined in **Chapter 5**, the novel zinc-containing polyoxotungstoantimonate alcohol oxidation catalysts $[Zn_2Sb_2(B\text{-}\alpha/\beta\text{-}ZnW_9O_{34})_2]^{14-}$, $\{\alpha/\beta\text{-}Zn_2Sb_2\}$ (**1a** and **2a**), have recently emerged as the first combination of the key $\{ZnW_9O_{34}\}$-building block with Sb^{3+} cations.[8] Moreover, important Sb(V)-containing active species $[Zn_2Sb^V{}_2(OH)_2(B\text{-}\alpha/\beta\text{-}ZnW_9O_{34})_2]^{12-}$ (**3** and **4**) were first isolated in single crystalline form together with various analytical techniques, and they are verified with high level computational methods in the preceding chapter. Following up on this work, the spectrum of synthetic conditions for the formation of *α*- and *β*-$\{Zn_2Sb_2\}$ isomers, repectively, is now investigated in more detail. In the following, this 0D tuning level, i.e. the creation of new POM motifs, is extended into an investigation of the 1D and

2D self-assembly properties of the lacunary $\{Zn_2Sb_2\}$ moiety.[9]

The countercations have a tremendous influence on POM assemblies which still remains challenging to control, because it is difficult to employ the wide range of cation-related effects for POM design in a targeted manner. Countercations direct the primary POM cluster type, they steer their packing motifs and the linkage of POM nodes, and they finally assist the formation of large "blackberry" POM aggregates.[10] From the application-oriented point of view, all-inorganic POM catalysts are favorable with respect to stability and recyclability[3] so that exploring the structure-directing potential of inorganic additives is crucial for informed POM production.[11]

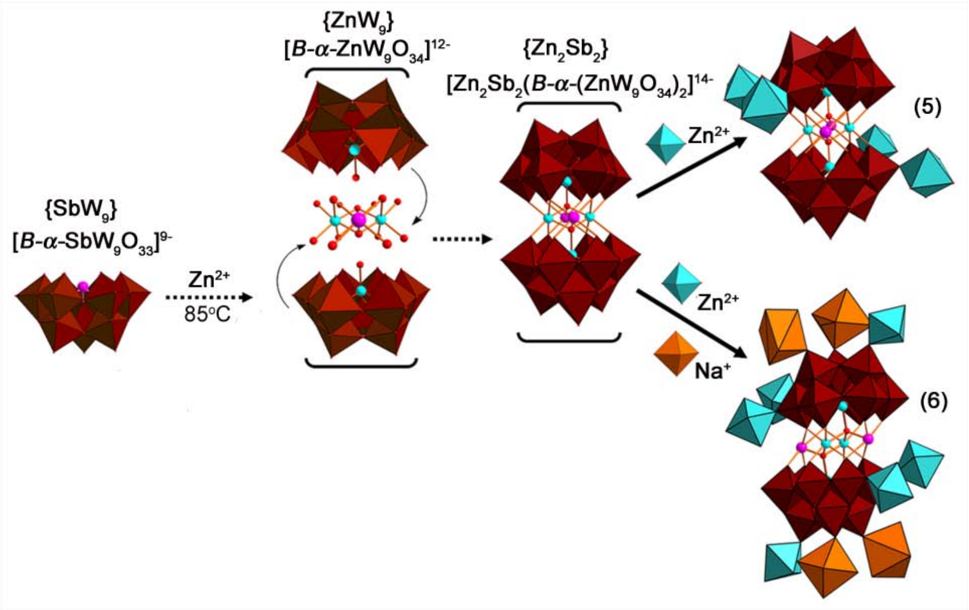

Figure. 6.1. Formation of the $[Zn_2Sb_2(B\text{-}\alpha\text{-}ZnW_9O_{34})_2]^{14-}$ building block from $[B\text{-}\alpha\text{-}SbW_9O_{33}]^{9-}$ precursor and subsequent Zn^{2+}-assisted transformation into nodes for 1D and 2D architectures.

Synopsis of results. The general approach outlined in this chapter directly proceeds from a 0D POM precursor over 1D polymeric chains to higher dimensional networks comprising of $\{Zn_2Sb_2\}$ by using Zn^{2+} cations as an attractive, low-cost and environmentally friendly control agent. As a result, two novel $\{Zn_2Sb_2\}$-based polymeric compounds $(NH_4)_5[Zn(H_2O)_6](H_3O)_3\{[Zn_2(H_2O)_8][Zn_2Sb_2(B\text{-}\alpha\text{-}ZnW_9O_{34})_2]\}\cdot 20H_2O$ **(5)** and $(NH_4)_2[Zn(H_2O)_6]_2\{[Na_2Zn_3(H_2O)_{19}][Zn_2Sb_2(B\text{-}\alpha\text{-}$

$ZnW_9O_{34})_2]\}\cdot 14H_2O$ **(6)** were obtained from the one-step reaction of the flexible lacunary $[B\text{-}\alpha\text{-}SbW_9O_{33}]^{9-}$ $\{SbW_9\}$[12] in the presence of zinc acetate by switching the initial Zn^{2+} concentration (Figure. 6.1). The first discovery of new transformation from the $\{SbW_9\}$ fragment into a *Keggin*-type $[B\text{-}\alpha\text{-}ZnW_9O_{34}]^{12-}$ $\{ZnW_9O_{34}\}$ unit was induced by heating and the addition of a zinc source in aqueous solution. Yellow crystals of **(5)** were formed in the presence of excess $Zn(OAc)_2$, whereas light yellow crystals of **(6)** were isolated with lower Zn^{2+} concentrations. Interestingly, the $\{SbW_9\}$ precursor is transformed into trivacant *Keggin* $[B\text{-}\alpha\text{-}ZnW_9O_{34}]^{12-}$ $\{ZnW_9\}$ in aqueous solution through heating at 85 °C and the addition of zinc cations (Figure. 6.1).

6.2. Experimental

6.2.1. Synthetic methods

Synthesis of $(NH_4)_5[Zn(H_2O)_6](H_3O)_3\{[Zn_2(H_2O)_8][Zn_2Sb_2(B\text{-}\alpha\text{-}ZnW_9O_{34})_2]\}\cdot 20H_2O$ (5)

0.377 g (0.150 mmol) of $Na_9[SbW_9O_{33}]\cdot 19.5H_2O$ was dissolved in 25 mL of water and heated to 85 ºC under stirring. After 20 min, 0.098 g (0.450 mmol) of $Zn(OAc)_2\cdot 2H_2O$ was added in individual portions. The solution underwent a color change from colorless to light yellow. The mixture was left stirring for 90 min at 85 ºC, followed by cooling to room temperature and filtration. In a second step, an additional amount of 0.033g (0.150 mmol) $Zn(OAc)_2\cdot 2H_2O$ was added under stirring for 0.5 h, followed by addition of 1.0 M NH_4Cl solution (0.25 mL) to the yellow filtrate. Slow evaporation of the solution afforded yellow crystals after approx. 10 d. Yield: 0.168 g, 38 % based on W. TGA showed a weight loss of 11.6 % in the 30 – 210 °C temperature range, corresponding to the loss of coordinating and solvent water molecules (expected 11.4 %). FT-IR (cm^{-1}): 1620(m), 1411(s), 932(vs), 854(vs), 837(s), 707(s), 675(m), 432(m). Raman (cm^{-1}): 1035 (vs), 993(vs), 872(s). Elemental analysis calcd. (found): W 56.49 (54.90); Zn 7.81 (8.55); Sb 4.16 (4.05); N 1.20 (1.13); H 1.67 (1.55).

Synthesis of $(NH_4)_2[Zn(H_2O)_6]_2\{[Na_2Zn_3(H_2O)_{19}][Zn_2Sb_2(B\text{-}\alpha\text{-}ZnW_9O_{34})_2]\}\cdot14H_2O$ (6)

The above synthetic procedure was modified for the synthesis of **(6)** as follows: an increased amount of $Zn(OAc)_2\cdot2H_2O$, i.e. 0.053 g (0.242 mmol) instead of 0.033 g (0.150 mmol) was added in the second step. Yield: 0.195 g, 42 % based on W. TGA displayed a weight loss of 13.1 % in the 30 - 160 ^oC temperature range, corresponding to the loss of coordinating and solvent water molecules (expected 13.2 %). FT-IR (cm^{-1}): 1623(m), 1419(s), 910(vs), 833(vs), 703(s), 671(m), 415(m). Raman (cm^{-1}): 1035 (vs), 991(vs), 869(s). Elemental analysis calcd. (found): W 54.05 (52.90); Zn 9.61 (9.81); Sb 3.97 (4.09); Na 0.75 (1.29); N 0.45 (0.40); H 1.61 (1.50).

6.2.2. Catalytic alcohol oxidation

Catalyst, solvent, substrate, and 30 % aqueous H_2O_2 were successively placed into a 10 mL round-bottom flask. A Teflon-coated magnetic stirring bar was added and the reaction mixture was stirred at 85 °C. Reaction conditions: 0.25 mmol substrate, 1.25 mmol (30 %) H_2O_2, 1.0 μmol catalyst, 0.50 ml H_2O, 85 ^oC, 7 h. All yields reported in this manuscript are based on alcohol conversion. Reaction products were characterized and quantified with a gas chromatograph (Finnigan Trace GC Ultra) equipped with a flame ionization detector and fitted with a ZB-5MS Phenomenex column (30 m length, 0.25 mm internal diameter, 0.25 μm film thickness) using dodecane as internal reference. Products were furthermore identified by GC-MS (Finnigan Trace DSQ GC-MS systems).

6.2.3. X-ray crystallography

Data collections of compounds **(5)** and **(6)** were performed on an Oxford Xcalibur Ruby CCD single-crystal diffractometer (MoK_α radiation, λ= 0.71073 Å) at 183(2) K. Routine Lorentz and polarization corrections were applied, and an absorption correction was performed using the program CrysAlis (multi-scan).[13] Structural analysis was performed using Win-GX for Windows software.[14] Direct methods were used to locate heavy metal atoms (SHELXS-97) and the remaining atoms were located from successive Fourier maps (SHELXL-97).[15] Hydrogen atoms were not included in the refinements and heavy metal atoms (Sb, Zn, and W, Na) were refined anisotropically. Oxygen atoms were refined isotropically, because anisotropic refinement of light atoms in POMs is often difficult in the presence of manifold heavy metal atoms.[16] A summary of crystal data and stuctures refinements for **(5)** and **(5)** was listed in the Annexes Table 10.11, and selected bond lengths are listed in the Annexes, Table 10.12.

6.3. Results and discussion

6.3.1. Crystal structures

The structural compositions of **(5)** and **(6)** were determined from X-ray crystallography data in combination with various additional analytical techniques. Single-crystal X-ray diffraction of compounds **(5)** and **(6)** shows that they display different triclinic arrangements of the sandwich-type $[Zn_2Sb_2(B\text{-}\alpha\text{-}ZnW_9O_{34})_2]^{14-}$ $\{Zn_2Sb_2\}$ polyanion which is linked by Zn^{2+} cations either into 1D polymeric chains in **(5)** or into 2D polymeric layers in **(6)**, respectively. The Zn/Sb-containing POMs-based polymeric structures can be steered into networks with different dimensionality through adjusting the Zn^{2+} concentration, respectively The $\{Zn_2Sb_2\}$ moiety contains a belt of two Zn^{2+} and two Sb^{3+} cations which link the trivacant *Keggin*-type $\{ZnW_9\}$ fragments in a sandwich-type fashion. The Zn1 and Zn1a atoms of this metal belt display distorted octahedral coordination by oxygen atoms, while the two central Sb atoms exhibit distorted square-pyramidal coordinations. Furthermore, the Zn2 and Zn2a heteroatoms are located on tetrahedral sites in the center of the $\{ZnW_9\}$ shells (Figure 6.2).

The bond valence sum (BVS) values of zinc (1.98-2.17 for **(5)**, 1.92-2.14 for **(6)**), antimony (3.10 for **(5)**, 2.98 for **(6)**) and tungsten atoms (5.90 -6.03 for **(5)** and 5.73-6.08 for **(6)**) are in good agreement with the oxidation states of +2, +3 and +6 as expected from all analytical methods (Tables 10.13 - 10.14 in the Annexes).[17]

The $\{Zn_2Sb_2\}$ building block of **(5)** furthermore links to four Zn^{2+} cations (Zn3) via terminal oxygen atoms of four different $\{WO_6\}$ octahedra (Figure 6.2a and Figure

6.3a). These zinc cations are connecting nodes between two neighboring {Zn_2Sb_2} units via Zn-O-W bonds (Zn3-O23-W4, Zn3-O13b-W5b, symmetry code: b, –*x*, -*y*, -*z*), and their coordination spheres are completed by four aqua ligands (Zn-O distances: 2.074(9)-2.134(11) Å). As a consequence, **(5)** displays a ladder-like 1D network of {Zn_2Sb_2} and Zn^{2+} linkers (Figure 6.3b and 6.3c). The polymeric chains are further connected into a 3D supramolecular network via extensive hydrogen bonding interactions between the terminal oxygen atom of the polyanion and the aqua ligand around Zn3 and Zn4 (O···O = 2.667-2.750 Å), between the μ_2-oxygen atom of the cluster and the aqua ligand of Zn4 (O···O = 2.760-3.037 Å), and between two aqua ligands of Zn3 and Zn4 (O···O = 2.834-3.049 Å; Figure 6.4).

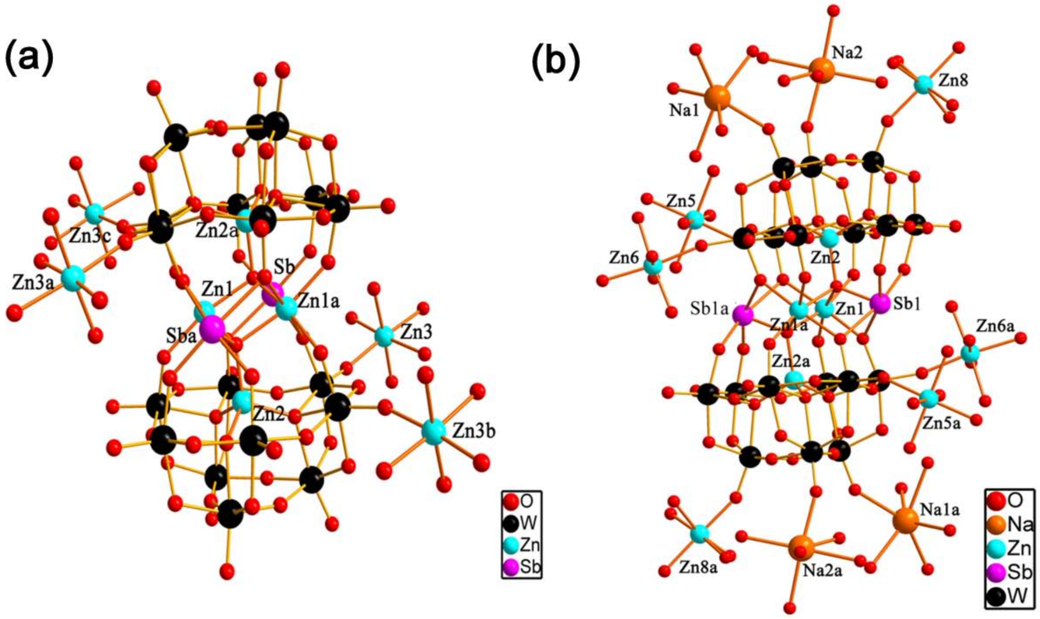

Figure 6.2. Ball-and-stick representation of (a) the polyoxoanion $[Zn_2Sb_2(B\text{-}\alpha\text{-}ZnW_9O_{34})_2]^{14-}$ in **(5)** (symmetry codes: *a, 1-x, -y,-z; b, -x,-y, -z; b, -x, -y, -z; c, 1+x, y, z;*), (b) the polyoxoanion $[Zn_2Sb_2(B\text{-}\alpha\text{-}ZnW_9O_{34})_2]^{14-}$ in **(6)** (symmetry codes: *a, -x, -y, 2- z*; color codes: O = red; W = black; Sb = pink; Zn = blue; Na = orange).

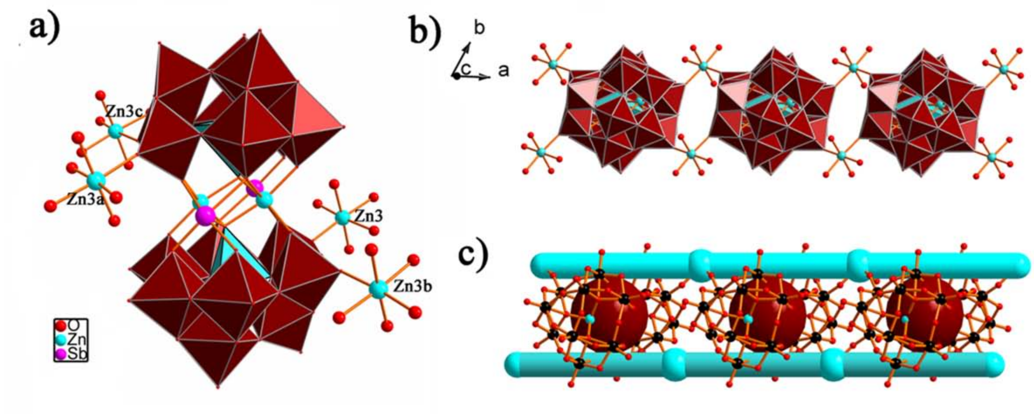

Figure. 6.3 Polyhedral/ball-and-stick representations of (a) $\{[Zn_2(H_2O)_8][Zn_2Sb_2(ZnW_9O_{34})_2]\}^{10-}$ polyanion **(5)**, (b) structure of the 1D polymeric connection in **(5)**, (c) schematic arrangement of 1D ladder-like chain along the *c* axis ($[Zn_2Sb_2(ZnW_9O_{34})_2]^{14-}$ = red spheres, Zn^{2+} linkers = blue pillars, symmetry codes: *a, 1-x, -y,-z; b, -x,-y, -z*; *b, -x, -y, -z; c, 1+x, y, z*).

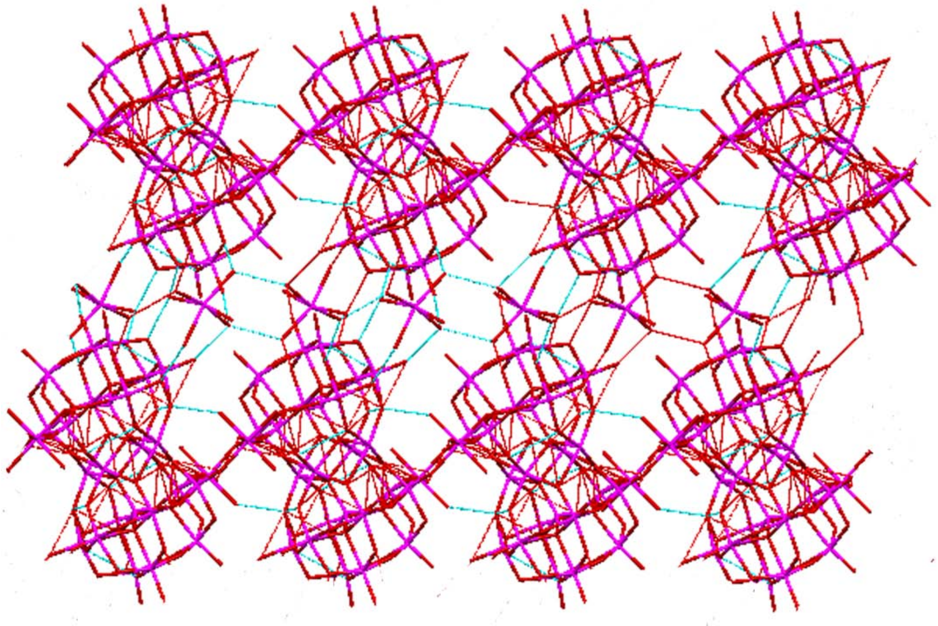

Figure 6.4. View of the 3D supramolecular framework of **(5)** projected along the *b* axis (hydrogen bonds are shown as dotted lines).

The $\{Zn_2Sb_2\}$ motif in **(6)** coordinates six zinc cations and four sodium cations through ten terminal oxygen atoms of ten different $\{WO_6\}$ octahedra (Figure 6.2b and Figure 6.5a). The octahedrally coordinated Zn^{2+} and Na^+ cations can be further differentiated into two subsets. Zn8 and Na2 are capping the $\{Zn_2Sb_2\}$ moieties and and their coordination environments are completed by five water molecules. Zn5 and Zn6 are two connecting nodes which coordinate two terminal oxygen atoms of two $\{Zn_2Sb_2\}$ units via Zn-O-W bonds (Zn5-O38-W13, Zn6-O55-W10, Zn5-O59a-W4a, Zn6-O54a-W2a, symmetry code: a, *-x, -y, 2- z*; Zn-O distances: 2.051(9)-2.143(9) Å) together with four aqua ligands, whereas the Na1 cation is attached to three $\{Zn_2Sb_2\}$ clusters through W12, W3 and W6b (*-x, 1-y, 1-z*) via μ-oxo bridges as a 3-connecting node.

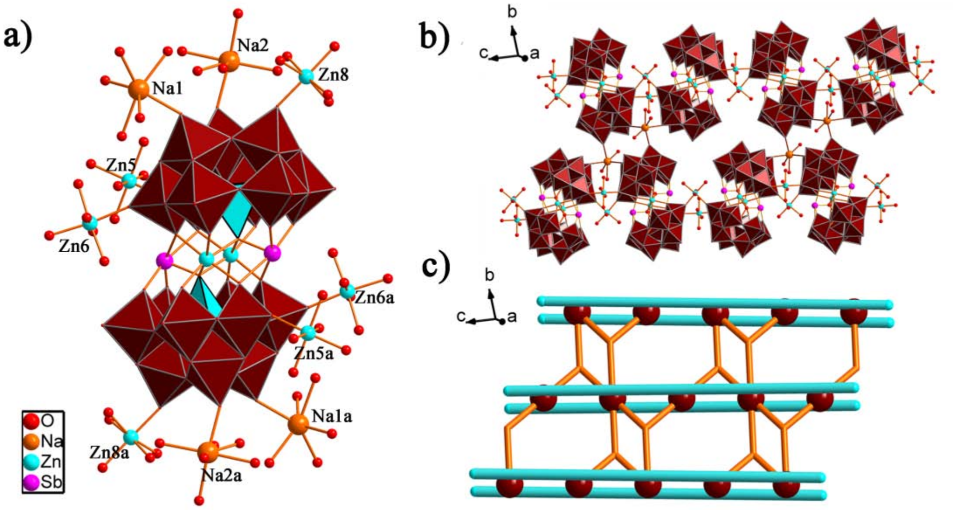

Figure 6.5 Polyhedral/ball-and-stick representations of **(6)**: (a) $[Na_2Zn_3(H_2O)_{19}Zn_2Sb_2(ZnW_9O_{34})_2]^{6-}$ polyanion, (b) 2D polymeric network, (c) construction principle of 2D layers ($[Zn_2Sb_2(ZnW_9O_{34})_2]^{14-}$ polyanions = red spheres, Zn^{2+} linkers = blue pillars, Na^+ linkers = yellow pillars, symmetry codes: *a, -x, -y, 2- z*).

This leads to a 2D sheet-like polymeric network of $\{Zn_2Sb_2\}$ clusters in **(6)** which is maintained by zinc and sodium cations (Figure 6.5b). The topology of this network can be described as follows: the $\{Zn_2Sb_2\}$ clusters represent 4, 6-connecting nodes, Na1 atoms are 3-connecting nodes and Zn5 as well as Zn6 are bridging connector ligands between two clusters (Figure. 6.5c). Therefore, the Schläfli symbol for this 3,4,6-connected trinodal network is $(3.4.5)^2$ $(3^2.4^2.5^2.6^2.7^4.8^2.9)$ $(3^2.6^2.7^2)$. The polymeric layer material **(6)** furthermore displays a solid state 3D supramolecular network through extensive hydrogen bonds via extensive hydrogen bonding interactions between the terminal oxygen atom of the polyanion and the aqua ligand around Zn8 and Zn5 (O···O = 2.686-2.818 Å), between the μ_2-oxygen atom of the cluster and the aqua ligand of Zn5, Zn6 (O···O = 2.659-3.004 Å), and between two aqua ligands of Zn6 and Zn5 (O···O = 2.743-2.899 Å; Figure 6.6).

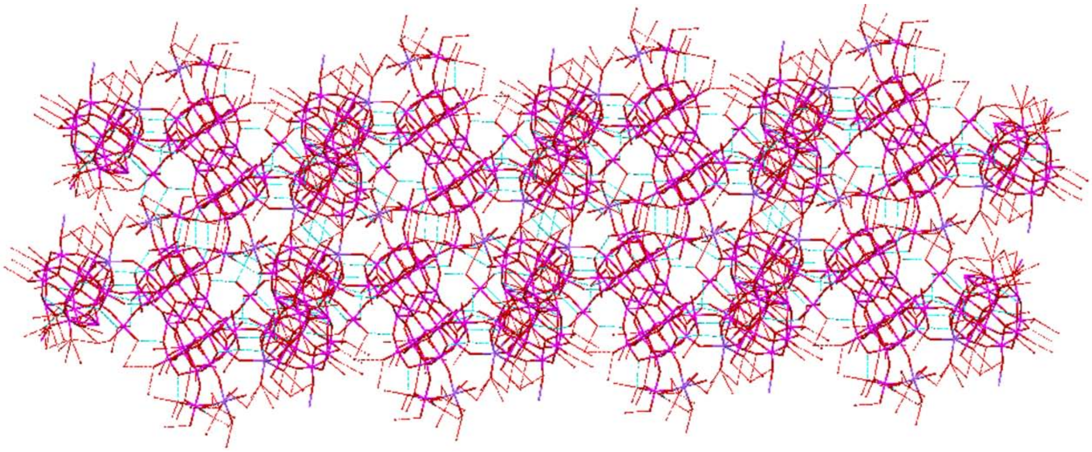

Figure 6.6. View of the 3D supramolecular framework of **(6)** along the *a* axis (hydrogen bonds are shown as dotted lines).

6.3.2. Analytical characterizations and properties

6.3.2.1. PXRD and TG characterizations

The powder X-ray diffraction (PXRD) patterns for **(5)** and **(6)** are presented in Figure 6.7 - 6.8. Phase purity of compounds **(5)** and **(6)** was confirmed by comparison of experimental PXRD patterns with simulated patterns from single-crystal X-ray diffraction data. Intensity differences between observed and calculated patterns may be due to sample preparation and orientation effects.

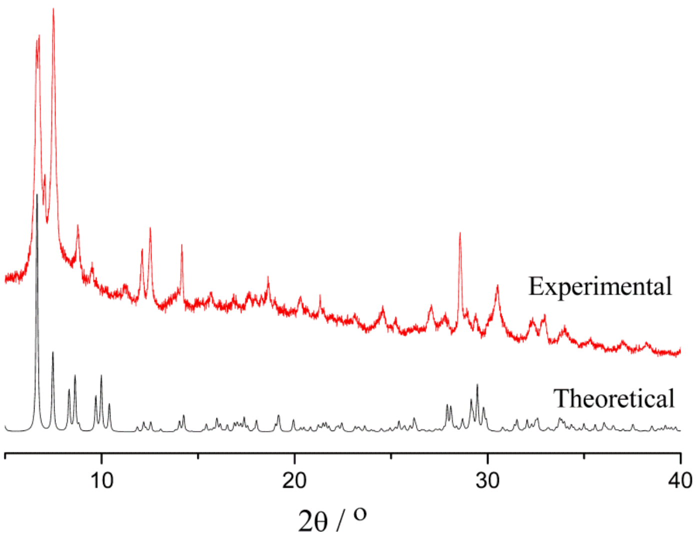

Figure 6.7. Powder X-ray diffraction pattern of bulk compound **(5)** *vs.* the calculated pattern.

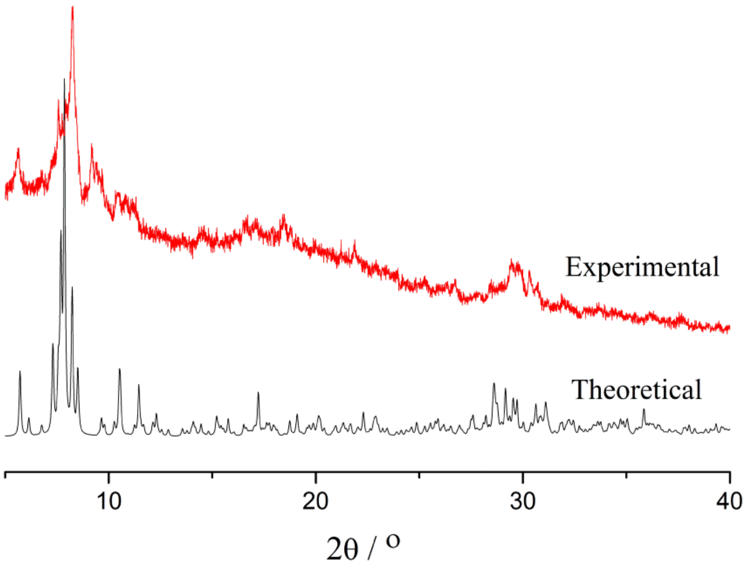

Figure 6.8. Powder X-ray diffraction pattern of bulk compound **(6)** *vs.* the calculated pattern.

The compounds **(5)** and **(6)** undergo similar thermal decomposition pathways as shown by the related shapes of their thermogravimetric (TGA) curves (Figure 6.9). Concerning the compound **(5)**, TGA show a rapid weight loss of 11.6 % (calcd. 11.4 %) in the 30 - 210 °C temperature range corresponding to the loss of lattice water molecules, followed by a slower weight loss between 130 - 580 °C, mainly caused by evaporation of ammonia. For the compound **(6)**, TGA displayed a weight loss of 13.1 % in the 30 - 160 °C temperature range, corresponding to the loss of coordinating and solvent water molecules (expected 13.2 %).

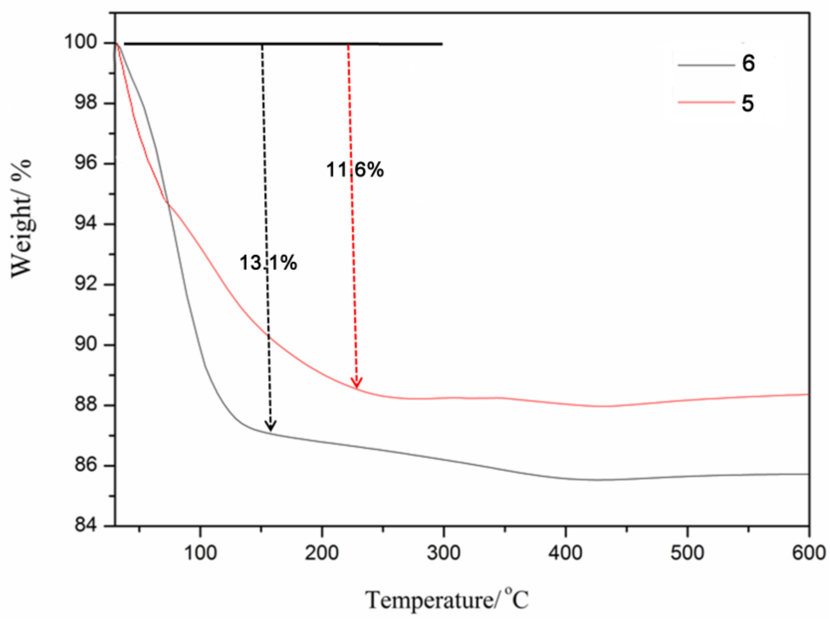

Figure 6.9. Thermogravimetric curves of compounds **(5)** and **(6)**.

6.3.2.2. Electrochemical characterization

Cyclic voltammetry (CV) data of **(5)** and **(6)** in aqueous solution are strongly pH-dependent (Figure 6.10). Upon higher pH values, the redox signals become weaker and finally vanish completely due to protonation effects. The quasi-reversible peak (I-I') between -0.5 and -1.0 V at pH 4.0 corresponds to redox processes at the W(VI) centers, whilst the irreversible oxidation peak (II') around 0.08 V can be assigned to the oxidation of metallic Sb(0) to oxygenic Sb^{3+}.[18]

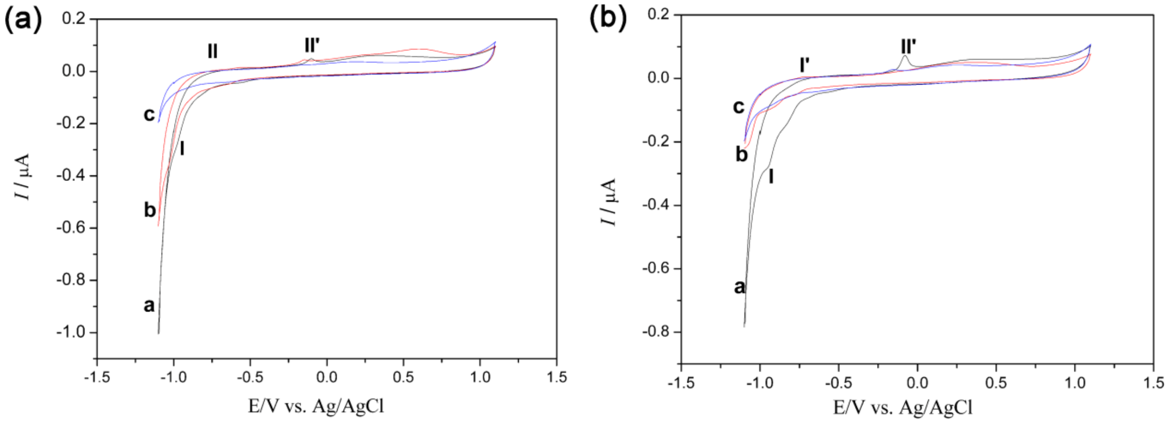

Figure 6.10. Cyclic voltammograms of (a) 0.1 mM compound **(5)**; (b) 0.1 mM compound **(6)** in (0.5 M CH_3COONa/CH_3COOH) buffer solution (scan rate 25 mV/s, GCE working electrode, Ag/AgCl reference electrode). Curve: pH = 3.0 **(a)**; pH = 4.0 **(b)**; pH = 5.0 **(c)**.

6.3.2.3. FT-IR and Raman spectroscopy

FT-IR spectra of compounds **(5)** and **(6)** display the characteristic vibration bands of the $\{ZnW_9O_{34}\}$ unit (Figure 6.11).[9,10] Absorption bands at 932(s), 837(vs), 707(vs) cm^{-1} for **(5)**, and at 910(s), 833(vs), 703(vs) for **(6)** are attributed to the characteristic $\upsilon(W\text{-}O_t)$, $\upsilon(W\text{-}O_b)$ and $\upsilon(W\text{-}O_c)$ frequencies, respectively. Resonances centered at 1620 and 1410 cm^{-1} can be assigned to $\delta(H\text{-}O\text{-}H)$ and $\delta(NH_4)$ vibrations which confirm the presence of water molecules and ammonium cations as determined from single crystal X-ray diffraction.

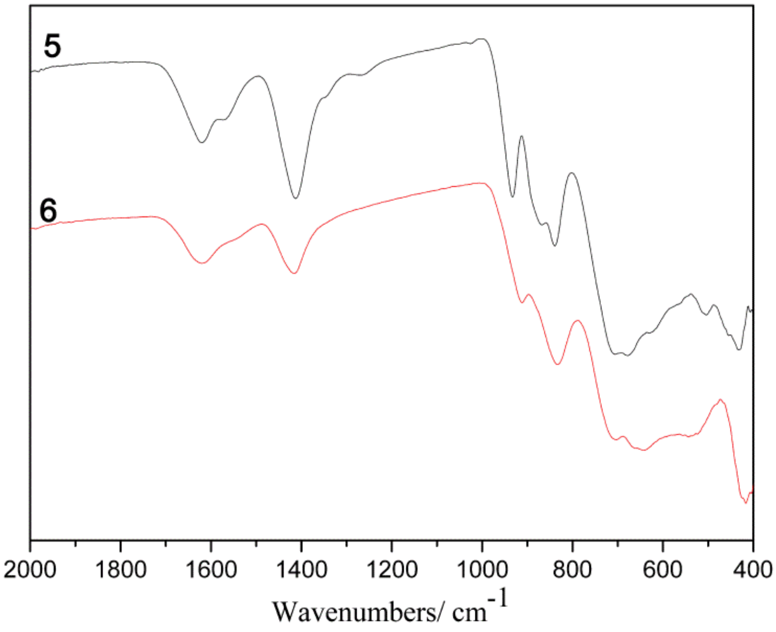

Figure 6.11. FT-IR spectra of **(5)** and **(6)** in solid state (recorded on KBr discs).

The υ(W-O$_t$) and υ(W-O$_b$) vibrations of **(5)** and **(6)** are furthermore evident from characteristic Raman bands at 951 and 881 cm^{-1} or 938 and 876 cm^{-1}, respectively (Figure. 6.12). Both FT-IR and Raman spectra agree with the results of X-ray structure determination.

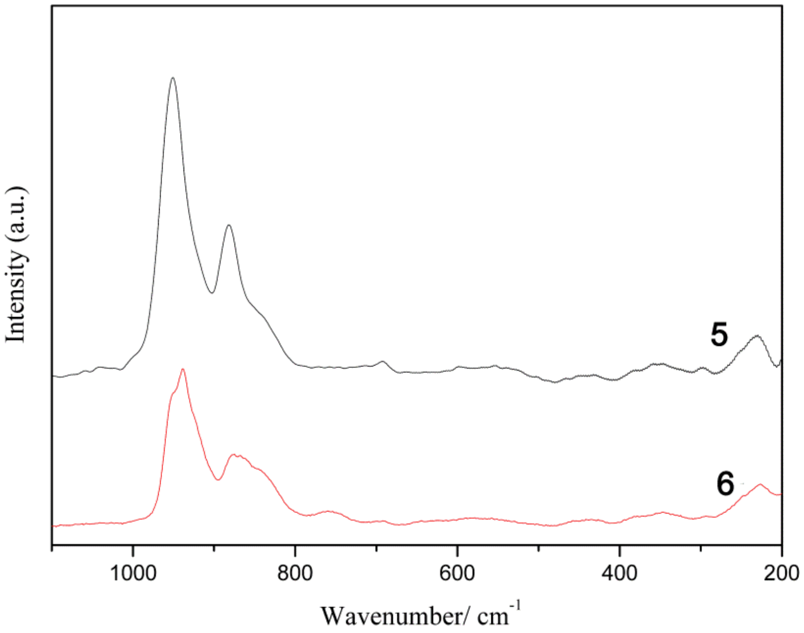

Figure 6.12. Solid state Raman spectra of **(5)** and **(6)**.

6.3.2.4. UV/Vis spectroscopy

The solid-sate UV/Vis spectra in the range between 190 and 700 nm (Figure 6.13) display two absorption bands centered at 265 and 312 nm for **(5)**, and 267 and 370 nm for **(6)**, respectively. Absorption bands at higher energies are assigined to p_π-d_π charge-transfer transitions of the $O_{b(c)}$→W bonds,[19] whereas the low energy bands are likely due to O→Zn charge transfer or W-O-Sb intervalence band transfer[6b] in the visible region. The colorless $\{SbW_9\}$ precursor is transformed into the visible light absorbing compounds **(5)** and **(6)** with band gaps of 2.98 and 2.76 eV, respectively.

The incorpation of Sb^{3+} and Zn^{2+} metal cations into sandwiched $\{Zn_2Sb_2\}$ polyanions through a hybridization of O_{2p} orbitals with d or s metal orbitals probably lead to the obvious shift of valence band position. This is a promising perspective for the development of visible-light-driven POM photocatalysts.

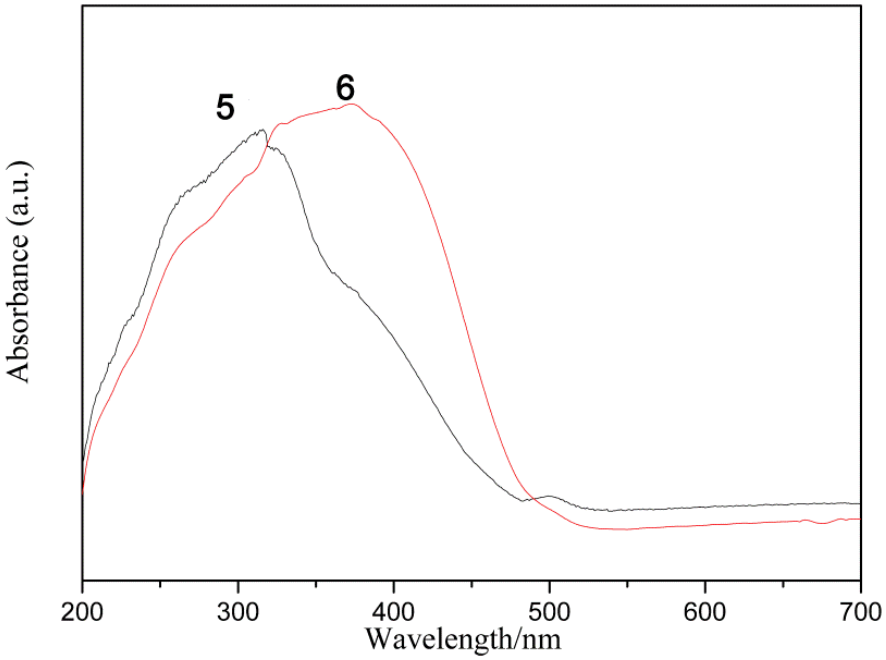

Figure 6.13. Solid state UV/Vis spectra of **(5)** and **(6)**. (band gap: E_g (eV) = hc / $\lambda \approx 1240$ / λ_{onset}, h = Planck’s constant; c = speed of light in vacuum.)

6.3.2.5. Photoluminescence properties

As the d^{10} cations can influence the photoluminescent properties of the different TM cluster arrangements, room temperature photoluminescent spectra of both compounds **(5)** and **(6)** were recorded (Figure 6.14). Excitation at 325 nm **(5)** and 385 nm **(6)** led to related blue photoluminescence of both compounds with four characteristic emission peaks around 423, 443, 484 and 530 nm. The closed d^{10} electronic shell configuration of Zn^{2+} cations leads to the absence of d-d transitions in the photoemission spectra. However, ligand-to-metal charge transfer (LMCT) processes are based on transitions *p* orbitals from ligand to different metal orbitals, i.e. d orbitals, low-lying s orbitals or empty p orbitals.[20] Therefore, the emission peaks around 423 and 443 nm are probably connected to $\{Zn_2Sb_2\}$ cluster formation and LMCT phenomena.[12] In line with photoluminescence spectra of other Zn-containing POMs with related lacunary building blocks,[19] the emission peaks around 484 nm of **(5)** and **(6)** arise from $^3T_{1u} \rightarrow {}^1A_{1g}$ transitions derived from O → W LMCT transitions within the $\{SbW_9\}$ fragments.

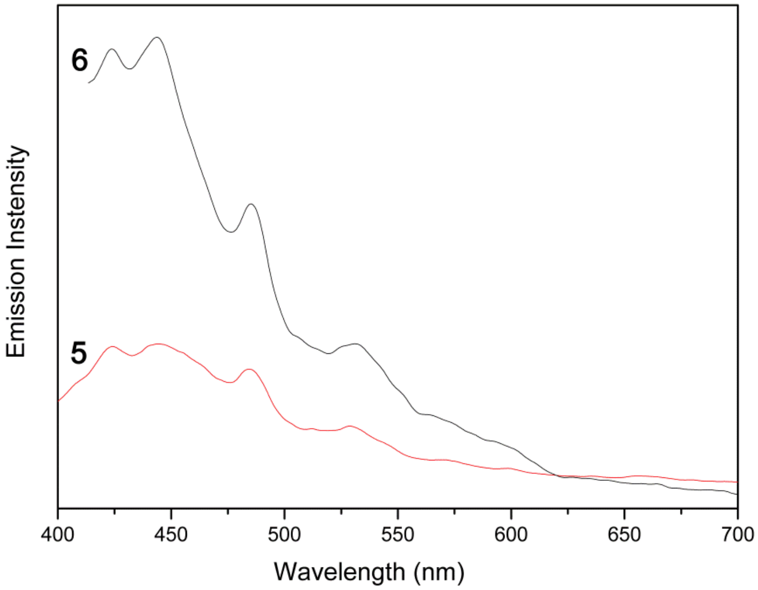

Figure 6.14. Photoluminescence spectra of **(5)** and **(6)** recorded in aqueous solution at room temperature (excitation wavelengths at 325 and 385 nm, respectively).

6.3.3. Catalytic oxidation of cyclohexanol

Moreover, we also explored catalytic studies for homogeneous oxidation of cyclohexanol into cyclohexanone by **(5)** and **(6)** in the presence of H_2O_2 at 85 ^{o}C for 7h (Scheme 6.1, experimental sections). The catalytic efficiency of **(6)** is lower than of **(5)** (yields: 98% for **(5)** and 87% for **(6)**, respectively). This may be due to a higher extent of Na- and Zn-assisted linking among the catalytically active $\{ZnW_9\}$ units which might shield their active sites. Further detail investigations into the influence of preparative history and crystal structure on the catalytic properties of zinc-containing polyoxotungstoantimonates are currently under way.

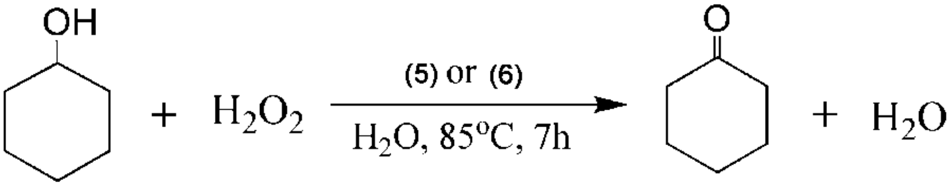

Scheme 6.1 Cyclohexanol oxidation catalyzed by **(5)** and **(6)**.

6.4. Conclusions

In conclusion, two novel 1D and 2D polyoxometalate (POM) frameworks **(5)** and **(6)** based on the new $[Zn_2Sb_2(\alpha\text{-}B\text{-}ZnW_9O_{34})_2]^{14-}$ building block were selectively obtained from one-pot transformations of the trilacunary *Keggin*-type $[B\text{-}\alpha\text{-}SbW_9O_{33}]^{9-}$ precursor via Sb/Zn exchange, followed by self-assembly of the sandwich-type polyanions. The new solution-based transformation of the $\{SbW_9\}$ fragment into a *Keggin*-type $[B\text{-}\alpha\text{-}ZnW_9O_{34}]^{12-}$ unit was induced by heating and addition of a zinc source. The Zn/Sb-containing POMs-based polymeric structures can be steered into networks with different dimensionality through adjusting the Zn^{2+} concentration, respectively. Furthermore, electrochemical and luminescence properties of **(5)** and **(6)** were investigated. Preliminary catalytic studies show that the polymeric POMs catalysts **(5)** and **(6)** also exhibit high catalytic activity in homogeneous alcohol oxidation of cyclohexanol, compared to the discrete POMs catalysts ***α-/β*-[$Zn_2Sb^{III}_2$]**. Further investigations of POMs with multiple metal centers for catalytic applications are currently under way. The present results open up new ways to explore and to control assemblies and structural transformations of TM-POM-based coordination polymers as a tuneable functional materials.

References

[1] (a) Mizuno, N.; Uchida, S.; and Uehara, K. *Pure Appl. Chem*., **2009**, 81, 2369–2376. (b) Antonova, E.; Naether, C.; Koegerler, P.; Bensch, W. *Angew. Chem. Int. Ed*., **2011**, 50, 764–767. (c) Nohra, B.; El Moll, H.; Albelo, L. M. R.; Mialane, P.; Marrot, J.; Mellot-Draznieks, C.; O'Keeffe, M.; Biboum, R. N.; Lemaire, J.; Keita, B.; Nadjo L.; Dolbecq, A.; *J. Am. Chem. Soc*., **2011**, 133, 13363–13374. (d) Thorimbert, S.; Hasenknopf, B.; Lacote, E. *Isr. J. Chem*., **2011**, 51, 275–280. (e) Errington, R. J.; Petkar, S. S.; Middleton, P. S.; McFarlane, W. *J. Am. Chem. Soc*., **2007**, 129, 12181–12196.

[2] (a) Hutin, M.; Long, D.-L.; Cronin, L. *Isr. J. Chem*., **2011**, 51, 205–214. (b) Long, D.-L.; Burkholder, E.; Cronin, L. *Chem. Soc. Rev*., **2007**, 36, 105–121.

[3] Kikukawa,Y.; Yamaguchi, K.; Mizuno, N. *Angew. Chem. Int. Ed*., **2010**, 49, 6096–6100.

[4] Niu, J.-Y.; Ma, X.; Zhao, J.-W.; Ma, P.-T.; Zhang, C.; Wang, J.-P. *CrystEngComm*, **2011**, 13, 4834–4837.

[5] Kikukawa,Y.; Yamaguchi, K.; Mizuno, N. *Angew. Chem. Int. Ed*., **2010**, 49, 6096–6100.

[6] Tang, J.; Yang, X.-L.; Zhang, X.-W.; Wang, M.; Wu, C.-D. *Dalton Trans*. **2010**, 39, 3396–3399.

[7] Liu, Y.; Liu, B.; Xue, G.; Hu, H.; Fu, F.; Wang, J. *Dalton Trans*., **2007**, 3634–3639.

[8] Ni, L.; Patscheider, J.; Baldridge, K. K.; Patzke, G. R. *Chem. Eur. J*. **2012**, 18, 13293–13298.

[9] Ni, L.; Patzke, G. R. *CrystEngComm.* **2012**, 14, 6778–6782.

[10] Yin, P.; Li, D.; Liu, T. *Isr. J. Chem.*, **2011**, 51, 191–204.

[11] Michailovski, A.; Rüegger, H.; Sheptyakov, D.; Patzke, G. R. *Inorg. Chem.*, **2006**, 45, 5641–5652.

[12] Bösing, M.; Loose, I.; Pohlmann, H.; Krebs, B. *Chem. Eur. J.*, **1997**, 8, 1232–1237.

[13] Oxford Diffraction, CrysAlis CCD and CrysAlis RED, Oxford Diffraction Ltd., Abingdon, UK, **2005**.

[14] Farrugia, L. J. *J. Appl. Crystallogr.* **1999**, 32, 837–838.

[15] G. M. Sheldrick, SHELX97, *Programs for Crystal Structure Analysis*; Release 97-2; University of Göttingen; Göttingen: Germany, **1997**.

[16] (a) Sadakane, M.; Dickman, M. H.; Pope, M. T. *Inorg. Chem*. **2001**, 40, 2751–2755. (b) du Peloux, C.; Dolbecq, A.; Mialane, P.; Marrot, J.; Rivière, E.; Sécheresse, F. *Inorg. Chem.* **2002**, 41, 7100–7104. (c) Gaunt, A. J.; May, L.; Collison, D.; Fox, D. *Inorg. Chem*. **2003**, 42, 5049–5051. (d) Lei, C.; Mao, J.-G.; Sun, Y.-Q.; Song, J.-L. *Inorg. Chem.* **2004**, 43, 1964–1968. (e) Mazeaud, A.; Dromzee, Y.; Thouvenot, R. *Inorg. Chem*. **2000**, 39, 4735–4740. (f) Juraja, S.; Vu, T.; Richardt, P. J. S.; Bond, A. M.; Cardwell, T. J.; Cashion, J. D.; Fallon, G. D.; Lazarev, G.; Moubaraki, B.; Murray, K. S.; Wedd, A. G. *Inorg. Chem*. **2002**, 41, 1072–1078. (g) Dolbecq, A.; Cadot, E.; Eisner, D.; Sécheresse, F. *Inorg. Chem*. **1999**, 38, 4217–4223. (h) Villanneau, R.; Proust, A.; Robert, F.; Viellet, P.; Gouzerh, P. *Inorg. Chem*. **1999**, 38, 4981–4985. (i) Volkmer, D.; Bredenkötter, B.; Tellenbröker, J.; Kögerler, P.; Kurth, D. G.; Lehmann, P.; Schnablegger, H.; Schwahn, D.; Piepenbrink, M.; Krebs, B. *J. Am. Chem. Soc.* **2002**, 124, 10489–10496.

[17] (a) Brown, I. D.; Altermatt, D. *Acta Crystallogr., Sect. B.* **1985**, 41, 244–247. (b) Trzesowska, A.; Kruszynski, R.; Bartczak, T. J. *Acta Crystallogr. Sect. B,* **2004**, 60, 174–178.

[18] Jung, G.; Rhee, G. K. *J. Electroanal. Chem.*, **1997**, 436, 277–280.

[19] J. Tao, J.-X. Shi, M.-L. Tong, X.-X. Zhang and X.-M. Chen, *Inorg. Chem.*, **2001**, 40, 6328–6330.

[20] Barbieri, A.; Accorsi, G.; Armaroli, N. *Chem. Commun.*, **2008**. 2185–2193.

7. Zn/Sb-Polyoxotungstate Oxidation Catalysts with Tailored Cores: Structural, Computational and Reactivity Studies on a POM Family

7.1. Introduction

Contemporary POM science has become a great interdisciplinary melting pot where structural and materials chemistry meet at the interface between solid state and molecular design to open up an unmatched variety of application fields. [1] In particularly, development of catalysis benefits considerably from newly discovered POMs as oxidation catalysts for essential organic transformations.[2] Nevertheless, two crucial remaining open problems still need to be addressed to tap the full design potential of POMs as prototype homogeneous catalysts, namely predictive structural control over new motifs and comprehensive understanding of their catalytic mechanisms.

Among the growing multitude of POM architectures, transition metal substituted POMs (TMSPs) have been regarded as the largest subclass particularly for innovative catalyst development.[3] Sandwich-type TMSPs encompass by far the most representatives due to their flexible building block principally which permits the stable incorporation of various metal cores between a variety of lacunary POM shells. Tri-lacunary fragments of the α-*Keggin* type {B-α-XW_9O_{33}} (X = As^{III}, Sb^{III}, Bi^{III}, Te^{IV}, Se^{IV}) have emerged as especially flexible hosts[4-16] for a variety of core types and nuclearities: from mononuclear Ti-POMs [4] over dinuclear Ti-[5] and Zn-, Mn- or Co-POMs,[6] respectively, to tri-[6],[7],[8], tetra-[9] and pentanuclear cores.[10] Furthermore, hexanuclear cores have also been reported for V-based[11] or Mn- or Cu[12]-sandwiched POMs.[13] Representative examples for sandwiched Zn-rich cores include $[Zn_6Cl_6(\alpha\text{-}XW_9O_{33})_2]^{12-}$ (X = As^{III}, Bi^{III}),[14] $[M_6(imi)_6(B\text{-}\alpha\text{-}HAsW_9O_{33})^2]$ (M = Ni^{2+}, Zn^{2+}, Mn^{2+}; imi = imidazole),[15] $[Zn(Hen)_6(B\text{-}\alpha\text{-}HAsW_9O_{33})_2]$ (en = ethylenediamine),[16] and $[Zn_6(phen)_2(AsW_9O_{33})_2]^{4-}$ (phen = phenanthroline)[14a]. However, the exploration of tunable synthetic routes to full control the composition of TM central clusters from mono- to hexa- nuclear in the one sandwiched TMSPs system, still remains a key challenge. In particular, the modification of polyoxoanions with TM central cores grafted onto the nucleophilic oxygen atoms of TM cores may be an effective route to increase the surface electronegativity and to activate the surface oxygen atoms of such polyanions for oxidation and epoxidation catalysis.

Such investigations are of crucial importance to close the gap between considerable progress in POM catalyst development and the persisting lack of knowledge about their actual reactive sites and reaction pathways that has been opening up during the past decades of intense research into this topic.[17-20] Outstanding examples include the highly efficient $[WZnM_2(H_2O)_2(ZnW_9O_{34})_2]^{q-}$ (M = Mn^{II}, Ru^{III}, Zn^{II}, Pd^{II}, Rh^{III}) catalyst series for liquid-phase oxidations with hydrogen peroxide reported by *Neumann* et al. [17] and $[(Mn^{II}(H_2O)_3(SbW_9O_{33})_{12})]^{12-}$ developed by *Krebs* et al. for regioselective epoxidation processes.[18] Recent progress on Zn-containing POM catalysts was achieved by *Mizuno* et al. on sandwich-type Zn(II)-containing silicotungstates for the oxidation of secondary alcohols[19] or by the thermally induced isomerization of a metastable precursor POM into a zinc-cored silicotungstate with a central hexaprismane motif.[20] Nevertheless, three key issues remain to be resolved to date for the majority of POM oxidation catalysts which facilitate industrially relevant organic reactions. The first open question is the identification of their active sites which may either be located in the core (as frequently anticipated but rarely proven), in the lacunary shells or might as well arise from an interaction of both parts. Second, the methodological limits for the isolation of often short-lived competent POM intermediates remain a roadblock on the way of coherent mechanistic models. Third, modeling of transition states and reaction pathways involved in POM-catalyzed organic transformations remain very demanding when performed for complete and unrestricted POM architectures in genuine solvent environments.

Here, we present the first controlled access to step-wise increasing Zn-core nuclearities sandwiched between tri-lacunary *Keggin* $\{B\text{-}\alpha\text{-}SbW_9O_{33}\}$ shells, which brought forward a new family of more than 10 structurally characterized members of this series as economic and robust oxidation catalysts. Catalytic alcohol oxidation performance tests permitted a new degree of systematic insight into their structure-activity relationships. Furthermore, high level theoretical calculations in solvent environments provide unprecedented insight into the hitherto poorly understood mechanisms of POM-catalyzed oxidative transformations. Therefore, the research results in this chapter pushes the boundaries of oxocluster-based homogeneous catalysis on the synthetic, catalytic and computational level.

Synthetic tailoring: We have established tuneable synthetic routes to a large family of sandwich-type Zn/Sb-POMs. For the first time, we exert full control over the core nuclearity of a POM catalyst series as represented by more than 10 members of the $\{Zn_nNa_{6-n}(B\text{-}\alpha\text{-}SbW_9O_{33})_2\}$ (n = 3-6) family.

Catalytic routes via core design: We demonstrate with comprehensive catalytic tests that the POM tailoring parameters, such as different core compositions (Cu-belt or Zn-belt), variations of zinc content etc., exert key influence on the catalytic activity. Hydroperoxo- or peroxotungstate intermediates were identified as active species with a wide range of spectroscopic and analytical methods. The crucial importance of POM belt construction is evident from comparison of the $\{Zn_nNa_{6-n}(B\text{-}\alpha\text{-}SbW_9O_{33})_2\}$ (n = 3-6) catalyst series with $[\alpha/\beta\text{-}Zn_2Sb^{III}_2(ZnW_9O_{34})_2]^{14-}$ catalysts containing active Sb centers.[21]

Computational insights: Spectroscopic and catalytic results are corroborated with solution-based modeling of intermediates and transition states involved in Zn-POM catalyzed cyclohexanol oxidation. We present theoretical insight into the hitherto unknown reaction mechanism on an unprecedented high level of theory.

7.2. Experimental section

7.2.1. Synthetic methods

Synthesis of $Na_9Zn[Zn_4Na_2(H_2O)_8(SbW_9O_{33})_2][Zn_{2.6}Na_{0.4}(H_2O)_{2.6}(SbW_9O_{33})]\cdot45H_2O$ **$\{Zn_4\text{-}Zn_{5.2}$ (7a)$\}$**. 0.754 g (0.26 mmol) of $Na_9[SbW_9O_{33}]\cdot19.5H_2O$ was dissolved in 25 mL of water and heated to 85 ºC under stirring. After 20 min, 0.259 g (0.90 mmol) of $Zn(SO_4)_2\cdot7H_2O$ was added in individual portions at pH values around 5.5 ~ 6.5. The solution was left stirring for 90 min at 85 ºC, cooled to room temperature and filtered. Slow evaporation of the solution afforded colourless crystals. Yield: 0.468g, 62.3 % based on W. TGA showed a weight loss of 10.5 % in the 30 - 240 ^{o}C temperature range, corresponding to the loss of coordinating and solvent water molecules (expected 11.2%). FT-IR (cm^{-1}): 1624(vs), 1140(m), 1119(m), 946(vs), 897(vs), 834(s), 728(m). 634(m), 519(m), 470(w). Raman (cm^{-1}): 961(vs), 888(s), 848(m), 797(w), 695(w), 515(w), 312(m), 224(m). Elemental analysis calcd. (found). W 57.29 (57.90); Zn 6.03 (6.24); Sb 4.21 (4.29); Na 2.92 (3.44); H 1.27 (1.12).

Synthesis of $NaZnH_8$ $[Zn_4Na_2(H_2O)_8(SbW_9O_{33})_2][Zn_{2.6}Na_{0.4}(H_2O)_{2.6}(SbW_9O_{33})]\cdot 46H_2O$ **{Zn_4-$Zn_{5.2}$ (7b)}**. The synthesis was performed as described above for **Zn_4-$Zn_{5.2}$ (7a)** with one alteration: 2~5 drops NH_4Cl solution (1.0 M) were added dropwise to the filtrate. Slow evaporation of the solution can afford coloress crystals **Zn_4-$Zn_{5.2}$ (7a)** mixed with small amounts of another block-shaped crystals **Zn_4-$Zn_{5.2}$ (7b)**. FT-IR (cm^{-1}): 1629(vs), 939(vs), 838(vs), 675(m). 621(m), 514(m), 432(w). Raman (cm^{-1}): 966(vs), 885(s), 848(m), 700(w), 530(w), 448(w), 373(m), 318(m), 225(m). Elemental analysis calcd. (found). W 58.17 (56.90); Zn 6.13 (5.84); Sb 4.28 (4.27); Na 0.81 (3.00); H 1.34 (1.16).

Synthesis of $Na_8(NH_4)_2H_9\{[Zn_5NaCl_3(H_2O)_4(SbW_9O_{33})_2][Zn_{5.2}Na_{0.8}(H_2O)_{5.2}(SbW_9O_{33})_2]\}[SbCl_6]_{0.5}\cdot 43H_2O$ **{Zn_5-$Zn_{5.2}$ (8)}**, $Na_4H_9[Zn_6(H_2O)Cl_5(SbW_9O_{33})_2]\cdot 44H_2O$ **{Zn_6 (9a)}**, and $Na_2H_7[Zn_5Na(H_2O)_5Cl_2(SbW_9O_{33})_2]\cdot 33H_2O$ **{Zn_5 (10)}**. The above synthetic procedure was modified by the addition of 8~12 drops NH_4Cl solution (1.0 M) to the filtrate. Slow concentration at room temperature led to the formation of large block-shaped crystals of $Na_2Zn(SO_4)_2\cdot 4H_2O$ as a side product together with a mixture of **{Zn_5-$Zn_{5.2}$ (8)}**, **{Zn6 (9a)}** and **{Zn_5 (10)}**. As the narrow preparative window for these compounds renders their separation practically impossible, we summarize their crystallographic data in Table 10.14- 10.15 (Annexes).

Synthesis of $(NH_4)_{12}[Zn_6Cl_6(SbW_9O_{33})_2]\cdot 16H_2O$ **{Zn_6 (9b)}**. The synthetic method for **Zn_6 (9b)** is similar as described above for the synthesis of **Zn_4-$Zn_{5.2}$ (7)** except for addition of 15~30 drops of NH_4Cl solution (1.0 M) to the filtrate. Slow evaporation of the solution afforded colorless crystals. Yield: 0.391g, 53.3% based on W. TGA showed a weight loss of 5.0 % in the 30-198 ^oC temperature range, corresponding to the loss of coordinating and solvent water molecules (expected 5.0 %), followed by a slower weight loss of 7.9 % between 202 – 515 ^oC caused by release of ammonia and hydrogen chloride (expected 7.6 %). FT-IR (cm^{-1}): 1618(vs), 1408(vs), 970(m), 946(vs), 894(vs), 858(s), 826(s), 708(m). 665(m), 522(m), 470(w). Raman (cm^{-1}): 968(vs), 936(m), 886(w), 843(s), 693(w), 522(w), 312(m), 223(m). Elemental analysis calcd. (found): W 57.87 (58.30); Zn 6.86 (6.77); Sb 4.26 (4.30); Cl 3.72 (3.39); N 2.93 (2.13); H 1.41 (1.10).

Synthesis of $Na_7[Zn_5Na(H_2O)_5(CH_3COO)_2(SbW_9O_{33})_2]\cdot27H_2O$ **{Zn_5(11a)}** and $Na_6H_4[Zn_5Na(H_2O)_4Cl(CH_3COO)_2(SbW_9O_{33})_2]\cdot36H_2O$ **{Zn_5(11b)}**. Method for **Zn_5 (11a)**: 0.190g (0.87 mmol) of $Zn(OAc)_2\cdot2H_2O$ was dissolved in 25 mL of water and heated to 85 ºC under stirring. After 20 min, 0.754 g (0.26 mmol) of $Na_9[SbW_9O_{33}]\cdot19.5H_2O$ was added in individual portions at pH values around 6.0 ~ 6.5. The mixture was left stirring for 90 min at 85 ºC, cooled to room temperature and filtered. Slow evaporation of the solution afforded colourless crystals (**11a**; Yield: 0.294g, 38.8 % based on W. TGA showed a weight loss of 9.9% in the 30 - 190 ^{o}C temperature range, corresponding to the loss of coordinating and solvent water molecules (expected 10.2%), followed by a slower weight loss of 2.0% between 200 – 408 ^{o}C caused by release of acetate ligands (expected 2.6%). FT-IR (cm^{-1}): 1622(vs), 1411(s), 929(vs), 870(vs), 846(s), 698(vs), 626(s), 503(m), 430(w). Raman (cm^{-1}): 959(vs), 932(m), 893(s), 846(m), 695(w), 514(w), 314(m), 223(m). Elemental analysis calcd. (found): W 56.90 (55.40); Zn 5.62 (5.51); Sb 4.18 (4.10); Na 3.16 (3.55); C 0.82 (0.66); H 1.23 (0.87).

For **Zn_5 (11b)**: 0.754 g (0.26 mmol) of $Na_9[SbW_9O_{33}]\cdot19.5H_2O$ was dissolved in 25 mL of water and heated to 85 ºC under stirring. After 20 min, 0.300g (1.37 mmol) of $Zn(OAc)_2\cdot2H_2O$ was added in individual portions. The solution underwent a colour change to light yellow at pH values around 6.0 ~ 6.5. The mixture was left stirring for 90 min at 85 ºC, cooled to room temperature and filtered. Addition of 5 drops of NH_4Cl solution (1.0 M) to the yellow filtrate, followed by slow evaporation of the solution afforded colourless crystals **(11b)** mixed with small amount of yellow crystal of $Na_{14}[\beta\text{-}Zn_2Sb^{III}_2(ZnW_9O_{34})_2]\cdot46H_2O$[21] TGA showed a weight loss of 9.6 % in the 30 – 210 ^{o}C temperature range, corresponding to the loss of coordinating and solvent water molecules (expected 11.0 %), followed by a slower weight loss of 3.6% between 210 – 446 ^{o}C caused by release of acetate ligands and hydrogen chloride (expected 2.6 %). FT-IR (cm^{-}

^{1}): 1622(vs), 1411(s), 929(vs), 870(vs), 846(s), 698(vs), 626(s), 503(m), 430(w). Raman (cm^{-1}): 960(vs), 934(m), 892(s), 843(m), 783(w), 688(w), 514(w), 444(w), 314(m), 223(m). Elemental analysis calcd. (found): W 55.51 (55.90); Zn 5.48 (5.32); Sb 4.08 (4.22); Na 3.08 (3.11); Cl 0.59 (0.48); C 0.80 (0.67); H 1.44(1.29).

Synthesis of $Na_5H_4[Zn_4Na_2(H_2O)_7(CH_3COO)(SbW_9O_{33})_2]\cdot 28H_2O$ {**Zn_4 (12a)**} and $Na_5(NH_4)_5H_2[Zn_{4.1}Na_{1.9}Cl_3(H_2O)_7(CH_3COO)(SbW_9O_{33})_2]\cdot 24.5H_2O$ **{Zn_4 (12b)}**. The synthetic ethod for **Zn_4(12a)** is similar as described above for the synthesis of **Zn_5(11a)** with one alteration: the addition of 5-10 drops of NH_4Cl solution (1.0 M) to the filtrate. Slow evaporation of the solution afforded colourless crystals. Yield: 0.545g, 73 % based on W. TGA showed a weight loss of 7.8 % in the 30-160 ^{o}C temperature range, corresponding to the loss of coordinating and solvent water molecules (expected 7.9 %). FT-IR (cm^{-1}): 1628(s), 1571(s), 1413(s), 937(vs), 888(vs), 848(s), 712(m). 679(m), 503(m), 430(w). Raman (cm^{-1}): 959(vs), 875(s), 848(s), 799(w), 690(w), 517(w), 316(m), 225(m). Elemental analysis calcd. (found): W 58.10 (57.00); Zn 4.59 (4.69); Sb 4.28 (4.21); Na 3.23 (3.53); N 0.73 (0.51); H 1.29(1.12), C 0.42 (0.68).

Method for **Zn_4(12b)** is similar as described above for the synthesis of **Zn_5(11a)** except for addition of 35-40 drops NH_4Cl solution (1.0 M) to the filtrate. Slow evaporation of the solution afforded colourless crystals. Yield: 0.308 g, 40 % based on W. TGA showed a weight loss of 8.9 % in the 30 – 205 ^{o}C temperature range, corresponding to the loss of coordinating and solvent water molecules (expected 8.5%), FT-IR (cm^{-1}): 1626(s), 1414(s), 931(vs), 871(vs), 848(vs), 702(s), 684(s), 625(m), 503(m), 430(w). Raman (cm^{-1}): 1041(m), 968(vs), 935(s), 898(s), 851(s), 782(w), 693(w), 517(w), 449(w), 319(m), 223(m). Elemental analysis calcd. (found): W 56.63 (57.10); Zn 4.47 (4.65); Sb 4.16 (4.23); Na 2.36 (2.94); Cl 1.82 (0.59); N 1.19 (1.34); H 1.55(1.46), C 0.41 (0.45).

Synthesis of $(NH_4)_4Na_7[Zn_4Na_2Cl_3(H_2O)_5(SbW_9O_{33})_2]\cdot 16H_2O$ **{Zn_4 (12c)}** and $Na_{6.5}H_4[Zn_{3.5}Na_{2.5}Cl_2(H_2O)_{6.5}(SbW_9O_{33})_2]\cdot 25H_2O$ **{$Zn_{3.5}$ (13)}**. The experimental strategy is similar as described above for the synthesis of **Zn_5 (11a).** The only alteration is the addition of 15-25 drops NH_4Cl solution (1.0 M) to the filtrate. Slow evaporation of the solution afforded a mixture of three crystals (**12a**, **12c** and **13)**.

For **Zn_4 (12c)**: TGA showed a weight loss of 7.3 % in the 30 - 180 °C temperature range, corresponding to the loss of coordinating and solvent water molecules (expected 6.7 %), followed by a slower weight loss of 2.9% between 180 – 410 °C caused by release of ammonia and hydrogen chloride (expected 3.2 %). FT-IR (cm^{-1}): 1626(s), 1404(s), 935(vs), 876(s), 837(s), 716(m), 673(m), 509(m), 431(w). Raman (cm^{-1}): 966(vs), 890(s), 878(s), 791(w), 697(w), 529(w), 324(m), 229(m). Elemental analysis calcd. (found): W 58.73 (56.40); Zn 4.64 (4.81); Sb 4.32 (4.81); Cl 1.88 (1.58); H 1.03 (1.28); N 0.99 (1.00).

For **$Zn_{3.5}$ (13)**: TGA showed a weight loss of 9.6 % in the 30 - 210 °C temperature range, corresponding to the loss of coordinating and solvent water molecules (expected 10.0 %). FT-IR (cm^{-1}): 1628(s), 1419(s), 928(vs), 867(vs), 851(s), 698(m), 500(m), 431(w). Raman (cm^{-1}): 953(vs), 895(s), 878(s), 794(w), 687(w), 518(w), 442(w), 318(m), 231(m). Elemental analysis calcd. (found): W 58.53 (56.50); Zn 4.04 (4.29); Sb 4.31 (4.21); Cl 1.25 (0.97); H 0.60 (1.00).

Synthesis of $Na_9[Zn_3Na_3(H_2O)_9(SbW_9O_{33})_2]\cdot 42H_2O$ **{Zn_3 (14)}**. The polyanion $[Zn_3(H_2O)_3(SbW_9O_{33})_2]^{12--}$ has been firstly reported by *Kortz* et al in 2001.[6] In the following, a different synthetic approach was employed.. Synthesis of **Zn_3(14)** was similar as described above for the synthesis of **Zn_4_$Zn_{5.2}$(7a)** with one alteration: 0.863 g (3 mmol) $Zn(SO_4)_2\cdot 7H_2O$ instead of 0.259 g (0.90 mmol). Yield: 0.523g, 67.5 % based on W.

Synthesis of $Na_7Cs_2Zn_{1.6}H_{1.8}[Zn_2(H_2O)_6(WO)_2(\beta\text{-}SbW_9O_{33})_2]Cl_4\cdot 32H_2O$ **{Zn_2W_2} (15)** The polyanion $[Zn_2(H_2O)_6(WO_2)_2(\beta\text{-}SbW_9O_{33})_2]^{10-}$ has been firstly reported by *Krebs* et al in 2002.[22] Here, an alternative method was employed to obtain the cesium salt of $[Zn_2Sb_2W_{20}O_{70}]^{10-}$ **(9):** 0.754 g (0.26 mmol) of $Na_9[SbW_9O_{33}]\cdot 19.5H_2O$ was dissolved in 25 mL of sodium acetate buffer (0.5M, pH 4.4) and heated to 85 ºC under stirring. After 20 min, 0.259 g (0.90 mmol) of $Zn(SO_4)_2\cdot 7H_2O$ and 0.659 g (2.00 mmol) $Na_2WO_4.2H_2O$ were added in individual portions. The solution was left stirring for 90 min at 85 ºC, cooled to room temperature and filtered. Addition of 1.0 M CsCl solution (0.5mL) to the colorless filtrate and slow evaporation at room temperature afforded colorless crystals.

7.2.2. Catalytic alcohol oxidation

Catalyst, solvent, substrate, and 30 % aqueous H_2O_2 were successively placed into a round-bottom flask for alcohol oxidation reactions. A Teflon-coated magnetic stirring bar was added and the reaction mixture was stirred at 85°C. Detailed reaction conditions are given in the caption of Table 7.2. All yields reported in this manuscript are based on alcohol conversion. Reaction products were characterized and quantified with a gas chromatograph (Finnigan Trace GC Ultra) equipped with a flame ionization detector and fitted with a ZB-5MS Phenomenex column (30 m length, 0.25 mm internal diameter, 0.25 μm film thickness) using dodecane as internal reference. Products were furthermore identified by GC-MS (Finnigan Trace DSQ GC-MS systems).

7.2.3. X-ray crystallography

Data collections of all compounds were performed on an Oxford Xcalibur Ruby CCD single-crystal diffractometer (MoK_α radiation, λ= 0.71073 Å) at 183(2) K. Routine Lorentz and polarization corrections were applied, and an absorption correction was performed using the program *CrysAlis* (multi-scan).[23] The structural analysis was performed using the *Win-GX for Windows* software.[24] Direct methods were used to locate heavy metal atoms (SHELXS-97). The remaining atoms were located from successive Fourier maps (SHELXL-97).[25] Hydrogen atoms were not included in the refinements. Heavy metal atoms (Sb, Zn, W and Na) were refined anisotropically and oxygen atoms were refined isotropically. The lighter atoms in POMs are generally difficult to refine anisotropically due to the presence of manifold heavy metal atoms.[26] The Zn7 and Na3 sites are site-occupancy disordered with the occupancies of 0.6 (0.4) for Zn7 (Na3) in **(7a)**. For **(7b)**, W6 and W7 exhibit a disorder over two positions with site occupancies of 0.7 and 0.3 respectively. W10, W15, W16, W17, W18, W23, W24 and W31 are site-occupancy disordered with half occupancies each. Zn6 and Na2 are site-occupancy disordered with occupancies of 0.6 for Zn6 and 0.4 Na2 in **(8)**. O33 and Cl2 sites attached to the Zn2 atom are site-occupancy disordered with quarter occupancies in **(9a)**, as Cl2 sits on the mirror plane, this result in one half-occupied chloride and two quarter occupied water molecules just next to the mirror plane. Zn3 and Na1 sites are site-occupancy disordered with half occupancies each in **(10)**. Na1 and Zn5 sites are site-occupancy disordered with occupancies of 0.9 for Na1 and 0.1 for Zn5 in **(12b)**, Finally, Zn2 and Na3 sites are site-occupancy disordered with half occupancies each in **(13)**. Crystal data and structure refinement details for all compounds are summarized in Table 10.15-10.17 (Annexes).

7.3. Results and discussion

7.3.1. Structural description of the catalysts

A series of novel sandwich-type Zn containing-polytungstoantimonates as catalysts for H_2O_2-assisted alcohol oxidation were isolated from the tri-lacunary precursor $Na_9[B\text{-}\alpha\text{-}SbW_9O_{33}]\cdot 19.5\ H_2O$ **{SbW₉}** in the presence of $Zn(OAc)_2$ or $Zn(SO_4)_2$ using the initial NH_4^+ concentration as an efficient and straightforward control parameter (see Exp. part). Single-crystal X-ray diffraction analyses reveal a family of ten new heteropolyanions $\{Zn_nNa_{6-n}\ (B\text{-}\alpha\text{-}SbW_9O_{33})_2\}$ (n = 3-6) consisting of two identical $[B\text{-}\alpha\text{-}SbW_9O_{33}]^{9-}$ moieties which are linked by a wide variety of Zn^{2+} ion cores into sandwich-type TMSPs (Figure 7.1 and 7.2).

The structures of twelve polyoxoanions of $\{[Zn_4Na_2(H_2O)_8(SbW_9O_{33})_2][Zn_{2.6}Na_{0.4}(H_2O)_{2.6}(SbW_9O_{33})]\}^{11-}$ **(7a**, **7b)**, $\{[Zn_5NaCl_3(H_2O)_4(SbW_9O_{33})_2][Zn_{5.2}Na_{0.8}(H_2O)_{5.2}(SbW_9O_{33})_2]\}^{17-}$ **(8)**, $[Zn_6(H_2O)Cl_5(SbW_9O_{33})_2]^{11-}$ **(9a)** and $[Zn_6Cl_6(SbW_9O_{33})_2]^{12-}$ **(9b)**, $[Zn_5Na(H_2O)_5Cl_2(SbW_9O_{33})_2]^{9-}$ **(10)**, $[Zn_5Na(H_2O)_5(CH_3COO)_2(SbW_9O_{33})_2]^{9-}$ **(11a)**, $[Zn_5Na(H_2O)_4Cl(CH_3COO)_2(SbW_9O_{33})_2]^{10-}$ **(11b)**, $[Zn_4Na_2(H_2O)_7(CH_3COO)(SbW_9O_{33})_2]^{9-}$ **(12a)**, $[Zn_{4.1}Na_{1.9}Cl_3(H_2O)_7(CH_3COO)(SbW_9O_{33})_2]^{12-}$ **(12b)**, $[Zn_4Na_2Cl_3(H_2O)_5(SbW_9O_{33})_2]^{11-}$ **(12c)**, $[Zn_{3.5}Na_{2.5}Cl_2(H_2O)_{6.5}(SbW_9O_{33})_2]^{10-}$ **(13)** could be determined by single-crystal X-ray diffraction in combination with elemental and thermogravimetric analyses (see Table 10.15-10.17 in the Annexes and Figure 7.15). Their polyhedral/ball-and-stick representations are shown in Figure 7.1 and 7.2.

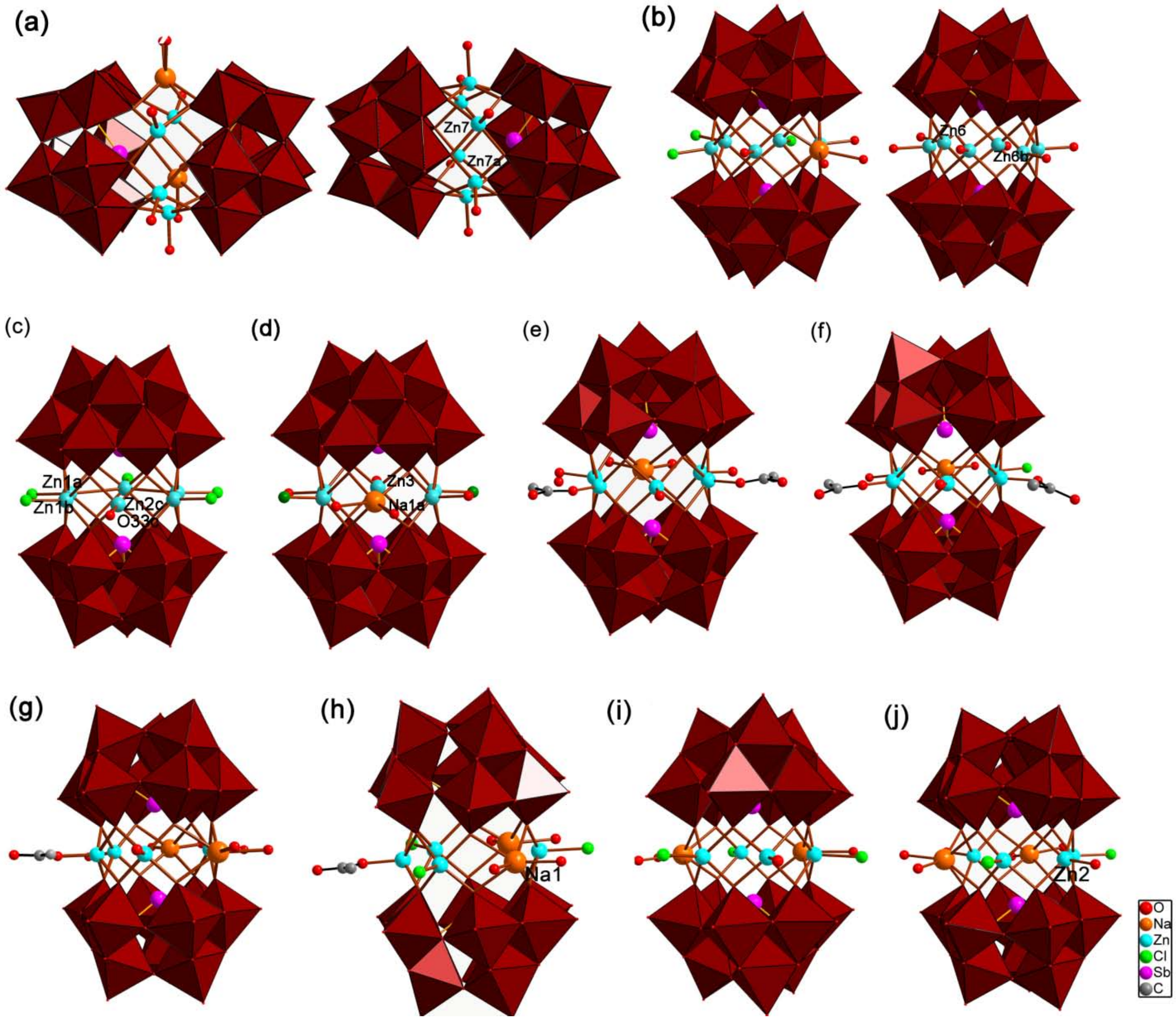

Figure 7.1. Polyhedral representation of the polyoxoanions of (a) **{Zn$_4$-Zn$_{5.2}$} (7a or 7b),** only the major site-occupancy of the disordered Zn7 (Na3) is shown for clarity in (**7a**), Symmetry codes: a, -*x*, *1*-*y*,*1*- *z* for (**7a**); (b) **{Zn$_5$-Zn$_{5.2}$} (8)**, only major site-occupancy of the disordered Zn6 (Na2) is shown for clarity, symmetry codes: b, *1*-*x*, *1*-*y*, *1*-*z*; (c) **{Zn6} (9a)**, Cl2 and O33c positions are site-occupancy disordered with the quarter-occupancies, symmetry codes: a, *x*, -*y*, -*z;* b, -*1*-*x*, -*y*, -*z;* c, -*1*-*x*, *y*, -*z*; (d) **{Zn5} (10)**, the half-occupancy position of the disordered Na1a (Zn3a) is shown for clarity, symmetry codes: a, 1-*x*, -*y*, *1*-*z*; (e) **{Zn$_5$} (11a)**; (f) **{Zn$_5$} (11b)**; (g) **{Zn$_4$} (12a)**; (h) **{Zn$_4$} (12b)**; (i) **{Zn$_4$} (12c)**; (j) **{Zn$_{3.5}$} (13)**, the half-occupied position of the disordered Zn2 (Na3) is shown for clarity. (color codes: WO$_6$ octahedra, red; Sb, pink; W, black; Zn, blue; Na, orange; O, red; C, grey; Cl, green).

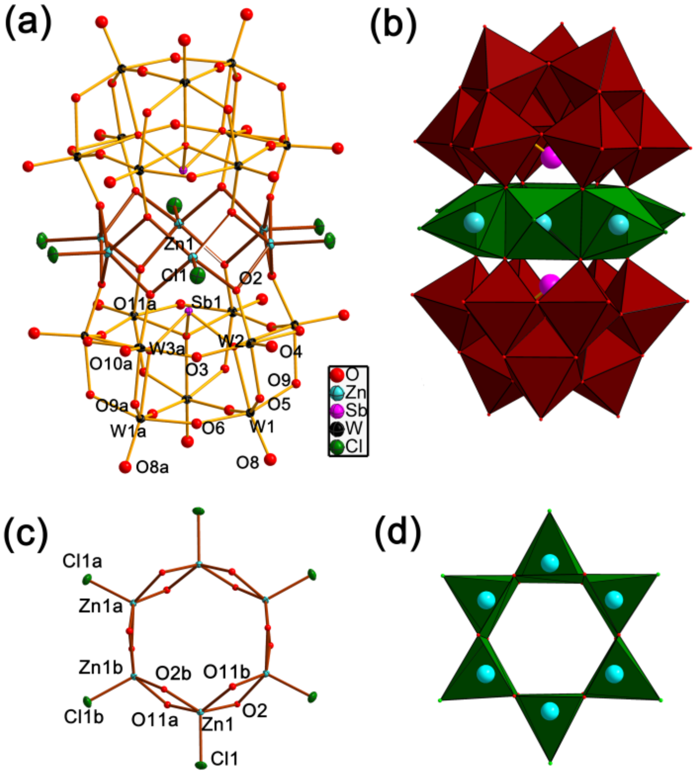

Figure 7.2. (a) Ball-and-stick representations of **Zn_6 (9b)** (thermal ellipsoids of heavy atoms at 50 % probability level). (b) Polyhedral representations of **Zn_6 (9b)**. (c) Ball-and-stick view of the sandwich-type TM belt $[ZnO_2Cl]_6^{18-}$ (d) Polyhedral presentation of the sandwich-type TM belt $[ZnO_2Cl]_6^{18-}$. (Symmetry codes: a, *-0.5+x, 0.5-y, 1-z*; b, *-1+x, 1.5-y, 0.5+z.* Color codes: WO_6 octahedra, red; $Zn(O_4Cl)$ square pyramids, green; Sb, pink; W, black; Zn, blue; O, red; Cl, green).

As each of these new sandwich-type POMs is composed of two **$\{SbW_9\}$** units surrounding a different central transition metal (TM) belt, the **Zn_6 (9b)** is selected as a representative example to discuss the entire structure in more detail. The subsequent structural discussion of the other members of the series is only focused on the variations in the Zn core. Figure 7.2 shows the structure of the $[Zn_6Cl_6(SbW_9O_{33})_2]^{12-}$ polyanion {**Zn_6 (9b)**} described as two $[B\text{-}\alpha\text{-}SbW_9O_{33}]^{9-}$ units connected by a hexagonal Zn_6 ring $[Zn_6Cl_6O_{12}]$ with D_{3d} symmetry resulting from the presence of an inversion center. The polyoxoanion is closely related to the $[Cu_6Cl_6(AsW_9O_{33})_2]^{12-}$ and $[Mn_6Cl_6(AsW_9O_{33})_2]^{12-}$ polyanions containing Cu_6- and Mn_6-hexagons as central building blocks.[13] Each of the zinc atoms displays a related five-fold coordinated $[ZnO_4Cl]$ environment with square-pyramidal geometry, being coordinated by four terminal oxygen atoms from two **$\{SbW_9\}$**

units with Zn-O bond lengths of 2.061(8) – 2.077(8) Å and one chlorine atom [Zn-Cl, 2.222(1) Å] (Figures 7.2 c and 7.2 d). Six zinc atoms form an approximately equatorial hexagon by sharing their oxygen atoms (with a first-neighbour Zn···Zn distance of 3.160(2) Å, a Zn-O-Zn bond angle of 99.6(3)°, neighbouring Zn-Zn-Zn angles of 119.96(6)°, and second- and third-neighbour Zn···Zn distance of 5.473(2) and 6.320(2) Å (Figure 7.2c). Furthermore, we did not observe glide or any other distortion of **{SbW$_9$}** subunits with respect to each other, whereas the glide dislocation observed by *Robert* et al. in the polyanion $[Cu_3(H_2O)_2(AsW_9O_{33})_2]^{12-}$ is due to the lone-pair repulsion between the two As atoms.[27]

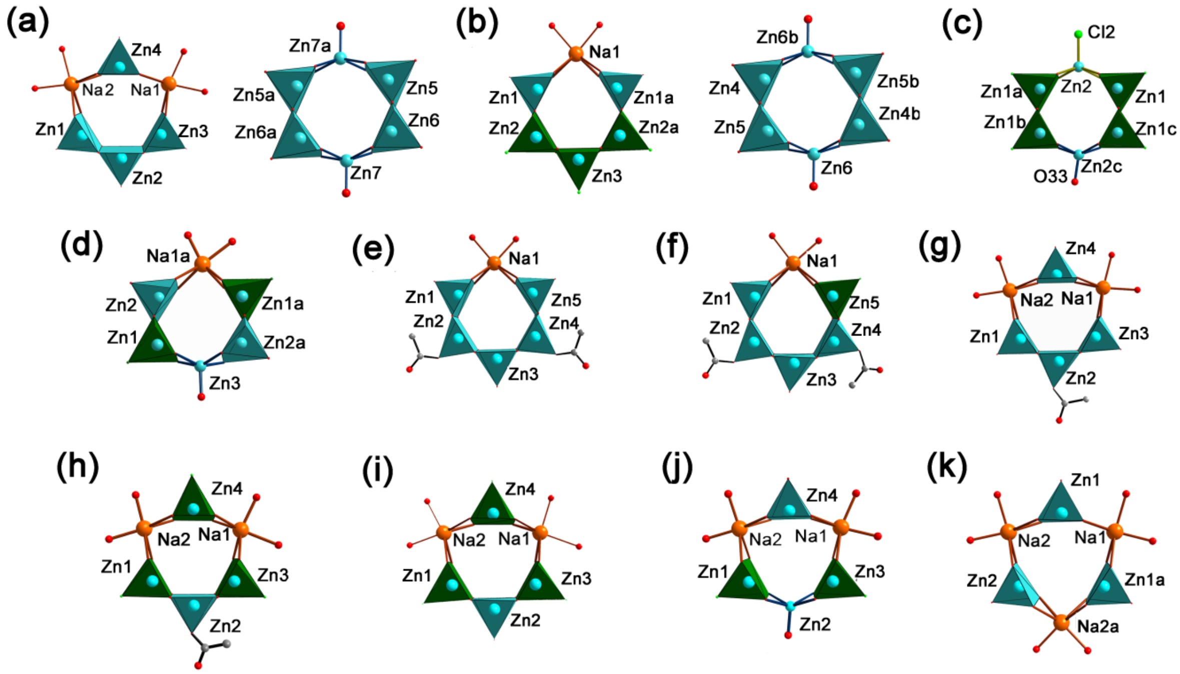

Figure 7.3. Polyhedral/ball-and-stick representations of sandwich central clusters of (a) **Zn_4-$Zn_{5.2}$ (7a, 7b)**, symmetry code: a, -*x*, *1-y*,*1-z*; (b) **Zn_5-$Zn_{5.2}$(8)**, symmetry codes: a, *x*, *0.5-y*, *z*; b, *1-x*, *1-y*, *1-z*; (c) **Zn6 (9a)**, a, *x*, *-y*, *-z;* b, -*1-x*, *-y*, *-z;* c, -*1-x*, *y*, *-z*; (d) Zn$_5$ **(10)**, symmetry code: a, 1-*x*, -*y*, *1*- *z*; (e) **Zn$_5$ (11a)**; (f) **Zn$_5$ (11b)**; (g) **Zn$_4$ (12a)**; (h) **Zn$_4$ (12b)**; (i) **Zn$_4$ (12c)**; (j) **Zn$_{3.5}$ (13)**; (k) **Zn$_3$ (14)**, symmetry code: a, 1-*x*, *y*, *0.5-z* (color codes: ZnO$_5$ square pyramids = blue polyhedra, Zn(O$_4$Cl) square pyramids = green polyhedra; spheres: Zn = blue, O = red, Na = yellow, Cl = green, C = grey; for disordered positions, only the most relevant atoms are shown for clarity in ball-and-stick representation).

Meanwhile the large family of sandwich-type polytungstoantimonates {$Zn_nNa_{6-n}(B$-α-$SbW_9O_{33})_2$} (n = 3-6) containing **{α-SbW$_9$}** *Keggin* fragments with unique central transition metal belts was further expanded successfully. Their construction principles are dimeric POMs comprising two trilacunary α-*Keggin* fragments which are connected by a TM central belt consisting of a maximum of six cation positions. They can either be completely occupied by transition metal Zn atoms in **Zn$_6$ (9b)**, or Na cations can occupy the additional vacancies when the number of Zn centers is below six, thus leading to vacancies in the central belt. The average numbers n of transition metal Zn centers in the present POM family are 3, 3.5, 4, 4.1, 5, 5.2, and 6 (Figure 7.3).

Interestingly, two independent sandwich-type polyoxoanions coexisting in the asymmetric units of **{Zn$_4$-Zn$_{5.2}$} (7a, 7b)** or **{Zn$_5$-Zn$_{5.2}$} (8)** were first reported respectively (Figure 7.1a and 7.1b). For example, single-crystal X-ray diffraction reveals that both compounds **(7a** and **7b)** have the same polyanions of $[Zn_{5.2}Na_{0.8}(H_2O)_{5.2}(SbW_9O_{33})_2]^{7-}$ together with $[Zn_4Na_2(H_2O)_8(SbW_9O_{33})_2]^{8-}$. The first polyanion $[Zn_{5.2}Na_{0.8}(H_2O)_{5.2}(SbW_9O_{33})_2]^{7-}$ contains four Zn^{2+} atoms (Zn5, Zn6, Zn5a, Zn6a) with one terminal water ligand comprising two binary units of square pyramids $[ZnO_4(H_2O)]$. Two vacancy sites between these pyramid pairs exhibit positional disorder with site occupancies of 0.6 (Zn7) and 0.4 (Na3), respectively (Figure 7.3a). The other $[Zn_4Na_2(H_2O)_8(SbW_9O_{33})_2]^{8-}$ polyanion contains a Zn_4 cluster (Figure 7.1a and Figure 7.3a). The cyclic arrangement within the central belt is completed by four Zn^{2+} and two Na^+ ions resulting in idealized C_{2v} symmetry in the sandwich-type structure. Three adjacent, edge-shared Zn-triad $[ZnO_4(H_2O)]$ square pyramids (Zn1, Zn2 Zn3) and one unique $[ZnO_4(H_2O)]$ fragment (Zn4) are separated by two Na ions (Na1, Na2) which complete the six-membered ring (Figure 7.3a). The structure of the Zn_4-containing polyanion in {**Zn$_4$-Zn$_{5.2}$**} **(7a)** is very similar to tetracopper-substituted polytungstoarsenate $[Cu_4K_2(H_2O)_8(AsW_9O_{33})_2]^{8-}$.[9] In {**Zn$_5$-Zn$_{5.2}$**} **(8)**, the first polyanion $[Zn_{5.2}Na_{0.8}(H_2O)_{5.2}(SbW_9O_{33})_2]$ with a $Zn_{5.2}$-TM cluster is identical to the one found in **{Zn$_4$-Zn$_{5.2}$} (7a** or **7b)**. The structure of second polyanion $[Zn_5NaCl_3(H_2O)_4(SbW_9O_{33})_2]^{10-}$ contains five Zn^{2+} cations and one vacancy in the Zn_5 central belt (Figure 7.1b and Figure 7.3b) with idealized C_{2v} symmetry. Three Zn atoms (Zn2, Zn2a and Zn3) with one terminal chloride and other two Zn atoms (Zn1, Zn1a) with one terminal water ligand comprise square pyramids [ZnO_4Cl] and [$ZnO_4(H_2O)$], respectively, in the central metal core. The remaining vacant TM position is occupied by a Na^+ cation with two terminal water molecules resulting in six-coordinated trigonal prismatic geometry (Figure 7.3b). In **Zn6 (9a)**, the TM core is very similar to a hexagonal Zn_6 ring [$Zn_6Cl_6O_{12}$] of **Zn6 (9b)**. Four Zn^{2+} atoms (Zn1, Zn1a, Zn1b, Zn1c) with one terminal chloride ligand comprising two binary units of square pyramids [$Zn(O_4Cl)$]. The other two Zn atoms (Zn2 and Zn2c) between these pyramid pairs are bound to either one terminal water molecule (O33) or one terminal chloride ligand (Cl2) in **(9a)**, leading to the average formation of a $[Zn_6Cl_5(H_2O)O_{12}]^{17-}$ hexagonal Zn_6 core. Actually, the O33 atom is statistically disordered over two positions with quarter occupancies each, whereas the Cl2 atom is also quarter occupied, but its location on the mirror plane leads to half occupancy in total (Figure 7.1c and Figure 7.3c). In the polyanion $[Zn_5Na(H_2O)_5Cl_2(SbW_9O_{33})_2]^{9-}$ of **Zn_5 (10)**, Zn1/Zn1a with one terminal chloride ligand and Zn2/Zn2a with one terminal water ligand construct two binary Zn moieties via adjacent edge-sharing [ZnO_4Cl] and [$ZnO_4(H_2O)$] square pyramids. The remaining two sites between these Zn double units exhibit positional disorder with site occupancies of 0.5 (Zn3) and 0.5 (Na1) (Figure 7.1d and Figure 7.3d), resulting in C_{2h} symmetry. In **Zn_5 (11a)** and **Zn_5 (11b)**, both polyanions contain five adjacent Zn atoms, and one Na^+ ion occupies the remaining site (Figure 7.1e and Figure 7.3e for **Zn_5 (11a)**; Figure 7.1f and Figure 7.3f for **Zn_5 (11b)**). Among the five zinc atoms of **(11b)**, both Zn1 and Zn3 have one terminal water molecule; Zn2 and Zn4 are coordinated by a monodentate acetate ligand, and Zn5 has a chloride ligand. However, the three Zn atoms (Zn1, Zn3 and Zn5) carrying a terminal water molecule are separated by Zn2 and Zn4 atoms coordinated with one monodentate acetate in **Zn_5 (11a)**. Interestingly, the coordination environment of two acetate ligands to Zn2 and Zn4 atoms is symmetric in **(11a)** resulting in C_{2v} symmetry, whereas the symmetry of the polyanion is reduced to C_s in **(11b)** due to unsymmetric acetate ligands of Zn2 and Zn4 and one Cl ligand of Zn5 (Figure 7.3e and 7.3f). In **Zn_4 (12a)**, one monodentate acetate ligand coordinating to Zn2 other than terminal water is the only difference in comparison with the tetra-Zn containing polyanion in {**Zn_4_$Zn_{5.2}$**} **(7a)**. This also results in symmetry reduction from C_{2v} to C_s (Figure 7.1g and Figure 7.3g). The polyanions of **Zn_4 (12b)** and **Zn_4 (12c)** incorporate four zinc ions which are not equivalent (Figure 7.1h and Figure 7.3h for **Zn_4 (12b)**, Figure 7.1i and Figure 7.3i for **Zn_4 (12c)**). Three of the Zn centers (Zn1, Zn3 and Zn4) with a terminal Cl ligand resulting in [ZnO_4Cl] square pyramids, whereas the fourth center Zn2 is connected to an acetate liagnd in **(12b)** or to a water molecule in **(12c)** forming a unique [$ZnO_4(H_2O)$] square pyramid (Figure 7.3h and 7.3i). Two sodium Na1 and Na2 ions fill the vacant positions between the Zn atoms in **Zn_4 (12c)**. One of these two vacant sites exhibits positional disorder with site occupancies of 0.9 (Na1) and 0.1 (Zn5) in **(12b)** (Figure 7.3h). These arrangements lead to C_s symmetry in **(12b)** and C_{2v} symmetry in **(12c)**, respectively. More interestingly, single crystal X-ray diffraction analyses revealed that two compounds **(12b)** and **(12c)** are enantiomers which crystallize in the chiral space group $P2_12_12_1$. We observed left- and right-handed helical chains in the structures of **(12b)** and **(12c)**, respectively. They derive from the connection of neighboring sandwich-type polyanions via additional Na^+ linkers into helical chains which are further assembled into chiral 3D open frameworks (Figure 7.4). The chiral properties of both compounds are thus due to their helical packing motif in the solid state. The last new obtained polyanion among the series, **$Zn_{3.5}$ (13)**, is different from the known Zn_3-containing polyanion $[Zn_3Na_3(H_2O)_9(SbW_9O_{33})_2]^{9-}$ **{Zn_3(14)}** with idealized D_{3h} symmetry [6] (Figure 7.1j and Figure 7.3j for **$Zn_{3.5}$ (13)**; Figure 7.3k and Figure 7.20a for **Zn_3(14)**) with respect to the following structural properties: (a) The three zinc ions are not equivalent in central belt of **(13)**, whereas **(14)** incorporates three equivalent zinc atoms with a terminal water ligand. In **$Zn_{3.5}$ (13)**, only Zn4 is attached to a water molecule, whereas the remaining two Zn centers (Zn1 and Zn3) have a terminal chloride ligand; (b) three additional vacant positions between the zinc ions are not equivalent in **$Zn_{3.5}$ (13)**, whereas three equal sodium cations occupy these sites in **Zn_3(14)**. In **$Zn_{3.5}$ (13)**, crystallographic data indicate positional disorder on the mixed occupied site between Zn1 and Zn3 atoms with 50 % occupancy of Zn2 and Na3, respectively.

Bond valence sum calculations (BVS) values of tungsten, antimony, zinc and sodium for all the compounds indicate no changes on the oxidation states of the metal ions which correspond to +6 (W), +3 (Sb), +2 (Zn), +1 (Na), and no protonated oxygen atoms were observed within the sandwich-type POMs (Table 10.18-10.20 in the Annexes).[28] Furthermore, only few mono- and di-TM substituted sandwich-type POMs based on trilacunary α-*Keggin* [α-XW_9O_{33}]$^{9-}$ (X= As, Bi, Sb, Te) fragments were reported to date. The mono-Ti(IV) polyanion [$(TiO)Na_5(H_2O)_{10}(SbW_9O_{33})_2$]$^{11-}$ has been discovered by *Cronin* and coworkers in 2010.[4] Its central cluster comprises a titanium center with an unprecedented Ti=O bond, while the additional five vacant positions are occupied by Na^+.

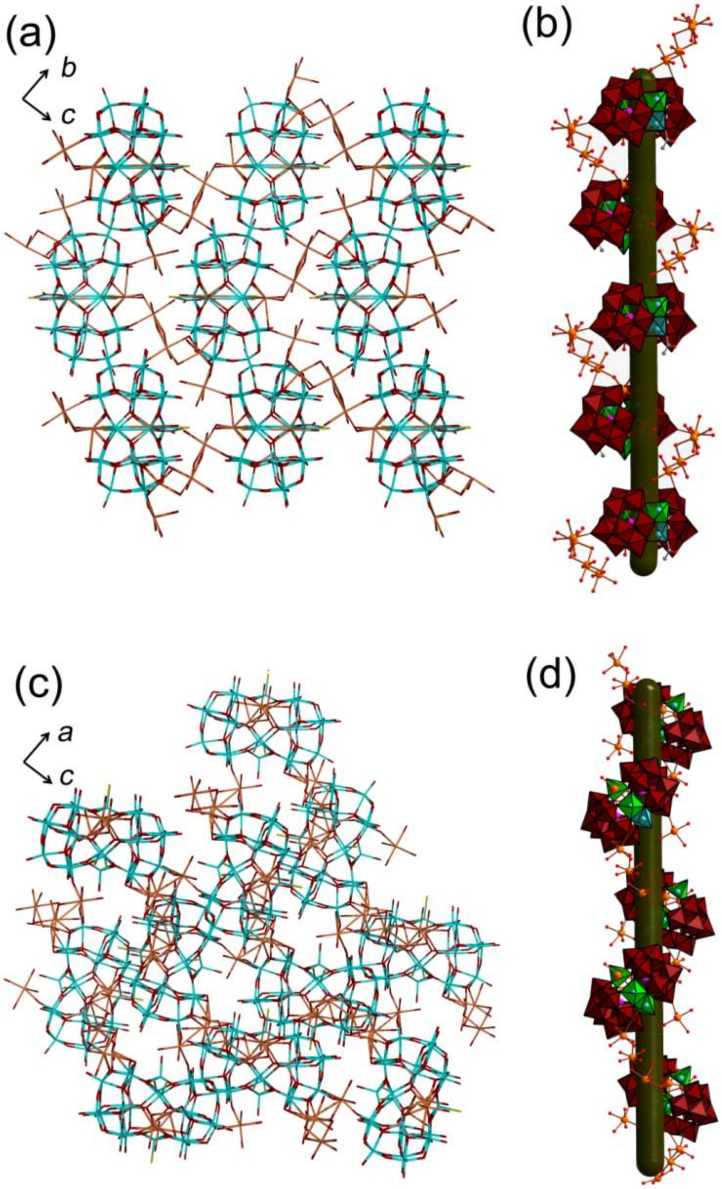

Figure 7.4. (a) The 3D open-framework structure of **Zn_4 (12b**) viewed along the *a* axis; (b) left-handed helices in **Zn_4 (12b**); (c) 3D open-framework structure of **Zn_4 (12c**) viewed along the *ac* plane; (d) right-handed helices in **Zn_4 (12c)**.

Earlier, *Kortz* et al. reported di-TM substituted sandwich-type polyanions $[(\alpha\text{-}AsW_9O_{33})_2WO(H_2O)M_2(H_2O)_2]^{10-}$ (M = Zn^{2+}/Mn^{2+}/Co^{2+}) with statistical disorder of all M^{2+} ions and one W atom in the central belt positions.[6] In addition, *Kortz* et al. characterized the di-Ti(IV) containing polyanion $[(\alpha\text{-}AsW_9O_{33})_2WO(H_2O)Ti_2(OH)_2]^{8-}$ with a central belt consisting two titanium centers, one tungsten center and three cesium ions occupying the remaining cation positions.[5] In order to expand the newly synthesized large family of sandwich-type polytungstoantimoates, attempts were made to synthesize mono-nuclear $[ZnNa_5(\alpha\text{-}SbW_9O_{33})_2]^{11-}$ and di-nuclear $[Zn_2Na_4(\alpha\text{-}SbW_9O_{33})_2]^{10-}$ by applying a variety of reaction conditions (e.g. adjusting the molar ratio $\{SbW_9\}/Zn^{2+}$ or changing buffer media and countercations). However, no low-nuclearity mono- and di-Zn substituted polytungstoantimoates of the $[Zn_nNa_{6\text{-}n}(B\text{-}\alpha\text{-}SbW_9O_{33})_2]^{n\text{-}12}$ (n =1, 2) sandwich-type were obtained. Only the *Krebs*-type di-Zn containing $[Zn_2(H_2O_2)_6(WO)_2(\beta\text{-}SbW_9O_{33})_2]^{10-}$ **$\{Zn_2W_2\}$ (15)** polyanion based on the $\{\beta\text{-}SbW_9\}$ fragment could be accessed through the synthetic procedures applied on this reaction system (see Exp. Part, Figure 7.20e). The POM precursor $[\alpha\text{-}SbW_9O_{33}]^{9-}$ isomerized into the β-type anion in solution, and furthermore probably dimerized into $[Zn_2Sb_2W_{20}O_{70}]^{10-}$ polyanion through templating $[Zn(H_2O)_3]^{2+}$ moieties.[22]

7.3.2. Analytical characterization

7.3.2.1. PXRD and TGA characterizations

The phase purity of the large family of compounds {**(7a, 7b)**, **(9b)**, **(11a)**, **(11b)**, **(12a)**, **(12b)**, **(12c)**, **(13)** and **(14)**} obtained in this thesis was confirmed with PXRD measurements (Figures 7.5-7.14), while mixed phases (**8**, **9a** and **10**) were excluded. The diffraction peaks of both calculated patterns from single-crystal X-ray diffraction data and experimental patterns match very well. The phase purity of all compounds obtained in this study was confirmed with PXRD measurements. Intensity differences may be due to preferred orientation of the powder samples and sample preparation effects.

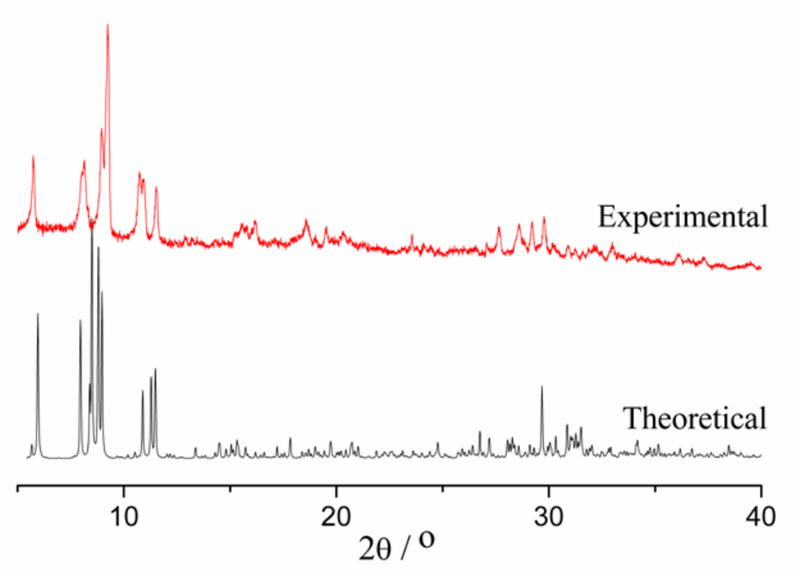

Figure 7.5. Powder X-ray diffraction pattern of bulk **Zn_4-$Zn_{5.2}$ (7a)** vs. calculated pattern.

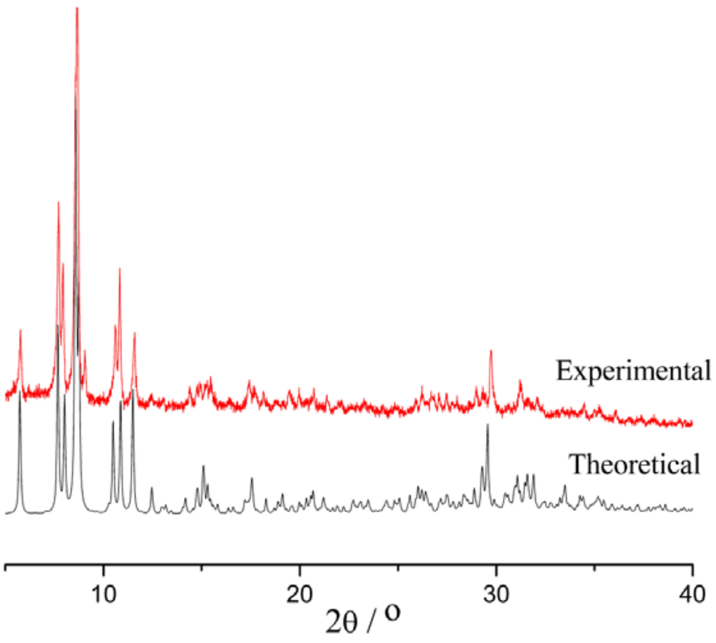

Figure 7.6. Powder X-ray diffraction pattern of bulk **Zn_4-$Zn_{5.2}$ (7b)** vs. calculated pattern.

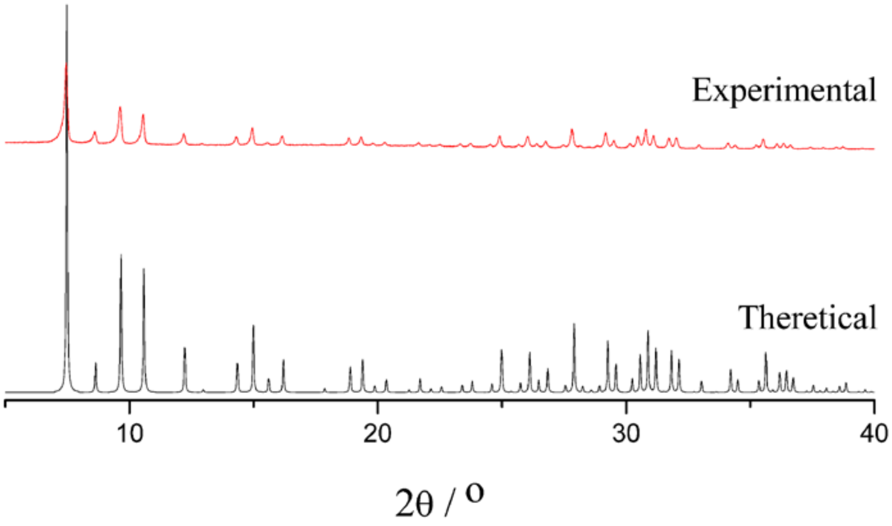

Figure 7.7. Powder X-ray diffraction pattern of bulk **Zn$_6$ (9b)** vs. calculated pattern.

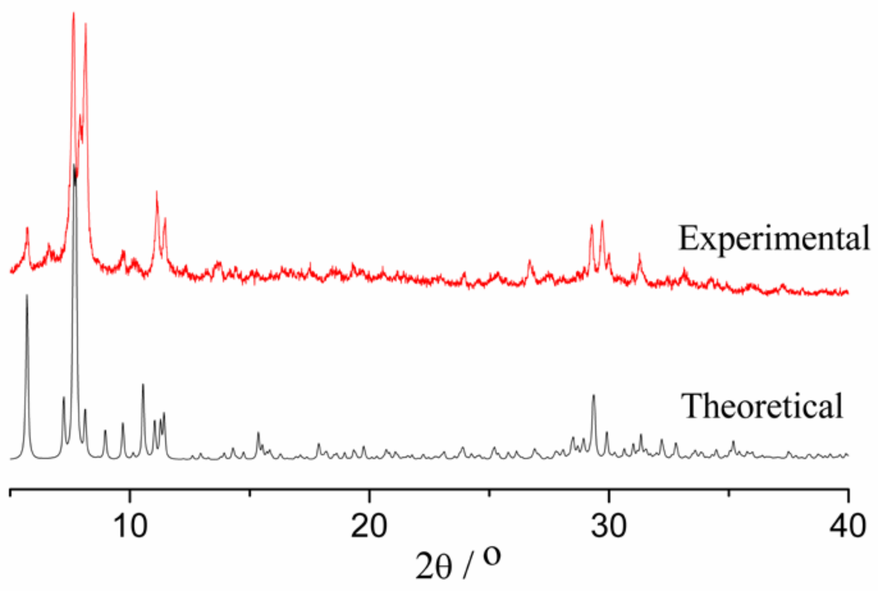

Figure 7.8. Powder X-ray diffraction pattern of bulk **Zn$_5$ (11a)** vs. calculated pattern.

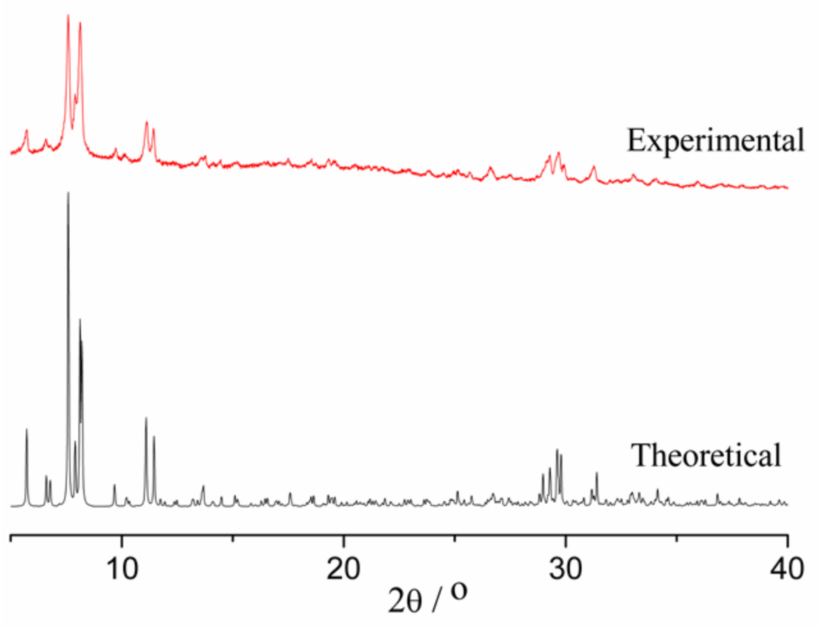

Figure 7.9. Powder X-ray diffraction pattern of bulk **Zn_5 (11b)** vs. calculated pattern.

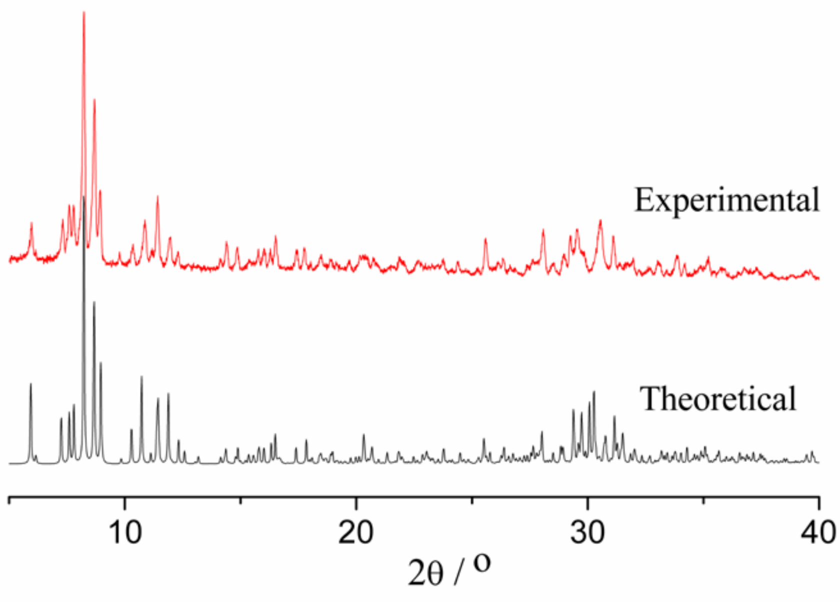

Figure 7.10. Powder X-ray diffraction pattern of bulk **Zn_4 (12a)** vs. calculated pattern.

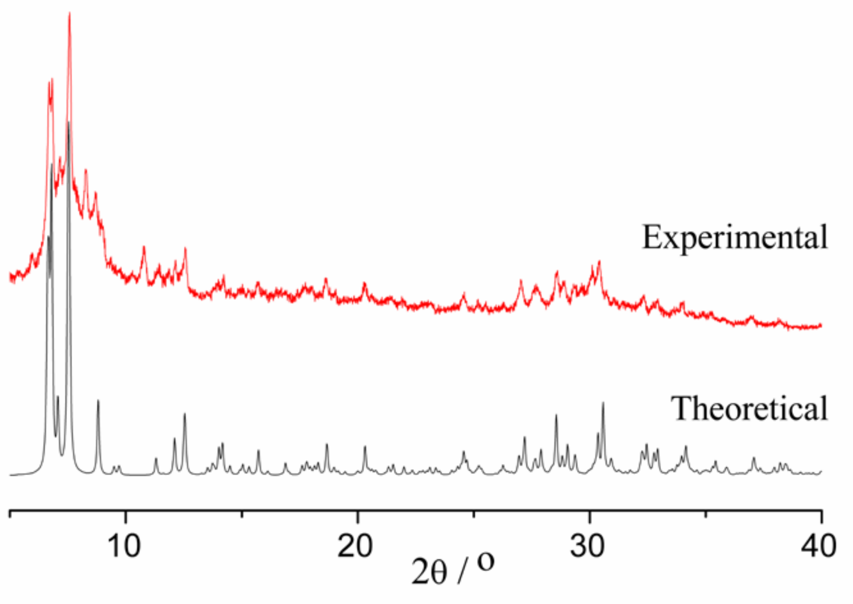

Figure 7.11. Powder X-ray diffraction pattern of bulk **Zn$_4$ (12b)** vs. calculated pattern.

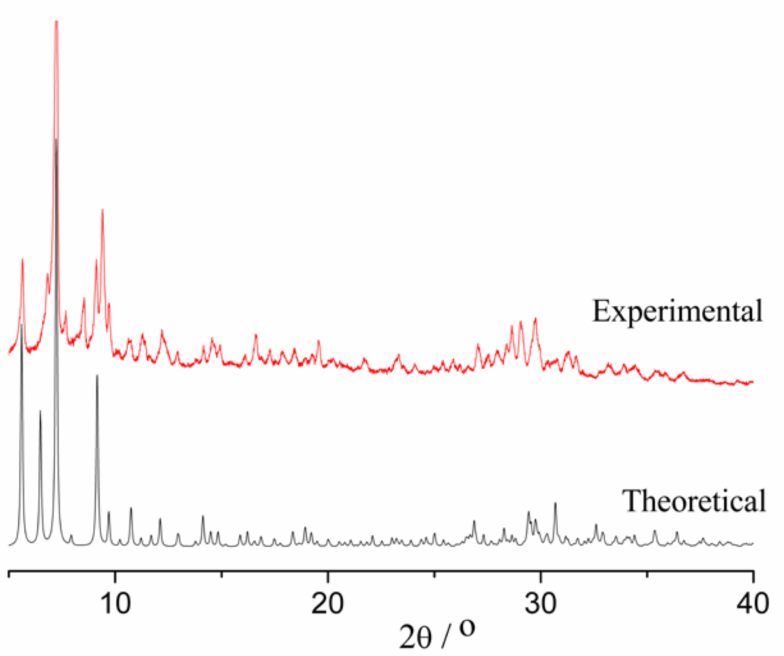

Figure 7.12. Powder X-ray diffraction pattern of bulk **Zn$_4$ (12c)** vs. calculated pattern.

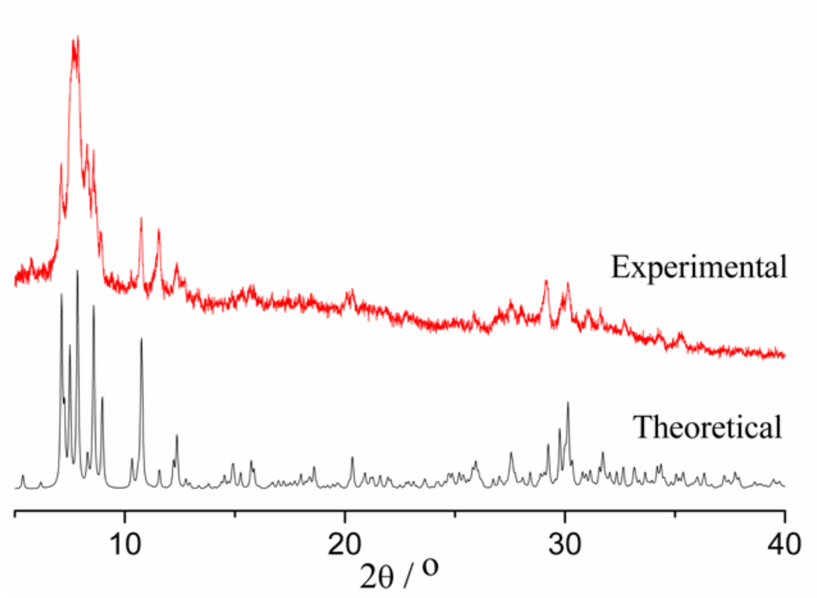

Figure 7.13. Powder X-ray diffraction pattern of bulk **$Zn_{3.5}$ (13)** vs. calculated pattern.

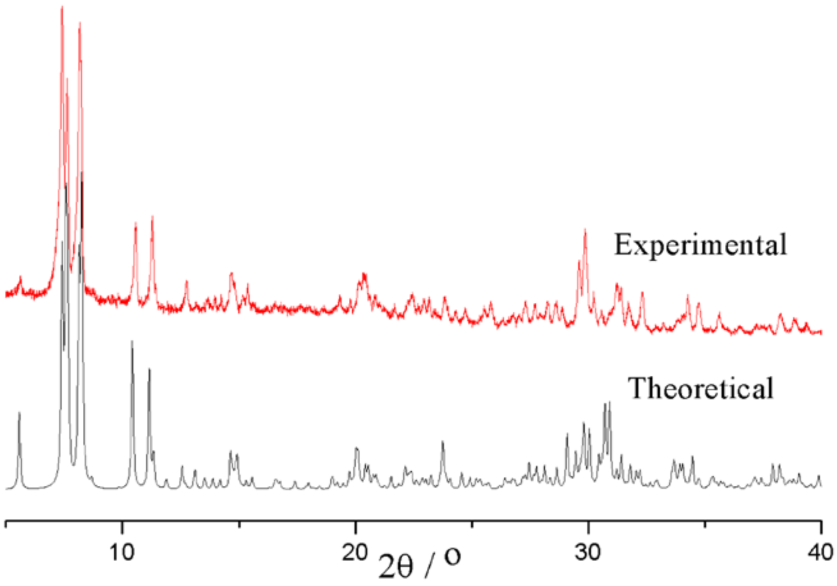

Figure 7.14. Powder X-ray diffraction pattern of bulk **Zn_3 (14)** vs. calculated pattern.

TGA measurements on **Zn_4_$Zn_{5.2}$ (7a), Zn_6 (9b), Zn_5 (11a), Zn_4 (12a), $Zn_{3.5}$ (13)** and **Zn_3 (14)** were performed under a nitrogen flow in the temperature range from 30 to 600 °C (Figure 7.15). For compound **(7a)**, TGA showed a weight loss of 10.5 % in the 30 - 240 °C temperature range, corresponding to the loss of coordinating and solvent water molecules (expected 11.2%). The corresponding values are 7.8 % (calcd. 7.9 %) for (**12a)**, 9.6 % (calcd. 10.0 %) for (**13**), and 13.8 % (calcd. 14.5 %) for (**14**). For compound (**9b)**, TGA showed a weight loss of 5.0 % in the 30-198 ^{o}C temperature range, corresponding to the loss of coordinating and solvent water molecules (expected 5.0 %), followed by a slower weight loss of 7.9 % between 202 - 515 ^{o}C caused by release of ammonia and hydrogen chloride (expected 7.6 %). TGA of (**11a**) showed a weight loss of 9.9% in the 30-190 ^{o}C temperature range, corresponding to the loss of coordinating and solvent water molecules (expected 10.2%), followed by a slower weight loss of 2.0% between 200-408 ^{o}C caused by release of acetate ligands (expected 2.6%).

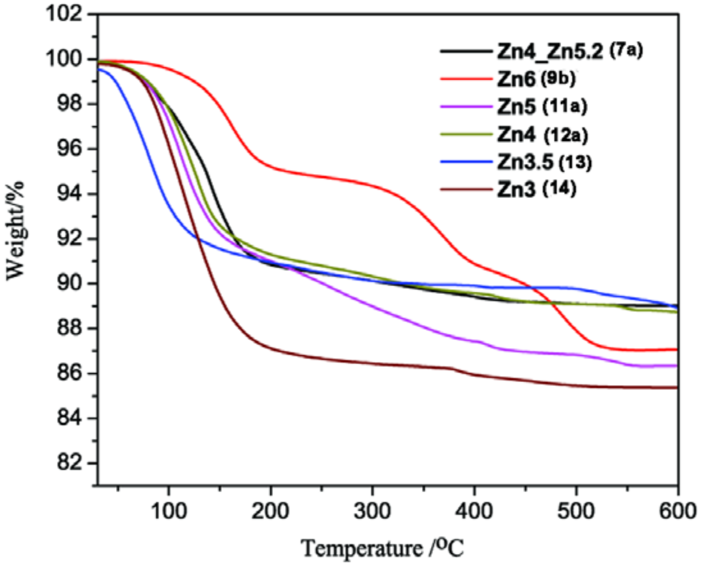

Figure 7.15. Thermogravimetric curves of **Zn_4_$Zn_{5.2}$ (7a), Zn_6 (9b), Zn_5 (11a), Zn_4 (12a), $Zn_{3.5}$ (13)** and **Zn_3 (14).**

7.3.2.2. Electrochemical characterization

The redox properties of compounds **Zn_4_$Zn_{5.2}$ (7a), Zn_6 (9b), Zn_5 (11a), Zn_4 (12a), $Zn_{3.5}$ (13)** and **Zn_3 (14)** were characterized by cyclic voltammetry (CV) in 1.0 M NaCl solution over the potential range of +1.0 to -1.0V (Figures 7.16). The irreversible redox couple (I-I’) between -0.75 and -0.85 V corresponds to the redox processes of the W^{6+} centers. However, the reduction waves (I) of the W centers gradually disappeared with the decrease of the oxidation peak around -0.80 V from Zn_6-containing POMs with hexagonal Zn-centers towards the Zn_3-containing POM with trigonal motifs. Moreover, the second reduction peak at -0.544 V (II) was only observed in the compound **Zn_3 (14)**.

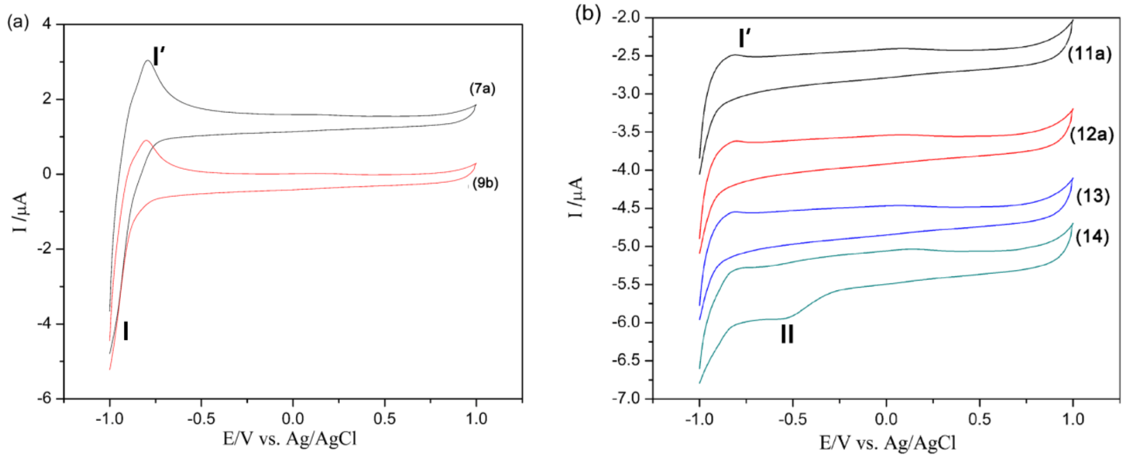

Figure 7.16. Cyclic voltammograms of (a) **Zn_4_$Zn_{5.2}$ (7a)**, **Zn_6 (9b)** in (1.0 M) NaCl buffer solution, (b) 1mM **Zn_5 (11a)**, **Zn_4 (12a)**, **$Zn_{3.5}$ (13)** and **Zn_3 (14)** in (1.0 M) NaCl buffer solution (scan rate 25 mV/s, GCE working electrode, Ag/AgCl reference electrode).

7.3.2.3. FT-IR and Raman spectroscopy

FT-IR and Raman spectra of the compounds **Zn_4_$Zn_{5.2}$ (7a)**, **Zn_6 (9b)**, **Zn_5 (11a)**, **Zn_4 (12a)**, **$Zn_{3.5}$ (13)** and **Zn_3 (14)** in the solid state are closely related, and the characteristic peaks are assigned to W-O vibrations (Figures 7.17, 7.18, and detailed assignment in Table 7.1).

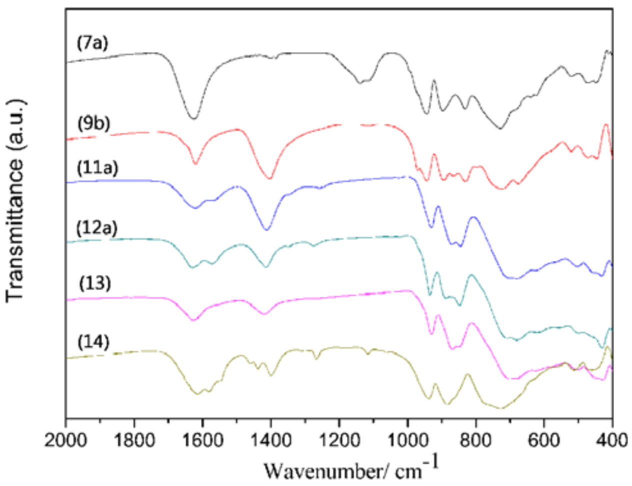

Figure 7.17. Solid state FT-IR spectra of the compounds **Zn_4_$Zn_{5.2}$ (7a)**, **Zn_6 (9b)**, **Zn_5 (11a)**, **Zn_4 (12a)**, **$Zn_{3.5}$ (13)** and **Zn_3 (14)**.

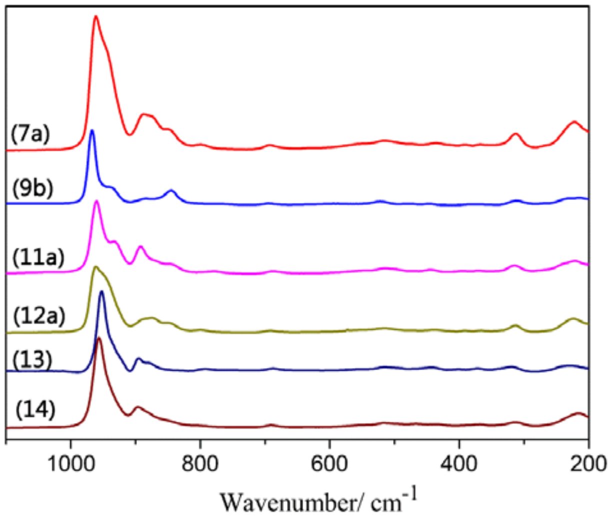

Figure 7.18. Solid state Raman spectra of the compounds **Zn_4_$Zn_{5.2}$ (7a)**, **Zn_6 (9b)**, **Zn_5 (11a)**, **Zn_4 (12a)**, **$Zn_{3.5}$ (13)** and **Zn_3 (14)**.

Table 7.1. Vibrational features (FT-IR and Raman) for **(Zn_4_$Zn_{5.2}$ (7a)**, **Zn_6 (9b)**, **Zn_5 (11a)**, **Zn_4 (12a)**, **$Zn_{3.5}$ (13)**, **Zn_3 (14)**, and the $Na_9[B\text{-}\alpha\text{-}SbW_9O_{33}]\cdot 19.5H_2O$ **{SbW_9}** precursor.

Label		**Band assignments^{a} (cm^{-1})**					
{SbW_9}		$\delta(HOH)$	$\delta(NH_4)$	$\nu(W{=}O_d)$	$\nu_{as}(W\text{-}O_b)$	$\nu_{as}(W\text{-}O_c)$	$\delta(W\text{-}O_{b,c}\text{-}W)$
	IR	1617		959, 922	893	770, 710	
	Raman			961, 943	905, 873	795, 688	438, 338
(7a)		$\delta(HOH)$	$\delta(NH_4)$	$\nu(W{=}O_d)$	$\nu_{as}(W\text{-}O_b)$	$\nu_{as}(W\text{-}O_c)$	$\delta(W\text{-}O_{b,c}\text{-}W)$
	IR	1624		946	897, 834	728	
	Raman			961	888, 848	797,695	515
(9b)		$\delta(HOH)$	$\delta(NH_4)$	$\nu(W{=}O_d)$	$\nu_{as}(W\text{-}O_b)$	$\nu_{as}(W\text{-}O_c)$	$\delta(W\text{-}O_{b,c}\text{-}W)$
	IR	1624	1418	946	858, 824	708, 665	512,434
	Raman			996, 969	886, 843	693	522
(11a)		$\delta(HOH)$	$\delta(NH_4)$	$\nu(W{=}O_d)$	$\nu_{as}(W\text{-}O_b)$	$\nu_{as}(W\text{-}O_c)$	$\delta(W\text{-}O_{b,c}\text{-}W)$
	IR	1622	1411	929	870, 846	698	503, 430
	Raman			960, 932	892, 843	783, 688	514, 444

(12a)		*δ(HOH)*	*δ(NH_4)*	*ν(W=O_d)*	*ν_{as}(W-O_b)*	*ν_{as}(W-O_c)*	*δ(W-$O_{b,c}$-W)*
	IR	1628	1413	937	888, 848	712, 679	503, 430
	Raman			959	875, 848	799, 690	517
(13)		*δ(HOH)*	*δ(NH_4)*	*ν(W=O_d)*	*ν_{as}(W-O_b)*	*ν_{as}(W-O_c)*	*δ(W-$O_{b,c}$-W)*
	IR	1626	1404	935	876, 837	716, 673	509, 431
	Raman			966	890, 878	791,697	529, 324
(14)		*δ(HOH)*	*δ(NH_4)*	*ν(W=O_d)*	*ν_{as}(W-O_b)*	*ν_{as}(W-O_c)*	*δ(W-$O_{b,c}$-W)*
	IR	1610		940, 941	883	730	507,461
	Raman			954	892, 860	690	517, 365

[a]. W=O_d, terminal; W-O_b, corner-sharing; W-O_c, edge-sharing.

7.3.2.4. UV/Vis spectroscopy

Solid state UV-Vis spectra of the compounds **Zn_4_$Zn_{5.2}$ (7a)**, **Zn_6 (9b)**, **Zn_5 (11a)**, **Zn_4 (12a)**, **$Zn_{3.5}$ (13)** and **Zn_3 (14)** in the range between 190 and 600 nm have two characteristic absorptions bands at 200-210 and 260-300 nm in common. The absorption band at higher energy can be ascribed to the pπ-dπ charge-transfer transitions of the O_t-W bonds, whereas the low-energy absorption band is due to the pπ-dπ charge-transfer transitions of the $O_{b,c}$-W bonds (Figure 7.19).

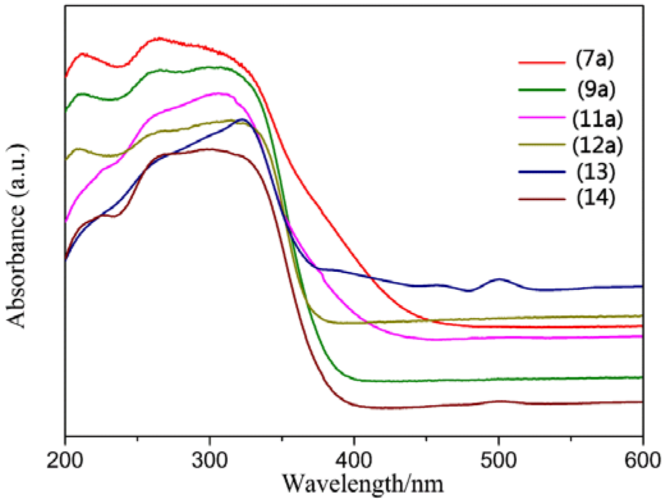

Figure 7.19. Solid state UV/vis spectra of the compounds **Zn_4_$Zn_{5.2}$ (7a)**, **Zn_6 (9b)**, **Zn_5 (11a)**, **Zn_4 (12a)**, **$Zn_{3.5}$ (13)** and **Zn_3 (14)**.

7.3.4. Catalytic performance tests of the Zn-POM family.

The large series of novel sandwich-type Zn/Sb-POMs was investigated for cyclohexanol oxidation performance, and all the members exhibit remarkable catalytic activities (Table 7.2). The model substrate cyclohexanol reacted with hydrogen peroxide and the sandwich-type Zn-POM catalysts {**Zn_4_$Zn_{5.2}$ (7a)**, **Zn_6 (9b)**, **Zn_5 (11a)**, **Zn_4 (12a)**, **Zn_3 (14)**} in a biphasic reaction system (organic substrate/water), under aerobic conditions at 85 ^{o}C for 7h to afford high yields (around 94%-99%) of cyclohexanone throughout (Table 1, entries 1-5). However, when the reactions were performed at 50 ^{o}C for 7 h, cyclohexanone yields sharply decreased to around 23%-31% (Table 7.2, entries 6-10). As a consequence, high reaction temperatures can notably improve cyclohexanol conversion into cyclohexanone. Meanwhile, both *Krebs*-type hereopolyanions $[Zn_2Sb_2W_{20}O_{70}]^{10-}$ {Zn_2W_2} **(15)** (Figure 7.20e) and tungstoantimonate $[Sb_2W_{22}O_{74}(OH)_2]^{12-}$ [**Error! Bookmark not defined.**] (Figure 7.20d) also displayed high catalytic activities at 85 ^{o}C with respective cyclohexanone yields around 96 % and 92 % (entries 11, 13). In comparison, the trilacunary *Keggin* POM ligand $Na_9[SbW_9O_{33}]\cdot 19.5H_2O$, the high valent Anderson-type Sb-POM $K_5Na_2[Sb^{V}W_6O_{24}]\cdot 12H_2O$ [29] (Figure 7.20f), and paratungstate $[H_2W_{12}O_{42}]^{10-}$ [30] (Figure 7.20g) were less active, providing lower cyclohexanone yields of ca. 77 %, 60 % and 73 % respectively, at 85 ^{o}C, and very low yields of ca. 11 %, 7 % and 14 %, respectively at 50 ^{o}C (entries 15-20). The above results thus show that the different building blocks of the POMs can exert an important influence on the catalytic efficiency of alcohol oxidation.

Moreover, in our preceding study (**Chapter 5**), both of the Zn/Sb containing sandwich-type POMs $[\alpha/\beta\text{-}Zn_2Sb^{III}{}_2(ZnW_9O_{34})_2]^{14-}$ {**α/β-[Zn_2Sb_2]** isomers} (Figure 7.20i and 7.20j) showed high catalytic activity for various alcohol oxidation processes at 85 ^{o}C.[21] In the preceding **Chapter 5**, it was shown that their high valent Sb^{V}-containing derivatives $[\alpha/\beta\text{-}Zn_2Sb^{V}{}_2(OH)_2(ZnW_9O_{34})_2]^{12-}$ {**α/β-[$Zn_2Sb^{V}{}_2(OH)_2$]**} (Figure 7.20h) are involved in the catalytic cycle as active catalysts.[21] Here, further experimental investigations prove that oxidation of cyclohexanol hardly proceeded in the presence of **α/β-Zn_2Sb_2** isomers at

Table 7.2. Oxidation of cyclohexanol with different Zn-POMs and reference POM catalysts.[a]

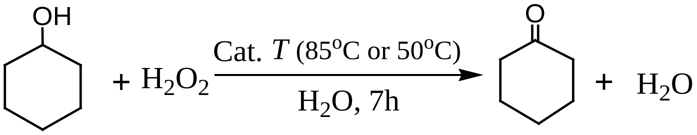

Exp.	**Catalyst**	***T* (°C)**	**Yield (mmol %)^b**
1	$Zn_4\_Zn_{5.2}$ **(7a)**	85	97
2	Zn_6 **(9b)**	85	>99
3	Zn_5 (11a)	85	96
4	Zn_4 (12a)	85	95
5	Zn_3 **(13)**	85	98
6	$Zn_4\_Zn_{5.2}$ **(7a)**	50	29
7	Zn_6 **(9b)**	50	31
8	Zn_5 (11a)	50	27
9	Zn_4 **(12a)**	50	26
10	Zn_3 **(14)**	50	27
11	Zn_2W_2 **(15)**	85	96
12	Zn_2W_2 **(15)**	50	25
13	$[Sb_2W_{22}O_{74}(OH)_2]^{12-}$ [22]	85	92
14	$[Sb_2W_{22}O_{74}(OH)_2]^{12-}$	50	22
15	$[SbW_9O_{33}]^{9-}$ [22a]	85	77
16	$[SbW_9O_{33}]^{9-}$	50	11
17	$[Sb^{V}W_6O_{24}]^{7-}$ [29]	85	60
18	$[Sb^{V}W_6O_{24}]^{7-}$	50	7
19	$[H_2W_{12}O_{42}]^{12-}$ [30]	85	73
20	$[H_2W_{12}O_{42}]^{10-}$	50	14
21	$[\alpha\text{-}Zn_2Sb^{III}{}_2(ZnW_9O_{34})_2]^{14-}$[21]	50	3
22	$[\beta\text{-}Zn_2Sb^{III}{}_2(ZnW_9O_{34})_2]^{14-}$ [21]	50	3
23	$[\alpha\text{-}Zn_2Sb^{V}{}_2(OH)_2(ZnW_9O_{34})_2]^{12-}$ [21]	50	25
24	$\{Cu_6\}$[12]	85	13
25	$\{Cu_3\}$[6]	85	10
26	$\{Cu_6\}$	50	29
27	$\{Cu_3\}$	50	27

[a] Reaction conditions: 0.25 mmol substrate,1.25 mmol (30 %) H_2O_2, 1.0 μmol catalyst, 1.0 mL H_2O, 85 or 50 °C, 7 h. [b] Organic products were identified and quantified by GC-MS and GC with calibrations using pure corresponding standards and dodecane as an internal standard. Yield (%) = [cyclohexanone] / initial [cyclohexanol] × 100%. Product distributions were not significantly affected by carrying out the reactions in N_2 amosphere.

lower temperature (50 °C, entries 21 and 22), whereas high valent $\mathrm{Sb^{V}}$-**{α-[$\mathbf{Zn_2Sb^{V}_2(OH)_2}$]}** species still show almost equivalent catalytic activity at 50 °C (yield ca. 25%, entry 23) in comparison with the newly synthesized Zn-POMs series (entries 6-10). This further confirms that H_2O_2-assisted transformation of the catalytic precursors **α/β-[$\mathbf{Zn_2Sb_2}$]** into the high valent $\mathrm{Sb^{V}}$- **α/β-[$\mathbf{Zn_2Sb^{V}_2(OH)_2}$]**} species is essential to initiate the catalytic cycle at 85 °C.

Moreover, hexa- and tri-copper substituted sandwich-type polyoxometalates $[Cu_6Cl(SbW_9O_{33})_2]^{7-}$ {**$\mathbf{Cu_6}$**} [12] (Figure 7.20c) and $[Cu_3(SbW_9O_{33})_2]^{12-}$ {**$\mathbf{Cu_3}$**} [6] (Figure 7.20b) were included as reference catalysts in the present catalytic system. In contrast to the Zn-POM catalyst family, cyclohexanol oxidation reaction proceeded less efficiently at 85 °C than at 50 °C in the presence of {**$\mathbf{Cu_6}$**} with a hexagonal metal core or {**$\mathbf{Cu_3}$**} with trigonal copper core motifs (entries 24-27). In other words, the Cu-containing sandwich-type POMs {**$\mathbf{Cu_6}$**} and {**$\mathbf{Cu_3}$**} are catalytically inert, affording very low yields (ca. 13% and 10%, respectively, at 85 °C) compared to the newly synthesized Zn-POMs (yields ca. 94 % - 99 %). In order to investigate this interesting phenomenon in more depth, sandwich-type-type POM stability in aqueous media was confirmed by FT-IR and Raman spectroscopy first. Solid state and solution FT-IR or Raman spectra of **$\mathbf{Zn_6}$ (9b)** and **{$\mathbf{Cu_3}$}** compounds as representative examples are practically identical, respectively (Figure 7.21 and Figure 7.22), thus indicating the stability of both POM types in solution. After the oxidation process, **$\mathbf{Zn_6}$ (9b)** and **{$\mathbf{Cu_3}$}** catalysts could easily be recycled through phase separation. FT-IR and Raman spectra of the recycled catalysts correspond to those of freshly prepared catalysts (Figure 7.21and 7.22), suggesting that the structural motifs of sandwich-type-type POMs based-catalysts were preserved during the whole catalytic process. Moreover, catalyst **$\mathbf{Zn_6}$ (9b)** still can maintain its high catalytic activity over several runs as shown by the constantly high cyclohexanone yields around 98 % after three cycles (Table 7.3).

Next, the hydrogen peroxide utilization efficiency during cyclohexanol oxidation with **$\mathbf{Zn_6}$ (9b)** and **{$\mathbf{Cu_3}$}** catalysts is summarized in Table 7.4. H_2O_2 contents were quantified by UV-vis spectroscopy via formation of the characteristic yellow-orange peroxotitanium complex $[Ti(O_2)(OH)(H_2O)_3]^{+}$ (Figure 7.23).[31] The initial dismutation process of hydrogen peroxide does not proceed fast at 50 °C in the absence of POMs catalysts so that the remaining hydrogen peroxide content was around 90 % after the reaction (Table 7.4, entry 2). However, the decomposition rate was quickly increased at elevated temperature 85°C with 36 % of residual H_2O_2 at 85 °C (Table 7.4, entry 1). In the presence of transition metal substituted sandwich-type POMs **Zn_6 (9b)** and **$\{Cu_3\}$**, the remaining hydrogen peroxide at 50 °C sharply decreased from ca. 90 % to ca. 27% and 8%, respectively (Table 7.4, entry 4 and 6), and H_2O_2 was almost completely consumed at 85 °C (Table 7.4, entry 3 and 5). Consequently, the consumption process of active oxygen from H_2O_2 oxidant involves two competitive reactions of alcohol oxidation and hydrogen peroxide dismutation in transition metal complex catalyzed oxygenation of organic substrates,[32] which has also been observed by *Krebs* et al. for diene epoxidation catalyzed by sandwich-type $[Mn^{II}(H_2O)_3(SbW_9O_{33})_2]^{12-}$.[18] In the present case, the **Zn_6 (9b)** POM catalyzes both alcohol oxidation and hydrogen peroxide dismutation reactions thoroughly and simultaneously at 85 °C. However, hydrogen peroxide dismutation as a significant side reaction became dominant in the presence of **$\{Cu_3\}$** POM at 85 °C in favor of cyclohexanol oxidation which only afforded very low yields. The above observations indicate that the composition of the central TM belt of sandwich-type POM catalysts plays a significant role in H_2O_2-assisted alcohol oxidation.

Table 7.3. Oxidation of cyclohexanol over different cycles with **Zn_6 (9b)**.[a]

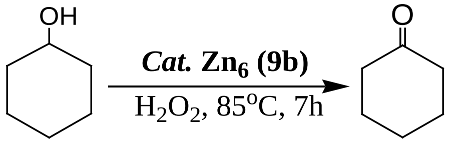

Cycle	Product (Yield %)[c]
	9b[a]
1	cyclohexanone (99)
2	cyclohexanone (98)
3	cyclohexanone (98)

[a] Reaction conditions: 0.25 mmol of substrate, 1.25 mmol (30 %) of H_2O_2, 1.0 μmol of catalyst **Zn_6 (9b)**, 0.50 mL of H_2O, 85 °C, 7 h. Yields (%) were determined by GC analyses by using pure corresponding samples as calibration standards and dodecane as an internal standard.

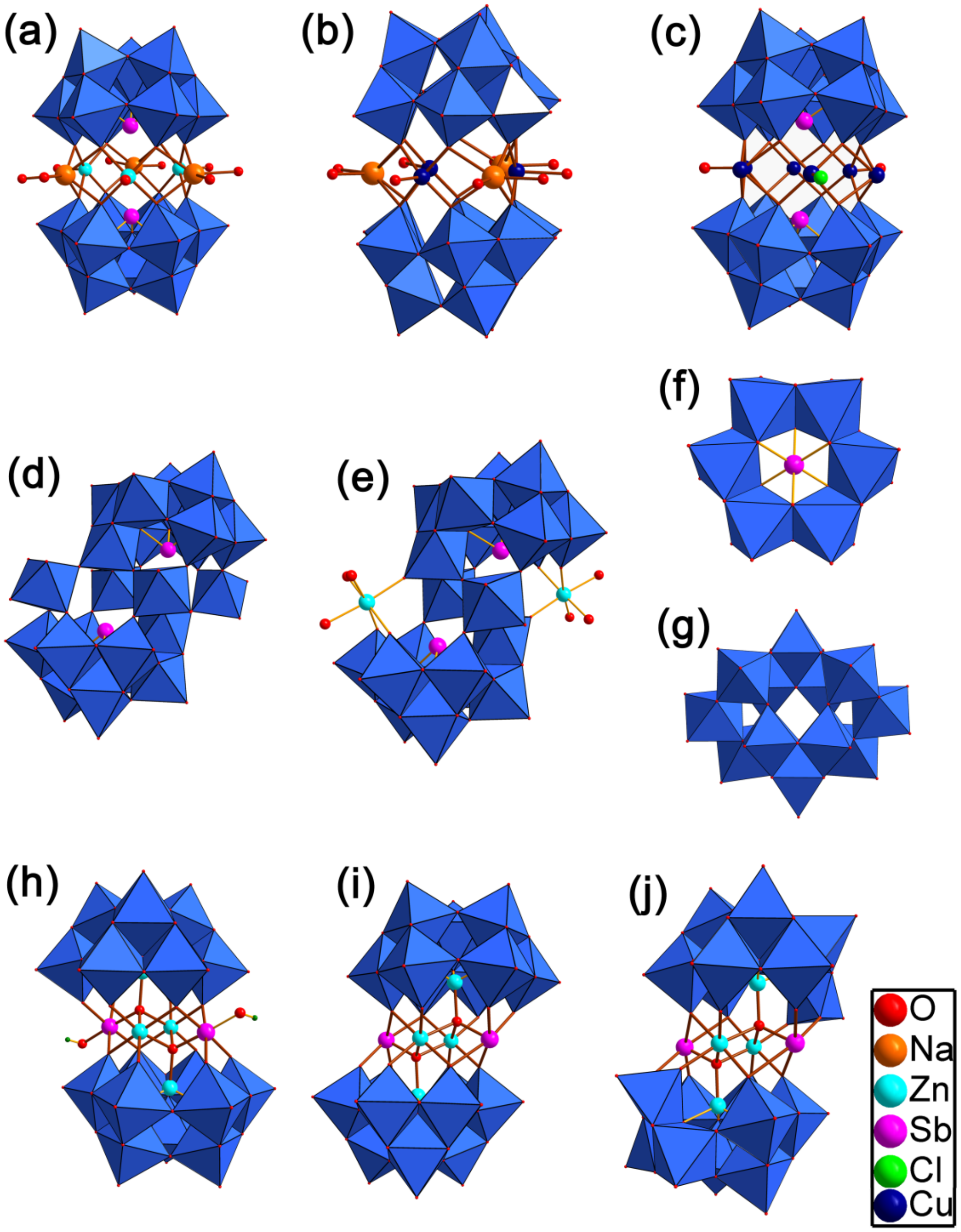

Figure 7.20. Polyhedral representations of (a) sandwich-type $[Zn_3Na_3(H_2O)_9(SbW_9O_{33})_2]^{9-}$ {**Zn₃(14)**}, (b) sandwich-type $[Cu_3Na_3(H_2O)_9(SbW_9O_{33})_2]^{9-}$ **{Cu₃}**, (c) sandwich-type $[Cu_6Cl(H_2O)_2(SbW_9O_{33})_2]^{7-}$ **{Cu₆}**, (d) *Krebs*-type $[Sb_2W_{22}O_{74}(OH)_2]^{12-}$, (e) *Krebs*-type $[Zn_2Sb_2W_{20}O_{70}]^{10-}$, (f) Sb(V)-substituted Anderson-type $[Sb^{V}W_6O_{24}]^{7-}$, (g) paratungstate $[H_2W_{12}O_{42}]^{10-}$, (h) Sb(V)-substituted sandwich-type $[\alpha\text{-}Zn_2Sb^{V}{}_2(OH)_2(ZnW_9O_{34})_2]^{12-}$, (i) and (j) sandwich-type $[\alpha/\beta\text{-}Zn_2Sb^{III}{}_2(ZnW_9O_{34})_2]^{14-}$ {α/β-Zn_2Sb_2 isomers}(color codes: WO_6 octahedra, light blue; Sb, pink; Zn, fair blue; Cu, dark blue, Na, orange; O, red; Cl, green)

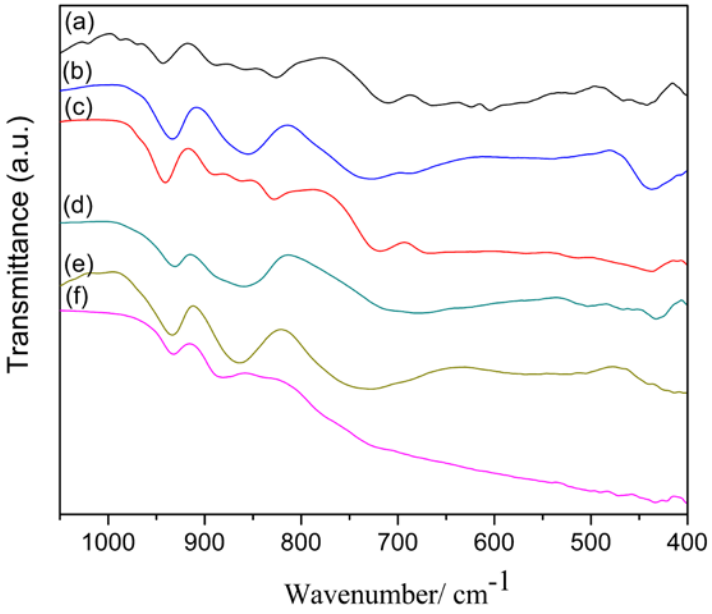

Figure 7.21. FT-IR spectra of (a) **Zn$_6$ (9b)** in the solid state, **(b) Zn$_6$ (9b)** after cyclohexanol oxidation, (c) **Zn$_6$ (9b)** in aqueous solution, (d) **{Cu$_3$}** in the solid state, (e) **{Cu$_3$}** after the oxidation of cyclohexanol, (f) **{Cu$_3$}** in aqueous solution.

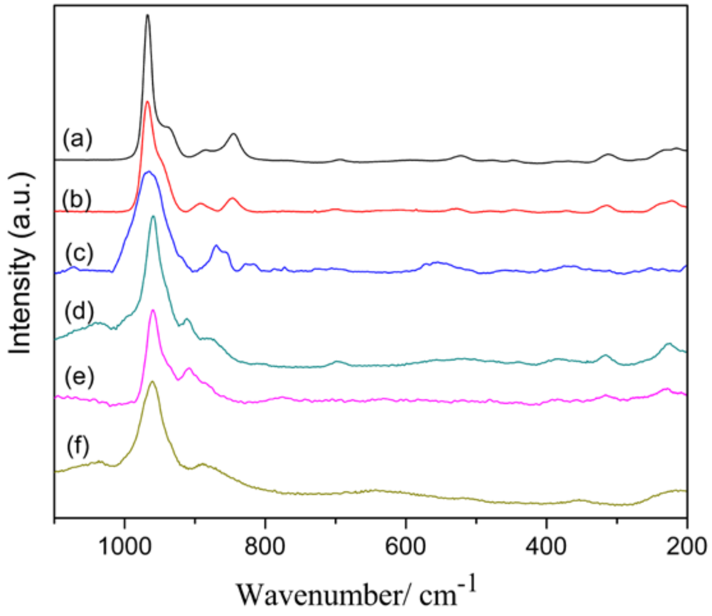

Figure 7.22. Raman spectra of (a) fresh catalyst **Zn$_6$ (9b**) in the solid state, (b) **Zn$_6$ (9b)** in aqueous solution, (c) **Zn6 (9b**) after cyclohexanol oxidation, (d) fresh catalyst **{Cu$_3$}** in the solid state, (e) **{Cu$_3$}** in aqueous solution, (f) **{Cu$_3$}** after cyclohexanol oxidation.

Table 7.4. Residual hydrogen peroxide after oxidation of cyclohexanol.[a]

Entry	System	*T* (°C)	Residual hydrogen peroxide (mmol %)[b]
1	No catalyst	85	36
2	No catalyst	50	90
3	Zn_6 **(9b)**	85	trace
4	Zn_6 **(9b)**	50	27
5	$\{Cu_3\}$	85	trace
6	$\{Cu_3\}$	50	8

[a] Reaction conditions: 0.25 mmol substrate,1.25 mmol (30 %) H_2O_2, 1.0 μmol catalyst, 0.50 mL H_2O, 85 or 50 °C, 7 h. [b] Residual Hydrogen peroxide (mmol %) = mmoles of unreacted hydrogen peroxide/initial mmoles of hydrogen peroxide × 100. Hydrogen peroxide was quantified by the titanyl method [31]

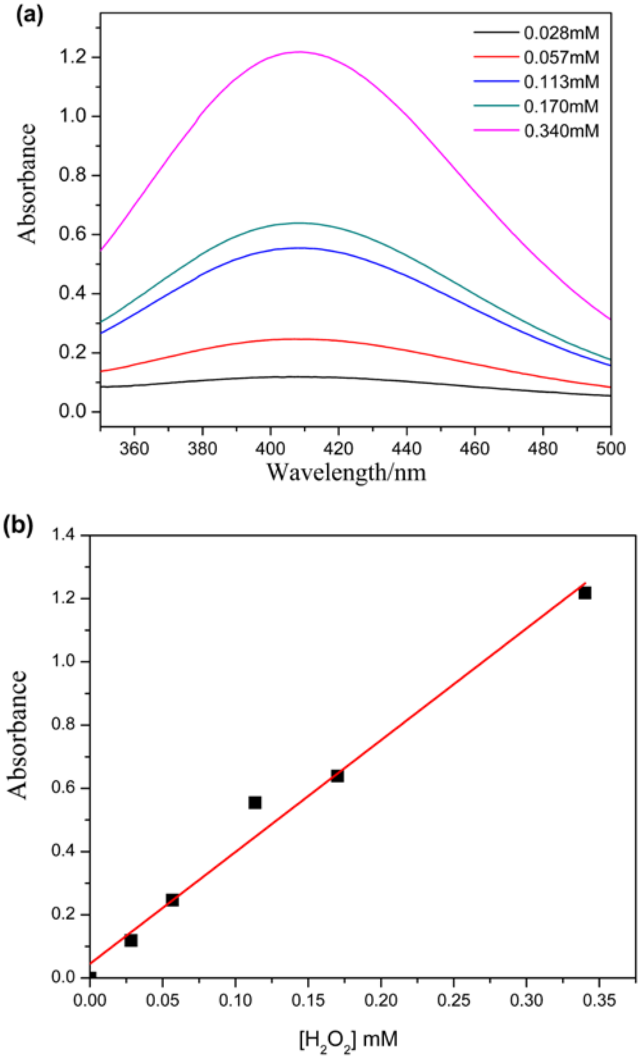

Figure 7.23. (a) UV/Vis spectra of the solutions of the $Ti(O_2)^{2+}$ complex, $[TiOSO_4]$ = 24.39 mM in 2.15 mM H_2SO_4, $[H_2O_2]$ = 0.028-0.340 mM; (b) absorbance at 410 nm *vs.* H_2O_2 concentration.

7.3.5. Catalytic reaction pathways

To gain further insights into the catalytic mechanism, kinetic studies on cyclohexanol oxidation with the new Zn-substituted POMs {**Zn_4_$Zn_{5.2}$ (7a)**, **Zn_6 (9b)**, **Zn_5 (11a)**, **Zn_4 (12a)**, and **Zn_3 (14)**} were performed (Figure 7.24). All Zn-substituted POMs {**Zn_4_$Zn_{5.2}$ (7a)**, **Zn_6 (9b)**, **Zn_5 (11a)**, **Zn_4 (12a)**, and **Zn_3 (14)**} and **{SbW_9}** POMs display quasi-exponential curves, and no induction period was observed for the generation of cyclohexanone. As shown in Figure 7.24, cyclohexanol oxidation proceeded much more rapidly with **Zn_6 (9b)** and **Zn_4_$Zn_{5.2}$ (7a)** than with other Zn-substituted sandwich-type POMs {**Zn_5(11a)**, **Zn_4(12a)**, and **Zn_3(14)**} at 85 °C. After only 30 min, ketone yields higher than 40 % were obtained both in the presence of **(7a)** and **(9b)** in comparison to lower yields around 18-25% with (**11a**), **(12a)**, and **(14)**. Higher yields (93% for **Zn_6 (9b)**, 88% for **Zn_4_$Zn_{5.2}$ (7a)**) can be achieved within 4 h, and both are close to maximum reaction efficiency (ca. 98 % for **Zn_6 (9b)** and 95 % for **Zn_4_$Zn_{5.2}$ (7a)** after 5 h. In contrast to **Zn_5(11a)**, **Zn_4(12a)** and **Zn_3(14)** catalysts, cyclohexanone formation afforded lower yields after 4 h (71%, 72% and 82%, respectively), and maximum yields of 95 % - 98 % were achieved after 7 h. Moreover, the catalytic efficiency of **{SbW_9}** is lower than for all of the Zn-containing POMs **{(7a), (9b), (11a)**, **(12a)** and **(14)}**. The present investigations strongly indicate that the numbers of zinc centers in TM central belt exerts a relevant effect on the catalytic properties of sandwich-type Zn-substituted POMs.

Furthermore, it was shown in **Chapter 5** that the isomeric catalysts [α-$Zn_2Sb^{III}_2(ZnW_9O_{34})_2]^{14-}$ **{α-[Zn_2Sb_2]}** displayed sigmoidal kinetic curves with a long induction period around 60 min corresponding to transformation of the pre-catalyst {**α-[Zn_2Sb_2]}** into the catalytically reactive high valent Sb^V-containing derivatives [α-$Zn_2Sb^V_2(OH)_2(ZnW_9O_{34})_2]^{12-}$ {**α-[$Zn_2Sb^V_2(OH)_2$]**}.[21] However, no induction time was observed during cyclohexanol oxidation with the Zn-substituted sandwich-type POMs {**Zn_4_$Zn_{5.2}$ (7a)**, **Zn_6 (9b)**, **Zn_5 (11a)**, **Zn_4 (12a)**, and **Zn_3 (14)**}. Therefore, the catalytic mechanism for alcohol oxidation catalyzed by new Zn-substituted POMs such as **Zn_6 (9b)** is most probably different from the pathway described for the isomeric catalysts{**α/β-[Zn_2Sb_2]}**.

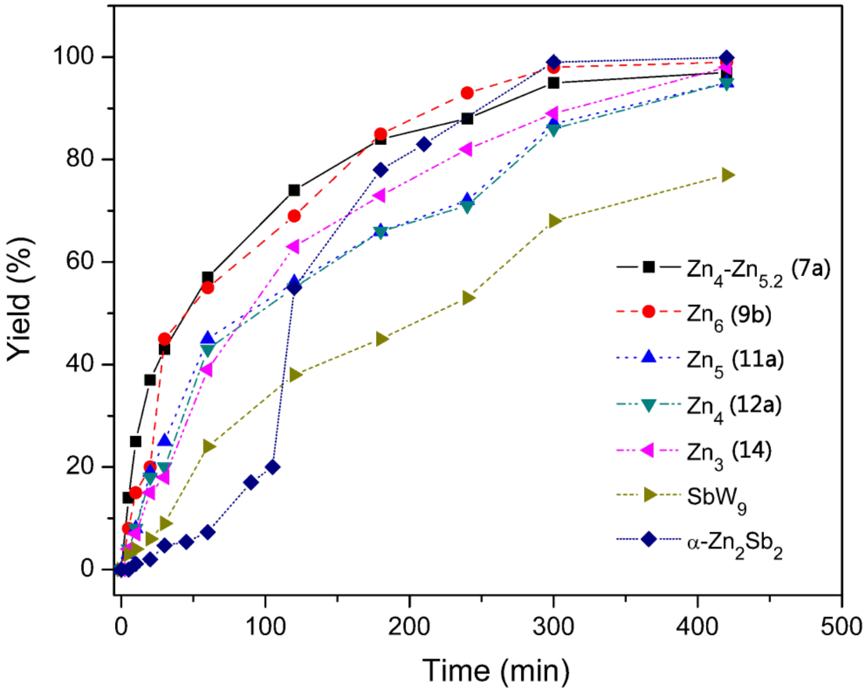

Figure 7.24. Kinetic profiles for the oxidation of cyclohexanol catalyzed by **$Zn_4\_Zn_{5.2}$ (7a)**, **Zn_6(9b)**, **Zn_5(11a)**, **Zn_4(12a)**, **Zn_3(14)**, **{SbW_9}** ligand, and ***α*-Zn_2Sb_2**. (reaction conditions: 1.0 µmol catalyst: 0.25 mmol alcohol, 1.25 mmol H_2O_2 (30 %), T = 85 °C, yield (%) = [cyclohexanone] / initial [cyclohexanol] × 100%, C_0 = initial [cyclohexanol], C = initial [cyclohexanol]-[cyclohexanone]).

Next, $[Zn_6Cl_6(SbW_9O_{33})_2]^{12-}$ {**Zn_6** (9b)} with a hexagonal core motif was applied as standard catalyst in order to study the reactivity of the Zn-POMs towards hydrogen peroxide. Reference FT-IR and Raman spectra of **Zn_6 (9b)** in aqueous solution agree well with solid state spectra, which underlines the oxidative stability of the POM motif (Figure 7.25a and 7.25b). FI-IR spectra are altered after addition of hydrogen peroxide and the appearance of a new peak at 835 cm^{-1} typically is attributed to the formation of a peroxo species (Figure 7.25c), as had been observed before for the $[SbW_9O_{33}]^{9-}$ [33] and $[WZnRh^{III}(ZnW_9O_{34})_2]^{10-}$ catalysts.[17c] After decomposition of the excess H_2O_2 through treatment with aqueous KI solution, the peak at 835 cm^{-1} disappeared and the resulting FT-IR spectrum was identical to that of the pristine $[Zn_6Cl_6(SbW_9O_{33})_2]^{12-}$ polyanion (Figure 7.25d).

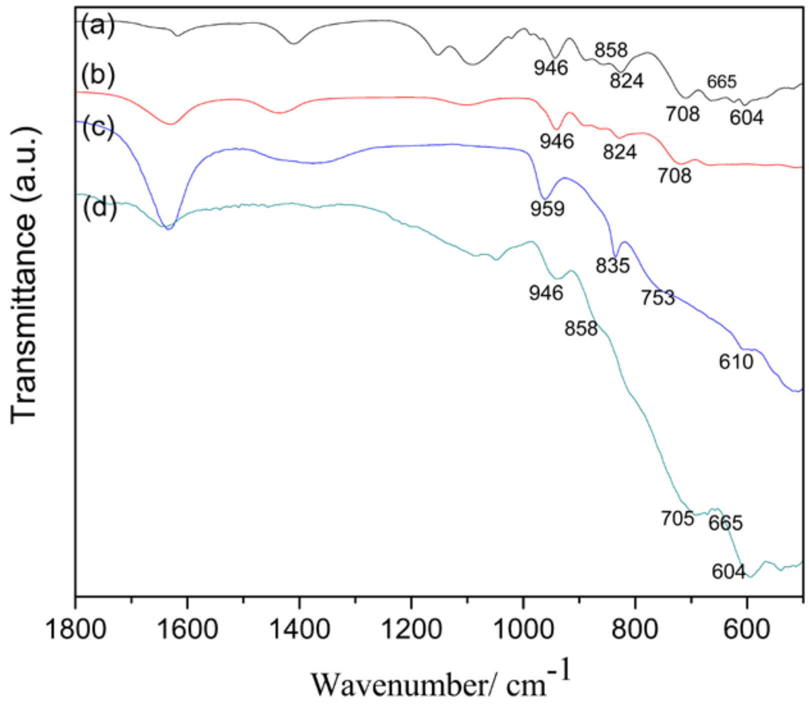

Figure 7.25. FT-IR spectra of (a) **Zn_6 (9b)** in the solid state, (b) **Zn_6 (9b)** in aqueous solution, (c) **Zn_6 (9b)** after treatment with a 50-fold excess of excess of H_2O_2 in aqueous solution, (d) after deposition of excess 30% H_2O_2 with aqueous KI solution.

Raman spectra of **Zn_6 (9b)** in both solid state and aqueous solution are in line with the FT-IR data, (Figure 7.26a and 7.26b), thus providing additional important evidence for POM stability in solution. Addition of small amounts of hydrogen peroxide ($[H_2O_2]/[$**(9b)**$]$ = 1-5) to a **Zn_6 (9b)** gives rise to slight differences in the Raman spectra compared to **Zn_6 (9)** in the absence of hydrogen peroxide (Figure 7.26 b-d). A new weak band appears at 875 cm^{-1} which arises from the stretching ν(O-O) vibration of H_2O_2.[34] Larger amounts of hydrogen peroxide ($[H_2O_2]/[$**(9)**$]$ = 50) turns the solution into a white emulsion within a few minutes at 85 ^oC. The obtained Raman spectrum differs considerably from the above results (Figure 7.26 e). The intensity of the strongest band at 960 cm^{-1} is decreased and new rather weak line at 992 cm^{-1} is ascribed to $\nu_{as}(W=O_d)$ of new species.[35] Two significant new bands appear at 619 and 556 cm^{-1}, which can be assigned to characteristic stretching vibrations $\nu_s[W(O)_2]$ and $\nu_{as}[W(O)_2]$ of the peroxo structural unit $[W(O_2)]$.[34] The FT-IR and Raman spectra in their entirety clearly indicate the formation of a W-peroxo species which is a plausible intermediate species involved in the oxidation of alcohols.

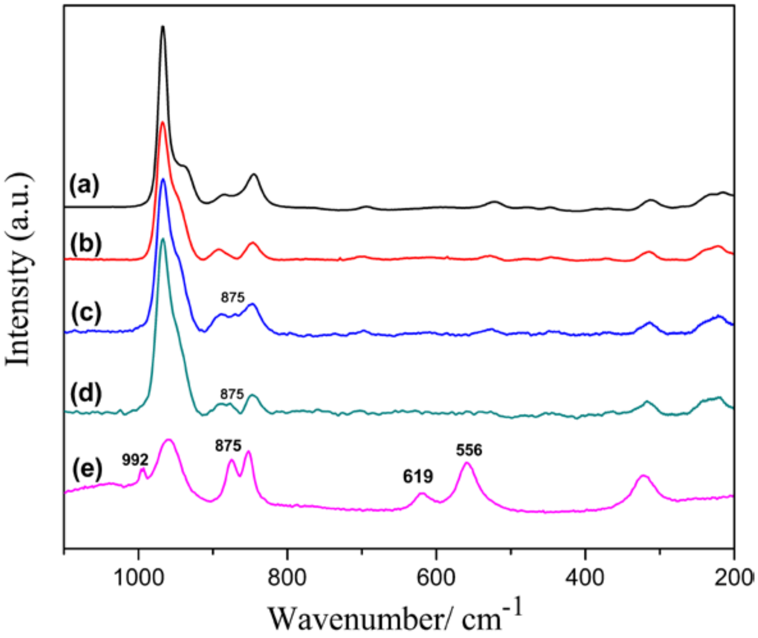

Figure 7.26. Raman spectra of **Zn6 (9b)**: (a) in the solid state; (b) in the absence of H_2O_2 in aqueous solution; (c) $[H_2O_2]$/**[(9b)]** = 1 in aqueous solution; (d) $[H_2O_2]$/**[(9b)]** = 5 in aqueous solution; (e) $[H_2O_2]$/[**(9b)**] = 50 in aqueous solution.

Based on these results, Scheme 7.1 summarizes a proposed peroxometal-mediated catalytic pathway for cyclohexanol oxidation with hydrogen peroxide in the presence of **Zn$_6$ (9b)** and analogous catalysts (Scheme 7.1).[35] In the first steps of the catalytic cycle, the reactive catalyst **(9b)** reacts with hydrogen peroxide to form active intermediates tungsten-peroxo (WOO) species (**Int2**) or tungsten-hydroperoxo (WOOH) species (**Int1**) both via a initial four-membered cyclic transition state (**TS1**).[33, 36] Two possible reaction mechanisms are postulated: Either a tungsten-peroxo (WOO) species (**Int2**) is formed in a process that releases H_2O directly through (**TS1**) or the original terminal (W=O) group captures a hydrogen atom from H_2O_2 to simultaneously transform from (**TS1**) into a tungsten-hydroperoxo (WOOH) species (**Int1**), so that the subsequent formation of (**Int2)** can occur from (**Int1)** with release of H_2O. In the final steps of the catalytic cycle, reactivity of the formed tungsten-peroxo (WOO) species (**Int2**) with cyclohexanol then proceeds as depicted in Scheme 7.1 via (**TS2**), resulting in the original catalyst plus water and cyclohexanone. Moreover, the W centers (e.g., W2 or W3a in Figure 7.2a) are most probably the active sites in the vicinity of zinc metal belt which mediate the oxidation process.[17c, e] The zinc metal centers probably exert an essential cooperative effect on the activation of hydroperoxo or peroxo-tungstate species. Further theoretical insight into the electronic structures of selected Zn-POM catalysts and their detail catalytic reaction pathways are now in progress.

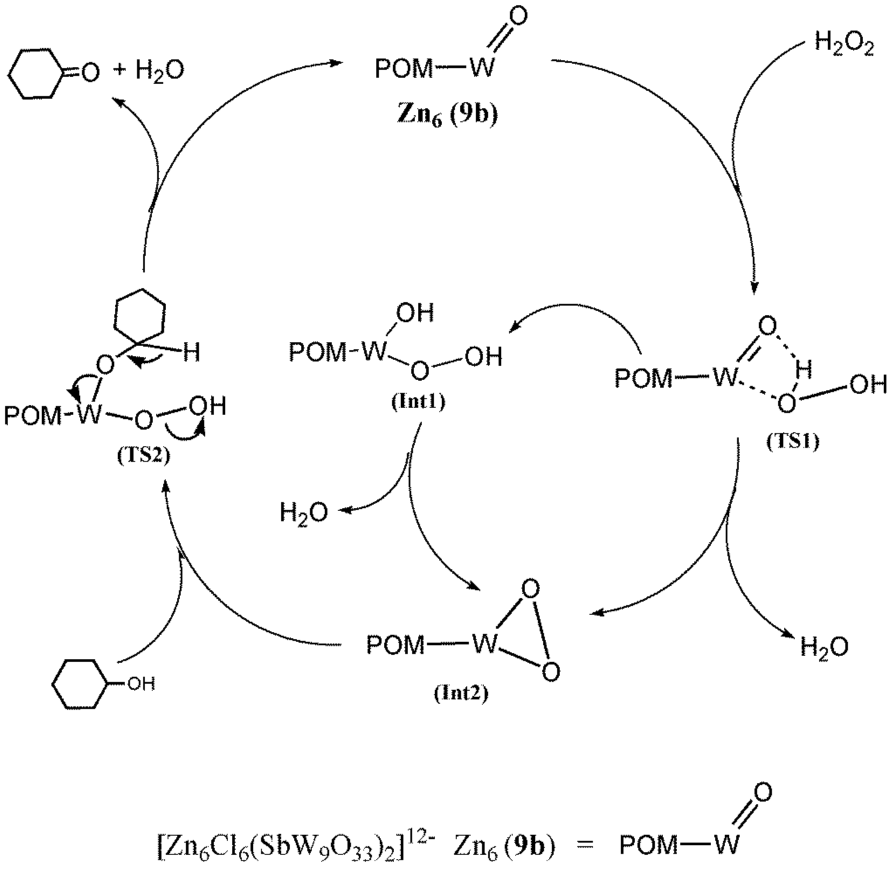

Scheme 7.1. Proposed catalytic scheme for cyclohexanol oxidation with catalyst Zn6 **(9b)**.

7.4 Conclusion

In this chapter, a series of novel sandwich-type $\{Zn_nNa_{6-n}(B\text{-}\alpha\text{-}SbW_9O_{33})_2\}$ (n=3-6) family members was obtained from tuneable synthetic routes with full control over the core nuclearity of the Zn/Sb POMs. The more than 10 members of this newly synthesized

Zn/Sb-POM family exhibit remarkable catalytic efficiency for alcohol oxidation, compared to many different reported POM building blocks. Furthermore, they retain catalytic activity after recycling. A comprehensive investigation of the catalytic tailoring parameters demonstrated that varying core compositions (Cu-belt or Zn-belt) and variations of zinc content in sandwich-type Zn/Sb-POMs family exerts a key influence on the catalytic activity. Moreover, hydroperoxo- or peroxotungstate intermediates were identified as active species involved in the catalytic cycle with a wide range of spectroscopic and analytical methods. Therefore, the peroxometal-based catalytic mechanism for catalytic alcohol oxidation with the new Zn/Sb-POMs series completely differs from the pathway described for {α/β-[Zn_2Sb_2]} catalysts with Sb^V active centers. In short, these results not only brought forward an accessible “hands-on” Zn/Sb-POM model system to understand the relationships between POM structures and their catalytic activity, but they also open up a rational approach to shed new light on the elusive mechanism behind important POM-assisted organic transformations.

References

[1] (a) Pope, M. T. *Heteropoly and Isopoly Oxometalates*, Springer, Berlin, **1983**. (b) Pope, M. T.; Müller, A. *Angew. Chem.*, *Int. Ed.*, **1991**, 30, 34–48. (c) Hill, C. L.; Prosser-McCartha, C. M. *Coord. Chem. Rev*. 1995, 143, 407–455. (d) *Polyoxometalate Molecular Science* (Eds.: Borras-Almenar, J. J.; Coronado, E.; Müller, A.; Pope, M. T.) Kluwer, Dordrecht, 2004. (e) Long, D.-L.; Tsunashima, R.; Cronin, L.; *Angew. Chem. Int. Ed.* **2010**, 49, 1736–1758. (f) *Chem. Rev*. (Ed.: C. L. Hill), **1998**, 98, 1–389 (*Special Issue on Polyoxometalates*). (g) Okuhara, T.; Mizuno, N.; Misono, M. *Adv, Catal*. **1996**, 41, 113–252. (h) Hill, C. L.; Prosser-McCartha, C. M. *Coord. Chem. Rev*. **1995**, 143. (i) *Polyoxometalates: From Platonic Solids to Antiretroviral Activity* (Eds.: Pope, M. T.; Müller, A. Kluwer, Dordrecht, **1994**. (j) *Polyoxometalate Chemistry for Nano-Composite Design*; Yamase, T.; Pope, M. T.; Eds.; Kluwer: Dordrecht, The Netherlands, **2002**. (k) Dolbecq, A.; Dumas, E.; Mayer, C. R.; Mialane, P.; *Chem. Rev*. **2010**, 110, 6009–6048**.** (l) *Polyoxometalate Chemistry: From Topology via Self-Assembly to Applications.* (Eds.: Pope, M. T.; Müller, A.) Kluwer, Dordrecht, **2001**.

[2] (a) Kozhevnikov, I. V. Catalysis by polyoxometalates; John Wiley & Sons, Chichester, **2002**. (b) Mizuno, N.; Yamaguchi, K.; Kamata, K. *Coord. Chem. Rev*. 2005, 249, 1944–1956. (c) Witte, P. T.; Alsters, P. L.; Walther, J.; Müllner, R.; Pöchlauer, P.; Sloboda-Rozner, D.; Neumann, R. Org. *Process Res. & Development* **2004**, 8, 524–531. (d) Kamata, K.; Yonehare, K.; Sumida, Y.; Yamaguchi, K.; Hikichi, S.; Mizuno, N. *Science* **2003**, 300, 964–966; (e) Kamata, K.; Yonehare, K.; Nakagawa, Y.; Uehara, K.; Mizuno, N. *Nature Chem*. **2010**, 2, 478–483.

[3] (a) Tourné, C. M.; Tourné, G. F.; Zonnevijlle, F. *J. Chem. Soc., Dalton Trans*. **1991**, 143–151. (b) Yin, Q.; Tan, J. M.; Besson, C.; Geletiij, Y. M.; Musaev, D. G.; Kuznetsov, A. E.; Luo, Z.; Hardcastle, K. I; Hill, C. L. *Science* **2010**, 328, 342–345. (c) Stracke, J. J.; Finke, R. G. *J. Am. Chem. Soc.* **2011**, 133, 14872–14875. (d) Bösing, M.; Nöh, A.; Loose, I.; Krebs, B. *J. Am. Chem. Soc.* **1998**, 120, 7252–7259. (e) Neumann, R.; Dahan, M. *Nature*. **1997**, 388, 353–355.

[4] McGlone, T.; Vilà-Nadal, L.; Miras, H. N.; Long, D.-L.; Poblet, J. M.; Cronin, L. *Dalton Trans*. **2010**, 39, 11599–11604.

[5] Hussain, F.; Bassil, B. S.; Kortz, U.; Kholdeeva, O. A.; Timofeeva, M. N.; Oliveira, P. de.; Keita B.; and Nadjo, L. *Chem. Eur. J.* **2007**, 13, 4733–4742.

[6] Kortz, U.; Al-Kassem, N. K.; Savelieff, M. G.; Al Kadi, N. A.; Sadakane, M. *Inorg. Chem*. **2001**, 40, 4742–4749.

[7] Sazani, G.; Dickman, M.H.; Pope, M.T., *Inorg. Chem*. **2000**, 39, 939–943.

[8] (a) Bi, L.-H.; Reicke, M.; Kortz, U.; Keita, B.; Nadjo, L.; Clark, R. J. *Inorg. Chem*. **2004**, 43, 3915–3920. (b) Bi, L.-H., Kortz, U., Keita, B., Nadjo, L., and Daniels, L. *Eur. J. Inorg. Chem*. **2005**, 3034–3041.

[9] Kortz, U.; Nellutla, S.; Stowe, A. C.; Dalal, N. S.; Tol, J. V.; Bassil, B. S. *Inorg. Chem*. **2004**, 43, 144–154.

[10].Bi, L.-H.; Kortz, U. *Inorg. Chem*. **2004**, 43, 7961–7962.

[11] Han, Z.; Zhang, Q.; Gao, Y.; Wu, J.; Zhai, X. *Dalton Trans*., **2012**, 41, 1332–1337.

[12] Yamase T.; Fukaya, K.; Nojiri, H.; Ohshima,Y. *Inorg.Chem*. **2006**,45,7698–7704.

[13] Bi, L.-H.; Li, B.; Wu, L.-X.; Bao, Y.-Y. *Inorg. Chim. Acta*, **2009**, 362, 3309–3313.

[14].(a) Chang, S.; Qi, Y.F.; Wang, E.B.; Zhang, Z.M.; *Inorg. Chim. Acta*, **2009**, 362, 453–457. (b) Tan, H. Q.; Zhang, Z. M.; Liu, D.; Qi, Y. F.; Wang E. B.; and Li. Y. G.; *J. Cluster Sci.*, **2008**, 19, 543–550.

[15] Zhao, Z.; Zhou, B.; Zheng, S.; Su, Z.; Wang, C.; *Inorg. Chim. Acta*, **2009**, 362, 5038–5042.

[16] Niu, J.-Y.; Ma, X.; Zhao, J.-W.; Ma, P.-T.; Zhang, C.; and Wang, J.-P. *CrystEngComm*, **2011**, 13, 1834–1836.

[17] (a) Sloboda-Rozner, D.; Alsters, P.; Neumann, R. *J. Am. Chem. Soc.* **2003**, 125, 5280–5281. (b) Neumann, R.; Khenkin, A. M. *Inorg. Chem.* **1995**, 34, 5753–5760; (c) Neumann, R.; Khenkin, A. M. *J. Mol. Catal. A.* **1996**, 114, 169–180; (d) Neumann, R.; Dahan, M.; *J. Am. Chem. Soc.* **1998**, 120, 11969-11976. (e) Neumann, R.; Gara, M.; *J. Am. Chem. Soc.* **1995**, 117, 5066–5074.

[18] Bösing, M.; Noh, A.; Loose, I.; Krebs, B. *J. Am. Chem. Soc*. **1998**, 120, 7252–7259.

[19]. Kikukawa, Y., Yamaguchi, K. & Mizuno, N. *Angew. Chem. Int. Ed.* **2010**, 49, 6096–6100.

[20]. Kikukawa, Y., Yamaguchi, K. & Mizuno, N. *Inorg. Chem*. **2010**, 49, 8194–8196.

[21] Ni, L.; Patscheider, J.; Baldridge, K. K.; Patzke, G. R.; *Chem. Eur. J.* **2012**, 18, 13293–13298.

[22] (a) Loose, I. Droste, E. B sing, M. Pohlmann, H. Dickmann, M. H. Rosu, C. Pope, M. T. Krebs, B. *Inorg. Chem*. **1999**, 38, 2688–2694. (b) Piepenbrink, M.; Limanski, E.M.; Kreb, B. *Z. Anorg. Allg. Chem*. **2002**, *628*, 1187–1191.

[23] Oxford Diffraction, CrysAlis CCD and CrysAlis RED, Oxford Diffraction Ltd., Abingdon, UK, **2005**.

[24] Farrugia, L. J. *J. Appl. Crystallogr.* **1999**, 32, 837–838.

[25] Sheldrick, G. M. SHELX97, *Programs for Crystal Structure Analysis*; Release 97-2; University of Göttingen, Göttingen: Germany, **1997**.

[26] (a) Sadakane, M.; Dickman, M. H.; Pope, M. T. Inorg. Chem. 2001, 40, 2751–2755. (b) du Peloux, C.; Dolbecq, A.; Mialane, P.; Marrot, J.; Rivière, E.; Sécheresse, F. *Inorg. Chem*. **2002**, 41, 7100–7104. (c) Gaunt, A. J.; May, L.; Collison, D.; Fox, D. *Inorg. Chem*. **2003**, 42, 5049–5051. (d) Lei, C.; Mao, J.-G.; Sun, Y.-Q.; Song, J.-L. *Inorg. Chem*. **2004**, 43, 1964–1968. (e) Mazeaud, A.; Dromzee, Y.; Thouvenot, R. *Inorg. Chem*. **2000**, 39, 4735–4740. (f) Juraja, S.; Vu, T.; Richardt, P. J. S.; Bond, A. M.; Cardwell, T. J.; Cashion, J. D.; Fallon, G. D.; Lazarev, G.; Moubaraki, B.; Murray, K. S.; Wedd, A. G. *Inorg. Chem*. **2002**, 41, 1072–1078. (g) Dolbecq, A.; Cdot, E.; Eisner, D.; Sécheresse, F. *Inorg. Chem*. **1999**, 38, 4217–4223. (h) Villanneau, R.; Proust, A.; Robert, F.; Viellet, P.; Gouzerh, P. *Inorg. Chem*. **1999**, 38, 4981–4985. (i) Volkmer, D.; Bredenkötter, B.; Tellenbröker, J.; Kögerler, P.; Kurth, D. G.; Lehmann, P.; Schnablegger, H.; Schwahn, D.; Piepenbrink, M.; Krebs, B. *J. Am. Chem. Soc*. **2002**, 124, 10489–10496.

[27] Robert, F; Leyrie, M.; Hervé, G. *Acta Crystallogr*. **1982**, B38, 358–362.

[28] Brown, I. D.; Altermatt, D. *Acta Crystallogr. Sect. B*. **1985**, 41, 244–247.

[29] Lee, U.; Sasaki, Y. *Bull. Korean Chem. Soc*. **1987**, 8, 1–3.

[30] Redrup, K. V.; and Weller, M. K. *Dalton Trans*., **2009**, 4468–4472.

[31] (a) Allsopp, C. B.; Leach, W. G. *Analyst*, **1941**, 66, 371–372. (b) Patrick, W. A.; and Wagner, H. B. *Anal. Chem*.. **1949**, 21, 1279–1280. (c) O'Sullivan, D. W.; and Tyree, M. *Int J Chem Kinet* , **2007**, 39, 457–461.

[32] Cotton, F. A.; Wilkinson, G. *Advanced Inorganic Chemistry*, 5th ed.; Wiley: New York, **1988**.

[33] Ingle, R. H.; Kala Raj, N. K.; Manikandan, P. *J. Mol. Catal. A* **2007**, 262, 52–58.

[34] (a) Campbell, N. J.; Dengel, A. C.; Edwards, C. J; Griffith, W. P. *J. Chem. Soc., Dalton Trans*. **1989**, 6, 1203–1208. (b) Aubry, C.; Chottard, G.; Platzer, N.; Bregeault, J. M.; Thouvenot, R.; Chauveau, F.; Huet, C.; Ledon, H. Inorg. Chem. **1991**, 30, 4409–4415.

[35] Sheldon, R. A.; Arends, I. W. C. E.; Dijisman, D. *Catal. Today* **2000**, 57, 157–166.

[36] Adam, W.; Alsters, P. L.; Neumann, R.; Saha-Möller, C. R.; Sloboda-Rozner, D.; Zhang, R. *Synlett*, **2002**, 12, 2011–2014.

8. Summary

Polyoxometalates (POMs) are a large family of metal-oxygen clusters of the early transition metals in high oxidation states, most commonly of V^{V}, Mo^{VI}, and W^{VI}. Development of polyoxometalate (POM) clusters is an interdisciplinary research field between nano- and molecular chemistry that opens up a wide variety of possible applications. Besides current electro-, magneto-, medicinal and photochemistry, contemporary catalysis also benefits considerably from POM chemistry, especially through the development of acid and oxidation catalysts for essential organic transformations in the chemical industry. Extensive efforts have been currently focused on the design and assembly of novel POM-based clusters which exhibit unique structures and fascinating properties. The present thesis is thus divided into two research parts: **PART 1 (Chapter 3-4)** covers the systematic structural design of novel lanthanoid-substituted polyoxometalates (LSPs) with fascinating topology, photochemical and magnetic properties; **PART 2 (Chapter 5-7)** is focused on the design and assembly of new transition metal-substituted polyoxometalates (TMSPs) for oxidation catalysis and the investigation of underlying catalytic mechanisms.

In the first part of the thesis (Chapter 3-4), the trivacant *Keggin* $[A\text{-}\alpha\text{-}SiW_9O_{34}]^{10-}$ is employed as a versatile inorganic precursor to construct lanthanoid containing POMs with diverse structural motifs and properties. The structural variety of lanthanoid-containing POMs (LSPs) extending from discrete building blocks to polymeric networks, can be steered by a flexible choice of synthetic parameters such as the pH value, countercations, stoichiometry, temperature, etc. In Chapter 3, the *Keggin*-type $\{SiW_9\}$ precursor was transformed into the open *Wells-Dawson* anion $[A\text{-}\alpha\text{-}Si_2W_{18}O_{66}]^{16-}$ via the incorporation of lanthanoid cations. Five novel polymeric Ln-based open *Wells-Dawson* POMs $[Ln_2(H_2O)_7Si_2W_{18}O_{66}]^{10n-}$ (Ln = Gd^{III} **(Gd-1**, **Gd-2**), Tb^{III} (**Tb-2)**, Dy^{III} (**Dy-2)**, Ho^{III} (**Ho-2**)) were isolated from the one-step reaction of the $[A\text{-}\alpha\text{-}SiW_9O_{34}]^{10-}$ $\{SiW_9\}$ precursor in buffer solutions. Furthermore, the **Gd-1** compound consists of a 3D network structure, whereas the remaining compounds **Gd-2**, **Tb-2**, **Dy-2** and **Ho-2** contain 2D polyoxotungstate sheets. The **Tb-2** and **Dy-2** compounds exhibit room temperature photoluminescence upon excitation, and the **Ho-2** compound displays photochromic behavior. The magnetic behavior of **Gd-1** and **Gd-2** between 2 and 300 K was found to be paramagnetic and in agreement with the spin of non interacting gadolinium centers. Subsequently, Chapter 4 presents four newly obtained open *Wells-Dawson* polyanions $\{LnSi_2W_{18}O_{66}\}$ [Ln = Eu^{III} (**Eu-1** and **Eu-2**), Tb^{III} (**Tb-1**)] and the sandwich-type polyanion $[Eu(\alpha\text{-}SiW_{11}O_{39})_2]^{13-}$ (**Eu-3**). These syntheses are representative examples of synthetic control over POMs for the lanthanoid-assisted conversion of the versatile $[A\text{-}\alpha\text{-}SiW_9O_{34}]^{10-}$ precursor. The effects of structure-directing lanthanoid influences in combination with synthetic fine-tuning were illustrated by the reaction of the lacunary POM $\{SiW_9\}$ with Eu as a mid lanthanoid. First, the spectrum of 2D and 3D architectures for this POM type was expanded by newly introducing Eu^{III} as a mid-lanthanoid to the series (**Eu-1** and **Eu-2**). Secondly, the surprisingly pronounced influence of countercations on the synthetic protocol was illustrated: even a very slight change of Cs^+ concentration can be sufficient to bring forward a new 3D representative of the $\{LnSi_2W_{18}O_{66}\}$-type (**Tb-1**). Furthermore, the long sought-after transformation of the $\{SiW_9\}$ into the 0D sandwich-type geometry of $[Eu(\alpha\text{-}SiW_{11}O_{39})_2]^{13-}$ (**Eu-3**) was finally obtained through step-wise alterations of the overall ionic strength for Eu-based protocols. The key photoluminescent, electrochemical and magnetic properties of all newly produced materials were also investigated.

In the second part of the thesis (Chapter 5-7), transition metal-substituted polyoxometalates (TMSPs) are newly developed as tuneable and versatile catalysts for alcohol oxidation. However, any crystallographic identification of POM intermediates in catalytic alcohol oxidation cycles has not been accomplished to date, which leaves key mechanistic questions open. Initially, two novel Zn/Sb-POM catalysts $\alpha\text{-}/\beta\text{-}[Zn_2Sb_2(ZnW_9O_{34})_2]^{14-}$ **$\{\alpha\text{-}/\beta\text{-}[Zn_2Sb^{III}_2]\}$ (1a, 2a)** were obtained from an efficient and selective preparative strategy using NH_4^+ as a very versatile structure-directing agent (Chapter 5). The observed spontaneous β-/α-isomerization process agrees well with computational studies. Both **$\alpha\text{-}/\beta\text{-}[Zn_2Sb^{III}_2]$** isomers are efficient, recyclable and selective catalysts for homogenous alcohol oxidation. Furthermore, for the first time, important Sb(V)-containing active species $\alpha/\beta\text{-}[Zn_2Sb^V_2(OH)_2(B\text{-}\alpha\text{-}ZnW_9O_{34})_2]^{12-}$ **$\{\alpha\text{-}/\beta\text{-}[Zn_2Sb^V_2(OH)_2]\}$ (3, 4)** are characterized with single crystal X-ray diffraction methods together with various analytical techniques, and their structural features as well as their electrophilicity were analyzed with high level computational methods (collaboration with Prof. Kim K. Baldridge). These high valent compounds play a key role in initiating and maintaining the catalytic cycle (Chapter 5). The preparative access to these new Zn/Sb-POMs was furthermore extended into a more general approach proceeding directly from a 0D POM precursor over 1D polymeric chains to higher dimensional networks comprising of {Zn_2Sb_2} (Chapter 6). This was pursued by using Zn^{2+} cations as a flexible connecting linkers in Chapter 6. Two novel {Zn_2Sb_2}-based polymeric compounds **(5)** and **(6)** emerge from the one-step reaction of the lacunary $[B\text{-}\alpha\text{-}SbW_9O_{33}]^{9-}$ {SbW_9} precursor with Zn^{2+} cations in aqueous solution. This newly discovered transformation from the {SbW_9} fragment into a *Keggin*-type $[B\text{-}\alpha\text{-}ZnW_9O_{34}]^{12-}$ {ZnW_9O_{34}} unit was induced by heating and the addition of a zinc source in aqueous solution. Compound **(6)** with 2D sheets was formed with excess Zn^{2+}, whereas **(5)** with 1D ladders was obtained at lower Zn^{2+} concentrations. The electrochemical and luminescence properties of **(5)** and **(6)** were investigated. The polymeric POMs catalyst **(5)** and **(6)** also exhibit high catalytic activity in homogeneous alcohol oxidation of cyclohexanol, compared to the discrete POMs catalysts α-/β-[$Zn_2Sb^{III}_2$]. Therefore, this work provides a new pathway to explore and to control assemblies and structural transformations of TMSP-based high-dimensional coordination polymers with modulated functionality for new catalytic and other up-to-date applications.

Finally, Chapter 7 demonstrates that tuneable synthetic routes are capable of bringing forward 12 structurally characterized members of the large sandwich-type Zn/Sb-POM family {$Zn_nNa_{6-n}\,(B\text{-}\alpha\text{-}SbW_9O_{33})_2$} ($n$ = 3-6) by exerting full control over the core nuclearity of a POM catalyst series. The comprehensive catalytic alcohol oxidation performance tests permitted a new degree of systematic insight into the POM tailoring structural parameters, such as different core compositions (Cu-belt or Zn-belt), variations of zinc content etc., which exert key influence on the catalytic activity. Hydroperoxo- or peroxotungstate intermediates were identified as active species with a wide range of spectroscopic and analytical methods. The crucial importance of POM belt construction is evident from comparison of the {$Zn_nNa_{6-n}\,(B\text{-}\alpha\text{-}SbW_9O_{33})_2$} (n = 3-6) catalyst series with [α/β-$Zn_2Sb^{III}_2$] catalysts containing active Sb centers. This systematic investigation combines progress in oxocluster-based homogeneous catalysis on the synthetic, catalytic and computational level.

All in all, this thesis demonstrates that a systematic and comprehensive approach (synthetic optimization – mechanistic studies – materials applications) in POM chemistry paves new way to the targeted development of functional POMs materials for key industrial processes and urgent energy applications.

9. Zusammenfassung

Polyoxometallate (POMs) sind eine grosse Familie von molekularen Metall-Sauerstoff-Verbindungen der frühen Übergangsmetalle in hohen Oxidationszuständen, mit V^{V}, Mo^{VI} und W^{VI} als häufigsten Vertretern. Die Entwicklung von Polyoxometallaten ist hochgradig interdisziplinär: Beiträge aus der Struktur- und Materialchemie im Grenzgebiet zwischen Festkörper- und Moleküldesign eröffnen ein unerreicht vielfältiges Feld an Anwendungen. Neben der aktuellen Elektro-, Magneto-, Medizinal- und Photochemie profitiert auch die Katalyse von POMs, vor allem in Form von Säure- und Oxidationskatalysatoren für wichtige organische Reaktionen in der chemischen Industrie. Heutzutage werden bedeutende Anstrengungen unternommen, um neue POM-basierte Moleküle mit einzigartigen Strukturen und faszinierenden Eigenschaften zu entwickeln. Die vorliegende Doktorarbeit umfasst daher zwei Hauptteile: **TEIL 1 (Kapitel 3-4)** befasst sich mit der systematischen Entwicklung von neuen Lanthanoid-substituierten Polyoxometallaten (LSPs) mit faszinierender Topologie, sowie photochemischen und magnetischen Eigenschaften. **TEIL 2 (Kapitel 5-7)** behandelt die Entwicklung von neuen Übergangsmetall-substituierten Polyoxometallaten (TMSPs) für die oxidative Katalyse sowie die vertieften Untersuchung der zugrundeliegenden katalytischen Mechanismen.

Der erste Teil der Arbeit (Kapitel 3-4) etabliert das trivakante *Keggin*-Ion $[A\text{-}\alpha\text{-}SiW_9O_{34}]^{10-}$ als vielseitigen Ausgangsstoff zur Konstruktion von LSPs mit verschiedenen Strukturmotiven und Eigenschaften. Diese strukturelle Vielfalt, von einzelnen Bausteinen hin zu polymeren Netzwerken, kann durch geeignete Wahl der Syntheseparameter (pH Wert, Kationen, Stöchiometrie, Temperature, etc.) flexibel beeinflusst werden. Im dritten Kapitel wird der *Keggin*-Prekursor $\{SiW_9\}$ via den Einbau von Lanthanoid-Kationen in das offene *Wells-Dawson*-Anion $[A\text{-}\alpha\text{-}Si_2W_{18}O_{66}]^{16-}$ überführt. Aus einfachen („one-step“) Reaktionen des $[A\text{-}\alpha\text{-}SiW_9O_{34}]^{10-}$ $\{SiW_9\}$ Vorläufers in Pufferlösungen konnten fünf neue polymerische Ln-basierte offene *Wells-Dawson* POMs $[Ln_2(H_2O)_7Si_2W_{18}O_{66}]^{10n-}$ (Ln = Gd^{III} (**Gd-1**, **Gd-2**), Tb^{III} (**Tb-2**), Dy^{III} (**Dy-2**), Ho^{III} (**Ho-2**)) isoliert werden. Die Verbindung **Gd-1** besteht aus einer 3D-Netzwerkstruktur, wohingegen die restlichen Verbindungen (**Gd-2**, **Tb-2**, **Dy-2** und

Ho-2) aus 2D-Schichten aufgebaut sind. Unter Anregung weisen **Tb-2** und **Dy-2** Raumtemperatur-Photolumineszenz auf, und **Ho-2** zeichnet sich durch interessantes photochromisches Verhalten aus. In Übereinstimmung mit dem Spin der nicht-interagierenden Gd-Zentren verhalten sich **Gd-1** und **Gd-2** paramagnetisch im Temperaturbereich von 2 bis 300 K. Im vierten Kapitel werden die vier neu synthetisierten offenen *Wells-Dawson*-Polyanionen $\{LnSi_2W_{18}O_{66}\}$ [Ln = Eu^{III} (**Eu-1** and **Eu-2**), Tb^{III} (**Tb-1**)] sowie das neue Sandwich-Polyanion $[Eu(\alpha\text{-}SiW_{11}O_{39})_2]^{13-}$ (**Eu-3**) vorgestellt. Deren Synthese veranschaulicht die Herausforderungen der Synthesekontrolle bei der Ln-assistierten Umwandlung des $[A\text{-}\alpha\text{-}SiW_9O_{34}]^{10-}$ Bausteines. Die Reaktion des lakunaren POMs $\{SiW_9\}$ mit dem mittleren Lanthanoid Eu illustriert das subtile Wechselspiel zwischen dem Lanthanoid-Ionenradius und der Feinregulierung synthetischer Parameter. Wird die Lanthanoid-Serie (Gd-Tb_Dy-Ho) mit Eu erweitert, vergrössert sich das Spektrum der 2D- und 3D-Architekturen (**Eu-1** und **Eu-2**). Des Weiteren zeigt sich der überraschend grosse Einfluss der Gegenionen auf die Synthese: Bereits eine sehr kleine Änderung der Cs^+ Konzentration kann zur Ausbildung einer neuen 3D Variante des $\{LnSi_2W_{18}O_{66}\}$-Typs führen (**Tb-1**). Auch die Transformation des $\{SiW_9\}$ Bausteines in die 0D Sandwich-Geometrie des $[Eu(\alpha\text{-}SiW_{11}O_{39})_2]^{13-}$ (**Eu-3**) wurde schlussendlich durch schrittweise Änderung der Ionenstärke in den Eu-basierten Protokollen erreicht. Die wichtigen photolumineszenten, elektrochemischen und magnetischen Eigenschaften aller neu hergestellter Materialien wurden ebenfalls untersucht.

Im zweiten Teil der Arbeit (Kapitel 5-7) werden Übergangsmetall-substituierte Polyoxometallate (TMSPs) als abstimmbare und breit anwendbare Katalysatoren für die homogene Alkoholoxidation verwendet. Da generell POM-Intermediate in der katalytischen Alkoholoxidation bis heute noch nicht kristallographisch identifiziert werden konnten, bleiben gewisse mechanistische Fragen noch offen. Kapitel 5 präsentiert zwei neue Zn/Sb-POM Katalysatoren $\alpha\text{-}/\beta\text{-}[Zn_2Sb_2(ZnW_9O_{34})_2]^{14-}$ $\{\alpha\text{-}/\beta\text{-}[Zn_2Sb^{III}_2]\}$ (**1a**, **2a**), die mittels NH_4^+ als einfachem strukturdirigierendem Agens hergestellt wurden. Die experimentell beobachtete spontane Isomerisierung des *β*-Isomers zum α-Isomer ist in guter Übereinstimmung mit theoretischen Untersuchungen (Zusammenarbeit mit Prof. Kim K. Baldridge). Die $\{\alpha\text{-}/\beta\text{-}[Zn_2Sb^{III}_2]\}$ Isomere sind effiziente, rezyklierbare und selektive Katalysatoren zur homogenen Alkoholoxidation. Ausserdem konnte zum ersten Mal die aktive Sb^{V}-Spezies α/β-$[Zn_2Sb^{V}_2(OH)_2(B\text{-}\alpha\text{-}ZnW_9O_{34})_2]^{12-}$ $\{\alpha\text{-}/\beta\text{-}[Zn_2Sb^{V}_2(OH)_2]\}$ (**3**, **4**) mit Einkristalldiffraktion und diversen anderen Methoden charakterisiert und bezogen auf Struktur und Eigenschaften mit Berechnungen auf hohem Niveau verifiziert werden. In Kapitel 6 wird der allgemeine Ansatz, direkt vom 0D POM Ausgangsstoff über 1D polymere Ketten zu höher-dimensionalen Netzwerken aus $\{Zn_2Sb_2\}$ durch Einsatz von Zn^{2+} als verknüpfendes Kation weiterverfolgt. Aus der einfachen („one-step“) Reaktion des lakunaren $[B\text{-}\alpha\text{-}SbW_9O_{33}]^{9-}$ $\{SbW_9\}$ Vorläufers mit Zn^{2+}-Kationen konnten erfolgreich zwei neue $\{Zn_2Sb_2\}$-basierte Polymer-Verbindungen ((**5**) und (**6**)) isoliert werden. Heizen in einer Zn^{2+}-haltigen Lösung führte zur neuartigen Umwandlung des $\{SbW_9\}$ Fragments in eine $[B\text{-}\alpha\text{-}ZnW_9O_{34}]^{12-}$ $\{ZnW_9O_{34}\}$ Einheit vom *Keggin*-Typ. Verbindung (**6**) mit einer 2D Schichtstruktur bildete sich mit einem Überschuss an Zn^{2+}, während die 1D Leiterstruktur von (**5**) bei tieferen Zn^{2+}-Konzentrationen entstand. Die elektrochemischen und photolumineszenten Eigenschaften beider Verbindungen wurden untersucht. Im Vergleich zu den monomeren POM-Katalysatoren $\alpha\text{-}/\beta\text{-}[Zn_2Sb^{III}_2]$ zeigen auch die polymerartigen Katalysatoren (**5**) und (**6**) hohe katalytische Aktivität in der homogenen Alkoholoxidation von Cyclohexanol. Diese Arbeit bereitet daher den Weg zur Erkundung und Kontrolle der Synthese und der strukturellen Umwandlung von TMSP-basierten höher-dimensionalen Koordinationspolymeren mit modulierter Funktionalität für neue katalytische und andere zeitgenössische Anwendungen.

Kapitel 7 präsentiert zum ersten Mal die vollständige Kontrolle über die Anzahl der Atome im Kernbereich eines Sandwich-POMs. Die Serie von zwölf strukturell charakterisierten Zn/Sb-Sandwich-POMs aus der Familie der $\{Zn_nNa_{6-n}(B\text{-}\alpha\text{-}SbW_9O_{33})_2\}$ (n = 3-6) POMs wurde durch Feinregulierung des Synthesewegs zugänglich. Die umfassenden katalytischen Tests zur Alkoholoxidation erlaubten einen neuen Grad an systematischer Einsicht in die strukturellen Parameter zur Feinabstimmung von POM-Katalysatoren (z. B. die Zusammensetzung des Kerns (Cu- oder Zn-Gürtel), die Variation des Zn-Gehalts etc.), die hohen Einfluss auf die katalytische Aktivität haben. Eine grosse Anzahl spektroskopischer und analytischer Methoden identifizierte Hydroxo- oder Peroxowolframat-Intermediate als aktive Spezies. Der entscheidende Einfluss der Zusammensetzung des POM-Zentralkerns wird klar, wenn man die $\{Zn_nNa_{6-n}(B\text{-}\alpha\text{-}SbW_9O_{33})_2\}$ (n = 3-6) Katalysatoren mit $[\alpha/\beta\text{-}Zn_2Sb^{III}_2]$ Katalysatoren vergleicht, die aktive Sb-Zentren enthalten. Dieser Teil der vorliegenden Doktorarbeit erweitert die Grenzen der Oxocluster-basierten homogenen Katalyse auf dem Niveau der Synthese, der Katalyse und der theoretischen Berechnungen.

In ihrer Gesamtheit demonstriert diese Arbeit den systematischen Forschungsansatz (Syntheseoptimierung – mechanistische Studien – Anwendungen der erhaltenen Materialien) in der POM-Chemie und bereitet gleichzeitig den Weg für neue Entwicklungen im Bereich der funktionalen POM-Materialien für industrielle Prozesse sowie für aktuelle Anwendungen im Bereich der Energietechnologie.

10. Annexes

Table 10.1. Crystallographic data for compounds **Gd-1**, **Gd-2, Tb-2**, **Dy-2** and **Ho-2**.

	Gd-1	**Gd-2**	**Tb-2**	**Dy-2**	**Ho-2**
empirical formula	$CsCaH_{68}Na_2Gd_4O_{100}Si_2W_{18}Cl$	$C_2Cs_{3.5}H_{51}Gd_3Na_{2.5}O_{91}Si_2W_{18}$	$Cs_3H_{50}Na_2Tb_3O_{90}Si_2W_{18}$	$C1Cs_3H_{50}Dy_3Na_4O_{90.5}Si_2W_{18}Cl1$	$Cs_3H_{50}Ho_3Na_4O_{91}Si_2W_{18}$
fw (g·mol^{-1})	5917.18	5890.84	5777.10	5888.93	5857.12
T (K)	183(2)	183(2)	183(2)	183(2)	183(2)
λ (Å)	0.71073	0.71073	0.71073	0.71073	0.71073
crystal system, S. G.	monoclinic, *C2/c*	triclinic, *P-1*	triclinic, *P-1*	triclinic, *P-1*	triclinic, *P-1*
a (Å)	26.1719(4)	12.8242(1)	12.9462(2)	12.8335(3)	12.9422(12)
b (Å)	20.7408(4)	15.7895(2)	15.7702(2)	15.7343(3)	15.6464(8)
c (Å)	39.3620(8)	23.2486(3)	23.1831(3)	23.1443(4)	23.0735(12)
α (°)	90.00	99.591(1)	99.135(1)	99.304(2)	99.062(4)
β (°)	94.021(2)	97.904(1)	98.002(2)	98.206(2)	98.117(6)
γ (°)	90.00	91.547(1)	93.398(1)	92.871(2)	93.777(6)
V (Å^3)	21314..1(7)	4591.65(9)	4611.6(1)	4551.9(1)	4549.2(5)
Z	8	2	2	2	2
abs. coeff (mm^{-1})	22.476	26.064	25.939	26.248	26.318
$d_{calc.}$ (Mg·m^{-3})	3.719	4.307	4.263	4.293	4.226
F(000)	20756	5141	5116	5085	4992
crystal size (mm)	0.38×0.06×0.04	0.15×0.08×0.05	0.23×0.22×0.13	0.23×0.18 ×0.06	0.11×0.09×0.08
GOF on F^2	0.885	0.996	1.065	0.921	0.916
R_1 [I > 2 σ(I)]	0.0490	0.0384	0.0414	0.0401	0.0515
wR_2 [I > 2σ(I)]	0.0914	0.0906	0.0986	0.0837	0.1075

$R_1 = \sum(Fo - Fc)/\sum Fo$ and $wR_2 = \{\sum w(Fo^2 - Fc^2)^2/\sum w(Fo^2)^2\}^{1/2}$

Table 10.2. Crystallographic data for compounds **Eu-1**, **Eu-2**, **Eu-3**, and **Tb-1**.

	Eu-1	**Eu-2**	**Eu-3**	**Tb-1**
Empirical formula	$Cl_2Cs_{1.25}Eu_4Na_2O_{103}Si_2W_{18}$	$C_2Cl_2Cs_3Eu_3Na_3O_{103}Si_2W_{18}$	$ClCs_{2.70}EuNa_7O_{109}Si_2W_{22}$	$ClCsNa_2O_{104.5}Si_2Tb_4W_{18}$
fw (g·mol^{-1})	5904.34	6031.98	6552.08	5887.50
Crystal system	monoclinic	triclinic	triclinic	monoclinic
Space group	*C2/c*	*P-1*	*P-1*	*C2/c*
a (Å)	26.1593(5)	12.80109(17)	13.2672(2)	26.0814(4)
b (Å)	20.7104(5)	15.80696(18)	19.8634(3)	20.6816(3)
c (Å)	39.3602(9)	23.2340(2)	20.3149(3)	39.2781(5)
α (°)	90.00	99.5644(9)	96.8044(10)	90.00
β (°)	93.840(2)	97.8707(10)	104.6383(10)	93.8510(10)
γ (°)	90.00	91.5937(10)	92.5846(10)	90.00
V (Å^3)	21276.3(8)	4586.13(9)	5127.65(13)	21139.0(5)
Z	8	2	2	8
Completeness	97.7 % (to theta = 28.28°)	99.9 % (to theta = 27.10°)	99.9 % (to theta = 26.37°)	99.9 % (to theta = 28.28°)
abs. coefficient (mm^{-1})	22.304	25.857	26.308	22.643
$d_{calc.}$ (Mg·m^{-3})	3.687	4.368	4.244	3.700
F(000)	20486	5234	5667	20400
Crystal size (mm)	0.83 x 0.13 x 0.11	0.21 x 0.12 x 0.07	0.18 x 0.06 x 0.04	0.78 x 0.12 x 0.08
Gof	0.874	1.043	1.024	1.048
final R_1[a]	0.0454	0.0464	0.0399	0.0471
wR_2 indices [$I > 2\sigma(I)$][b]	0.0956	0.1177	0.1032	0.1154
largest diff. peak and hole (e.Å^{-3})	3.804 and -5.792	3.995 and -3.163	4.225 and -4.333	5.346 and -5.035

$R_1 = \Sigma(Fo - Fc)/\Sigma Fo$ *and* $wR_2 = \{\Sigma w(Fo^2 - Fc^2)^2/\Sigma w(Fo^2)^2\}^{1/2}$

Table 10.3. Crystallographic data for compounds **α-NH$_4$-[Zn$_2$Sb$_2$] (1a), α-Na-[Zn$_2$Sb$_2$] (1b)**, **β-Na-[Zn$_2$Sb$_2$] (2a)** and **β-NH$_4$-[Zn$_2$Sb$_2$] (2b)**.

	α-NH$_4$-[Zn$_2$Sb$_2$] (1a)	**α-Na-[Zn$_2$Sb$_2$] (1b)**	**β-Na-[Zn$_2$Sb$_2$] (2a)**	**β-NH$_4$-[Zn$_2$Sb$_2$] (2b)**
empirical formula	$N_{10}O_{92}Sb_2W_{18}Zn_6$	$Na_{12}O_{132}Sb_2W_{18}Zn_4$	$Na_{14}O_{114}Sb_2W_{18}Zn_4$	$N_{14}O_{80}Sb_2W_{18}Zn_4$
fw (g·mol^{-1})	5557.08	6202.08	5960.06	5290.34
temperature (K)	183(2) K	183(2) K	183(2) K	183(2) K
wavelength (Å)	0.71073	0.71073	0.71073	0.71073
crystal system, space group	orthorhombic, *Pnnm*	monoclinic, *C 2/m*	triclinic, *P-1*	triclinic, *P-1*
a (Å)	19.4676(4)	26.0708(11)	13.513(3)	12.3221(3)
b (Å)	16.1138(4)	14.7487(2)	14.384(3)	12.6634(4)
c (Å)	14.5572(3)	22.1367(9)	15.253(2)	16.3295(4)
α (deg)	90	90	65.501(2)	92.986(2)
β (deg)	90	133.746(7)	89.4877(17)	99.402(2)
γ (deg)	90	90	72.043(2)	116.926(3)
volume (Å^3)	4566.55(17)	6149.0(3)	2541.1(9)	2218.16(12)
Z	2	2	1	1
Abs coeff. (mm^{-1})	24.806	18.122	21.904	24.992
Density (calcd.) (Mg·m^{-3})	4.042	3.350	3.893	3.960
F(000)	4840	5484	2620	2292
crystal size (mm^3)	0.44 × 0.21 × 0.18	0.43 × 0.32 × 0.18	0.21 × 0.20 × 0.05	0.25 × 0.16 × 0.08
goodness-of-fit on F^2	1.108	1.060	1.085	1.156
$R_1[I > 2\sigma(I)]$	0.0466	0.0489	0.0440	0.0494
wR_2 $[I > 2\sigma(I)]$	0.1160	0.1454	0.1270	0.1418

$R_1 = \sum(Fo - Fc)/\sum Fo$ *and* $wR_2 = \{\sum w(Fo^2 - Fc^2)^2/\sum w(Fo^2)^2\}^{1/2}$

Table 10.4. Crystallographic data for compounds ***α*-[$Zn_2Sb^V{}_2(OH)_2$] (3)** and ***β*-[$Zn_2Sb^V{}_2(OH)_2$] (4)**.

	***α*-[$Zn_2Sb^V{}_2(OH)_2$] (3)**	***β*-[$Zn_2Sb^V{}_2(OH)_2$] (4)**
empirical formula	$N_8Na_4O_{98}Sb_2W_{18}Zn_4$	$N_{10}Na_2O_{90}Sb_2W_{18}Zn_4$
formula weight (g·mol^{-1})	5586.24	5440.28
temperature (K)	183(2) K	183(2) K
wavelength (Å)	0.71073	0.71073
crystal system, space group	monoclinic, *$P2_1/n$*	triclinic, *P-1*
a (Å)	12.8395(2)	13.1043(3)
b (Å)	16.6109(2)	16.5663(4)
c (Å)	21.6204(4)	22.4691(6)
α (deg)	90	70.400(2)
β (deg)	104.6849(17)	73.951(2)
γ (deg)	90	70.622(2)
volume (Å^3)	4460.48(13)	4259.35(18)
Z	2	2
Abs coefficient (mm^{-1})	24.898	26.052
density (calcd.) (Mg·m^{-3})	4.159	4.242
F(000)	4876	4732
crystal size (mm^3)	0.23 x 0.21 x 0.18	0.38 x 0.06 x 0.05
goodness-of-fit on F^2	1.100	1.048
$R_1[I > 2\sigma(I)]$	0.0375	0.0444
$wR_2\ [I > 2\sigma(I)]$	0.0890	0.0885

$R_1 = \sum(Fo - Fc)/\sum Fo$ and $wR_2 = \{\sum w(Fo^2 - Fc^2)^2/\sum w(Fo^2)^2\}^{1/2}$

Table 10.5. Bond valence sums (BVS) for **α-NH_4-[Zn_2Sb_2] (1a)**, **β-Na-[Zn_2Sb_2] (2a)**.

α-NH_4-[Zn_2Sb_2] (1a)							
Zn1	2.0406	Zn2	2.1554	Sb1	3.0836	W1	5.8846
W2	5.9389	W3	5.9102	W4	6.0088	W5	5.9955
O1	1.6039	O2	1.5820	O3	1.7870	O4	1.9720
O5	1.7477	O6	1.9531	O7	1.7864	O8	1.8960
O9	2.0654	O10	2.0598	O11	1.5595	O12	1.6944
O13	1.9732	O14	1.5619	O15	1.9760	O16	1.5399
O17	1.8159	O18	1.9243	O19	2.0116	O20	1.9075
β-Na-[Zn_2Sb_2] (2a)							
Zn1	2.0241	Zn2	2.1435	Sb1	3.0462	W1	5.7966
W2	5.8924	W3	6.0339	W4	5.9767	W5	5.8388
W6	5.8288	W7	5.8977	W8	5.8596	W9	5.8810
O1	1.8866	O2	1.7465	O3	1.7218	O4	1.6849
O5	1.7016	O6	1.5036	O7	2.0424	O8	1.8039
O9	2.0363	O10	1.9791	O11	1.5068	O12	1.8820
O13	1.7781	O14	1.5566	O15	1.4694	O16	2.0112
O17	1.8022	O18	1.9375	O19	1.9960	O20	1.9212
O21	2.0665	O22	1.9126	O23	1.6857	O24	1.8087
O25	1.8130	O26	1.9159	O27	1.4599	O28	1.5067
O29	1.6093	O30	2.0507	O31	1.8397	O32	1.7260
O33	2.0677	O34	1.9207				

Table 10.6. Bond valence sums (BVS) for **α-[Zn$_2$Sb$^{V}_2$(OH)$_2$] (3)** and **β-[Zn$_2$Sb$^{V}_2$(OH)$_2$](4)**.

α-[Zn$_2$Sb$^{V}_2$(OH)$_2$] (3)							
Zn1	2.1645	Zn2	2.2947	Sb1	4.6297	W1	6.0622
W2	5.9855	W3	5.9668	W4	5.8808	W5	5.9656
W6	5.9031	W7	5.9023	W8	5.9387	W9	5.9723
O1	1.5640	O2	1.5659	O3	1.5626	O4	1.9724
O5	2.0059	O6	1.9447	O7	1.7474	O8	1.8036
O9	1.7284	O10	1.8284	O11	1.7884	O12	1.9468
O13	1.9232	O14	1.5013	O15	1.9703	O16	1.5689
O17	1.7872	O18	1.5047	O19	1.5191	O20	1.7412
O21	1.6022	O22	2.0125	O23	1.7408	O24	1.7621
O25	2.0942	O26	2.1313	O27	2.0907	O28	1.9858
O29	1.9551	O30	1.7608	O31	1.9867	O32	1.8278
O33	2.1071	O34	1.9473	O35	0.8726		

β-[Zn$_2$Sb$^{V}_2$(OH)$_2$] (4)							
Zn1	1.9988	Zn2	2.2342	Sb1	4.9513	W1	5.9607
W2	5.8816	W3	5.9864	W4	5.9232	W5	6.0488
W6	5.8826	W7	6.0347	W8	5.9086	W9	5.8855
O1	1.7510	O2	1.6705	O3	1.8628	O4	1.5819
O5	1.8318	O6	1.6138	O7	1.9595	O8	1.8848
O9	2.0536	O10	1.9176	O11	1.6678	O12	1.9315
O13	1.8427	O14	1.5525	O15	1.5368	O16	1.9432
O17	1.8029	O18	1.9286	O19	2.0602	O20	1.7782
O21	2.0035	O22	2.0181	O23	1.6847	O24	1.8028
O25	1.7524	O26	1.9825	O27	1.5542	O28	1.5096
O29	1.5988	O30	2.0715	O31	1.8147	O32	1.8167
O33	2.0961	O34	1.9278	O35	0.9098		

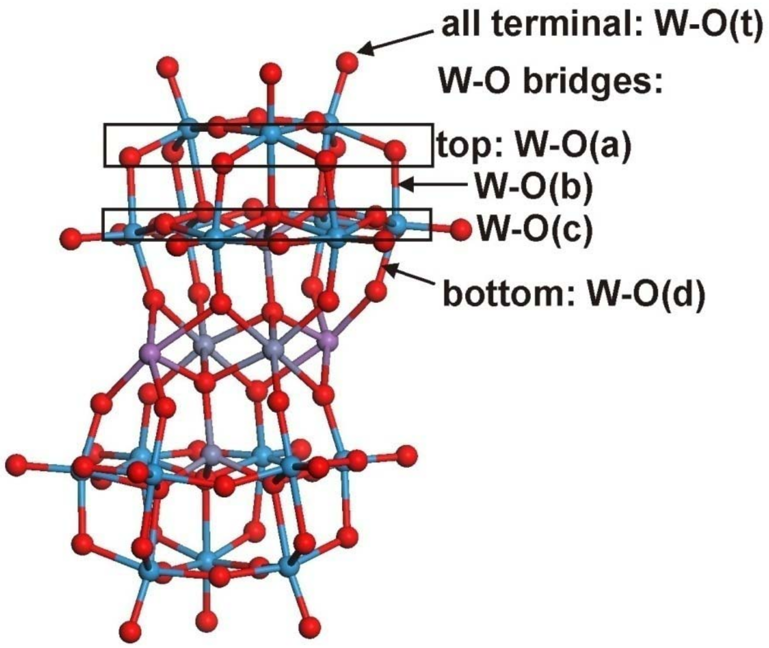

Figure 10.1. Assignment of bond types for comparison of theoretical and experimental data**.**

Table 10.7. Comparison of theoretical and experimental bond lengths for the ***α*-[Zn_2Sb_2]** type.

Bond type	***α*-NH4-[Zn_2Sb_2] (1a)**		***α*-[Zn_2Sb_2] (calc.)**
Sb-O	O(19)-Sb(1)	1.973(12)	2.010
	O(18)-Sb(1)	2.073(10)	2.108
	O(20)-Sb(1b)	2.380(10)	2.429
Zn-O (oct.)	Zn(1)-O(20)	2.096(10)	2.118
	Zn(1)-O(3)	2.072(10)	2.143
	Zn(1)-O(19)	2.134(9)	2.179
Zn-O (tet.)	Zn(2)-O(10)	1.945(9)	1.953
	Zn(2)-O(19)	1.943(12)	1.988
	Zn(2)-O(9)	1.934(14)	1.955
W-O(t)	O(2)-W(5)	1.725(12)	1.764
	O(1)-W(4)	1.729(16)	1.763
	O(16)-W(3)	1.739(11)	1.765
	O(11)-W(1)	1.733(11)	1.767

	O(14)-W(2)	1.752(11)	1.772
W-O(b)	O(8)-W(3)	1.971(10)	1.989
	O(5)-W(1)	2.027(10)	2.057
	O(7)-W(2)	2.084(10)	2.117
	O(9)-W(4)	2.193(14)	2.254
	2 x O(10)-W(5)	2.241(9)	2.317
W-O(a)	O(7)-W(5)	1.888(10)	1.891
	O(4)-W(4)	1.894(10)	1.911
	O(5)-W(5)	1.911(10)	1.907
	O(4)-W(5)	1.951(10)	1.950
	O(13)-W(5)	1.922(3)	1.964
	O(8)-W(4)	1.953(10)	1.983
W-O(c)	O(15)-W(3)	1.937(10)	1.953
	O(15)-W(2)	1.904(10)	1.955
	O(6)-W(1)	1.930(3)	1.960
	O(12)-W(1)	1.954(9)	1.949
	O(17)-W(3)	1.979(8)	1.975
	O(12)-W(2)	2.024(10)	2.000
W-O(c)	O(10)-W(2)	2.135(6)	2.165
	O(10)-W(1)	2.167(6)	2.191
	O(9)-W(3)	2.175(6)	2.197
W-O(d)	O(3)-W(2)	1.777(7)	1.809
	O(20)-W(1)	1.801(8)	1.861
	O(18)-W(3b)	1.870(7)	1.887

Symmetry transformation for **(1a)**: *b, -x+1,-y,-z+1*

Table10.8. Comparison of theoretical and experimental bond lengths for the ***β*-[Zn$_2$Sb$_2$]** type.

Bond type	***β*-Na-[Zn$_2$Sb$_2$] (2a)**		***β*-[Zn$_2$Sb$_2$] (calc.)**
Sb-O	O(19)-Sb(1)	1.964(7)	2.006
	O(16)-Sb(1)	2.007(8)	2.064
	O(18)-Sb(1)	2.047(8)	2.064
	O(34)-Sb(1)	2.482(7)	2.635
Zn-O (oct.)	O(34)-Zn(1)	2.101(7)	2.155
	O(3)-Zn(1)	2.056(8)	2.111
	O(24)-Zn(1)	2.078(9)	2.111
	O(20)-Zn(1)	2.086(7)	2.155
	O(19)-Zn(1b)	2.126(8)	2.161
	O(19)-Zn(1)	2.165(7)	2.161
Zn-O (tet.)	O(30)-Zn(2)	1.943(8)	1.965
	O(9)-Zn(2)	1.939(8)	1.973
	O(33)-Zn(2)	1.925(7)	1.965
	O(19)-Zn(2)	1.967(7)	2.034
W-O(t)	O(2)-W(7)	1.733(9)	1.763
	O(14)-W(2)	1.736(9)	1.766
	O(29)-W(3)	1.744(8)	1.758
	O(11)-W(4)	1.747(8)	1.766
	O(4)-W(9)	1.748(10)	1.758
	O(6)-W(5)	1.748(9)	1.772
	O(27)-W(6)	1.758(9)	1.763
	O(15)-W(1)	1.760(8)	1.763
	O(28)-W(8)	1.769(9)	1.773
W-O(a)	O(1)-W(9)	1.516(11)	1.854
	O(13)-W(7b)	1.870(9)	1.900
	O(21)-W(3)	1.891(8)	1.937
	O(22)-W(6)	1.893(7)	1.939
	O(23)-W(3)	1.894(8)	1.900
	O(5)-W(7)	1.900(8)	1.933
	O(12)-W(3)	1.908(8)	1.970
	O(7)-W(9)	1.918(8)	1.942
	O(10)-W(6)	1.929(9)	1.980
	O(21)-W(7)	1.931(8)	1.937
	O(8)-W(3)	1.941(8)	1.933

Table 10.8 (ctd.). Comparison of theoretical and experimental bond lengths for ***β*-[Zn_2Sb_2]** isomers.

Bond type	***β*-Na-[Zn_2Sb_2] (2a)**	***β*-[Zn_2Sb_2] (calc.)**
W-O(a)	O(31)-W(9) 1.949(8)	1.980
	O(31)-W(6) 1.953(9)	1.939
	O(32)-W(6) 1.963(8)	1.854
	O(22)-W(7) 1.989(8)	1.971
	O(12)-W(9) 1.989(8)	1.939
W-O(b)	O(22)-W(6) 1.893(7)	1.937
	O(8)-W(5) 1.972(8)	2.025
	O(13)-W(2) 2.072(8)	2.069
	O(5)-W(4) 2.084(8)	2.069
	O(23)-W(1b) 2.098(8)	1.955
	O(30)-W(6) 2.154(7)	2.159
	O(33)-W(3) 2.207(7)	2.201
	O(30)-W(9) 2.240(8)	2.187
	O(9)-W(7) 2.260(7)	2.271
W-O(d)	O(24)-W(8) 1.770(9)	1.805
	O(20)-W(4) 1.782(7)	1.837
	O(3)-W(1) 1.801(8)	1.805
	O(34)-W(2) 1.810(7)	1.837
	O(18)-W(5) 1.854(8)	1.910
W-O(c)	O(16)-W(8) 1.885(8)	1.910
	O(26)-W(2) 1.913(7)	1.976
	O(10)-W(4) 1.914(9)	1.980
	O(7)-W(5) 1.922(8)	1.970
	O(17)-W(1b) 1.945(8)	1.955
	O(25)-W(4b) 1.954(9)	1.942
	O(26)-W(1) 1.956(7)	1.976
	O(17)-W(5) 1.967(8)	1.942
	O(25)-W(2) 1.981(8)	1.955
	O(32)-W(8) 1.983(8)	2.025
	O(33)-W(1b) 2.129(8)	2.187
	O(30)-W(8) 2.141(7)	2.157
	O(9)-W(2b) 2.148(8)	2.065
	O(9)-W(4) 2.150(7)	2.159
	O(33)-W(5) 2.204(8)	2.201

Symmetry transformation for **(2a)**: *b, -x,-y+1,-z.*

Table 10.9. Comparison of theoretical and experimental bond lengths for **α-[$Zn_2Sb^{V}_2(OH)_2$] (3)**.

Bond type	**α-[$Zn_2Sb^{V}_2(OH)_2$] (exp.)**		**α-[$Zn_2Sb^{V}_2(OH)_2$] (calc.)**
Sb(V)-O	O(33)-Sb(1)	1.970(7)	1.987
	O(35)-Sb(1)	1.975(8)	1.994
	O(28)-Sb(1)	2.008(7)	2.057
	O(29)-Sb(1)	2.020(8)	2.057
	O(31)-Sb(1b)	2.051(7)	2.018
	O(34)-Sb(1)	2.063(7)	2.018
Zn-O (oct.)	O(32)-Zn(1)	1.987(8)	2.013
	O(30)-Zn(1b)	2.022(7)	2.013
	O(33)-Zn(1b)	2.049(7)	2.118
	O(33)-Zn(1)	2.093(7)	2.118
	O(34)-Zn(1)	2.177(7)	2.301
	O(31)-Zn(1)	2.184(8)	2.301
Zn-O (tet.)	O(25)-Zn(2)	1.904(7)	1.974
	O(27)-Zn(2)	1.908(7)	1.938
	O(33)-Zn(2)	1.918(7)	1.928
	O(26)-Zn(2)	1.927(7)	1.928
W-O(t)	O(1)-W(1)	1.728(8)	1.754
	O(3)-W(3)	1.730(8)	1.754
	O(2)-W(2)	1.731(8)	1.755
	O(11)-W(9)	1.718(8)	1.763
	O(21)-W(8)	1.722(8)	1.756
	O(16)-W(5)	1.728(8)	1.753
	O(19)-W(7)	1.740(8)	1.756
	O(18)-W(6)	1.745(9)	1.763
	O(14)-W(4)	1.745(8)	1.753
W-O(b)	O(10)-W(8)	1.959(7)	1.973
	O(23)-W(9)	1.965(7)	2.083
	O(7)-W(5)	2.002(8)	1.968
	O(8)-W(6)	2.008(8)	2.083
	O(24)-W(4)	2.048(7)	1.968
	O(9)-W(7)	2.053(7)	1.973
	O(26)-W(1)	2.190(7)	2.291
	O(25)-W(3)	2.205(7)	2.291
	O(27)-W(2)	2.218(7)	2.231

Table 10.9 (ctd.). Comparison of theoretical and experimental bond lengths for **α-[$Zn_2Sb^{V}_2(OH)_2$] (3)**.

Bond type	α-[$Zn_2Sb^{V}_2(OH)_2$] (exp.)		α-[$Zn_2Sb^{V}_2(OH)_2$] (calc.)
W-O(a)	O(22)-W(1)	1.893(7)	1.954
	O(24)-W(3)	1.894(7)	1.951
	O(9)-W(2)	1.901(7)	1.960
	O(8)-W(1)	1.905(8)	1.894
	O(5)-W(2)	1.907(7)	1.925
	O(4)-W(3)	1.907(7)	1.943
	O(5)-W(3)	1.926(7)	1.954
	O(7)-W(1)	1.931(8)	1.951
	O(10)-W(2)	1.936(7)	1.960
	O(22)-W(2)	1.937(7)	1.925
	O(4)-W(1)	1.939(7)	1.943
	O(23)-W(3)	1.968(7)	1.894
W-O(c)	O(12)-W(9)	1.899(8)	2.038
	O(13)-W(4)	1.916(7)	1.964
	O(15)-W(6)	1.916(8)	1.943
	O(6)-W(8)	1.917(7)	1.949
	O(15)-W(7)	1.929(8)	1.949
	O(17)-W(5)	1.938(8)	1.913
	O(20)-W(8)	1.939(8)	1.967
	O(13)-W(5)	1.948(7)	1.964
	O(6)-W(9)	1.949(7)	1.943
	O(17)-W(6)	1.982(7)	2.038
	O(20)-W(7)	2.001(8)	1.967
	O(12)-W(4)	2.034(8)	1.913
	O(26)-W(6)	2.131(7)	2.174
	O(27)-W(7)	2.139(7)	2.195
	O(25)-W(4)	2.142(7)	2.203
	O(26)-W(5)	2.168(7)	2.203
	O(27)-W(8)	2.179(7)	2.195
	O(25)-W(9)	2.189(7)	2.174
W-O(d)	O(30)-W(7)	1.799(7)	1.915
	O(28)-W(5)	1.842(7)	1.980
	O(29)-W(6)	1.845(8)	1.806
	O(31)-W(9)	1.913(8)	1.806
	O(34)-W(8b)	1.919(7)	1.915
	O(32)-W(4b)	1.791(8)	1.980

Symmetry transformation for **(3)**: *b*, *-x,-y,-z.*

Table 10.10. Comparison of theoretical and experimental bond lengths for **β-[Zn$_2$Sb$^{V}{}_2$(OH)$_2$] (4)**.

Bond type	**β-[Zn$_2$Sb$^{V}{}_2$(OH)$_2$] (exp.)**		**β-[Zn$_2$Sb$^{V}{}_2$(OH)$_2$] (calc.)**
Sb(V)-O	O(35)-Sb(1)	1.944(9)	1.977
	O(16)-Sb(1)	1.960(8)	2.014
	O(19)-Sb(1)	1.962(8)	1.999
	O(18)-Sb(1)	1.999(8)	2.014
	O(34)-Sb(1)	2.014(8)	2.089
	O(20)-Sb(1)	2.030(8)	2.089
Zn-O (oct.)	O(3)-Zn(1)	1.991(8)	2.008
	O(24)-Zn(1)	1.991(9)	2.008
	O(19)-Zn(1)	2.060(8)	2.109
	O(34)-Zn(1)	2.014(8)	2.370
	O(20)-Zn(1)	2.306(9)	2.370
	O(19)-Zn(1a)	2.111(8)	2.109
Zn-O (tet.)	O(30)-Zn(2)	1.908(8)	1.949
	O(9)-Zn(2)	1.912(8)	1.962
	O(33)-Zn(2)	1.928(8)	1.949
	O(19)-Zn(2)	1.951(8)	2.028
W-O(t)	O(2)-W(7)	1.702(10)	1.755
	O(4)-W(9)	1.724(10)	1.752
	O(27)-W(6)	1.734(10)	1.754
	O(29)-W(3)	1.720(9)	1.754
	O(6)-W(5)	1.715(9)	1.755
	O(11)-W(4)	1.702(9)	1.755
	O(15)-W(1)	1.736(9)	1.763
	O(28)-W(8)	1.743(10)	1.752
	O(14)-W(2)	1.731(9)	1.763
W-O(b)	O(22)-W(6)	1.896(9)	1.967
	O(31)-W(6)	1.938(10)	1.940
	O(12)-W(9)	1.937(8)	1.967
	O(5)-W(4a)	1.954(9)	1.968
	O(13)-W(2a)	1.969(8)	1.968
	O(8)-W(5)	1.979(9)	2.041
	O(23)-W(1)	2.073(9)	1.940
	O(33)-W(3)	2.220(8)	2.197
	O(9)-W(7)	2.236(8)	2.259

Table 10.10 (ctd.). Comparison of theoretical and experimental bond lengths for **β-[$Zn_2Sb^{V}_{2}(OH)_2$] (4)**

Bond type	**β-[$Zn_2Sb^{V}_{2}(OH)_2$] (exp.)**		**β-[$Zn_2Sb^{V}_{2}(OH)_2$] (calc.)**
W-O(a)	O(1)-W(9)	1.866(10)	1.864
	O(21)-W(7)	1.878(9)	1.924
	O(8)-W(3)	1.899(8)	1.903
	O(23)-W(3)	1.904(9)	2.005
	O(32)-W(6)	1.911(10)	1.903
	O(13)-W(7)	1.920(8)	1.949
	O(5)-W(7)	1.959(9)	1.949
	O(12)-W(3)	1.929(8)	1.940
	O(21)-W(3)	1.953(9)	1.967
	O(31)-W(9)	1.961(10)	1.967
	O(7)-W(9)	1.965(9)	1.970
	O(10)-W(6a)	1.991(8)	2.005
W-O(c)	O(26)-W(2)	1.862(9)	1.905
	O(7)-W(5)	1.889(9)	1.915
	O(9)-W(2)	2.155(8)	2.189
	O(10)-W(4)	1.887(9)	1.905
	O(17)-W(1)	1.927(9)	1.903
	O(25)-W(4)	1.959(8)	1.991
	O(26)-W(1a)	1.988(9)	2.005
	O(17)-W(5)	1.980(8)	2.041
	O(25)-W(2)	1.992(8)	1.991
	O(9)-W(4)	2.175(8)	2.189
	O(33)-W(1)	2.143(8)	2.165
	O(30)-W(8)	2.155(8)	2.165
W-O(d)	O(24)-W(8)	1.794(8)	1.958
	O(18)-W(5)	1.865(8)	1.915
	O(34)-W(2)	1.933(8)	1.958
	O(20)-W(4)	1.982(8)	1.958
	O(3)-W(1)	1.776(8)	1.807

Symmetry transformation for **(4)**: *a*, *-x+1,-y+1,-z+1.*

Table 10.11. Crystallographic data and structural refinements for compounds **(5)** and **(6).**

	(5)	**(6)**
empirical formula	$N_5O_{105}Sb_2W_{18}Zn_7$	$N_2Na_2O_{113}Sb_2W_{18}Zn_9$
formula weight ($g\cdot mol^{-1}$)	5760.44	6023.13
temperature (K)	183(2) K	183(2) K
wavelength (Å)	0.71073	0.71073
crystal system, S. G.	*triclinic, P-1*	*triclinic, P-1*
a (Å)	12.2783(3)	13.5263(2)
b (Å)	13.4654(4)	16.2490(3)
c (Å)	16.2018(5)	23.9792(3)
α (deg)	89.352(2)	75.2216(13)
β (deg)	80.399(2)	79.1367(12)
γ (deg)	63.474(3)	76.9441(16)
volume ($Å^3$)	2357.06(12)	4916.16(11)
Z	1	2
Abs coefficient (mm^{-1})	24.292	23.788
d (calcd.) ($Mg\cdot m^{-3}$)	4.058	4.069
F(000)	2519	5288
crystal size (mm^3)	0.22 x 0.18 x 0.15	0.18 x 0.13 x 0.05
goodness-of-fit on F^2	0.939	0.957
Reflections collected / unique	41560 / 11187	83437 / 23396
R(into)	0.0612	0.0629
$R_1[I > 2\sigma(I)]$	0.0414	0.0445
wR_2 indices $[I > 2\sigma(I)]$	0.0857	0.0927

$R_1 = \sum(Fo - Fc)/\sum Fo$ *and* $wR_2 = \{\sum w(Fo^2 - Fc^2)^2/\sum w(Fo^2)^2\}^{1/2}$

Table 10.12. Selected bond distances for compounds **(5)** and **(6)**.

Bond type	**(5)**		**(6)**	
Sb-O	Sb-O(29)	2.364(8)	Sb(1)-O(9)	1.981(7)
	Sb-O(30)	2.370(8)	Sb(1)-O(34)	2.066(8)
	Sb(b)-O(32)	1.978(7)	Sb(1)-O(35)	2.440(8)
	Sb(b)-O(31)	2.091(8)	Sb(1)-O(50)	2.049(8)
	Sb-O(33)	2.062(8)	Sb(1a)-O(82)	2.425(8)
Zn-O (octahedral)	Zn(1)-O(28)	2.081(8)	Zn(1)-O(9)	2.135(8)
	Zn(1)-O(29)	2.083(8)	Zn(1a)-O(9)	2.134(8)
	Zn(1b)-O(30)	2.087(8)	Zn(1)-O(35)	2.058(8)
	Zn(1)-O(32)	2.138(7)	Zn(1)-O(46)	2.090(8)
	Zn(1b)-O(32)	2.126(7)	Zn(1a)-O(77)	2.086(9)
	Zn(1)-O(34)	2.086(7)	Zn(1)-O(82)	2.111(8)
Zn-O (tetrahedral)	Zn(2)-O(25)	1.937(7)	Zn(2)-O(9)	1.960(8)
	Zn(2)-O(26)	1.944(8)	Zn(2)-O(39)	1.938(8)
	Zn(2)-O(27)	1.943(7)	Zn(2)-O(62)	1.947(7)
	Zn(2)-O(32)	1.929(7)	Zn(2)-O(67)	1.947(8)
Zn-O (linker)	Zn(3a)-O(13)	2.079(7)	Zn(5)-O(38)	2.071(8)
	Zn(3)-O(23)	2.074(9)	Zn(5)-O(59)	2.095(8)
			Zn(6)-O(55)	2.097(8)
			Zn(6)-O(54)	2.090(8)
W-O$_{(t)}$ (terminal)	W(1)-O(2)	1.732(9)	W(1)-O(29)	1.728(8)
W-O$_{(b)}$ (corner-sharing)	W(1)-O(7)	1.937(8)	W(1)-O(12)	2.069(8)
	W(1)-O(8)	1.892(7)	W(1)-O(75)	1.945(8)
	W(1)-O(9)	1.910(8)	W(1)-O(78)	1.776(8)
	W(1)-O(10)	1.917(7)	W(1)-O(79)	1.947(8)
W-O$_{(c)}$ (edge-sharing)	W(1)-O(27)	2.211(7)	W(1)-O(69)	2.171(7)

Symmetry transformation for **(5)**: *a, -x,-y,-z*; *b, -x+1,-y,-z*; **(6)**: *a, -x,-y,-z+2*

Table 10.13. BVS calculations for **(5)**.

Zn1	2.0446	Zn2	2.1690	Zn3	1.9839	Sb1	3.0980	W1	6.0250
W2	5.9686	W3	6.0315	W4	6.0171	W5	5.9958	W6	5.9542
W7	5.9068	W8	5.9051	W9	5.9811	O1	1.5373	O2	1.5534
O3	1.5566	O4	1.9911	O5	1.8002	O6	1.7553	O7	1.9777
O8	1.6911	O9	1.7587	O10	2.0025	O11	1.8239	O12	1.7366
O13	1.8619	O14	1.9715	O15	1.6145	O16	1.7577	O17	1.5737
O18	1.9571	O19	1.5176	O20	1.7827	O21	1.5764	O22	2.0569
O23	1.9293	O24	1.8175	O25	2.0442	O26	2.1241	O27	2.0646
O28	1.8244	O29	2.9962	O30	2.0013	O31	1.8744	O32	1.6595
O33	2.0105	O34	1.7925						

Table 10.14. BVS calculations for **(6)**.

Zn1	1.9276	Zn2	2.1389	Zn5	1.9924	Zn6	2.0476	Sb1	2.9840
W1	6.0073	W2	6.0888	W3	6.0575	W4	5.7346	W5	6.0522
W6	5.9065	W7	5.9144	W8	5.8140	W9	5.8018	O3	1.7470
O4	1.9760	O10	2.0230	O12	1.7281	O17	1.7675	O21	2.0307
O26	1.7413	O28	1.8648	O29	1.5681	O30	1.7075	O31	1.7814
O32	1.9380	O33	1.8286	O36	1.8739	O45	1.5674	O47	1.7443
O51	1.6841	O52	1.9697	O53	2.0521	O54	1.8576	O56	1.6255
O59	1.7826	O65	1.9112	O69	2.0440	O74	1.7282	O75	1.7571
O78	1.7664	O79	1.9997	O88	1.7670				

Table 10.15. Crystallographic data for compounds **Zn_4_$Zn_{5.2}$ (7a, 7b)**, **Zn_5_$Zn_{5.2}$ (8)**, and **Zn_6 (9a)**.

	Zn_4_$Zn_{5.2}$ (7a)	**Zn_4_$Zn_{5.2}$ (7b)**	**Zn_5_$Zn_{5.2}$ (8)**	**Zn_6 (9a)**
empirical formula	$Na_{9.4}O_{155.1}Sb_3W_{27}Zn_{7.6}$	$Na_{3.4}O_{155.6}Sb_3W_{27}Zn_{7.6}$	$Cl_6Na_{10.8}O_{186.2}Sb_4W_{36}Zn_{11.2}$	$Cl_{2.5}Na_2O_{55.5}SbW_9Zn_3$
Formula weight ($g \cdot mol^{-1}$)	8523.72	8393.78	11277.94	2995.11
temperature (K)	183(2) K	183(2) K	183(2) K	183(2) K
wavelength (Å)	0.71073	0.71073	0.71073	0.71073
crystal system, space group	triclinic, *P-1*	triclinic, *P-1*	monoclinic, *P 21/m*	monoclinic, *I 2/m*
a (Å)	18.9374(3)	18.4894(4)	17.9505(5)	13.8088(3)
b (Å)	19.3606(3)	19.0382(4)	29.1987(7)	22.2457(6)
c (Å)	23.4938(4)	22.9996(5)	19.9727(6)	18.8037(7)
α (deg)	97.481(1)	95.6868(18)	90	90.00
β (deg)	106.936(2)	111.139(2)	111.596(3)	91.711(2)
γ (deg)	114.482(2)	113.156(2)	90	90.00
volume ($Å^3$)	7181.1(2)	6663.3(2)	9733.5(5)	5773.7(3)
Z	2	2	2	4
Abs coeff. (mm^{-1})	23.471	25.274	23.282	19.768
density (calcd.) ($Mg \cdot m^{-3}$)	3.942	4.184	3.848	3.446
F(000)	7446	7322	9829	5262
crystal size (mm^3)	0.37 × 0.10 × 0.08	0.28× 0.08× 0.06	0.32 × 0.15 × 0.08	0.42 × 0.22 × 0.18
goodness-of-fit on F^2	1.036	1.044	1.044	1.099
$R_1[I > 2\sigma(I)]$	0.0552	0.0700	0.0623	0.0459
$wR_2\ [I > 2\sigma(I)]$	0.1460	0.1486	0.1637	0.1114

$R_1 = \sum(Fo - Fc)/\sum Fo$ *and* $wR_2 = \{\sum w(Fo^2 - Fc^2)^2/\sum w(Fo^2)^2\}^{1/2}$

Table 10.16. Crystallographic data for compounds **Zn_6 (9b)**, **Zn_5 (10)**, **Zn_5 (11a)**, and **Zn_5 (12b)**.

	Zn_6 (9b)	**Zn_5 (10)**	**Zn_5 (11b)**	**Zn_5 (11a)**
empirical formula	$Cl_6N_{12}O_{82}Sb_2W_{18}$ Zn_6	$Cl_2Na_3O_{104}Sb_2W_{18}$ Zn_5	$C_4ClNa_7O_{110}Sb_2$ W_{18} Zn_5	$C_4Na_8O_{102}Sb_2W_{18}$ Zn_5
formula weight (g·mol^{-1})	5637.84	5683.52	5884.07	5743.61
temperature (K)	183(2) K	183(2) K	183(2) K	183(2) K
wavelength (Å)	0.71073	0.71073	0.71073	0.71073
crystal system, space group	cubic, *Pa-3*	monoclinic, *P21/n*	triclinic, *P-1*	triclinic, *P-1*
a (Å)	20.4570(2)	13.1622(2)	14.6516(2)	12.8845(2)
b (Å)	20.4570(2)	18.4520(2)	16.9215(3)	17.2672(2)
c (Å)	20.4570(2))	17.8549(2)	21.8451(3)	24.7811(3)
α (deg)	90	90.00	85.3900(10)	109.0320(10)
β (deg)	90	90.0400(10)	85.8240(10)	92.3630(10)
γ (deg)	90	90.00	66.0200(10)	106.6400(10)
volume (Å^3)	8561.03(14)	4336.40(9)	4927.72(13)	4938.19(11)
Z	4	2	2	2
Abs coeff. (mm^{-1})	26.640	25.940	22.828	22.746
density (calcd.) (Mg·m^{-3})	4.374	4.353	3.966	3.863
F(000)	9824	4966	5164	5024
crystal size (mm^3)	0.11 × 0.05 × 0.05	0.21× 0.20 × 0.18	0.35 × 0.18× 0.15	0.35 × 0.21× 0.15
goodness-of-fit on F^2	0.926	1.054	1.085	1.093
$R_1[I > 2\sigma(I)]$	0.0375	0.0397	0.0394	0.0476
wR_2 $[I > 2\sigma(I)]$	0.0652	0.0890	0.1027	0.1348

$R_1 = \sum(Fo - Fc)/\sum Fo$ *and* $wR_2 = \{\sum w(Fo^2 - Fc^2)^2/\sum w(Fo^2)^2\}^{1/2}$

Table 10.17. Crystallographic data for compounds **Zn_4 (12a)**, **Zn_4 (12b)**, **Zn_4 (12c)** and **$Zn_{3.5}$ (13)**.

	Zn_4 (12a)	**Zn_4 (12b)**	**Zn_4 (12c)**	**$Zn_{3.5}$ (13)**
empirical formula	$CNa_9O_{100}Sb_2W_{18}Zn_4$	$C_2Cl_3N_5Na_{6.87}O_{99.5}Sb_2W_{18}Zn_{4.13}$	$Cl_3N_4Na_9O_{87}Sb_2W_{18}Zn_4$	$Cl_2Na_9O_{97.5}Sb_2W_{18}Zn_{3.5}$
formula weight (g·mol^{-1})	5633.20	5773.14	5575.58	5619.41
temperature (K)	183(2) K	183(2) K	183(2) K	183(2) K
wavelength (Å)	0.71073	0.71073	0.71073	0.71073
crystal system, space group	triclinic, *P-1*	orthorhombic, *P212121*	orthorhombic, *P212121*	triclinic, *P-1*
a (Å)	12.9159(2)	15.3168(5)	19.3332(4)	13.2947(3)
b (Å)	16.1825(2)	24.8457(9)	19.3423(8)	17.9950(3)
c (Å)	22.6036(3)	26.740(3)	27.2404(12)	21.0745(4)
α (deg)	104.3200(10)	90.00	90	77.724(2)
β (deg)	96.6540(10)	90.00	90	85.282(2)
γ (deg)	105.8740(10)	90.00	90	68.877(2)
volume (Å^3)	4316.84(10)	10176.1(12)	10186.5(7)	4595.44(16)
Z	2	4	4	2
Abs coeff. (mm^{-1})	25.750	21.951	21.890	24.116
density (calcd.) (Mg·m^{-3})	4.374	3.768	3.636	4.061
F(000)	4918	10110	9712	4904
crystal size (mm^3)	0.26 × 0.10 × 0.05	0.38× 0.35 × 0.25	0.39 × 0.13 × 0.11	0.15 × 0.13 × 0.05
goodness-of-fit on F^2	0.959	1.048	1.056	1.028
$R_1[I > 2\sigma(I)]$	0.0298	0.0545	0.0725	0.0450
wR_2 $[I > 2\sigma(I)]$	0.0658	0.1320	0.1492	0.1132

$R_1 = \sum(Fo - Fc)/\sum Fo$ *and* $wR_2 = \{\sum w(Fo^2 - Fc^2)^2/\sum w(Fo^2)^2\}^{1/2}$

Table 10.18. Bond valence sums (BVS) for **Zn$_4$_Zn$_{5.2}$ (7a, 7b)**, **Zn$_5$_Zn$_{5.2}$ (8)**, and **Zn$_6$ (9a)**.

Zn$_4$_Zn$_{5.2}$ (7a)

Zn1	2.1010	Zn2	1.9684	Zn3	2.1795	Zn4	2.0618
Zn5	2.1371	Zn6	2.0381	Zn7	1.9517	Sb1	2.9534
Sb2	2.9977	Sb3	2.9904	W1	6.2422	W2	5.9633
W3	6.0282	W4	6.0082	W5	6.1323	W6	5.8627
W7	6.1017	W8	6.0207	W9	6.2158	W10	6.0895
W11	6.1273	W12	6.1701	W13	6.0662	W14	5.9996
W15	6.0858	W16	6.1066	W17	6.0525	W18	6.1959
W19	6.2193	W20	6.1455	W21	6.0388	W22	5.9551
W23	5.9749	W24	5.9749	W25	6.0989	W26	5.9964
W27	5.9725	Na1	1.1145	Na2	1.0617		

Zn$_4$_Zn$_{5.2}$ (7b) (Disordered W atoms were excluded)

Zn1	2.1002	Zn2	2.1217	Zn3	1.9522	Zn4	2.1247
Zn5	2.0070	Zn6	1.8876	Zn7	2.0886	Sb1	3.0084
Sb2	2.9870	Sb3	3.0164	W1	6.0890	W2	6.0189
W3	6.2695	W4	6.0633	W5	6.1355	W6	5.9091
W7	6.1307	W8	6.1415	W9	5.8985	W11	6.1273
W12	6.2807	W13	6.2866	W14	6.0984	W19	6.0302
W20	5.9560	W21	6.0842	W25	6.1268	W26	6.2898
W27	6.1015	Na1	1.1165	Na2	1.0814	Na1	1.1165

Zn$_5$_Zn$_{5.2}$ (8)

Zn1	2.0657	Zn2	2.0306	Zn3	2.3509	Zn4	1.9204
Zn5	2.3730	Zn6	2.2383	Na1	1.0062	Sb1	3.1525
Sb2	2.9597	Sb3	2.8858	W1	6.1551	W2	6.1516
W3	5.9077	W4	6.1594	W5	6.1781	W6	6.0161
W7	6.0577	W8	6.2436	W9	6.1767	W10	6.2448
W11	6.2129	W12	5.7972	W13	6.0636	W14	6.0324
W15	6.0355	W16	6.0021	W17	6.1377	W18	6.2369
W19	6.3357	Sb4					

Zn6 (9a)

Zn1	1.9642	Zn2	2.0202	W1	5.9731	W2	5.9884
W3	5.9459	W4	5.9885	W4	5.9515	Sb1	3.1322
Cl1	0.5059	Cl2	0.4705				

Table 10.19. Bond valence sums (BVS) for **Zn$_6$ (9b)**, **Zn$_5$ (10)**, **Zn$_5$ (11a)**, and **Zn$_5$ (11b)**.

Zn6 (9b)							
Zn1	1.9627	Cl1	0.5367	Sb1	3.1367	W1	6.1020
W2	6.0204	W3	6.0348				
Zn$_5$ (10)							
Zn1	2.0178	Zn2	1.9872	Zn3	1.7560	Na1	1.3497
Sb1	2.9161	W1	6.1090	W2	6.0546	W3	6.1400
W4	6.0417	W5	6.0612	W6	6.0045	W7	6.0436
W8	6.1674	W9	6.1058				
Zn$_5$ (11a)							
Zn1	2.1034	Zn2	2.0178	Zn3	2.1122	Zn4	1.9260
Zn5	1.8177	Na1	1.0432	Sb1	2.9202	Sb2	2.9508
W1	6.1802	W2	6.1738	W3	6.0888	W4	6.0681
W5	6.0933	W6	6.1144	W7	6.0896	W8	6.1000
W9	6.0492	W10	6.1078	W11	6.2000	W12	6.1056
W13	6.1329	W14	6.0299	W15	6.1269	W16	5.9737
W17	6.3062	W18	6.0397				
Zn$_5$ (11b)							
Zn1	2.1359	Zn2	2.0035	Zn3	2.0795	Zn4	1.9677
Zn5	2.1490	Na1	1.1157	Sb1	3.0728	Sb1	2.9375
W1	6.1151	W2	6.2581	W3	5.8676	W4	5.9575
W5	5.8611	W6	6.0404	W7	6.2257	W8	6.0343
W9	5.9265	W10	6.0034	W11	6.1007	W12	6.1411
W13	6.0847	W14	6.0483	W15	6.1621	W16	6.1164
W17	6.0603	W18	6.1490				

Table 10.20. Bond valence sums (BVS) for **Zn$_4$ (12a), Zn$_4$ (12b), Zn$_4$ (12c) and Zn$_{3.5}$ (13)**.

Zn$_4$ (12a)							
Zn1	2.1080	Zn2	1.9915	Zn3	2.1478	Zn4	2.1467
Na1	1.0400	Na2	1.0945	Sb1	2.9095	Sb2	2.9433
W1	6.0987	W2	6.0671	W3	6.0880	W4	6.0839
W5	6.1373	W6	6.1402	W7	6.0186	W8	6.0348
W9	6.0856	W10	6.1009	W11	6.1185	W12	6.1107
W13	6.0680	W14	6.0642	W15	6.0273	W16	6.1349
W17	6.0895	W18	6.1377				
Zn$_4$ (12b)							
Zn1	2.1349	Zn2	2.0124	Zn3	2.1953	Zn4	2.1896
Na1	1.0969	Na2	1.1675	Sb1	2.8644	Sb2	2.9082
W1	6.2356	W2	6.3261	W3	5.9509	W4	6.1529
W5	6.1161	W6	6.0460	W7	6.0194	W8	6.1544
W9	6.0335	W10	6.1179	W11	6.2375	W12	6.0638
W13	6.1188	W14	6.1882	W15	6.0471	W16	6.0904
W17	6.0457	W18	5.9521				
Zn$_4$ (12c)							
Zn1	2.0682	Zn2	1.8778	Zn3	2.1153	Zn4	2.1809
Na1	1.2616	Na2	1.2616	Sb1	3.0375	Sb2	3.0003
W1	6.4278	W2	6.2217	W3	6.1115	W4	6.2366
W5	6.0063	W6	6.0056	W7	6.0671	W8	6.1049
W9	5.9780	W10	6.0353	W11	6.4154	W12	5.9516
W13	6.1636	W14	6.2073	W15	6.3222	W16	5.7588
W17	6.0754	W18	6.4661				
Zn$_{3.5}$ (13)							
Zn1	2.1388	Zn2	2.1642	Zn3	2.0869	Na1	1.1366
Na1	1.0863	Na3	1.2036	Sb1	2.8193	Sb1	2.9409
W1	6.0831	W2	6.1839	W3	6.1642	W4	6.0607
W5	5.9553	W6	6.1527	W7	6.2057	W8	5.9830
W9	6.0342	W10	5.9933	W11	6.0925	W12	6.0026
W13	6.0757	W14	6.2384	W15	6.0351	W16	6.0412
W17	6.2023	W18	6.1435				

Lubin Ni

Institute of Inorganic Chemistry, University of Zurich,
Phone: +41 44 63 54678 Email: lubin.ni@aci.uzh.ch

Personal Information

Male, P.R. China, born on 13th August, 1982

Education

09/2009-Present PhD in Institute of Inorganic Chemistry, University of Zurich, Switzerland (Supervisor: Prof. G. R. Patzke)
Research topic: Novel Functional Polyoxometalate (POM) Materials: Synthetic Strategies and Applications.

09/2006-08/2009 M.Sc in Physical Chemistry, Xiamen University, China (Supervisor: Prof. Zhao-Hui Zhou)
Research topic: Synthesis, Characterization and Performance of Transition Metal Complexes with Aminopolycarboxylic Acids.

09/2001-07/2005 B.Sc in Applied Chemisty, AnHui Normal University, China
Research topic: Preparation and Performance of TiO_2 Photocatalytic Materials.

Publications

1. **Lubin Ni**, Bernhard Spingler, Kim K. Baldridge*, and Greta R. Patzke*, *Getting to the Core: Synthetic Control, Catalytic Activity and Reaction Pathways of Zn-Polyoxotungstate Oxidation Catalysts*. To be submitted.

2. **Lubin Ni,** Bernhard Spingler, Stephen Weyeneth, and Greta R. Patzke*, *Trilacunary Keggin-type POMs as Versatile Building Blocks for Lanthanoid Silicotungstates*. *Eur. J. Inorg. Chem.*, **2013**, 1681–1692. (Special Issue: Polyoxometalates, Invited paper).

3. **Lubin Ni,** Jörg Patscheider, Kim K. Baldridge*, and Greta R. Patzke*, *New Perspective on Polyoxometalates Catalysts: Alcohol Oxidation with Zn/Sb-Polyoxotungstate*. *Chem. Eur. J.* **2012**, 18, 13293–13298.

4. **Lubin Ni,** and Greta R. Patzke*, *1D- and 2D- architectures via Self-assembly of the Novel Sandwich-type Polyoxometalate* $[Zn_2Sb_2(B\text{-}\alpha\text{-}ZnW_9O_{34})_2]^{14-}$. *CrystEngComm*. **2012**, 14, 6778–6782.

5. **Lubin Ni,** Firsat Hussain, Bernhard Spingler, Stephen Weyeneth, and Greta R. Patzke*, *Lanthanoid-Containing Open Wells-Dawson Sillcotungstates: Synthesis, Crystal Strctures, and Properties*. *Inorg. Chem*, **2011**, 50, 4944–4955.

6. **Lu-Bin Ni,** Rong-Hua Zhang, Qiong-Xin Liu, Hua-Lin Zhang, Zhao-Hui Zhou*, *pH- and mol-ratio Dependent Formation of Zinc(II) Coordination Polymers with Iminodiacetic acid: Synthesis, Spectroscpic, Crystal Structure and Thermal Studies. J Solid State Chem*. **2009**, 182, 2698–2706.

7. Qiong-Xin Liu, **Lu-Bin Ni,** Fu-Pei Liang, Zhao-Hui Zhou*, Hui-Lin Wan, *pH and Molar Ratio Dependent Formations of Monomeric, Dimeric and Tetrameric Cobalt Malate Complexes. Polyhedron*. **2009**, 28, 917–922.

Conferences

1. **Lubin Ni,** and Greta R. Patzke. T*rilacunary Keggin-type POMs as Versatile Building Blocks for Lanthanoid-substituted POMs (LSPs) and Transition metal-substituted POMs (TMSPs).* The 2nd Frontiers in Metal Oxide Cluster Science Workshop (FMOCS 2012), Lanzarote, Spain (Oral communication)

2. **Lubin Ni,** and Greta R. Patzke. *Self-assembly of the Novel Zn/Sb-containing polyoxometalates.* The 7th Dorothy Crowfoot Hodgkin (DCH) symposium, Zurich, Switzerland (Poster)

3. **Lubin Ni,** Jörg Patscheider, Kim K. Baldridge, and Greta R. Patzke. *Novel Zn/Sb-containing polyoxometalates: crystal structures, modeling and catalytic studies.* Swiss Chemical Society (SCS) Fall Meeting 2012, Zurich, Switzerland (Poster)

4. **Lubin Ni,** Bernhard Spingler, Stephen Weyeneth, and Greta R. Patzke. *Lanthanoid Uptake of the Open Wells-Dawson Silicotungstate Anion* α-$[Si_2W_{18}O_{66}]^{16-}$*: Synthesis, Crystal Structures and Characterization.* The 6th Dorothy Crowfoot Hodgkin (DCH) symposium, Zurich, Switzerland (Poster)

5. L**ubin Ni,** Firasat Hussain, Bernhard Spingler, Stephen Weyeneth, and Greta R. Patzke. *New Lanthanoid-Containing Open Wells-Dawson Silicotungstates.* Swiss Chemical Society (SCS) Fall Meeting 2011, Lausanne, Switzerland (Poster)

Workshop and Trainings

1. 11/2012 Powder Diffraction School Structure and Microstructure, Paul Scherrer Institute (PSI), Switzerland.
2. 10/2012 Workshop OriginPro 9.0, Company ADDITIVE GmbH, University of Zurich, Switzerland.
3. 09/2011 Workshop on Computer methods in crystal structure systematics, Max Planck Institute for Solid State Research, Stuttgart, Germany.
4. 11/2010 MaNEP workshop on resonant X-ray techniques, Paul Scherrer Institute (PSI), Switzerland.
5. 11/2010-12/2010 Communications Skills for Leaders, Graduate School of Chemical and Molecular Sciences (CMSZH), University of Zurich, Switzerland.
6. 05/2010 English for work-Practical Skills B2, Sprachenzentrum der Universität und ETH Zürich, University of Zurich, Switzerland.
7. 04/2010 Teaching in English in a non-English speaking environment, University of Zurich, Switzerland.

Honors and Awards

2009-2012 China Scholarship Council Doctoral Fellowship

2012 Forschungskredit Fellowship Fund of the University of Zurich

2011 Excellent Award, The 6th "ChunHuiBei" Innovative and Entrepreneurial Contest, Guangzhou, China

2009 Outstanding Graduate Students of Xiamen University, China

2008 Excellent Student Award of Xiamen University, China

2002-2004 Outstanding Student Scholarship of AnHui Normal University, China